

Alma Mater Studiorum – Università di Bologna

DOTTORATO DI RICERCA IN

Chimica

Ciclo XXX

Settore Concorsuale: 03/C1

Settore Scientifico Disciplinare: CHIM06

TITOLO TESI

**Design, synthesis and characterizations of hybrid
nanosystems: nanomedicine applications in theranostics**

Presentata da: Ilaria Monaco

Coordinatore Dottorato

Supervisore

Prof. Aldo Roda

Prof. Mauro Comes Franchini

Esame finale anno 2018

Index

Abstract	1
Table of acronyms	2
1. Introduction	5
1.1 State of the art in Cancer Nanomedicine	5
1.2 Drug Delivery and theranostic nanosystems	8
1.2.1 Polymeric nanoparticles as drug delivery and theranostic nanosystems.....	13
1.2.2 Poly(d,l-lactic-co-glycolic acid)-b-poly(ethylene glycol)	16
1.2.3 Methods of preparations for polymeric nanoparticles	18
1.3 Hyperthermia therapy	21
1.3.1 Metallic nanoparticle as photothermal agents in hyperthermia therapy.....	25
1.3.2 Gold nanorods as photothermal agents.....	28
1.3.3 Magnesium nanoparticles as photothermal agents	31
1.4 Nanomaterials as diagnostic and imaging tools in nanomedicine	35
1.4.1 Photoacoustic imaging (PAI)	37
1.4.2 Contrast agents for photoacoustic imaging (PAI)	40
1.4.3 Gold nanostructures as PAI contrast agents	42
1.4.4 Magnetic Resonance Imaging (MRI)	45
1.4.5 Super paramagnetic nanoparticles as MRI contrast agents	48
1.5 Surface chemistry of metal nanoparticles	51
1.5.1 Self-assembled monolayer (SAM)	51
1.5.2 Silica shell as coating of metallic nanoparticles.....	53
2. Aim	57
3. Discussion	59
3.1 Synthesis of the precursors	59
3.1.1 Synthesis of the organic ligand 11-(4-mercaptobenzamido)undecanoate (ligand 1)	59
3.1.2 Organic functionalization of chitosan.....	61
3.1.3 Preparation of copolymers for polymeric nanocarriers	62
3.2. Polymeric nanoparticles as drug delivery systems against Glioblastoma Multiforme	64
3.2.1. Synthesis of chlorotoxin functionalized polymeric nanovectors for the treatment of Glioblastoma Multiforme in a combined approach with radiation therapy.....	65
3.2.2. Synthesis of aptamer functionalized polymeric nanovectors for the treatment of Glioblastoma thought the BBB	74
3.3 Synthesis of nanosystems for hyperthermia therapy	83

3.3.1 Gold nanorods as tools for photothermal therapy of Barrett Oesophagus	84
3.3.2 Magnesium nanoparticles as a highly biocompatible photothermal agent for hepatocellular carcinoma treatment.....	96
3.4 Synthesis of multicomponent nanosystems as dual imaging and theranostic agents against cancer.....	104
3.4.1. Synthesis of Dumbbell-Like Gold-Iron Oxide Nanoparticles (dl-AuFe NPs) as multifunctional nanosystems	106
3.4.2. Synthesis of a novel magnetic resonance–photoacoustic dual imaging nanosystem based on core–shell Fe ₃ O ₄ @SiO ₂ @Au NPs	116
4. Conclusions	127
5. Experimental section.....	129
5.1 Synthesis of ethyl 12-(4-mercaptobenzamido)dodecanoate (ligand 1)	129
5.1.1 Synthesis of 4,4'-disulfanediyldibenzoic acid.....	129
5.1.2 Synthesis of ethyl 11-aminododecanoate	130
5.1.3 Synthesis of bis-ethyl 11-(4-benzamido)dodecanoatedisulfide.....	131
5.1.4 Synthesis of ethyl 12-(4-mercaptobenzamido)dodecanoate (ligand 1)	132
5.2 Synthesis of poly(lactic-co-glycolic acid)-block-poly(ethylene glycol) (PLGA-b-PEG) copolymers	133
5.2.1 Synthesis of PLGA-b-PEG-NH ₂	133
5.2.2 Synthesis of PLGA-NHS.....	134
5.2.3 Synthesis of PLGA-b-PEG-COOH	135
5.3 Synthesis of modified chitosan chains.....	136
5.3.1 Synthesis of Chitosan-Thioglycolic Acid (Chitosan-TGA)	136
5.3.2 Synthesis of Chitosan- Hydrocaffeic Acid (Chitosan-HCA)	137
5.4 Synthesis of chlorotoxin functionalized polymeric nanovectors for the treatment of Glioblastoma Multiforme in a combined approach with radiation therapy.....	138
5.4.1 Synthesis of AgNPs	138
5.4.2 Synthesis of AgNPs-1.....	139
5.4.3 Synthesis of AgNPs-1-PNPs	140
5.4.4 Synthesis of AgNPs-1-PNPs-Cltx	141
5.5 Synthesis of aptamer functionalized polymeric nanovectors for the treatment of Glioblastoma thought the BBB.....	142
5.5.1 Synthesis of NVP-BEZ235@PNPs	142
5.5.2 Synthesis of NVP-BEZ235@PNPs-Gint.4 and NVP-BEZ235@PNPs-SCR.....	143
5.5.3 Synthesis of BODIPY@PNPs	144
5.5.2 Synthesis of BODIPY@PNPs-Gint.4 and BODIPY@PNPs-SCR	145
5.6 Gold nanorods as tools for photothermal therapy of Barrett Esophagus.....	146
5.6.1 Preparation of GNRs-CTAB	146
5.6.2 Preparation of GNRs-1	147
5.6.3 Synthesis of GNRs-1@PMs	148
5.6.4 Preparation of Curc@PMs.....	149

5.6.5 Preparation of GNRs-1/Curc@PMs	150
5.7 Magnesium nanoparticles as a highly biocompatible photothermal agent for hepatocellular carcinoma treatment.....	151
5.7.1 Synthesis of Chit–Mg MPs.....	151
5.8 Synthesis of Dumbbell-Like Gold-Iron Oxide Nanoparticles (dl-AuFe NPs) as multifunctional nanosystems	152
5.8.1 Synthesis of dl-AuFe ₃ O ₄ NPs	152
5.8.2 Synthesis of dl-AuFe ₃ O ₄ @Chit	153
5.9 Synthesis of a novel magnetic resonance–photoacoustic dual imaging nanosystem based on core–shell Fe₃O₄@SiO₂@Au NPs.....	154
5.9.1 Synthesis of Native Iron Oxide Nanoparticles, Fe ₃ O ₄ NPs.....	154
5.9.2 Synthesis of Core–Shell Iron Oxide–Silica Nanoparticles Fe ₃ O ₄ @SiO ₂ NPs.....	155
5.9.3 Synthesis of Core–Shell Iron Oxide–Silica–Gold Nanoparticles, Fe ₃ O ₄ @SiO ₂ @Au NPs	156
5.9.4 Synthesis of Lipophilic Fe ₃ O ₄ @SiO ₂ @Au NPs by Ligand Exchange.....	157
5.9.5 Synthesis of Fe ₃ O ₄ @SiO ₂ @Au@PMs.....	158
5.9.6 Conjugation of Folic Acid on Fe ₃ O ₄ @SiO ₂ @AuNPs@PMs	159
6. Bibliography	160

Abstract

The research project discussed in this PhD thesis concerns the development of drug delivery and theranostic systems for nanomedicine applications in cancer treatments.

In the first part, polymeric nanoparticles have been exploited as drug delivery systems for the treatment of Glioblastoma Multiforme. For this purpose, two different biomolecules, in one case Cholotoxin, a small peptide, and in the other case an antiPDGFRs-aptamer (GINT.4), have been employed as targeting agents conjugated on the polymeric nanoparticles surface. The second section of the project has been focused on the development of metallic nanoparticle for photothermal therapy, a cancer treatment consisting in the exposition of body tissue to an increasing of temperature (42-45°C) to induce cytotoxic effects on cancer cells. For this purpose, gold nanorods (GNRs) have been investigated as photothermal agent for the treatment of Barrett's esophageal. On the other hand, one pot-synthesis of chitosan coated magnesium nanoparticle has been fine-tuned in order to obtain high biocompatible nanoparticles characterized by a promising unexpected photothermal behaviour.

In the last part of the project, the synthesis of multicomponent nanosystems suitable for multimodal imaging or theranostic agents have been investigated. Two different multifunctional nanomaterials based on the incorporation of iron oxide and gold nanoparticles in the same nanosystem, have been realized. The first system consisted in dumbbell-like gold-iron oxide nanoparticles coated with chitosan that showed photothermal behaviour and also good capabilities as photoacoustic imaging contrast agents. The second system consisted in core-shell $\text{Fe}_3\text{O}_4@\text{SiO}_2@\text{Au}$ NPs entrapped in polymeric nanoparticles decorated with folic acid, have been tested in vivo for photoacoustic and magnetic resonance imaging detection of ovarian cancer.

Table of acronyms

Acronym	Significance
AAS	atomic absorption spectroscopy
Ag-nps	silver nanoparticles
Ag-nps-1	silver nanoparticles coated with 11-(4-mercaptobenzamido)undecanoate
Ag-nps-PVP	silver nanoparticles coated with polyvinylpyrrolidone
Ag-PNP	silver nanoparticles
Ag-PNP-CTX	silver nanoparticles entrapped in polymeric nanoparticles functionalized with chlorotoxin
APTMS	(3-aminopropyl)trimethoxysilane
ATP	adenosine triphosphate
BAR-T	Barrett's esophageal tumor
BBB	blood–brain barrier
BODI-PY	BODIPY505-515, lipophilic dye
BODI-PY@PNPs-Gint4.T	polymeric nanoparticles containing the lipophilic dye BODIPY505-515 functionalized on the surface with the aptamer Gint4.T
BODI-PY@PNPs-SCR	polymeric nanoparticles containing the lipophilic dye BODIPY505-515 functionalized on the surface with the scrambled aptamer SCR
BODY-PY@PNPs	polymeric nanoparticles containing the lipophilic dye BODIPY505-515
CDI	1,1-carbonyldiimidazole
Chit-Mg MPs	chitosan coated magnesium microparticles
CT	computed tomography
CTAB	cetyltrimethylammonium bromide
CTX	chlorotoxin
Curc@PMs	polymeric nanomicelles containing curcuma molecules
cw	continuous wave
DCC	N,N'-dicyclohexylcarbodiimide
DCM	dichloromethane
DIPEA	N,N-diisopropylethylamine
dl-AuFe NPs	dumbbell-like gold–iron oxide nanoparticles
dl-AuFe ₃ O ₄ @Chit	chitosan coated dumbbell-like gold–iron oxide nanoparticles
DLS	dynamic light scattering
DMF	dimethylformamide
DPSSL	diode pumped solid state laser
EAC	esophageal adenocarcinoma
EC ₅₀	half maximal effective concentration values
EDC	1-ethyl-3-(3-dimethylaminopropyl)carbodiimide
EMA	European Medicine Agency
EPR	enhanced permeability and retention
FA	folic acid
FDA	US Food and Drug Administration
Fe ₃ O ₄ NPs	iron oxide nanoparticles
Fe ₃ O ₄ @SiO ₂ @Au NPs	core–shell iron oxide–silica–gold nanoparticles

Fe ₃ O ₄ @SiO ₂ @Au@PMs	core-shell iron oxide-silica-gold nanoparticles coated with the 11-(4-mercaptobenzamido)undecanoate entrapped in polymeric micelles
Fe ₃ O ₄ @SiO ₂ @Au@PMs-FA	core-shell iron oxide-silica-gold nanoparticles coated with the 11-(4-mercaptobenzamido)undecanoate entrapped in polymeric micelles functionalized with folic acid
Fe ₃ O ₄ @SiO ₂ @Au@PMs-FA/fluo	core-shell iron oxide-silica-gold nanoparticles coated with the 11-(4-mercaptobenzamido)undecanoate entrapped in polymeric micelles functionalized with folic acid and fluorescein
Fe ₃ O ₄ @SiO ₂ @Au-1	core-shell iron oxide-silica-gold nanoparticles coated with the 11-(4-mercaptobenzamido)undecanoate
FTIR	fourier transform infrared spectroscopy
GBM	glioblastoma multiforme
Gint4.T	aptamer able to recognize platelet-derived growth factor receptors β on the blood-brain barrier
GNPs	gold nanoparticles
GNRs	gold nanorods
GNRs-1	Gold nanorods coated with 11-(4-mercaptobenzamido)undecanoate)
GNRs-1/Curc@PMs	polymeric nanomicelles containing lipophilic gold nanorods and curcuma
GNRs-1@PMs	polymeric nanomicelles containing lipophilic GNRs-1
GNRs-CTAB	gold nanorods coated with cetyltrimethylammonium bromide
Gy	gray
HAADF-STEM	high angle annular dark field scanning transmission electron microscopy
HCA	hydrocaffeic acid
HCA	hydrocaffeic acid
MES Buffer	2-(<i>N</i> -morpholino)ethanesulfonic acid Buffer
Mg MPs	magnesium microparticles
Mg NPs	magnesium nanoparticles
MMP-2	matrix metalloproteinase-2
MPS	mononuclear phagocytic system
MRI	magnetic resonance imaging
MTEOS	methyltriethoxysilane
NaOH	sodium hydroxide
NHS	N-hydroxysuccinimide
NIR	near-infrared spectroscopy
NMR	nuclear magnetic resonance
NPs	Nanoparticles
NVP-BEZ235@PNPs	polymeric nanoparticles containing the lipophilic drug NVP-BEZ235
NVP-BEZ235@PNPs-Gint4.T	polymeric nanoparticles containing the lipophilic drug NVP-BEZ235 functionalized on the surface with the aptamer Gint4.T
NVP-BEZ235@PNPs-SCR	polymeric nanoparticles containing the lipophilic drug NVP-BEZ235 functionalized on the surface with the scrambled aptamer

OI	optical imaging
PAI	photoacoustic imaging
PDGFR β	platelet-derived growth factor receptors β
PDI	polydispersity index
PET	positron electron tomography
PLGA-PEG	poly(d,l-lactic-co-glycolic acid)-b-poly(ethylene glycol)
PMs	polymeric micelles
PNPs	polymeric nanoparticles
PTT	photothermal therapy
PVP	polyvinylpyrrolidone
RES	reticuloendothelial system
RT-qPCR	real-time quantitative polymerase chain reaction analysis
SAM	self-assembled monolayer
SCR	scrambled aptamer
SELEX	systematic evolution of ligands by exponential enrichment method
SPECT	single-photon emission computed tomography
SPIONs	super paramagnetic iron oxide nanoparticles
TEM	transmission electron microscopy
TGA	thioglycolic acid
TGA	thermogravimetric analysis
THF	tetrahydrofuran
US	ultrasound
VSM	vibrating-sample magnetometer
XRD	X-ray diffraction

1. Introduction

1.1 State of the art in Cancer Nanomedicine

Nanotechnology is the science that concerns the study, the development and the production of systems characterized by any dimension between 1-100 nanometres. Indeed, small dimension confers to nanomaterials unique chemical-physical properties different from the bulk materials, and for this reason, in the last decades the use of nanomaterials in different area of researches such as electronic, engineering, biotechnology, biology and medicine, allowed a real technological revolution. Although IUPAC definition of nanoparticles is a particle with any shape of dimension in the 1-100 nm range, the term “nanoparticle” is commonly applied to structures that are up to several hundred nanometres in size.¹

Because cancer is set to become a major cause of morbidity and mortality in the coming decades in every region of the world, there is the necessity to better understand its biology in order to improve diagnostic devices and treatments.^{2,3}

Nowadays, the main cancer therapies consist of surgical intervention, radiation and chemotherapeutic drugs, which are often not efficacy and implicate different side effect as the death of healthy cells that cause the toxicity to the patients. In chemotherapy, the main complication is represented by the pharmaceutical properties of therapeutic molecules, such as the stability and the solubility, which can addict the circulating half-life and tumour accumulation making less efficient the therapy.

The nanotechnologies innovations applied to medicine allowed the development of *nanomedicine* and led to the possibility to overcome some of the main concerns of traditional cancer treatments by taking advantage by the interaction between the nanoparticles and biological systems but also discovering the therapeutic nature of some nanomaterials themselves.⁴ Cancer nanomedicine provides not only the use of nanoagents as drug delivery systems or diagnosis tools to improve the efficacy of traditional methodologies, but also the development of medical devices such as micro/nanoelectromechanical (MEM/NEM) device-based drug delivery or nanotechnology-based sensors for the detection of biomarkers.⁵

In the last years, *nanotherapies* have been developed by employing the use of several nanoparticles platforms such as liposomes, albumin nanoparticles and polymeric micelles as drug delivery systems, and developed innovative technologies based on nanomaterials able to

be used in hyperthermia, radiation, gene and RNA interference (RNAi) therapy and immunotherapy (**Figure 1**).

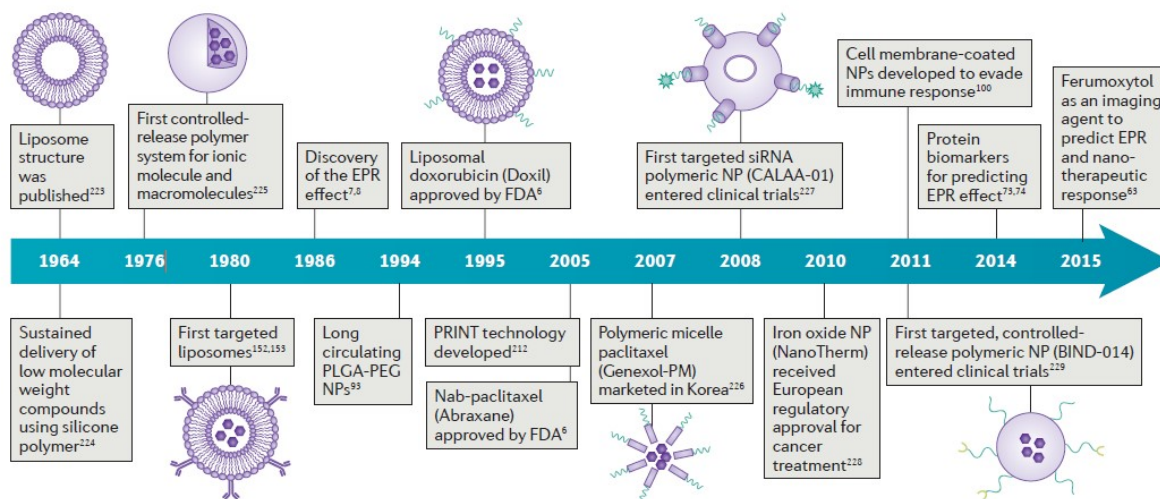


Figure 1. Historical timeline of major developments in the field of cancer nanomedicine. EPR, enhanced permeability and retention; FDA, US Food and Drug Administration; nab, nanoparticle albumin-bound; NP, nanoparticle; PLGA-PEG, poly(d,l-lactic-co-glycolic acid)-b-poly(ethylene glycol); PRINT, particle replication in non-wetting template; siRNA, small interfering RNA adapted from *Nat. Rev. Cancer* **17**, 20–37 (2016).

At now, few nano-drugs and nano-therapies have been available in clinic. Doxil® and Myocet®, consistent in doxorubicin encapsulated into liposomes, were the first class of therapeutic nanosystems to receive the clinical approval for cancer treatments. These formulations showed the possibility to reduce the dose-related cardiac toxicity concerning the doxorubicin and allowed the enhancement of its anticancer efficacy by enhancing patients tolerability.⁶

The second class of commercialized nanodrugs are represented by the Abraxane which consists in nanoparticles made of albumin-bound paclitaxel able to overcome the problems associated with administering hydrophobic taxol that induced hypersensitivity reactions.⁷

The mentioned examples of nanodrugs show as the nanotechnologies can deal with the challenges of cancer, improving the pharmacokinetic and the biodistribution of a chemotherapeutic drug or reducing the side effect associated to a therapy. However, clinical trials results revealed that the nanoformulations did not show an enhancement of efficacy compared with the conventional chemotherapeutic drug.⁸ In order to obtain an improvement of clinical efficacy of cancer treatment, the enhancement of the nanosystems design and nanomedicine strategy is necessary.

Polymeric micelles (as Genexol PM and NK105) and polymeric nanoparticles (CRLX101 and BIND-014) represent the new classes of cancer nanotherapeutic agents under clinical investigations.^{9,10}

However, recently discordant clinical trials results showed the necessity to improve the delivery strategies and also the possibility to involve a patients selection to identify those most likely to respond to the nanotherapy.¹¹

On the other hand, nanoparticles are largely investigated in the developing of “molecular imaging” in order to visualize and quantify biological processes at molecular and cellular levels in a non-invasive manner.¹² The possibility to combine in the same nanosystem therapy and the diagnostic functionalities led to the development of theranostic systems. This represents a promising strategy to monitor the pharmacokinetic, the accumulation of therapeutics and the progression of disease, giving important insights into heterogeneities both within tumour and between patients for potential personalized therapies.¹³

1.2 Drug Delivery and theranostic nanosystems

Drug delivery nanosystems are nanoparticles able to encapsulate a therapeutic agent in order to improve their therapeutic index by increasing its efficacy and reducing the toxicity. For this reason, a nanocarrier can represent a “second chance” for rejected chemodrugs, bringing out several advantages such as:

- the protection of the encapsulated drug from degradation due to the interactions with the biological environment;
- the enhancement of the pharmaceutical properties of therapeutic molecules (for example solubility, stability, circulating half-life and tumour accumulation);
- transcytosis of drugs across tight epithelial and endothelial barriers;

Because the accumulation of drug delivery nanosystems in the cancer site can be achieved by two main mechanisms: the *passive targeting* and *active targeting*.

To explain these mechanisms, the development of an efficient drug delivery system needs to take in account biological features of the tumour tissue (**Figure 2**). Generally, tissue in advanced cancer grade tends to develop new blood vessels from existing ones in order to transport oxygen and nutrients to the new cells in a process defined angiogenesis, which is the principal cause of the rapid growth of a tumour.¹⁴ The formed tumour vessels are characterized by a disorganized vasculature and numerous openings in the walls such as vesicles and transcellular holes, inter-endothelial junctions, and a discontinuous basement spaces between endothelial cells.¹⁵ These factors lead to the *enhanced permeability and retention (EPR) effect*, responsible of an enhancement of the permeability of tumour vessels compared to normal tissue. This phenomenon allows the passage of blood plasma components and other macromolecules into the interstitial space of the tumour, contributing to longer retention of these molecules.

The *passive targeting*, a mechanism involved in the drug delivery system pharmacokinetic, is a consequence of the *enhanced permeability and retention (EPR) effect*. This mechanism induces nanoparticles accumulation in the tumour tissue by the extravasation from their leaky vasculature and allows the release of the encapsulated agents into the vicinity of the tumour cells. Consequently, nanoparticles build up reaching higher concentration due to lack of efficient lymphatic drainage in solid tumour. Therefore, through *passive targeting*, a drug

delivery nanosystem can reduce the side effects caused by the diffusion of the conventional small-molecule in normal tissue, improving the accumulation of nanoparticles in the tumour tissue at a concentration five to ten times higher than in normal tissue in 1-2 days.¹⁶ The nanoparticles size has a great influence on the accumulation with the EPR effect; as reported in literature, nanoparticles with a diameter between 10 - 500 nm exhibit a good tendency to extravasate and accumulate within the tumor interstitium but other studies showed that particles with diameters lower than 200 nm are more effective.¹⁷ However, passive targeting showed significant drawbacks caused by the tumour heterogeneity, vascular permeability and different pharmacokinetic of each nanomaterials.¹⁸ The main problem consists in the clearance of nanoparticles from the bloodstream ascribable to the reticuloendothelial system (RES), which consists of phagocytic cells like monocytes and macrophages that are located in the spleen, lymph nodes, and Kupffer cells in the liver.

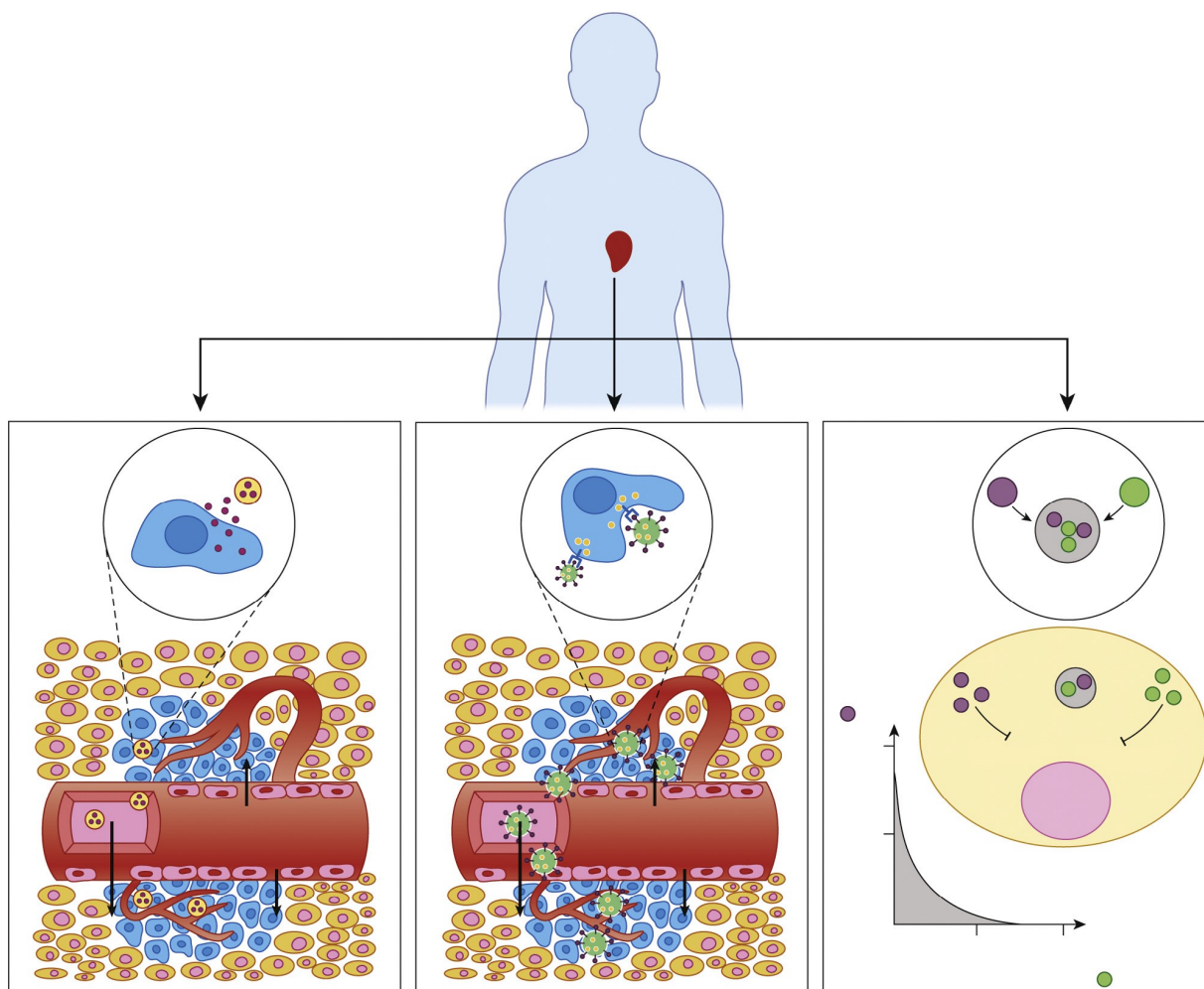


Figure 2. Passive targeting, active targeting, and combinatorial delivery. In passive targeting (left), nanoparticles (NPs) passively extravasate through the leaky vasculature via the enhanced permeability and retention (EPR) effect and preferentially accumulate in tumours. In active targeting (middle), targeting ligands on the surface of the NP trigger receptor-mediated endocytosis for enhanced cellular uptake. In combinatorial delivery (right), two or more therapeutic agents inhibit different or identical disease pathways for a synergistic effect from Trends Mol. Med. **21**, 223–232 (2015).

This phenomenon cause the high accumulation of the nanoparticles in the liver or spleen and can increase the toxicity of the nanomaterials due to the high dose.¹⁹

For this reason, the use of targeting agents able to be conjugated on the surface of nanosystems and to guide them to bind specific cells after extravasations, can improve the efficacy of the therapy by increasing their accumulation into the cancer site and by decreasing the collateral effect as toxicity in the health tissue.²⁰ To maximize the unique characteristic of the *active targeting* mechanism, the use of an active agent able to bind with high selectivity a surface marker (antigen or receptor) overexpressed on target cells relative to normal cells is required. Several classes of bio-agents such as, antibodies, engineered antibody fragments,²¹ proteins,²² peptides,²³ and aptamers,²⁴ have been employed as targeting agents, also different chemistry reactions have been developed to conjugate the these agent on nanoparticles surface. In the last years, the development of several nanocarriers for nanomedicine applications have been reported in literature (**Figure 3**).²⁵

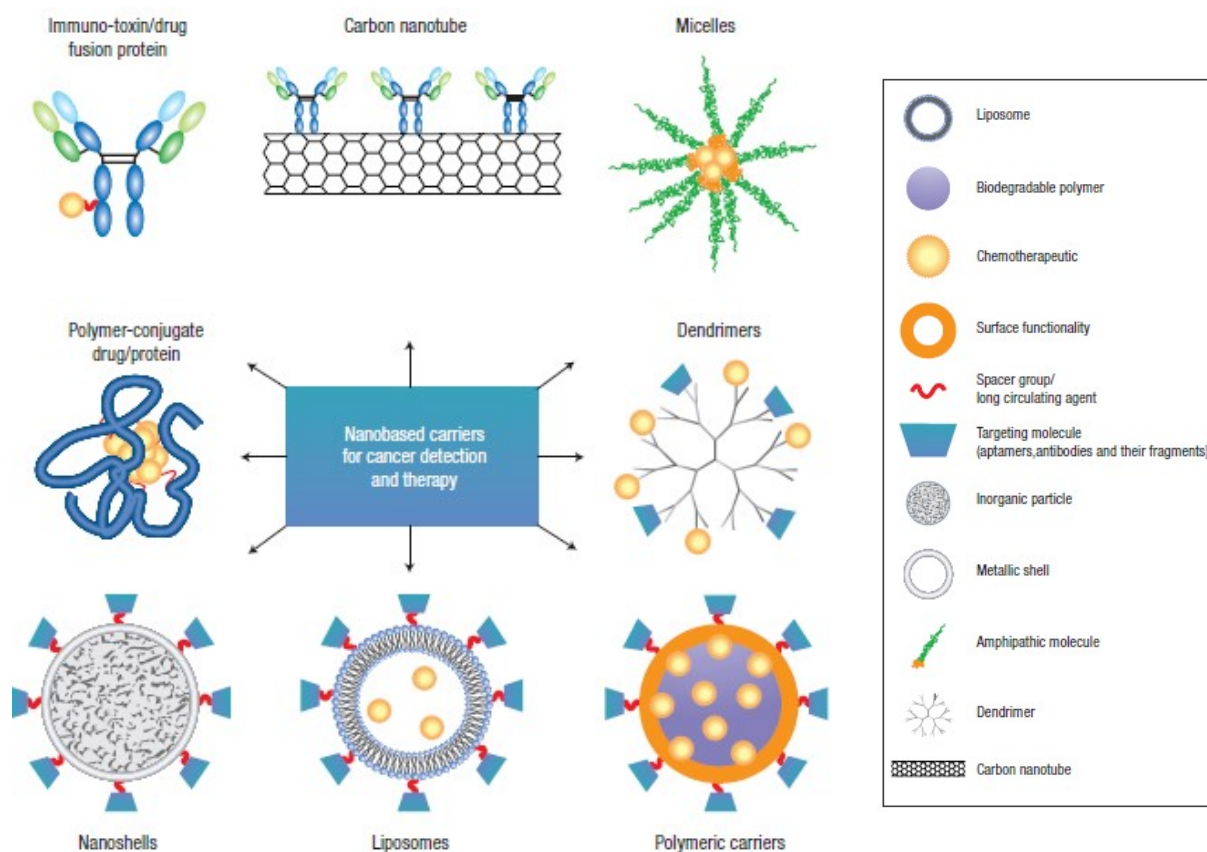


Figure 3. Images of nanocarriers for targeting cancer adapted from *Nat.Nanotechnol.* 2, 751-760 (2007). The main components of delivery nanosystems typically include a nanocarrier, a targeting moiety conjugated to the nanocarrier, and a cargo (such as the desired chemotherapeutic drugs).

The main research regarded the chemical components employed in the synthesis and formulation of these systems, that might be biocompatible and biodegradable materials and able to form nanocarriers with high efficiency of encapsulation of the therapeutic agents and with good robustness against degradation.

Carrier materials are classified in two main classes: the organic nanocarriers and inorganic nanocarriers. The first class includes nanocarriers constituted by smaller organic molecules, synthetic or natural bio-polymers, lipids and prefabricated dendrimers.²⁶ Among these, liposomes constituted by lipids, or polymeric micelles obtained with the self-assembly of amphiphilic polymers, represent common organic nanocarriers. These systems are constituted by an inner hollow space where a hydrophilic or hydrophobic therapeutic agent can be loaded (depending on the degree of hydrophilicity of the inner surface), and an outer hydrophilic shell able to stabilize the systems in the biologic environment. However, the major drawbacks of organic based- nanocarriers consist in their premature degradation in the body, which can cause undesired side effects due to drug loss. On the other hand, because their robustness, inorganic nanomaterials result less easily degraded during delivery compared to organic nanoparticles, and in addition, could provide additional functions, such as imaging contrast agent or therapeutic abilities, due to their peculiar physical properties. For example, optical properties of gold nanomaterials, based on surface plasmon resonance, have been investigated for the development of therapeutic agents in photothermal ablation therapy (**paragraph 1.3**) but also as contrast agents for photoacoustic imaging (**paragraph 1.4.1**). Magnetic properties of iron oxide nanoparticles have been largely studied in order to find efficient contrast agents for magnetic resonance imaging (MRI) (**paragraph 1.4.4**), but also as therapeutic agents in hyperthermia therapy after the application of an alternating magnetic field. In particular, these two examples show the possibility to integrate diagnostic and therapeutic functions into a single nanoparticle formulation, led to the development of theranostic nanosystems. By adopting Ferrari's classification, a theranostic nanoparticle can be dissected into at least three components: biomedical payload, carrier, and surface modifier, depending on both their roles and their physical locations, as shown in **Figure 4**.²⁷

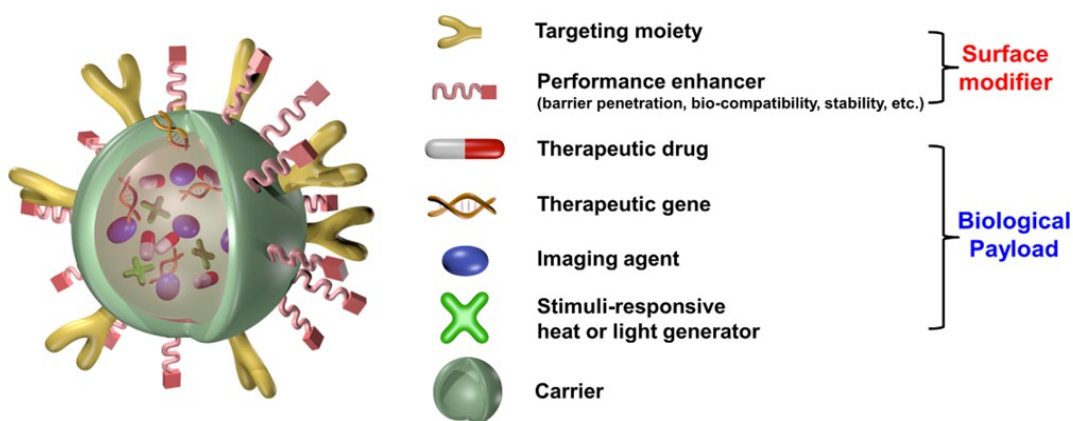


Figure 4. Schematic illustration of a multifunctional nanocomposite from Nat. Rev. Cancer **5**, 161–171 (2005).

The biomedical payload includes organic molecules or inorganic nanoparticles characterized by therapeutic or diagnostic functions. In particular, for specific materials, inorganic nanoparticles can be use their-self to make the therapy and the diagnosis of a specific pathological site, after an opportune surface functionalization able to improve their biocompatibility. Theranostic nanomedicine show the possibility to develop innovative strategies to investigate the pharmacokinetic and accumulation of nanocarriers, but also to monitor the progression of disease with imaging techniques. This represents the opportunity to achieve important insights into heterogeneities both within tumours and between patients for potential personalized treatment.

1.2.1 Polymeric nanoparticles as drug delivery and theranostic nanosystems

Polymeric nanoparticles represents a platform able to load chemotherapeutic drug or active molecules in order to improve their physiochemical and pharmacological properties; in addition, they can be chemically modified on the surface by introducing an active targeting able to guide the final systems to a specific pathological site.

Several materials have been investigated in order to realize an ideal polymeric based drug delivery system characterized by an efficient drug load ability and, at the same time, chemical physical properties able to give stability and to improve biodistribution *in vivo* of the final system.

At the beginning, non-biodegradable polymers such as poly(methyl methacrylate) (PMMA), polyacrylamide, polystyrene, and polyacrylates have been used as polymeric materials for medicine applications, including drug delivery, wound healing and antimicrobial activity. These systems have been designed in order to exhibit a rapid and efficiently clearance through faeces and urine and do not accumulate or distribute in tissues at toxic level because they cannot be easily degraded and excreted.²⁸ However, biological studies observed chronic toxicity and inflammatory reactions with the use of non-biodegradable materials. After these evidences, nanomedicine research has been focused in selecting polymer materials for drug delivery, which showed bioavailability, biocompatibility, straightforward production, sustained release and tunable degradation rate.²⁹ For these purposes, synthetic biodegradable polymers, such as poly(lactide) (PLA), poly(lactide-*co*-glycolide) copolymers (PLGA), poly(ϵ -caprolactone) (PCL), and poly(amino acids), and natural polymers such as chitosan, alginate, gelatine and albumin, have been extensively explored.

Beyond the research in the materials, nanoparticles biodistribution and internalization in tumour cells are deeply influenced by their size and surface properties.³⁰ Once injected in the body, nanoparticles are subjected to a mechanism of recognition and clearance by the reticuloendothelial system (RES) or mononuclear phagocytic system (MPS). These mechanisms consist of three steps: opsonisation, phagocytosis and clearance.

The opsonisation involves the coating of a foreign organism or particle by proteins called *opsonins*, which allows recognition of the particles by phagocytic cells and subsequent clearance from the bloodstream. Particle size can affect the mechanism of elimination, influencing on opsonin adsorption and therefore on phagocytosis.³¹ It is reported in literature that larger nanoparticles are usually cleared by the RES organs (lung, liver, or spleen), while

the smaller nano-objects, characterized by a retention time in the bloodstream, are removed by the renal system. In particular, nanoparticles with a diameter between 10–20 nm, show wide spread in various organs by crossing the tight endothelial junctions and are rapidly excreted through the glomeruli of kidney. Nanoparticles larger than 20 nm in diameter avoid filtration by the kidney, and smaller than 100 nm avoid a specific sequestration by sinusoids in spleen and fenestra of liver, which are approximately 150–200 nm in diameter.^{31,32} On the other hand, particles characterized by a diameter of 100–200 nm are usually taken up by receptor-mediated endocytosis while larger particles are internalized by phagocytosis (**Figure 5**).

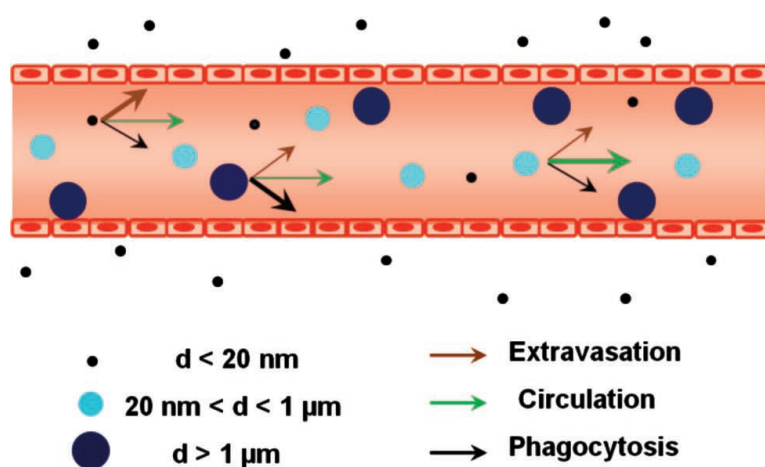


Figure 5. Size of the spherical nanoparticles determines the mechanism and rate of clearance. Spheres that are smaller than 20 nm readily pass through the tight endothelial junctions, resulting in a relatively rapid rate of clearance from the circulation. For large particles (e.g., $> 1 \mu\text{m}$), momentum forces begin to dominate and wall collisions become more common, resulting in rapidly uptake by the mononuclear phagocytic system. However, when the particle size falls between two extremes, all of these clearance mechanisms are minimized and circulation times are prolonged (the thickness of arrows represents the strength of the force) from Small **9**, 1521–1532 (2013).

The size can affect also the adhesion and the interaction with tumour cells and several studies in literature tried to identify the “right size” for a drug delivery system. Nevertheless, controversial results have been obtained. This outcome can be explained by considering the heterogeneity of tumour tissue that can diverge for cancer type, stage of disease, site in the body, causing different vasculature fenestrations for each tumour.

For this reason, it is hard to generalize the effect of the size on the internalization in the tumour cells that can be affected also by other nanoparticles parameters such as surface properties. Indeed, surface charge of nanoparticles can influence the absorption of plasma proteins (opsonins), leading to their recognition by macrophages, followed by phagocytosis and elimination. However, also in this case, the studies regarding the effect of surface charge on the circulation and biodistribution of nanoparticles led to inconsistent results due to the difference of nanoparticle types, the nature of charged groups, and other confounding factors

such as inhomogeneous particle size.^{7,33,34} In order to establish stability of colloidal suspension, might take in account *Zeta Potential* value, which consists in the measurement of the electric potential at the surface of the hydrodynamic layer. Nanoparticles with a zeta potential value higher than (+ /-) 30 mV are stable in suspension, because high negative or positive zeta potential values tend to repel each other reducing aggregation.³⁵

Surface hydrophobicity is the other parameter that might be considered in the design of drug delivery nanosystems. Indeed, the hydrophilic–lipophilic balance of nanomaterials influences the mechanism of opsonisation that results faster for the particles more hydrophobic due to the enhanced “adsorbability” of blood serum proteins onto their surface.

In order to reduce the clearance by opsonisation, shielding groups can be introduced onto the nanoparticles surface. Polyethylene glycol (PEG) represents the most widely material used in the constitution of a hydrophilic outer shells of drug delivery systems.³⁶ The “PEGylated” process can be achieved by grafting, entrapping, adsorbing or covalently binding to nanoparticles these molecules. Due to their flexibility and hydrophilicity, PEG molecules are able to stabilize nanoparticles by steric and not ionic effects especially, adopting an extended conformation able to repel the opsonins away from the nanoparticles (**Figure 6**). PEG molecules characterized by a molecular weight higher or equivalent to 2000 Da showed the optimal chain length necessary for reducing the RES clearance.³⁷

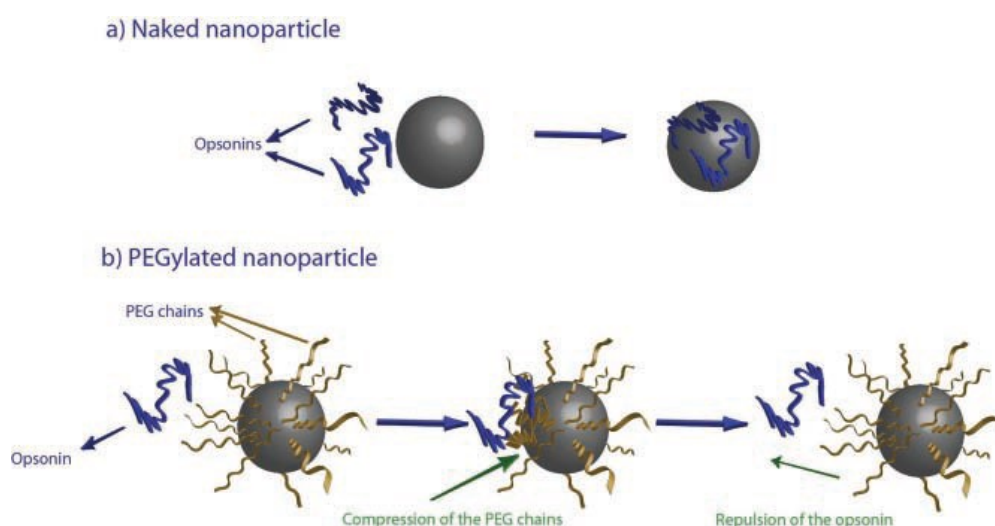


Figure 6. Representation of how PEGylation avoids clearance of NPs by the RES from Adv. Mater. 23, (2011).

1.2.2 Poly(d,l-lactic-co-glycolic acid)-b-poly(ethylene glycol)

In the last years, polymeric nanoparticles constituted by the di-block copolymer *poly(d,l-lactic-co-glycolic acid)-b-poly(ethylene glycol)* (PLGA-b-PEG) have been one of the most studied drug delivery systems. PLGA-b-PEG is constituted by a lipophilic portion made of PLGA, which confers it biodegradability and biocompatibility properties, and a hydrophilic portion made of PEG, which confers it the stealth behaviour.

Poly(lactic-co-glycolic acid) (PLGA) is a linear aliphatic polyester approved in 1989 by the FDA for drug delivery application, synthesized through the random ring-opening copolymerization of two cyclic dimers of glycolic and lactic acid, linked together by ester linkage in a casual order during copolymerization (**Figure 7**).

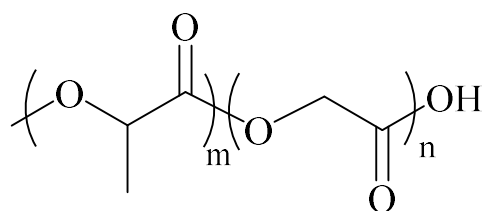


Figure 7. Chemical structure of poly(lactic-co-glycolic acid) (PLGA) constituted by **m** units of lactic acid and **n** units of glycolic acid.

It has been showed that the molar ratio of the individual monomer components (lactide and glycolide) in the polymer chain influences many properties of PLGA, such as degree of crystallinity, mechanical strength, swelling behaviour, and capability to hydrolyze.³⁸

Because these properties can affect the biodegradability of the material, an investigation of the optimal molar ratio has been carried out. The results showed that PLGA copolymer with a 50:50 molar ratio of the two monomer is hydrolysed much faster in comparison with the one containing higher quantity of either of two monomers.³⁹

Once the PLGA chains are released in aqueous media, such as in the body, undergo a hydrolytic degradation of the ester linkages. This process led to the formation of the two original monomers, lactic and glycolic acids that in body can be metabolized and eliminated as carbon dioxide and water or excreted unchanged in the kidney.⁴⁰

On the other hand, poly(ethylene glycol) (PEG) is a non-ionic hydrophilic polyether synthesized in a wide range of molecular weight from 300 to 100,000 Da, through polymerization of the monomer ethylene glycol (**Figure 8**). PEG is a biocompatible polymer but not biodegradable, indeed in the body, PEG chains are excreted unchanged in the kidney and does not undergo biodegradation process.

As discussed in the previous paragraph, PEG polymer is characterized by high hydrophilicity properties and for this reason is used to stabilize nanoparticles in aqueous media, to increase solubility, and to avoid aggregation of them by steric hindrance in production, storage, and applications.⁴¹

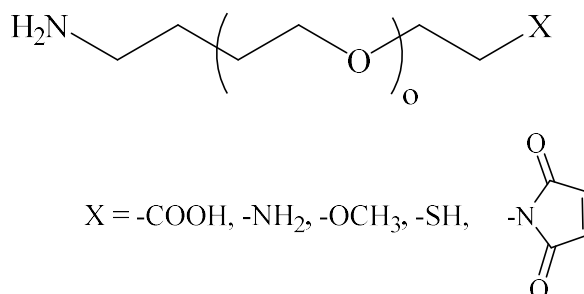


Figure 8. Chemical structure of poly(ethylene glycol) (PEG).

Beyond the biodegradability and biocompatibility of its components, PLGA-b-PEG assumes amphiphilic properties that make it suitable for the formation of polymeric nanoparticles and micelles. In the formation of polymeric nanoparticle, the PLGA-b-PEG chains undergo to a self-assemble generating a system in which the hydrophobic PLGA remains inside the micelles and the hydrophilic PEG goes outside creating a stabilizing shell.

Because the PEG molecules can be characterized by several terminal function groups (such as carboxylic ammine, maleimide, thiol groups), it is possible to obtain a functionalized copolymer PLGA-b-PEG-X (**Figure 9**). In this way, the obtained polymeric nanoparticles will characterize by the PEG functional groups on the surface able to conjugate specific target agents.

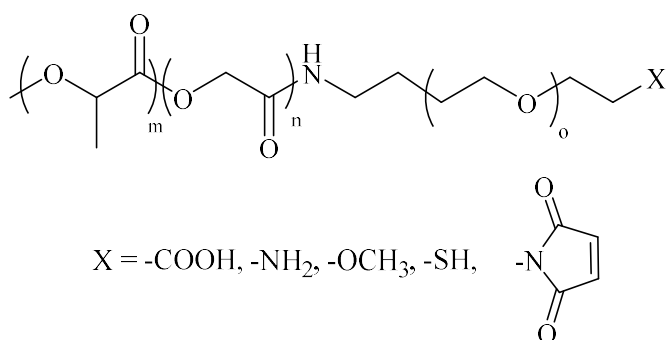


Figure 9. Chemical structure of poly(lactic-co-glycolic acid)-block-poly(ethylene glycol) (PLGA-b-PEG) with indicated the characteristic final functional groups.

1.2.3 Methods of preparations for polymeric nanoparticles

The main strategies developed for the synthesis of drug delivery systems based on polymeric nanoparticles (PNPs) are divided in two different approaches, methods in which preformed polymers are used or methods that involve the direct polymerization of monomers using classical polymerization or polyreactions.⁴²

The common techniques based on the use of preformed polymers are solvent evaporation, salting-out, dialysis and supercritical fluid technology.

In order to choose the suitable method for the synthesis, must be consider the chemical properties of polymeric material and/or of the agent that should be encapsulated, such as solubility and stability in organic solvent or in water.

PLGA-b-PEG is soluble in several organic solvents and due its amphiphilic properties, the synthesis of polymeric nanoparticles not required large amount of surfactant agents, able to stabilize in water the formed polymeric nanoparticles characterized by high hydrophobic properties. In particular, solvent evaporation and nanoprecipitation methods have been widely used for PLGA-b-PEG nanoparticles synthesis.⁴¹

The solvent evaporation technique consists in the preparation of emulsion with a not-miscible organic solvent and water. Based on the solubility properties of the agents that should be encapsulated, two main strategies for the formation of emulsions have been developed: the preparation of single-emulsions (*oil-in-water* (o/w)) or double-emulsions (*(water-in-oil)-in-water*, (w/o/w)).⁴³

In the *oil-in-water* (o/w) technique, an organic solution is prepared by dissolving polymer and lipophilic agents, which should be encapsulated, in volatile and water-immiscible organic solvents. The common solvents used for the solvent evaporation methods are dichloromethane, chloroform and ethyl acetate. Once prepared, the organic phase is added to a large amount of water, and the obtained biphasic solution is emulsified with high-speed homogenization or ultrasonication, followed by evaporation of the solvent, by continuous magnetic stirring at room temperature or under reduced pressure (**Figure 10**).

In order to stabilize the formed polymeric nanoparticles, surfactant agents are usually solubilized in the aqueous phase, such as sodium cholate, polyvinylalcohol (PVA), polyvinylpyrrolidone (PVP), poloxamers, or other molecules. During the emulsion process, the strong energy provided from homogenizator or ultrasonicator allows the formation of organic nanosized droplets in the surrounding water phase.

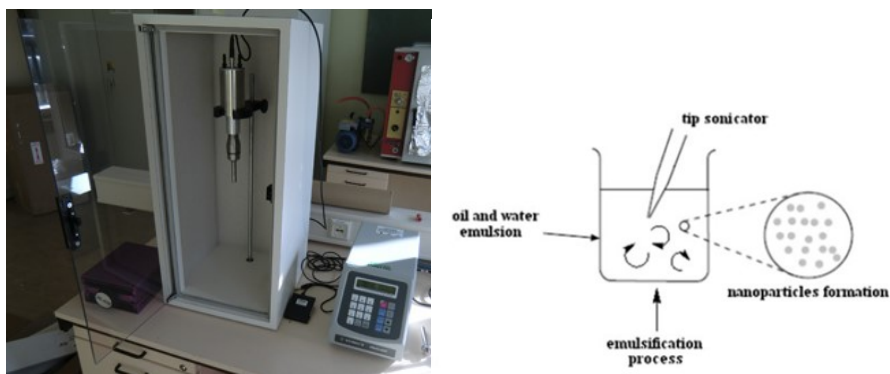


Figure 10. On the left, a picture of tip probe sonicator using for the solvent evaporation method, on the right a schematic representation of *oil-in-water* technique.

Because of the amphiphilic properties, PLGA-b-PEG molecules dissolved in the organic phase can form micelles without the presence of surfactant agents, constituted by an inner core, made of the hydrophobic PLGA portion, and surrounded by an external shell made of hydrophilic PEG chains, able to stabilize the nanomicelles in aqueous environment. Depending on the lipophilic agents entrapped, this method allows the obtainment of nanospheres with good index of polydispersity (PDI) and a diameter in the range 100–500 nm. In order to encapsulate hydrophilic agents, the solvent evaporation can be used by following the double-emulsions ((water-in-oil)-in-water, (w/o)/w) strategy, which involves two emulsion processes. First, a water phase is prepared by dissolving the hydrophilic agents in a small volume of water (W_1). The first emulsion process consists in the emulsion of the prepared aqueous phase W_1 with an organic phase prepared by dissolving the polymer in an organic solvent, as in the *oil-in-water* technique. In this case, the organic phase is in the majority compared to the aqueous phase, so an opposite situation respect to the *oil-in-water* emulsion is created and the water phase with the drugs dissolved-in remains inside the micelles core, while the oil phase constitutes the external environmental. After that a bigger amount of a second aqueous phase (W_2) is added to the previous emulsion and the entire system is re-emulsified to obtain the $w_1/o/w_2$ double emulsion; in this case, the secondary aqueous phase always contains surfactants or stabilizing agents. During this secondary emulsion, the organic phase remains entrapped between the two aqueous phases, the W_1 in the inner core and the W_2 that constitutes the external ambient. The organic solvent can be now removed by evaporation and the final system, dispersed in water with water in the inner core, can be obtained. In addition, when lipophilic agents are dissolved with the polymer in the organic phase, the w/o/w technique allows entrapping two different agents in the same polymeric nanoparticles, suitable for the development of theranostic nanosystems.

On the other hand, in nanoprecipitation method the organic phase is prepared by dissolving the polymer and lipophilic agents, in organic solvent miscible with water such as ethanol, tetrahydrofuran, acetone, hexane, dimethyl sulfoxide or dimethylformamide. This organic solution is mixed under vigorous stirring into water, which may contain surfactant or stabilizing agents. This method is based on the interfacial deposition of a polymer after displacement of a semipolar solvent, miscible with water, from a lipophilic solution. Rapid diffusion of the solvent into water results in the decrease of interfacial tension between the two phases, which increases the surface area and leads to the formation of small droplets of organic solvent (Figure 11).⁴⁴ The polymer dissolved in these droplets forms small macromolecules, that begins the nucleation process based on the aggregation of this nuclei which leads to the formation of polymeric nanoparticle.⁴¹ Particles formed with this technique can be obtained with small diameter (50–250 nm) and good polydispersity index (PDI).⁴⁵

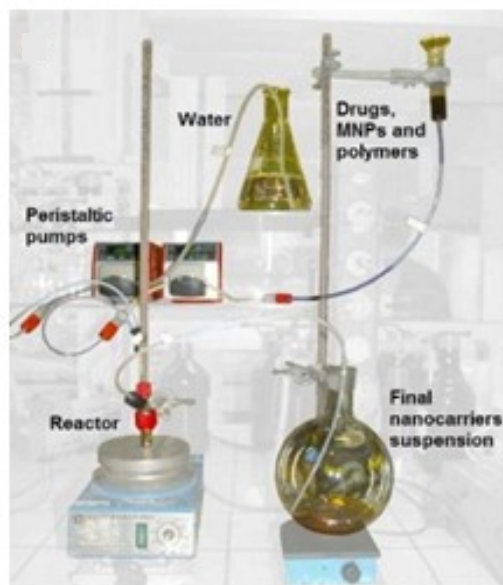


Figure 11. Schematic representation of the nanoprecipitation technique.

1.3 Hyperthermia therapy

Hyperthermia therapy (defined also thermal therapy) is a cancer treatment that consists in the exposition of body tissue to an increasing of temperature, just above the physiological temperature (42-45°C) to induce cytotoxic effects on cancer cells.

Indeed, cancer cells are more sensitivity to heat compared to healthy cells, and at those temperature, tend to undergo in apoptosis caused by denaturation of membrane and cytoplasmic proteins.⁴⁶ This phenomenon can be explained by considering the physiological differences between normal and tumour tissues; the disorganised and abnormal vasculature caused by angiogenesis, leads to a lower vessel density in tumour tissues, that makes heat dissipation hindered in comparison to healthy tissues.⁴⁷ For this reason, when hyperthermia is applied at temperatures over 42 °C, the temperature of tumour rises higher than that in normal tissue, because during heating tumour blood flow tends to decrease while in normal tissue it significantly increases. On the other hand, hyperthermia treatment at lower temperature than 42°C, tends to generate an increasing in the tumour blood flow, making cancer cells more sensitive to radiotherapy (radiosensitivity is favoured by good tissue oxygenation) and chemotherapy (drug delivery is increased by higher perfusion).⁴⁸ The synergic effect of hyperthermia with other traditional therapies has been investigated in clinical trials in the treatments of many types of cancer, showing a significant reduction in tumour size.⁴⁹ However, not all of these studies have shown increased survival in patients receiving the combined treatments.

There are three main types of hyperthermia treatments, *whole-body*, *regional or local*, which depend on the location, the depth and the stage of malignancy. *Whole-body hyperthermia* is used to treat metastatic cancer that has spread throughout the body and consists in the heating of the entire body through hot water baths, thermal chambers or infrared radiators. However, because the temperature increasing is not selective, this treatment can lead to major side effects due to regional differences in tissue characteristics, causing the production of dangerous temperatures in normal tissue. *Regional hyperthermia* consists to heat large areas of tissue (as a body cavity, organ or limb), generally affected by an advanced stage of tumour, by using external applicators or arrays of multiple applicators (microwave antennas). On the other hand, *local hyperthermia* is applied to treat small area, in particular localized tumours either superficially or in accessible body cavities, using various techniques that deliver energy to heat the cancer cells. Depending on the tumour location, there are several approaches to

local hyperthermia, which involve different types of energy used to apply heat, including microwave, radiofrequency, and ultrasound.⁵⁰

Because the limited spatial and temporal control, traditional hyperthermia treatments can cause burns to surrounding healthy tissues. For this reason, nanotechnology advantages have been largely investigated, in order to develop nano-sized heat agents able to promote localized temperature increasing in cancer cells.

The first approach of nanomedicine in hyperthermia therapy consisted in the use of magnetic nanoparticles as generators of heat, leading to the development of magnetic fluid hyperthermia (MFH).⁵¹ This technique, based on the conversion from magnetic energy into thermal energy in the supermagnetic nanoparticles subjected to an external alternative magnetic field, led to the development of the first hyperthermia clinical nanotherapy. In 2011, the nanomedicine company MagForce launched *NanoTherm*®, a clinical therapy based on ultras-small (~12 nm) iron-oxide magnetite (Fe₃O₄) coated by aminosilane for hyperthermia therapy of solid tumours (**Figure 12**).



Figure 12. Image of NanoTherm® produced by MagForce.

The treatment consists in the directly injection of *NanoTherm*® into the tumour and the subsequently application of an alternating magnetic field to generate heat, combined with fractionated stereotactic radiotherapy. Clinical trials results conducted in the treatment of multiform glioblastoma, an aggressive brain tumour, showed that thermotherapy using magnetic nanoparticles in conjunction with a reduced radiation dose is safe and effective and leads to longer over survival of patients, compared to conventional therapies.⁵²

Despite the good results obtained by using MFH, nanotechnology is also exploring other alternatives. In particular, the recent development of nanoparticles capable of efficient heat generation under illumination with laser radiation has attracted much attention for the last few years. Photothermal therapy (PTT) is an hyperthermia therapy based on the use of near-

infrared (NIR) laser photoabsorbers to generate heat in order to induce thermal ablation of cancer cells upon NIR laser irradiation.⁵³

PTT offers solutions to the limitations affecting other thermal therapies, for example, the possibility of eradicating tumours located nearby intrabody cavities by the use of low-loss and flexible optical fibers.⁵⁴ However, PTT of sub-tissue tumours non accessible by optical fibers is very restricted, due to the fact that human tissues show strong extinction coefficients in the optical range of the electromagnetic spectrum. This fact limits PTT only to the treatment of superficial tumours. In order to overcome this limitation, PTT must be performed by using specific excitation wavelengths at which human tissues are partially transparent. This can be achieved by using laser excitation wavelengths lying in the so-called biological windows (BW): the first Biological Window (I-BW, which extends from 700 up to 950 nm) and the second Biological Window (II-BW, 1000–1350 nm) (**Figure 13**).⁵⁵

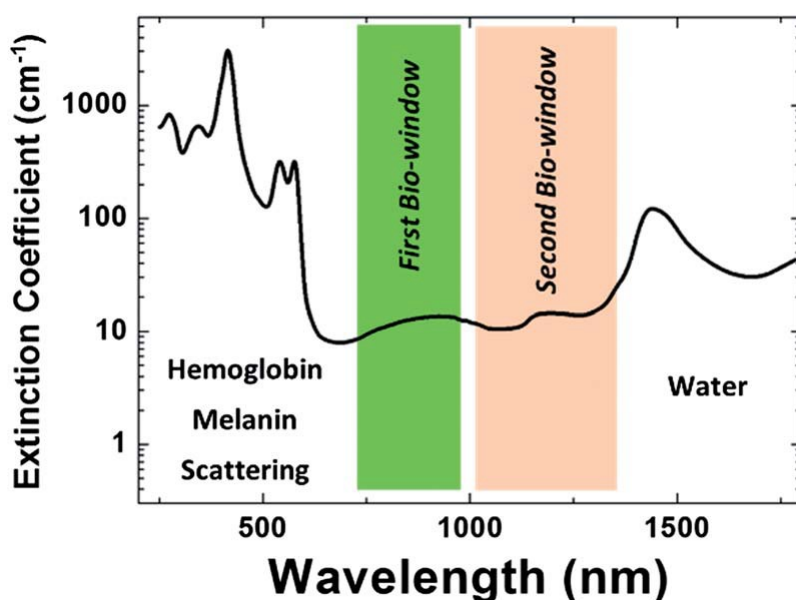


Figure 13. Extinction coefficient of a representative tissue. The different effects leading to light attenuation (such as the presence of haemoglobin, water and optical scattering) have been indicated. The spectral extensions of the two biological windows are also indicated. Figure adapted from Nanoscale, 2014, 6, 9494.

Therefore, nanoparticles able to absorb laser excitation wavelengths lying in the biological windows are suitable candidates as photothermal therapy agents, reducing the non-selective heating of healthy tissue and, at the same time, allowing a deep tissue penetration.

For these purpose, several studies have been conducted in order to design a nanosystems able to be used in clinical photothermal therapy. In 2008, Nanospectra Biosciences developed AuroLase® Therapy (**Figure 14**), a thermal ablation therapy of solid tumours based on the use of silica nanoparticles coated by a gold metal shell able to absorb near infrared laser

energy delivered by a fibre. This therapy is under clinical investigation at this current time for the treatments of head and neck cancer treatments.⁵⁶



Figure 14. Bag for the intravenously administration of AuroShell particles used in AuroLase® Therapy.

1.3.1 Metallic nanoparticle as photothermal agents in hyperthermia therapy

Metal nanoparticles have been largely studied as agents in photothermal cancer therapy (PTT) because of their ability to absorb light and rapidly convert it to heat.

This ability is ascribed to the resonant collective oscillation of the free electrons on the metal surface of the nanostructure in the presence of luminous radiation, a phenomenon called localized surface plasmon resonance (LSPR), which is common to all the nanoparticles but is particularly pronounced in those derived from transition metals (**Figure 15**).

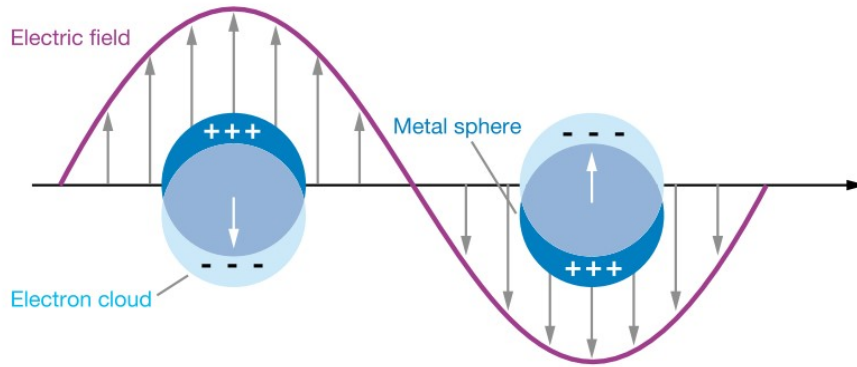


Figure 15. Schematic diagrams of localized surface plasmon (LSPR)

In PTT, when a nanoparticle is irradiated by laser beam, some of the incident photons are scattered by the nanoparticle while others are absorbed. The absorbed photons are responsible for heat production and luminescence. The total number of photons interacting with the metallic nanoparticles is determined by its extinction coefficient (α_{ext}), that is given by the:

$$\alpha_{\text{ext}} = \alpha_{\text{abs}} + \alpha_{\text{sct}}$$

where α_{abs} is the absorption coefficient and α_{sct} is the scattering coefficients

The extinction coefficient depends on the concentration of illuminated nanoparticles and on the extinction cross section ($\sigma_{\text{ext}} = \sigma_{\text{abs}} + \sigma_{\text{sct}}$, where σ_{abs} and σ_{sct} denote the absorption and scattering cross-sections, respectively).

The absorption efficiency, Φ_{abs} , of a given nanoparticle is traditionally defined as the number of absorbed photons divided by the total number of incident photons interacting with the nanoparticle (being either absorbed or scattered).

$$\Phi_{\text{abs}} = \alpha_{\text{abs}}/\alpha_{\text{ext}}$$

The energy absorbed by the nanoparticles (energy of incident photons multiplied by the total number of absorbed photons) can be released by either the emission of photons of different energy from that of incident photons (luminescence) or by the emission of phonons (i.e. by generating heat) (**Figure 16**).⁵³

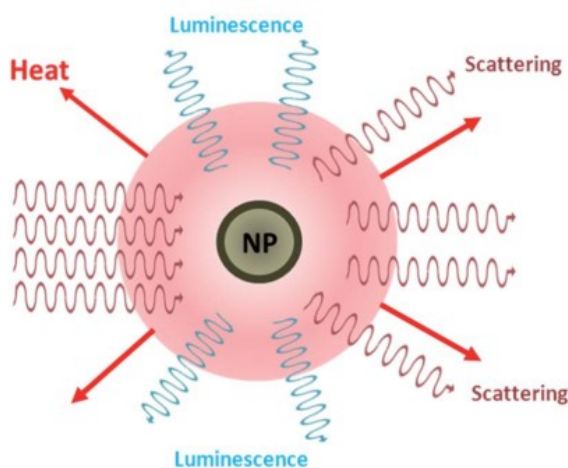


Figure 16. Schematic representation of the different processes activated when a light beam interacts with a nanoparticle. The presence of scattering, luminescence and heat generation are included. Heat and luminescence occur as a result of light absorption. Figure from *Nanoscale* **6**, 9494–9530 (2014).

However, the optical properties of metallic nanoparticles are strongly influenced by size, shape and environment. Indeed, the phenomenon of the LSPR can be described in details thank to the theory of Gustav Mie (1908), who solved the Maxwell equations giving a quantitative explanation of the resonance. Generally, simplified equations deriving from Mie theory are used to explain the importance of many parameters that strongly affects LSPR intensity and wavelength.⁵⁷ By way of illustration, for many metals in the bulk state free electron behaviour is predominant and the wavelength of the plasmon absorption peak depends on the equation:

$$\lambda^2 = \lambda_p^2 (\epsilon^\infty + 2\epsilon_m)$$

where

$$\lambda_p^2 = (2\pi c)^2 / \omega_p^2$$

is the metal's bulk plasma wavelength, ϵ^∞ is the high frequency dielectric constant due to interband and core electrons' transitions, ϵ_m is the dielectric constant of the surrounding medium and the resonance frequency (ω_p) is given by:⁵⁸

$$\omega_p = (N \cdot e^2 / \epsilon_0 \cdot m_e)^{1/2}$$

where N is the concentration of free electrons in the metal, e is the charge of the electron, m is the mass of the electron and ϵ_0 is the vacuum permittivity.

The equations shows that the LSPR is strongly affected by several factors such as size and shape of the nanoparticles and most of all by the nature of the surrounding environment due to a direct dependence on the dielectric constant of the medium (ϵ_m) in which the nanoparticles are dispersed. Therefore, every modification in the interface with the surrounding environment of these particles leads to significant shifts to the LSPR wavelength and intensity.

1.3.2 Gold nanorods as photothermal agents

Since from 5th B.C., the use of colloidal gold as a colorant has been known for its use in making ruby glass and providing reddish tinge to ceramics.⁵⁹

In 1857, the most important article in both the history of colloidal science and in the discussion of how light interacts with matter has been published by Faraday, who reported that the ruby glass was coloured because of the presence of finely dispersed gold particles.

Nowadays, it is well known that gold nanoparticles assume a peculiar red colour in solution due to the localized surface plasmon resonance (LSPR) at visible range of UV-Vis spectrum.

In the last decades, several studies have been focused on the development of gold nanostructures characterized by different size and the shape, in order to move the spectral location of surface plasmon resonance wavelength from the visible to the near infrared region.

At macroscopic level, the change in colour of colloidal solution of gold nanoparticles is an evidence of the increase of nanoparticles size or change of nanoparticles shape. For example, an aqueous dispersion of spherical gold nanoparticles with a diameter around 10 nm is characterized by a red colour; otherwise, when gold nanoparticles size increases to nearly 100 nm or changes in shape, such as a rod-like shape with aspect ratio of 3 (length 30 nm, diameter 10 nm), the colloidal dispersion appears bluish.

This phenomenon can be explained by considering the movement of λ_{SPR} in the UV-Vis spectra of gold nanostructures characterized by a different size and shape.

The possibility of tailoring the λ_{SPR} in a very wide range (from visible to infrared) by the adjustment of their dimensions, led to the development of GNPs with a great variety of geometries (nanocages, nanostars, nanoshells, and nano- hexapods).

Their unique optical properties, in addition to their biocompatibility, make gold nanomaterials promising candidates as light-activated heating nanoparticles in PTT applications. For this purpose, gold nanorods (GNRs) have been the most studied nanoparticles among the different non-spherical metallic nanoparticles.

Indeed, GNRs are characterized by the presence of two main absorption bands in the UV-Vis spectrum (**Figure 17a**):

- An intense absorption band at near infrared wavelengths, corresponding to electron oscillations along the longest dimension of the GNRs;
- A weak absorption band at visible wavelengths, corresponding to surface electron oscillations along the short dimension of the GNRs;

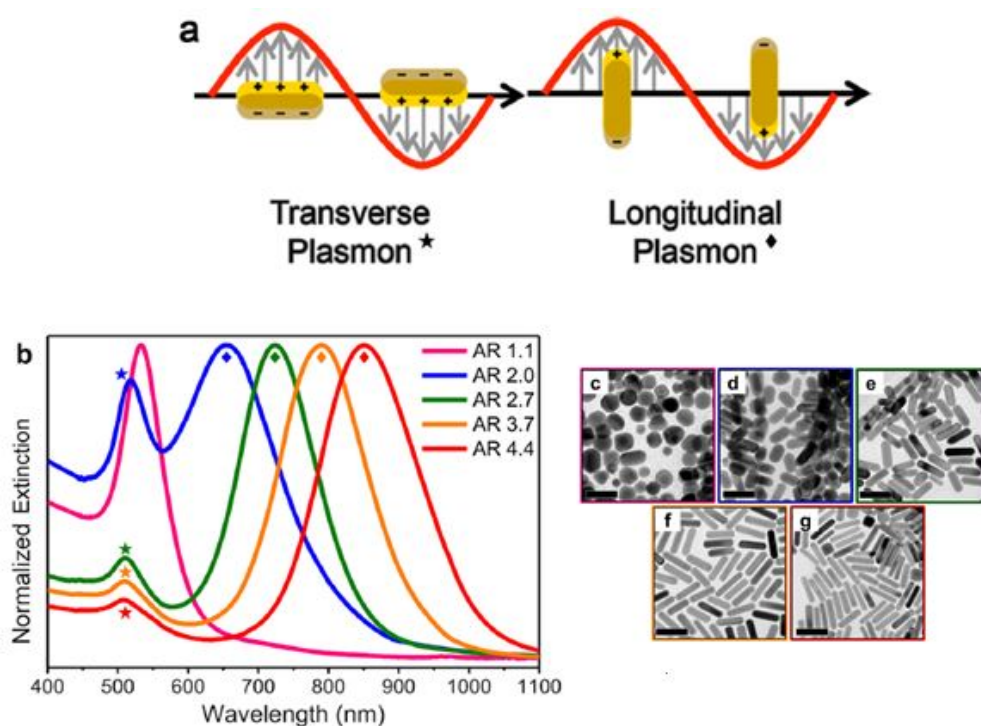


Figure 17. (a) Diagram depicting the conduction band electron oscillation (gray arrows) upon transverse and longitudinal localized surface plasmon resonances of gold nanorods. (b) Visible/near infrared extinction spectra of gold nanorods with different aspect ratios (ARs) showing transverse (★) and longitudinal (◆) extinction peaks. TEM images of gold nanorods (c) AR 1.1, (d) AR 2.0, (e) AR 2.7, (f) AR 3.7, and (g) AR 4.4. Scale bars are 50 nm. Figure adapted from *Langmuir* **32**, 9905–9921 (2016).

Several methodologies have been fine-tuned in order to obtain gold nanorods characterized by a rational control over the *aspect ratio* (*AR*). The *aspect ratio*, corresponding to ratio between length and width of GNRs, is primarily responsible for the change in their optical properties. By increasing the aspect ratio, the longitudinal plasmon resonance of GNRs moves towards high wavelengths up to 1200 nm (**Figure 17 b and c**).⁶⁰

This phenomenon is very important for the developing of photothermal agents based on gold nanostructures, which might be characterized by λ_{SPR} close to 800 nm, in other words placed in the first biological window in order to lead the minimum collateral heating effect on the healthy surrounding tissue.

In order to study the absorption efficiency of this particular gold rod geometry and size, several simulation studies have been carried out. The studies of El-Sayed *et al.* reported that GNRs usually show absorption efficiencies above 90% except when the GNR radius exceeds 20 nm. In particular, the results showed that the heating efficiency remains above 90%, when the GNR width (diameter) is kept close to 15 nm independently of the GNR length (at least for lengths as large as 160 nm). However, the absorption efficiencies predicted decrease down to 60% for GNRs characterized by a diameter greater than 15 nm.⁶¹

Usually, GNRs synthesis is based on the two-step “nuclear” method discovered by Zsigmondy, combining his synthesis technique with the Faraday’s method. Later this method has been fine-tuned and was defined “seed-mediated” method.

The method consists the synthesis in aqueous medium with the assistance of various surfactants, which act as both template and stabilizer for the growing nanoparticles against aggregation phenomena. Once the process is completed, the surfactant molecules remain adsorbed or deposited onto the surface of the nanoparticles, avoiding the post- synthesis collapse of the created nanoparticles. However, most of these surfactants are strongly toxic or simply not suitable for biomedical applications because they do not allow further synthetic medications. The removal of surfactants requires the development of specific ligands that would be able to replace them, to prevent the aggregation phenomena, and at the same time ensure that the specific desired final properties of GNRs are retained (**paragraph 1.5**).⁶²

1.3.3 Magnesium nanoparticles as photothermal agents

Magnesium is one of the most abundant element in the human body, in particular its form as divalent cation (Mg^{2+}) is involved in more than 300 known enzymatic reactions, playing an important role in many cellular processes.⁶³ In addition magnesium has role in many reactions involving ATP, protein and nucleic acid synthesis, mitochondrial activity and integrity, ion channel modulation, plasma membrane stabilisation and translational processes, as well as many other cellular functions.⁶⁴

Due to its biocompatibility, the use of magnesium in biomedical application has been largely investigated. The modern applications of magnesium-based biomaterials are similar to those that were attempted historically. At the beginning of 1900, numerous physicians studied the application of magnesium and magnesium alloy devices in vascular, orthopaedic and general surgery. However, without the ability to accurately alloy magnesium, and before the common application of coatings on implants, the corrosion could not be controlled sufficiently to promote its use as biomaterial.

Indeed, magnesium-based materials revealed a quickly degradation that affects their mechanical integrity for long time and showed the production of hydrogen gas in the organs able to cause tissue disruption. For these reasons, the most effective results were obtained from non-orthotopic applications, such as the suturing of organs.⁶⁵

In the late 1930s, Earl McBride conducted studies regarding the use of magnesium alloy as orthopaedic implants. During his studies, he found that corrosion of magnesium based materials resulted in a tissue reaction, could represent an advantage for specific applications in which the rapid corrosion of the implant materials utilized would outweigh the effect on the surrounding tissue.⁶⁶ Based on these results, the field of magnesium biomaterials has been growing exponentially, especially in the fields of investigation regarding the development of magnesium alloys for vascular applications, and the field devoted to identifying appropriate magnesium based materials for orthopaedic applications.

In the last decades, the properties of magnesium nanoparticles have been investigated in nanotechnology research, fascinated by the high biocompatibility of this nanomaterial related of its biodegradation into magnesium ions, which are completely absorbable by the human body. In particular, recent studies demonstrated that magnesium nanoparticles exhibit a pronounced plasmonic response that is tunable throughout the whole visible wavelength range.^{67,68} In particular, Sterl *et al.* reported that plasmonic response of magnesium nanodisks can be tuned by adequate choice of the disk diameter throughout the visible wavelength range,

from resonance wavelengths below 500 nm up to 800 nm and further into the near-infrared (**Figure 18**).⁶⁹

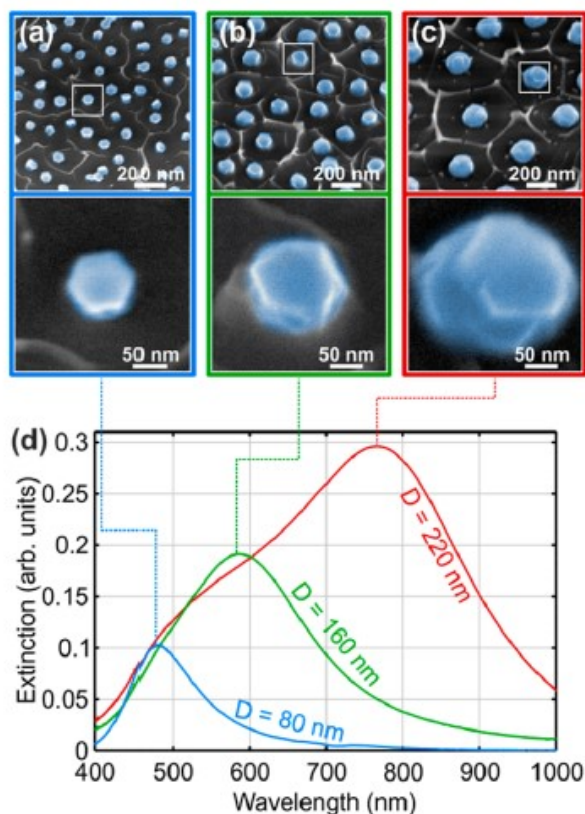


Figure 18. Magnesium nanodisks as a model system for magnesium plasmonics. (a–c) Colorized SEM images of magnesium nanodisks with average diameters of 80, 160, and 220 nm, respectively. (d) The resonance wavelength of such nanodisks can be tuned throughout the visible wavelength range by varying the diameter. Figure adapted from Nano Lett. **15**, 7949–7955 (2015).

Due to their plasmonic properties, magnesium nanoparticles has been studied as suitable agents for photothermal tumour therapy.^{70,71,72,73}

In 2012, Wang *et al.*, tested the direct injection of the magnesium nanoparticles into the tissues to measure the temperature changes of the materials subjected to laser heating (**Figure 19**).⁷² The obtained results showed the high ability of magnesium nanoparticles in hyperthermia applications and the related advantages comparing to other popular nanosystems. Compared to gold-based nanomaterials, the density of magnesium is much lower and therefore more particles can be loaded into the target tissues leading a more efficient treatment. Moreover, magnesium is beneficial to human health and its high abundant in nature makes magnesium cost-effective for clinical utilization.

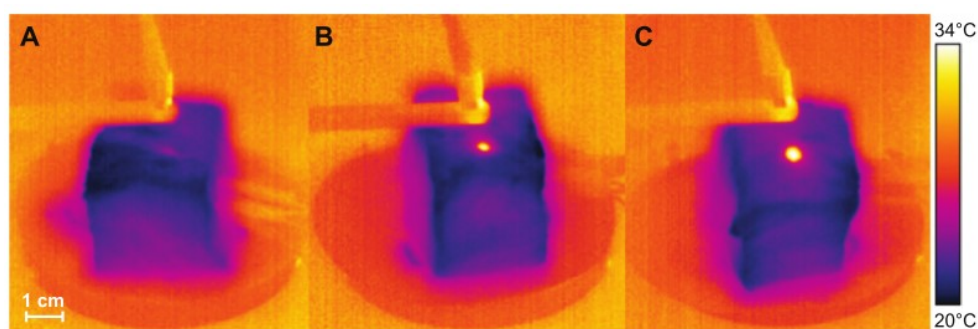


Figure 19. Thermal images of the pig tissue injected with water (A) 0.01 g/mL fresh magnesium nanoparticle aqueous solution (B) and 0.02 g/mL fresh magnesium nanoparticle aqueous solution (C) taken after 1 minute of laser irradiation at 1W. Figure from *Int. J. Nanomedicine* 7, 4715–4725 (2012).

Nevertheless, the results highlighted that there are still many problems to overcome in order to use magnesium nanoparticles as photothermal agents in clinics. First of all, the heating ability of magnesium nanoparticles is affected by variable sizes, structures of these particles and oxidation grade, therefore the influence of each parameter must be deeper investigated. Regarding the oxidation grade, they showed that only pure magnesium nanoparticles, which are often black in colour, are able of absorb light differently from oxidized magnesium nanoparticle (MgO nanoparticles), which are often white in colour. Because of their high reduction potential and high affinity toward oxidation, the synthesis of magnesium nanoparticles is quite challenging, and several synthetic methodologies have been developed in order to improve the process.

In addition, the electrode potential of magnesium can affected also heat generation ability of nanoparticles and their stability *in vivo*. Once magnesium nanoparticles are injected into the tissue, heat energy is produced because of chemical reaction between magnesium nanoparticles and water contained in the tissue.

However, magnesium nanoparticles showed a low reactivity with water below a certain temperature, such as the body core temperature of 37°C. Therefore, a suspension fluid containing the nanoparticles with an initial temperature around room temperature (25°C) can be easily injected into the target sample or tissues.

Because this phenomenon leads to a certain level of corrosion of the material, the control of the degradation rate of the magnesium nanoparticles used in hyperthermia is an important requirement. Indeed, the rapid corrosively degradation of the material represents an advantage considering the rapid absorption of magnesium ions into the body; however, if the rate of material degradation is too fast, the heating enhancement effect may not be maintained for long or fully occur. Regarding this, a protective coating on the nanoparticles might be a

feasible way to avoid their reacting with water as well as to control the degradation rate and further improve biocompatibility. Moreover, the surface coating formation can allow the possibility to introduce an active targeting on the nanoparticles surface, making the final system suitable for diagnostic and theranostic applications. For example, the study of *Jin et al.*, developed a laser scanning based thermography strategy for detecting the skin cancer by using magnesium nanoparticles conjugated with biomolecules (for example antibody) as active targeting.⁷³

1.4 Nanomaterials as diagnostic and imaging tools in nanomedicine

For a non-invasive diagnosis of patients, *in vivo* imaging techniques are powerful tools to visualize the abnormal state of the body and monitor biological situations at the target site. Several imaging techniques have been developed for this purpose, such as magnetic resonance imaging (MRI), positron electron tomography (PET), computed tomography (CT), single-photon emission computed tomography (SPECT), optical imaging (OI), ultrasound (US) and photoacoustic imaging (PAI). Because of the several physical processes behind each of these techniques, they are characterized by different depth of penetration and spatial resolution abilities.⁷⁴

PROS AND CONS OF IMAGING MODALITIES								
Technique	Labels	Signal measured	Strengths	Weaknesses	Cost	Throughput	Sensitivity (moles of label detected)	Resolution
PET	Radiolabelled molecules	Positrons from radionuclides	Highly sensitive	Can detect only one radionuclide, requires radioactivity	High	Low	10^{-15}	1-2 mm
SPECT	Radiolabelled molecules	γ -rays	Can distinguish between radionuclides, so more processes can be imaged at once	Requires radioactivity	High	Low	10^{-14}	1-2 mm
CT	None	X-rays	Fast, cross-sectional images	Poor resolution of soft tissues	High	Low	10^{-6}	50 μ m
MRI	Can use isotope-labelled molecular tracers	Alterations in magnetic fields	Harmless, high-resolution of soft tissues	Cannot follow many labels	High	Low	10^{-9} - 10^{-6}	50 μ m
Optical	Genetically engineered proteins and bioluminescent and fluorescently labelled probes	Light, particularly in the infrared	Easy, non-damaging technique readily adapted to study specific molecular events	Poor depth penetration	Low	High	10^{-12}	1-2 mm
Photoacoustic	Probes that absorb light and create sound signals	Sound	Better depth resolution than light	Information processing and machines still being optimized	Low	High	10^{-12}	50 μ m
Ultrasound	Microbubbles, which can be combined with targeted contrast agents	Sound	Quick, harmless	Poor image contrast, works poorly in air-containing organs	Low	High	10^{-8}	50 μ m

Figure 20. Table dealing the properties of imaging modalities adapted from Chem. Soc. Rev. **41**, 2656–2672 (2012).

As shown in **Figure 20**, microscopy and other techniques that use un-scattered photons provide high-resolution ($\sim 1 \mu\text{m}$) images, but only to a maximum depth of $\sim 1 \text{ mm}$ in most tissues. On the other hand, diffuse optical techniques such as fluorescence and near-infrared optical tomography, that exploit multiply scattered photons, can reach a depth of several centimetres but a lower spatial resolution ($> 1 \text{ mm}$).⁷⁵

For this reason, the combination of different imaging techniques in multimodality approach, showed the possibility to accomplish high sensitivity and high resolution simultaneously, providing more detailed anatomical or biological information about the target disease. The first example of multimodalities techniques is represented by PET/CT in 1998, while the first

commercial prototype of PET/MRI for a human scale hybrid scanner has been realized in 2007.⁷⁶ These findings showed the possibility to integrate high sensitivity of PET, used as a whole body screen to identify regions of interest, with high-resolution images for anatomical information of CT and MRI. In particular, MRI allowed the reduction of the volume of tissue that needs to be scanned and, consequently, the scan time required for high-resolution imaging. In order to take advantage from multimodal imaging, researchers focused their attention on the development of contrast imaging agents able to overcome the limitations of a single imaging modality, to provide more detailed information of the target site through targeted delivery.⁷⁴ For this purpose, nanotechnology showed the possibility to produce nanoscale multimodal imaging agents, constituted by inorganic nanoparticles, characterized by intrinsic imaging abilities, or organic nanoparticles (liposomes, micelles and polymeric) able to integrate more than two imaging agents on their surface or inside the core. Dealing with this, magnetic properties of iron oxide nanoparticles, led to the development of new contrast agents in magnetic resonance imaging (MRI).¹² On the other hand, the optical properties of gold nanomaterials make them suitable contrast agents in computed tomography (CT) imaging and photoacoustic imaging (PAI).

In addition, the possibility to combine in the same nanosystem, therapy and the diagnostic functionalities led to the development of theranostic systems. This strategy could be used to monitor the pharmacokinetic, the accumulation of therapeutics and the progression of disease, giving important insights into heterogeneities both within tumour and between patients for potential personalized therapies.¹³

1.4.1 Photoacoustic imaging (PAI)

Photoacoustic imaging (PAI) technique is an emergent imaging method based on the photoacoustic effect, a physical phenomenon that consists in the generation of acoustic waves from an object illuminated by pulsed (or intensity-modulated) electromagnetic continuous-wave (CW), especially light. Alexander Graham Bell discovered for the first time the photoacoustic effect in 1880, thanks to his studies on long-distance sound transmission.

During his experiments, he found out that when a solid sample was exposed to pulsed light beam, sound waves were directly produced by the bulk sample. The observed acoustic signal was noticed to be dependent on the sample material, suggesting the involvement of light absorption processes, which subsequently heat the sample generating a piston-like pressure wave in the surrounding gas. Later, further investigations showed that the sound could also be generated by materials exposed to ultraviolet (UV) or near-infrared (NIR) light.

However, the application of photoacoustic imaging to biomedicine date back to the last decade of the twentieth century, when more powerful light sources and more sensitive sound detectors were developed. These progresses demonstrated the presence of photoacoustic effect in optically scattering media and biological tissue, leading to the development of PA imaging (PAI). Nowadays, PAI is one of the largest research areas in the field of biomedical optics, showing the possibility to combining the advantages of both optical excitation and acoustic detection in a hybrid imaging technique able to achieve high sensitivity to optical absorption and the capability for deep imaging in soft tissue. In *photoacoustic imaging* (PAI), ultrasound waves are generated by irradiating tissues with modulated or pulsed laser light. Because sound waves are less scattered in tissue than photons they can propagate to a greater distance without losing their original propagation directions, providing PAI with high spatial resolution at depths. The absorption of photons by the chromophores in the sample results in the generation of an acoustic wave, which is then processed to form an image. The mechanism consists in a short laser pulse on the pathological tissue, which release photons able to propagate into the tissue and to be absorbed by endogenous chromophores (biomolecules, such as haemoglobin, DNA-RNA, lipids, water, melanin, and cytochromes). The absorption mechanism involved can be electronic, vibrational, stimulated Raman and surface plasmon resonance, depending on the molecules or agents stimulated by the irradiation. After laser irradiation, the absorbed optical energy is partially or completely converted into heat, through non-radiative relaxation of excited molecules (**Figure 21a**). The heat-produced generates pressure waves able to diffuse in tissue as ultrasound waves, which

can be detected outside the tissue by an ultrasonic transducer or transducer array to form an image that maps the original optical energy deposition inside the tissue (**Figure 21b**).⁷⁷

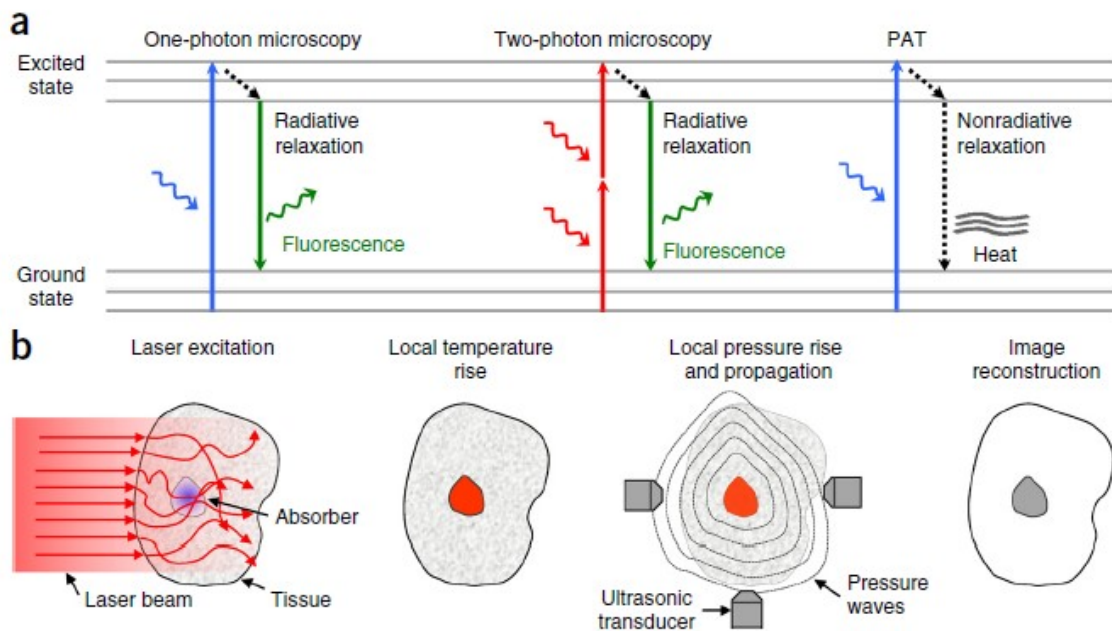


Figure 21 - Principles of photoacoustic tomography (PAT). (a) Jablonski diagram, illustrating the photon energy transfer in one-photon fluorescence microscopy, two-photon fluorescence microscopy, and PAT. The most common electronic absorption in the visible and ultraviolet spectral regions is shown. (b) Imaging principle of PAT. Figure from Nat. Methods **13**, 627–638 (2016).

Although PA and US image formation and the factors that affect spatial resolution and fidelity are mostly the same, the contrasts that generate the images are essentially different. A US image provides description of the *acoustic impedance mismatch* between different tissues: US contrast, therefore, depends on morphological features of the tissues, whilst PA represents the initial pressure distribution produced by the absorption of a pulse of laser light. With this configuration, it is possible to obtain two overlapped images: an explorative US trace and a PA contrast image, to make easier localization of the contrast into the sample (**Figure 22**).

Photoacoustic tomography (PAT) is referred to PAI as cross-sectional or three-dimensional (3D).⁷⁸ The spatial resolution and imaging depth within the reach of diffusive photons in PAT are highly scalable, offering the possibility to multiscale living biological structures ranging from organelles to organs. In particular, by using a laser irradiation in the NIR (620–950 nm) window, PAT can achieve a penetration depth of several centimetres with resolution on the order of a few hundred micrometres, scaling to <100 μm for shallower (<1 cm) penetration depths.

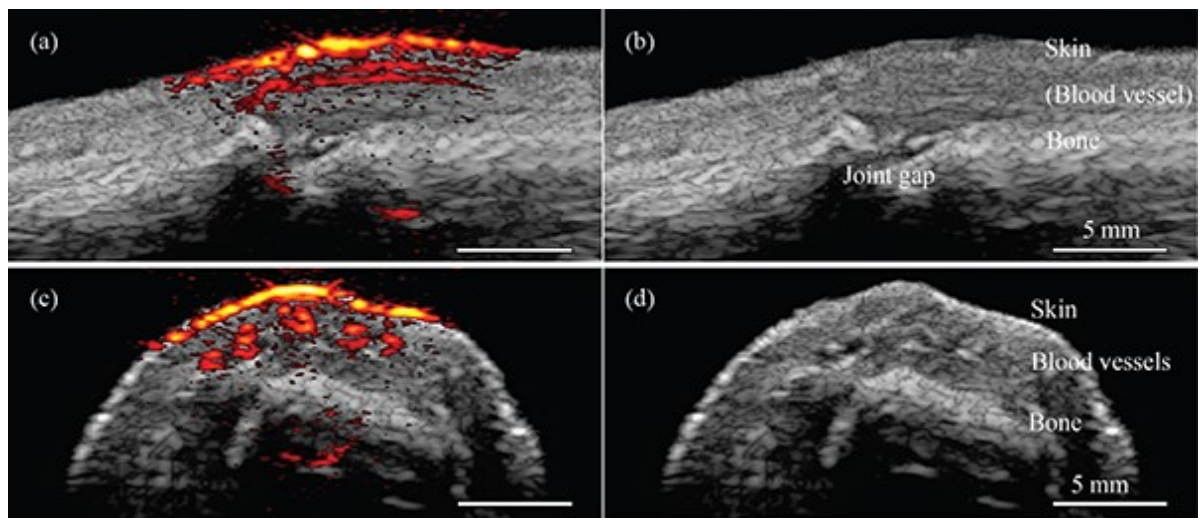


Figure 22. Photoacoustic/ultrasound images. The images on the right (b and d) show anatomical structures revealed by the ultrasound. The images on the left (a and c) show the photoacoustic data overlaying the ultrasound data. The bright yellow and red at the top of the finger show the skin and blood vessels running parallel to the finger. Figure from *Biomed. Opt. Express* 7, 5081 (2016).⁷⁹

In the last years, the potential of PAT for breast cancer imaging, brain imaging, and sentinel lymph node mapping have been investigated in pre-clinical studies.

Breast PAT imaging is under clinical application phase; recently, studies regarding the clinical feasibility of *PAmammography*, showed the possibility to identify the presence of malignant lesions.^{80,81} The investigators also discussed removal of imaging artefacts contributed by the skin surface signal and suggested that dark-field light delivery and multiview detection would probably help. In addition, methylene blue has been studied as contrast PAI imaging, for sentinel lymph node mapping a biopsy, highlighting high penetration depth and spatial resolution of this imaging technique.⁸²

Otherwise, PAT imaging of the human brain is still in the preclinical study phase. However, promising improve elements have been achieved in the past few years, raising confidence that PAT can be a highly useful clinical tool for non-invasive functional brain imaging.^{83,84}

1.4.2 Contrast agents for photoacoustic imaging (PAI)

In *photoacoustic imaging* (PAI), ultrasound waves are generated by irradiating tissues with modulated or pulsed laser light. In order to achieve penetration depths up to several centimetres, applications in biology and biomedicine need the use of optical wavelengths in the near-infrared (NIR, 700 – 1500 nm), due to high transparency of tissues in this range (**Figure 23**). Indeed, biomolecules in the tissue, such as haemoglobin, lipids, water and melanin, are able to absorb laser irradiation and generate a photoacoustic signal defined “endogenous contrast”. The endogenous contrast can be exploited to provide structural and functional information of tumour tissue for different applications in cancer research,⁷⁵ allowing the development of *in vivo* preclinical photoacoustic imaging methods for the tumour detection and molecular characterization,^{85,86} for therapeutic monitoring and for the identification and for the assessment of metastatic lymph nodes have been reported.⁸²

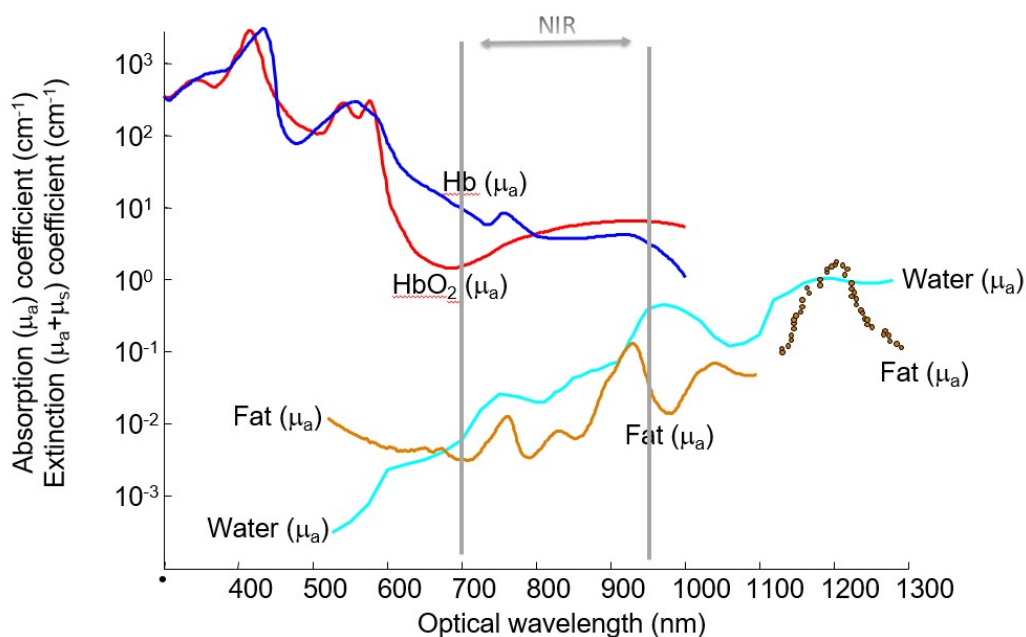


Figure 23. Photoacoustic imaging of endogenous chromophores.

For example, haemoglobin, the iron-containing oxygen-transport metalloproteins, present in the red blood cells assigned to deliver oxygen throughout the body, can be used as endogenous contrast agent in PAI for studying tumour angiogenesis. Indeed, when haemoglobin binds oxygen, it undergoes under structural and electronic modifications that cause changes in its absorption spectrum. This difference can be exploited in photoacoustic imaging in order to measure total haemoglobin concentration and oxygen saturation.⁸⁷ On the other hand, the absorption peaks at 930 and 1210 nm, relative to the second overtone of

abundant C–H bonds, can be used in PAI for mapping the lipid and collagen distribution *in vivo*, that are two critical markers for many kinds of diseases.⁸⁸ Although the intrinsic chromophores are useful to understand biological processes and provide structural and functional information of human tissues, they generate a background absorption in the photoacoustic signal that might be overcome through the design of exogenous contrast agents. An ideal contrast agent should be composed by a signalling compound, which produces the signal for imaging, and a targeting moiety able to identify a specific biological entity or process. In photoacoustic imaging the signalling compound corresponds to an exogenous agent able to absorb light in the near infrared (NIR) region (620 – 950 nm), in order to obtain an intensive photoacoustic signal besides a high penetration depth. In addition, PAI contrast agent must be biocompatible for the organism, and this prerogative can be achieved whether minimizing the toxicity, through the control of the administration route, dose and the immune response or optimizing elimination from the circulatory system and target tissue penetration, in order to reduce the accumulation in off-target tissues. In addition, they might be characterized by specific photophysical properties:

- high molar extinction coefficient to maximize the amount of light absorbed;
- sharply absorption peak to ensure unambiguous identification by spectral un-mixing even at low molar concentrations;
- high photostability to ensure that spectral features are not changed by light irradiation;
- low quantum yield to maximize the non-radiative conversion of light energy to heat;
- efficient conversion of heat energy to produce acoustic waves;

PAI exogenous agents can be small-molecule dyes, metallic or semiconducting nanostructures, and organic nanostructures, characterized by high chemical, physical and biochemical flexibility. Because their molar extinction coefficients are usually higher compared to those of small-molecule dyes nanoparticles, these agents are currently the largest class of contrast agents for molecular PAI. Indeed, nanosystems are characterized by a large surface area that can be chemically modified by introducing a large number of targeting moieties in order to increase the probability of target-binding. Different nanostructures characterized by different shapes and sizes (<1,000 nm, usually ~10–100 nm) and materials have been investigated as contrast agents in PAI. Among these gold nanomaterials, carbon nanotubes and graphene-based nanomaterials showed the most promising results.

1.4.3 Gold nanostructures as PAI contrast agents

Due to their inert nature and their unique optical and physicochemical properties, gold nanomaterials are the most promising candidates as PAI contrast agents.

As reported previously, the optical properties of gold nanomaterials are ascribed to the “localized surface plasmon resonance” (LSPR) (paragraph 1.3.1 and 1.3.2, Figure 16). This phenomenon, concerning the plasmon formations after a laser irradiation at an appropriate wavelength, consists in the oscillation of conduction electrons of gold nanostructure relative to the core. Plasmons convert the substantial part of the oscillation energy into heat detectable with PAI. Acting as a macroscopic dipole, gold nanostructures show higher extinction coefficient in the NIR range and higher PA conversion efficiency than organic small-molecule dyes. For example, the study of Wu et al. showed that the absorption of a single nanoshell with a diameter of 20 nm, corresponds to the absorption of 40000 molecules of indocyanine green, one of the most used NIR dye used for PAI.⁸⁹

The extinction coefficient (Q_{ext}) depends on the nanostructures morphologies and dimensions, usually gold nanorods show a higher Q_{ext} respect to gold nanoshells, which are characterized by a Q_{ext} comparable to gold nanospheres (Figure 24). An additional advantage of the use of gold nanostructure as PAI contrast agents is their photostability, which avoid the photobleaching phenomena, affecting conventional fluorophores.⁹⁰ In-depth studies have been carried out in order to fine-tune methodologies for synthesizing gold nanostructures characterized by different morphology and λ_{SPR} , in order to improve PAI application.

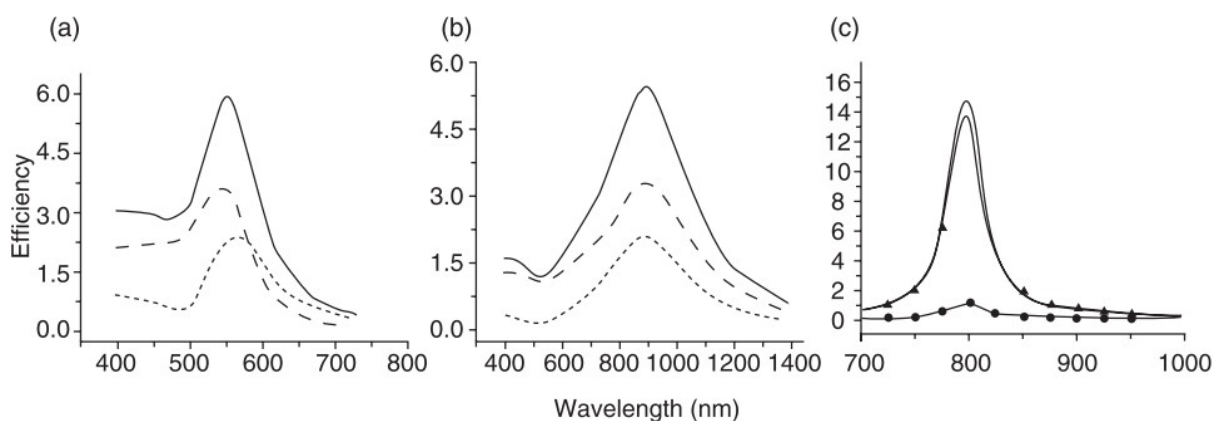


Figure 24. Calculated extinction (top curve), absorption (middle curve) and scattering (bottom curve) efficiencies for: (a) a 80 nm - diameter gold nanosphere; (b) a 70 nm - radius gold nanoshell with a 60 nm silica core; and (c) a 59.6 × 15.3 nm gold nanorods. Figure from Nanomaterials for the life Science Vol. 3: Mixed Metal Nanomaterials **3**, (2007).

Among these, gold nanorods and gold nanoshells revealed a great potential in PAI applications. Gold nanoshell are spherical particles with diameters typically ranging in size from 10 to 200 nm composed of a dielectric core coated by a thin gold shell. One of the most popular approach to construct gold nanoshells involves attaching small gold particles to the surface of silica core and, subsequently, using these sites as nuclei to seed shell growth when a gold salt is reduced in their presence (**Figure 25**).

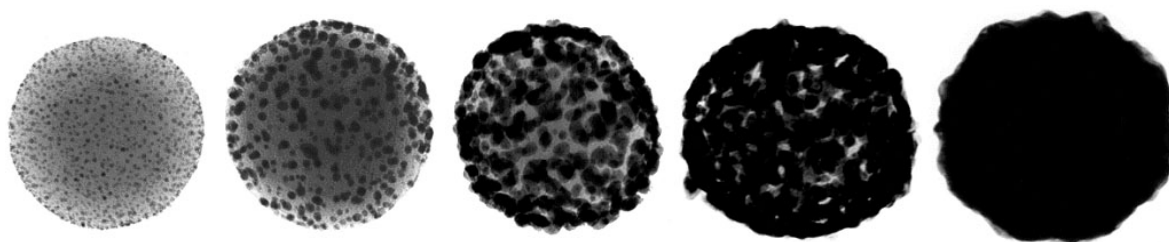


Figure 25. TEM images of gold nanoshell: initial (left) to complete (right) growth of gold shell around silica nanoparticle. Figure from *J. Control. Release* **155**, 344–357 (2011).⁹¹

In this type of synthesis, it should be possible to control the shell thickness by adjusting the amount of reducible salt present in solution. This thickness influences the plasmon modes of the particles and the position of λ_{SPR} which can be selectively tuned from 600 nm to greater than 1000 nm (**Figure 26**).⁹²

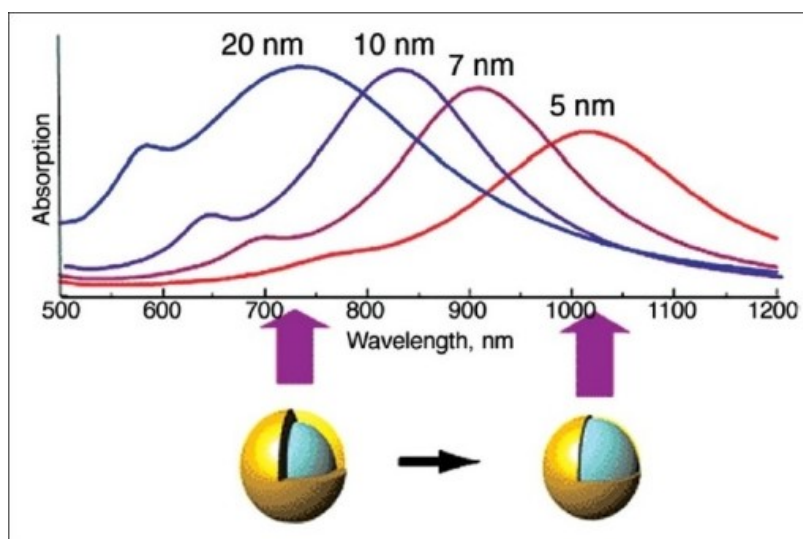


Figure 26. Gold nanoshell plasmon resonances for a 120-nm core with indicated shell thickness. Figure from *J. Pharm. Bioallied Sci.* **2**, 282 (2010).⁹³

In particular, the position of the extinction (plasmon resonance) peak, and the relative contributions of absorption and scattering to total extinction, can be tuned by changing two parameters:

- the radius of the inner core (r_1);
- the radius of outer shell (r_2);

For a given r_2 , the position of the extinction peak is determined by the core to shell ratio (r_1/r_2); for greater core to shell ratios (thinner gold shells), the peak becomes shifted to longer wavelengths.

In addition, due to the strong-affinity between gold and thiol group, the gold nanoshells surface can be chemical functionalized with organic molecules in order to enhance their biocompatibility and stability or to introduce active targeting.

1.4.4 Magnetic Resonance Imaging (MRI)

Magnetic resonance imaging (MRI) is a non-invasive diagnostic tool, that in the last decades have shown a great potential in the visualization of structural and functional information involving the human body. It is based on the nuclear magnetic resonance (NMR) phenomenon and on the development of a technique able to measure the magnetic characteristic of atomic nuclei.

The mechanism involves the application of an external strong magnetic field, able to induce the nuclei of protons to align their spins either parallel or antiparallel to the direction of magnetic field. During their alignment, the spins precess under a specified frequency, known as the Larmor frequency (ω_0 , **Figure 27 a**).

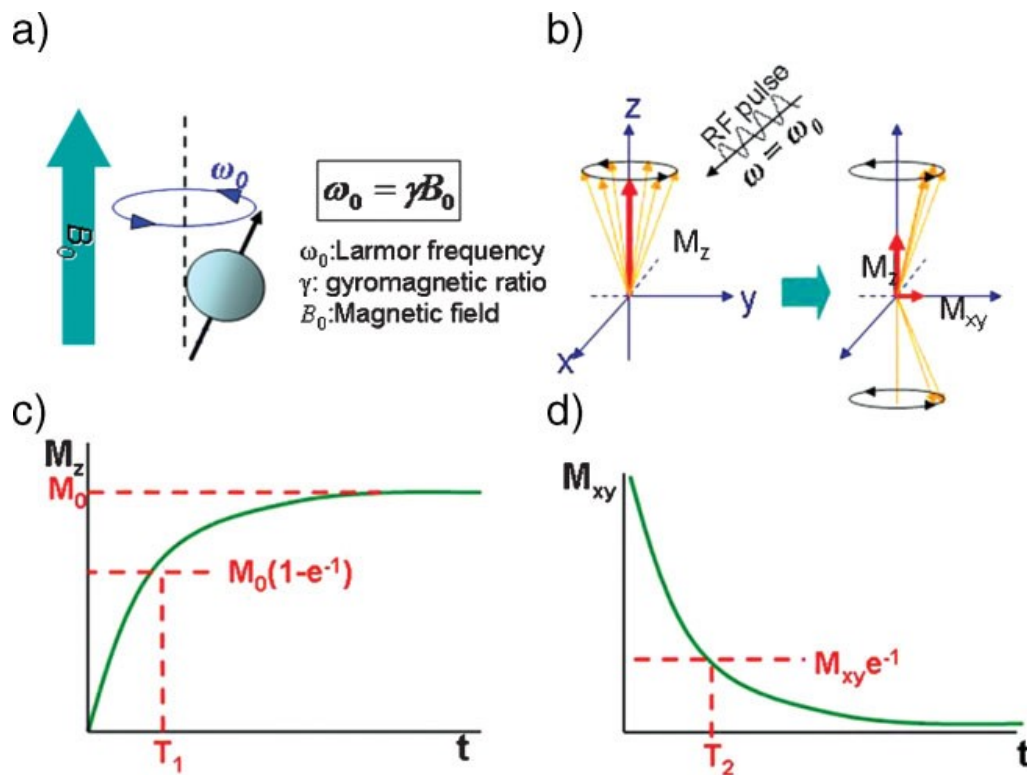


Figure 27. Principle of magnetic resonance imaging. a) Spins align parallel or antiparallel to the magnetic field and precess under Larmor frequency (ω_0). b) After induction of RF pulse, magnetization of spins changes. Excited spins take relaxation process of c) T1 relaxation and d) T2 relaxation. Figure from Adv. Mater. **21**, 2133–2148 (2009).

When a ‘resonance’ frequency in the radio-frequency (RF) range is introduced to the nuclei, the protons absorb energy and are excited to the antiparallel state. After the disappearance of the radio-frequency pulse, the excited nuclei relax to their initial, lower-energy state (**Figure 27 b**). There are two different relaxation pathways, the first, called longitudinal or T1 relaxation, involves the decreased net magnetization (M_z) recovering to the initial state

(**Figure 27 c**); the second, called transverse or T2 relaxation, involves the induced magnetization on the perpendicular plane (M_{xy}) disappearing by the dephasing of the spins (**Figure 27 d**).⁹⁴

This technique was discovered by Dr Isidor Rabi awarded noble prize in physic in 1944.⁹⁵ Thanks to Rabi's studies, Dr Damadian used for the first time NMR in biomedical applications to measure T1 and T2 relaxation times in rat tumours. In 1971 his results, published on *Science*, revealed that tumour tissue possessed longer T2 times than those of a normal tissue, and showed the possibility to use NMR technique for detecting malignant tumour. These studies constituted the foundation of magnetic resonance imaging (MRI) and leading to the production of the first MR images human in 1977 and the development of the first commercial whole-body MR scanner in 1980.

Although images obtained by purely MRI result sufficiently detailed, the small differences in relaxation time between normal tissues and lesions can be not enough clear, leading to a not accurate diagnosis. Indeed, MRI technique is characterized by a superb spatial resolution, but shows a limited sensitivity of its probes. For these reason, the use of contrast agents able to influence the proton relaxation times, can increase the visibility of organs or body regions, improving the signal differences between adjacent regions, such as “tissue and tissue”, “tissue and vessel”, and “tissue and bone”.⁹⁶

Nowadays, the development of efficient and safe contrast agents represents a crucial point for the MRI sensitivity enhancement. MRI contrast agents act by shortening T1 (longitudinal) and T2 (transversal) relaxation time of surrounding water protons in order to indirectly produce a signal-enhancing effect. The efficiency of an agent to shorten relaxation times is called relaxivity, which is calculated by ratio between the change in the relaxation rate and the concentration of the contrast agent. In MRI application on human body, the relaxivity can be affect by extrinsic factors including temperature, magnetic field strength and the tissue surroundings (water, plasma or blood).⁹⁷

Beyond an adequate relaxivity and susceptibility effects, in clinical application a contrast agent has to satisfy several requirements, such as tolerance, safety, low toxicity, stability, optimal bio-distribution, and elimination. T1 contrast agents are paramagnetic agents, composed of a metal ion, which has a permanent magnetic moment due to unpaired electrons (gadolinium (Gd^{3+}) or manganese (Mn^{2+})). Because of their toxicity, paramagnetic lanthanide ions are usually chelated by organic ligand, able to reduce their toxic effects caused by tissue accumulation in the body.⁹⁸ They produce positive contrast and create bright images (**Figure 28**).

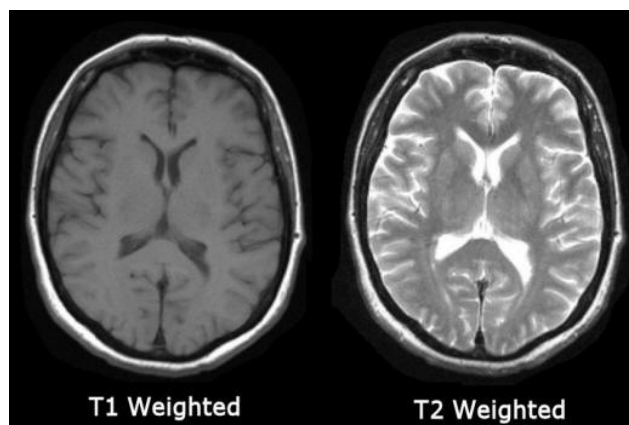


Figure 28. T1 weighted image (on the left) and T2 weighted image (on the right) of the same brain tissue. Figure from <http://casemed.case.edu/clerkships/neurology/NeurLrngObjectives/MRI.htm>

Gadolinium complexes are the most widely T1 contrast agents used in clinical applications, in particular for the detection of the breakage of the blood brain barrier (BBB) and of the changes in vascularity, flow dynamics, and perfusion. In the last decade, several organic molecules characterized by different chemical properties (ionic or non-ionic) and structures (linear or not linear), have been developed to chelate gadolinium ion, in order to improve the stability and the *in vivo* biodistribution of the final complex. Currently, several gadolinium-based contrast agents have been approved by the FDA (Food and Drug Administration) and EMA (European Medicine Agency), such as gadobenate (MultiHance), gadobutrol (Gadavist), gadodiamide (Omniscan), gadopentetate (Magnevist), gadoterate (Dotarem), gadoteridol (ProHance), gadoversetamide (OptiMARK), gadoxetate (Eovist), and gadofosveset (Ablavar, US only). However, recent studies showed that in patients affected by renal impairment, the administration of gadolinium contrast agents lead to the development of nephrogenic systemic fibrosis (NSF). In addition, deepened investigations have showed the accumulation of gadolinium in various tissues of patients not affected by renal impairment, including bone, brain, and kidneys. These evidences led to modifications in clinical practices in order to reduce the potential side effect associated to gadolinium tissue accumulation.⁹⁹

Because of their non-toxicity and rapidly clearance from the organism, super paramagnetic iron oxide nanoparticles (SPIONs) have been investigated as novel contrast agents in MRI.

In comparison with paramagnetic ions, SPIONs are T2 contrast agents made up of an iron oxide core or an iron/manganese (Fe/Mn) composite metal core covered by an external shell constituted by biomaterials able to prevent aggregation, but also to improve their biocompatibility and biodistribution *in vivo*. These contrast agents are able to form a significantly larger magnetic moment than the paramagnetic agents and produce a “negative contrast with a dark effect on MRI image (Figure 28).¹⁰⁰

1.4.5 Super paramagnetic nanoparticles as MRI contrast agents

Super paramagnetic iron oxide nanoparticles (SPIONs, usually magnetite (Fe_3O_4) or maghemite ($\gamma\text{-Fe}_2\text{O}_3$)) are nanoparticles that consist of a core of ferric (Fe^{3+}) and ferrous (Fe^{2+}) iron. They represent the first used magnetic nanoparticle-based contrast agents due to their chemical stability, lack of toxicity and biodegradability.

Under an external magnetic field, individual magnetic moments of SPIONs produce a fluctuating magnetic field, which is large in comparison to that produced by gadolinium. This allows the perturbation of the magnetic relaxation processes of the water protons diffused into SPIONs outer sphere, leading to a decrease of the spin–spin relaxation time (T_2) that involves the darkening of the corresponding area in T_2 -weighted MR images (**Figure 29**).¹²

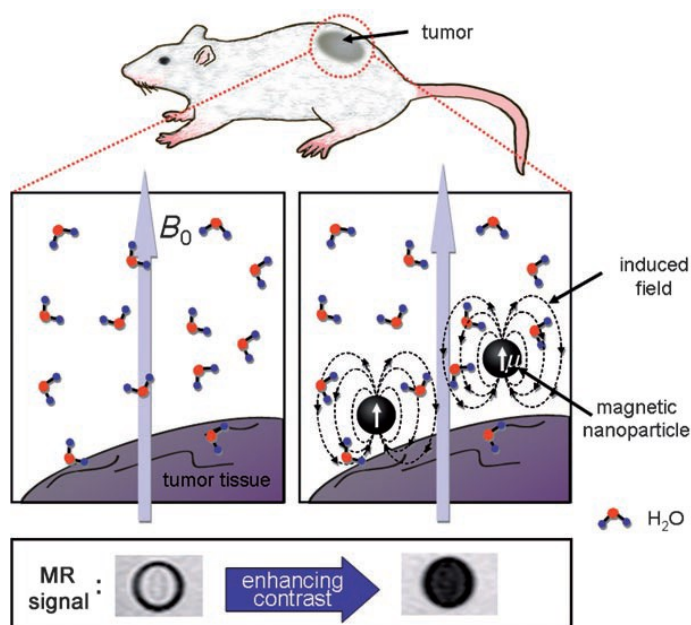


Figure 29. Magnetic resonance contrast effects of MNPs. Under an external field (B_0), magnetic nanoparticles are magnetized with a magnetic moment of μ and generate an induced magnetic field which perturbs the nuclear spin relaxation processes of the water protons. This perturbation leads to MR contrast enhancement, which appears as a darkening of the corresponding section of the image. Figure from *Angew. Chemie - Int. Ed.* **47**, 5122–5135 (2008).

SPIONs can alter the relaxation of local protons in a more efficient way than gadolinium, allowing the use of lower concentrations than Gd^{3+} -based agents. Also because they are iron-based agents with not potential for causing nephrogenic systemic fibrosis, they may be useful as an alternative to gadolinium-based contrast agents in patients with compromised renal function.¹⁰¹ However, SPIONs magnetic properties are influenced by the iron content of the core and the size. In the nanoscale regime, magnetism is influenced by the size, because the

surface spins are not-perfectly aligned to the external magnetic field (canted surface spin) and form a magnetically disordered spin-glass-like surface layer (**Figure 30**). On the other hand, in the ideal case, all of the magnetic spins in a bulk magnetic material are aligned parallel to the external magnetic field.

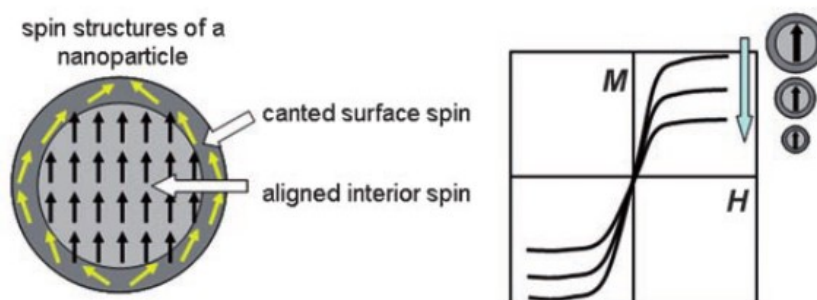


Figure 30. Surface spin canting effect of a nanoparticle upon magnetization (M = magnetic moment, H = external magnetic field). Figure adapted from *Angew. Chemie - Int. Ed.* **47**, 5122–5135 (2008).

The surface effect becomes more pronounced when the nanoparticles decrease, causing a dependence of the net magnetic moment with the nanoparticles size.

In particular, it has been demonstrated that the relaxivity coefficient (r_2) gradually increases for 4 nm, 6 nm, 9 nm, and 12 nm sized nanoparticles, and lead to an enhancement of the MR contrast signal.¹⁰² In addition, the magnetic properties of iron oxide nanoparticles can be greatly increased by doping with magnetically susceptible elements the native nanostructure, leading to shortening of T2. In particular, it has been showed that manganese-doped ferrite nanoparticles (MnFe_2O_4) have higher magnetic susceptibility, as compared with other divalent transition metal dopants (nickel or cobalt).

The synthesis methodologies used to obtain iron oxide nanoparticles characterized with high magnetization properties, lead to the formation of nanoparticles with hydrophobic properties, due to presence of the organic ligands on the surface. In order to enhance their solubility and stability in water at physiological pH, several molecules, polymers and biomaterials have been studied to find an ideal coating for making magnetic nanoparticles suitable for biomedical applications. However, it has been showed that the nature of this coating and the procedure followed to anchor it on the surface of the nanoparticles can affect the magnetic properties and relaxivity of the particulate contrast agents.¹⁰³

Among these, iron nanoparticles coated with biomaterials, such as dextran or polysaccharide, have showed promising results in clinical trials. In the middle of 1990, several iron-based MR contrast agents were developed for imaging of the liver and other cells of

the reticuloendothelial system (RES), because the selectively taken of SPIONs by Kupffer cells in the liver, spleen, and bone marrow after intravenous injection.

Among these T2-contrast agents commercial available consisted in dextran coated-SPIONs having diameters between 20 to 3,500 nm (Ferumoxsil or AMI-121, Ferucarbotran, OMP) and ultrasmall SPIO (USPIO) agents having diameters of less than 50 nm (AMI-277, MION-47, Sinerem®, Combidex®, Clariscan™).

However, in 2009 the commercial production of all of these RES agents has been ceased because of the lack of sales and poor performance in clinical trials. After that, several a deeper investigation has been carried out in order to overcome the challenges regarded the use of SPIONs as T2 contrast agents.

Currently, the potential of Ferumoxytol (Feraheme, AMAG Pharmaceuticals, Cambridge, MA) as iron-based MRI contrast agent is under clinical investigation (**Figure 31**).¹⁰⁴

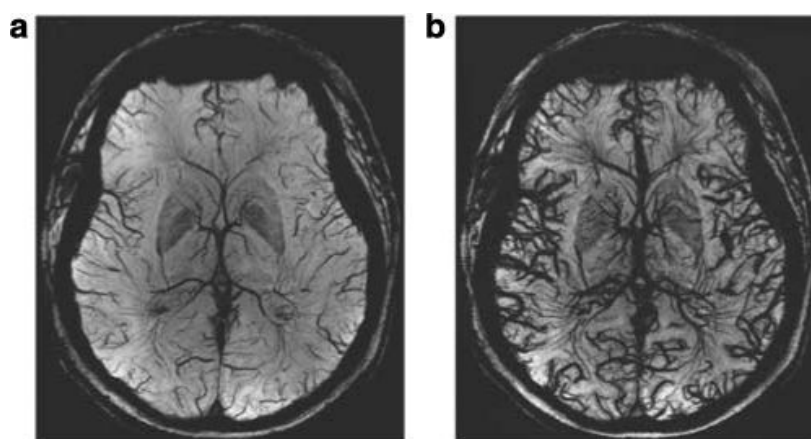


Figure 31. Ferumoxytol susceptibility-weighted imaging at 7 T in human brain Vasculature MRI before ferumoxytol (a) and after 4 mg/kg ferumoxytol (b).

Ferumoxytol is a commercially available ultrasmall superparamagnetic iron oxide (USPIO) agent surrounded by a carbohydrate coat, which has been originally used as an iron replacement therapy for patients with anaemia related to chronic renal insufficiency (**Figure 32**).¹⁰¹



Figure 32 Feraheme produced by AMAG Pharmaceuticals, consists in elemental iron 30mg/mL (as ferumoxytol 510mg/17mL).

1.5 Surface chemistry of metal nanoparticles

1.5.1 Self-assembled monolayer (SAM)

As highlighted several times in the previous paragraphs, a fundamental requirement for the use of metallic nanoparticles in biomedical application is their biocompatibility and their stability in aqueous medium at physiological conditions. Depending on the synthesis, metallic nanoparticles and metal oxide nanoparticles can be synthesized with hydrophobic or hydrophilic properties. In the both cases, the replacement of the original surfactants with specific organic ligands is necessary in order to improve their biocompatibility, and also enhance their stability. Indeed, these molecules can alter interfacial properties and have a significant influence on the stability of nanostructures of metals and metal oxides, also they can act as a physical or electrostatic barrier against aggregation, decreasing the reactivity of the surface atoms, or acting as an electrically insulating film.¹⁰⁵

Dealing with noble metal based nanostructures, such as gold and silver nanoparticles, they usually are synthesized in water medium with the assistance of various kind of surfactants, which stabilize the growing nanoparticles against aggregation phenomena.⁶⁰ These surfactants remain adsorbed or deposited onto the nanoparticles surface once the process is finished, avoiding post-synthesis collapse of the created nanoparticles. Unfortunately, most of these surfactants are strongly toxic or simply not suitable for biomedical application. In the case of gold nanorods, the synthesis is carried out in water in the presence of the cetyltrimethylammonium bromide (CTAB). However, it is demonstrated that this cationic surfactant in physiological conditions have a strong cytotoxic effect on healthy cells. For these reason, the development of specific ligands able to replace CTAB molecules, preventing the aggregation phenomena, and at the same time keeping unchanged the specific optical properties of GNRs, have been largely investigated.⁶²

On the other hand, iron oxide nanoparticles characterized by high quality and low size polydispersion, are usually synthesized through thermal decomposition in non-aqueous media, with the use of surfactants, which confer them hydrophobic properties. In this case, the surface modification of these metal oxide nanoparticles is necessary to make them suitable for nanomedicine applications. A suitable method to coat nanostructures is the formation of the so-called self-assembled monolayer (SAM). SAM consisted of organic molecules able to interact with the nanostructures surface and organize spontaneously into an ordered well-defined monolayer.

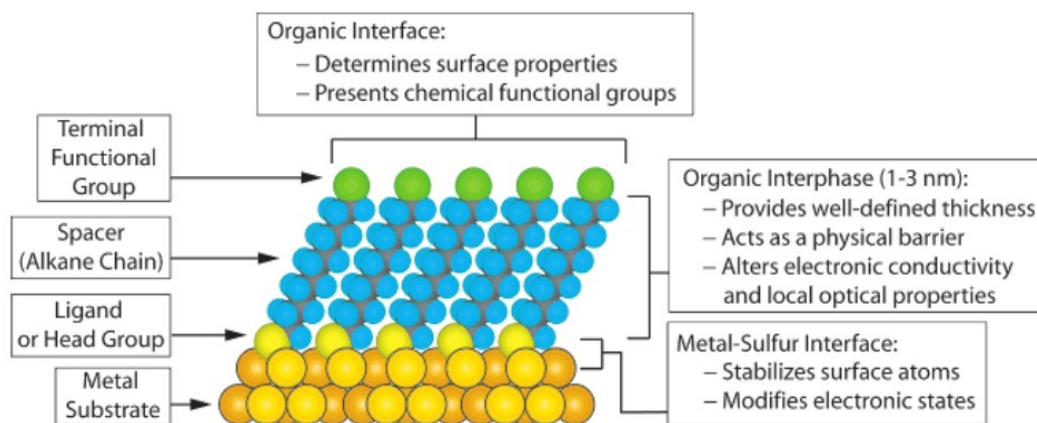


Figure 33. Schematic diagram of an ideal self-assembled monolayer (SAM). Figure from Chemical Reviews 105, (2005).

The molecules or ligands able to form SAMs have a chemical functionality, or *headgroup*, with a specific affinity for specific metals or metal oxides. In many cases, the *headgroup* also has a high affinity for the surface and can displace the surfactants from the surface. In addition, these molecules are characterized with a central body usually constituted by a long chain and finally a functional group, or tail, which will determine the properties both of the monolayer formed and of the entire system (**Figure 33**).

For what concerns the functional group that must bind to the metal surface, several studies have been performed in order to evaluate their affinity with different kinds of metal. The thiol group is the most used functional group to bind gold and silver surface, due to the great affinity of to the transition and noble metals. On the other hand, organic ligand characterized by “head groups” as catechol, 2,3-dihydroxybenzamide, phosphonic acid, and carboxylic acid have been investigated to bind the metal oxide nanostructures surface.¹⁰³

As regards the chain which constitutes the "body" of the ligand, previous studies demonstrated the importance of the presence of amide junctions and aromatic components, the first capable of forming hydrogen bridges between the various chains, the second able to give π -stacking interactions that ensure greater stability to the structure.⁴⁶

Finally, the terminal functional group of the ligand must confer the desired properties to the entire system. By introducing appropriate functional groups at the end of the ligands it is possible to obtain stability in different solvents or, for instance, make them react with common reactions of organic chemistry once they are already firmly anchored to the nanoparticles surface.

1.5.2 Silica shell as coating of metallic nanoparticles

As mentioned in the previous paragraph, in few cases the synthesis of metallic nanoparticles are carried out in non-aqueous solvents, obtaining nanoparticles with hydrophobic properties.

In particular, the synthesis of magnetic nanoparticles, such as iron oxide nanoparticles or manganese doped iron oxide nanoparticles, can involve high-temperature (up to 305 °C) reactions of metal precursors (such as acetylacetonate) with 1,2-hexadecanediol, oleic acid, and oleylamine. These methods allow obtaining magnetic nanoparticles characterized by high magnetization and controlling the size of the oxide nanoparticles by varying the reaction temperature or changing metal precursors.

However, in these reactions are formed hydrophobic nanoparticles, not suitable for nanomedicine applications and not characterized by functional groups suitable for bioconjugation. To solve this problem, hydrophobic nanoparticles might to be transferred into aqueous media by entrapping them in polymeric micelles, or by realizing surface modification, as the formation of self-assembled monolayer with hydrophilic ligands, or a silica coating. The silica coating approach consists in the formation a cross-linked silica shell on nanoparticles surface, in order to protect and stabilize the core nanoparticles in aqueous environment, and to enhance their biocompatibility due to its nontoxicity. It can be used for hydrophilic and hydrophobic nanoparticles of metals,¹⁰⁶ metal oxides, and quantum dots (QDs) in a size range of 1-100 nm.¹⁰⁷ By adjusting the reaction conditions, it is possible to obtain a silica coating characterized by a specific layer thickness and provide the nanoparticles surface of various functional groups in order to conjugate an active targeting (Figure 34).

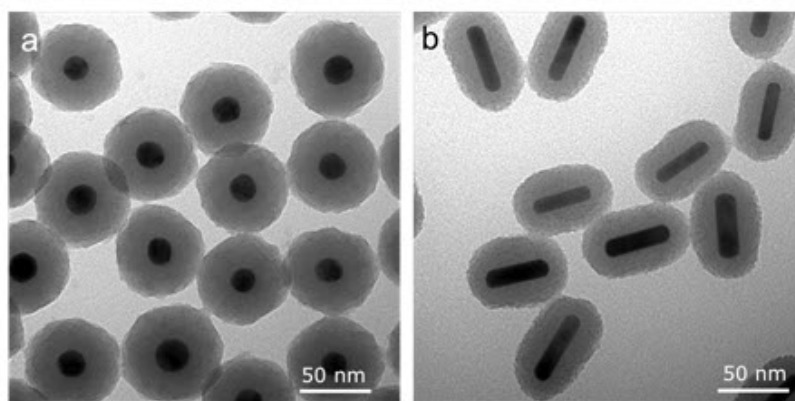


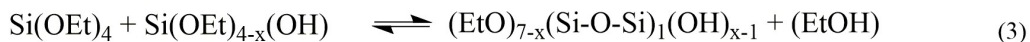
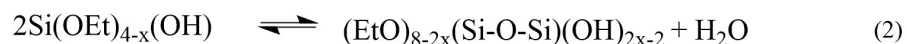
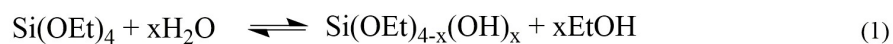
Figure 34. TEM images of iron oxide nanoparticles (a) and gold nanorods (b) coated by silica shell

Indeed, the specific properties of core nanoparticles, such as the saturation magnetization, luminescence intensity, the intensity of surface-enhanced Raman scattering signal, will decrease as the inert silica shells thickness increases, although silica shells can effectively prevent core nanoparticles from corrosion of the surrounding media, and an ultrathin silica shell is helpful in avoiding this decrease.¹⁰⁸

In particular the study of Chen *et al.* showed that silica coated gold nanorods can produce 3-fold higher photoacoustic signals than nanorods without silica coating characterized by the same optical properties.¹⁰⁹ This results showed how a dielectric shell on gold nanorods surface has a strong influence on the amplitude of the generated photoacoustic signal and also avoid the reshaping phenomenon of gold nanorods caused by laser irradiation and affect their absorption efficiency.¹¹⁰

Several kinds of functional silanes have been used in order to coat nanoparticles made of different materials. These molecules are characterized of trimethoxysilyl or silanol groups at one end, which undergo hydrolysis in a basic/acidic medium to form a silica shell, and a functional group at the other end, able to bind an active targeting on the core-shell systems surface. Two different strategies can be used to initiate the silica polymerization on the nanoparticles surface: the Stöber synthesis and the reverse microemulsion methods. The former cannot be applied to nanoparticles insoluble in the polar media, while the latter is an excellent alternative strategy for making silica coating on hydrophobic nanoparticles.

The Stöber method is based on sol-gel process and consists in two consecutive reactions that essentially govern the growth of silica particles. In the first step, TEOS undergoes hydrolysis in a mixed ethanol/ammonia solution to produce silanol monomers, in which the ethoxyl groups (-Si-OEt) are replaced with silanol groups (-Si-OH) (1). Subsequently, the silanol monomers undertake condensation between two silanol groups (2) to generate branched siloxane clusters, which are further linked to trigger the nucleation and growth of silica particles. Simultaneously, the silanol monomers may also react with the unhydrolyzed ethoxyl groups of TEOS via condensation between silanol and ethoxyl groups (3) to participate in the nucleation and growth of silica particles as well.¹⁰⁸



Because of the hydrolysis of TEOS is ammonia-catalysed, the size of silica particles can be readily tuned in a wide range from 10 to 500 by changing the ammonia concentration.

For the formation of core-shell systems, Stöber condition can be applied to nanoparticles soluble in the alcohol-water media, because in the silica coating formation the first step of hydrolysis reaction takes place with the hydroxyl groups on the nanoparticles surface (**Figure 35**).

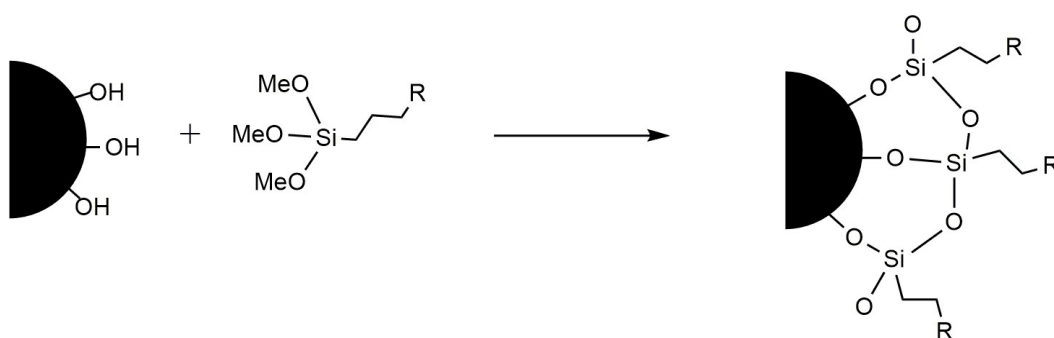


Figure 35. Silane conjugation chemistry for nanoparticles soluble in alcohol-water media

For this reason, different approaches have been developed in order to realise silica coating of hydrophobic nanoparticles. Among these, modification of Stöber's condition have been applied in order to develop new methods based on the formation of reverse micelle (reverse microemulsion method), methods based on the use of lipophilic silane monomers or trialkoxysilanes, able to minimize the shell thickness, and also the use of hydrophilic silanes able to confer water solubility to the final nanoparticles.¹⁰⁷

In particular, Ding *et al.* described the mechanism of reverse microemulsion method used to coat hydrophobic iron oxide nanoparticles, and deeply investigated the coating mechanism in the formation of core-shell systems (**Figure 36**).

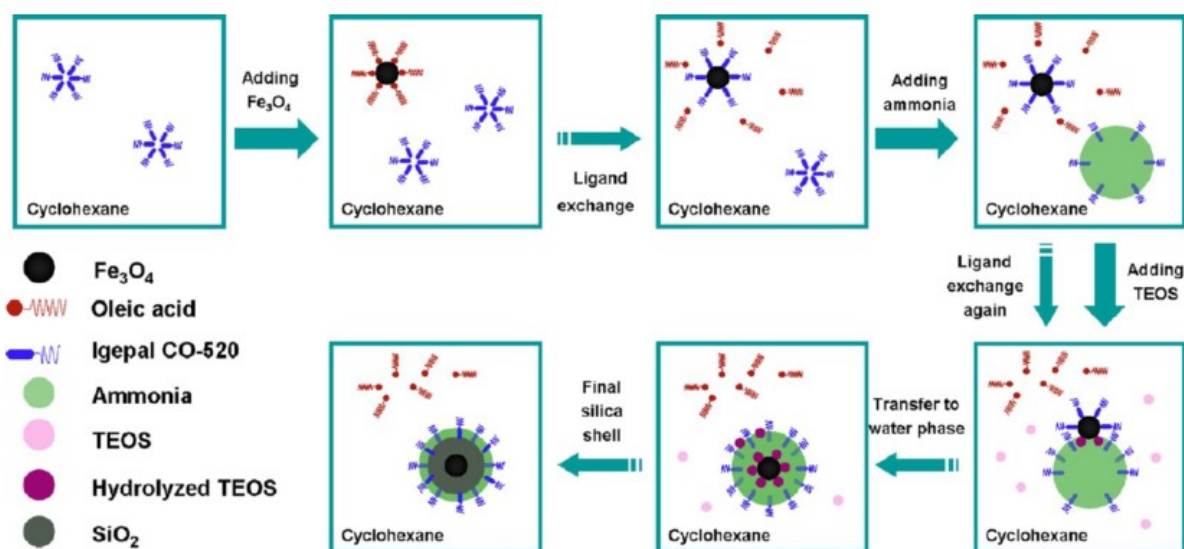


Figure 36. Illustration of the coating mechanism of SiO₂ on the surface of hydrophobic Fe₃O₄ nanoparticles. Figure from Chem. Mater. **24**, 4572–4580 (2012)

In this method, surfactant molecules (Igepal CO-520) are mixed in cyclohexane solution, and spontaneously aggregate and form the micelles in the organic solution. After that, hydrophobic nanoparticles (Fe₃O₄ NPs) are added to the solution, and the ligand exchange reaction between oleic acid and fractional surfactant molecules occurs on the surface of the Fe₃O₄ NPs with part of the surfactants still in the micelle form. The formed micelles will then be filled with ammonia upon its addition, and the micelle size is enlarged and forms a reverse microemulsion system. Subsequently, the added TEOS will hydrolyse at the oil/water interface and perform the ligand exchange with surfactant molecules chemically absorbed on the Fe₃O₄ NPs surface and then transfer the NPs to the water phase. Finally, the hydrolysed TEOS on the Fe₃O₄ NPs surface undergoes a condensation process and forms silica shells.

2. Aim

The aim of this project has been carried out a deep investigation on the potential of polymeric nanoparticles and metallic nanoparticles as theranostic nanosystems for cancer treatment.

For this purpose, several kinds of metallic nanoparticles have been designed, synthesized, modified on the surface and characterized, such as silver nanoparticles, gold nanorods, iron oxide nanoparticles, magnesium nanoparticles, and also multifunctional nanomaterials as dumbbell-like gold-iron oxide nanoparticles and iron-gold core-shell systems.

Indeed, as deepened in the introduction, metallic nanoparticles show intrinsic chemical-physic properties that make them suitable for therapeutic and/or diagnostic applications in medicine thus, in the last decades, their used in clinical applications has been largely investigated.

For this purpose, optical properties of gold nanomaterials have been employed in this project for the development of photothermal agents for hyperthermia therapy as well as photoacoustic imaging contrast agents. Furthermore, the incorporation of magnetic iron oxide nanoparticles with gold nanomaterials in the same nanosystem, led to the formation of multifunctional nanosystems that showed promising properties as theranostic and dual-imaging agents. Additionally, a one pot-synthesis of chitosan coated magnesium nanoparticle has been fine tuned in order to obtain nanoparticles characterized by high biocompatibility and unexpected photothermal behaviour.

However, a crucial point for metallic nanoparticles consists in their superficial coating that can affect the biocompatibility, stability and the toxicity of the whole final nanosystem. For this purpose, different strategies and different biomaterials have been employed in order to functionalize the metallic nanoparticles surface.

About this, one strategy consisted in the *ligand exchange reaction*, in which organic ligands can be chemically anchored or physically adsorbed on the nanoparticles surface to form a single or double layer, able to create repulsive (mainly steric) forces balancing the attractive forces acting on the nanoparticles.

In this way, the synthesized metallic nanoparticles have been coated with biomaterials or with specific designed organic molecules able to bind their surface. In particular, the use of organic molecules as coating can confer hydrophobic properties to metallic nanoparticles, allowing their entrapment in polymeric nanoparticles.

Indeed, the delivery *via* polymeric nanovectors of metallic nanoparticles or chemotherapeutic drugs characterized by hydrophobic properties, was the other strategy employed in this project for the development of theranostic platforms. For this purpose, the FDA approved copolymer

poly(lactic-co-glycolic acid)-block-poly(ethylene glycol) (PLGA-b-PEG) has been used in order to form polymeric nanoparticles characterized by high biocompatibility and able to conjugate on surface a biomolecule as active targeting. Another strategy consisted in the formation of a silica layer on metallic nanoparticles able to be further functionalized achieving the realization of a multifunctional nanosystems.

In the end, the biological properties of all the developed nanosystems have been tested *in vitro* and *in vivo*, in order to investigate their potential as drug delivery and theranostic systems in nanomedicine applications.

3. Discussion

3.1 Synthesis of the precursors

In order to achieve the surface functionalization of the synthesized metallic nanoparticles, specific organic molecules and biopolymers have been synthesized or opportunely modified. Indeed, these molecules must be characterized by specific functional groups and molecular structures, in order to bind the metal atoms on the nanoparticles surface and to form a self-assembled monolayer able to stabilize the final nanosystems (**paragraph 1.5**).

In this section, the synthetic strategies developed to obtain the organic materials used in the surface functionalization of the metallic nanoparticles, have been reported.

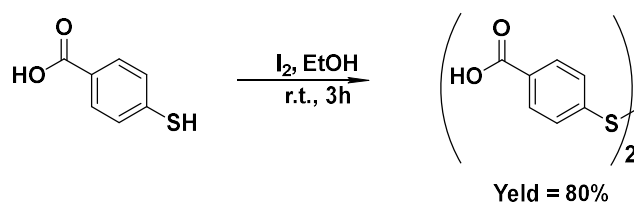
In particular, the synthesis of organic ligand (ethyl 11-(4-mercaptobenzamido)undecanoate), the organic functionalization of chitosan chains and the synthesis of the copolymer poly(lactic-co-glycolic acid)-block-poly(ethylene glycol) (PLGA-b-PEG) will be described.

3.1.1 Synthesis of the organic ligand 11-(4-mercaptobenzamido)undecanoate (ligand 1)

With the intent to coat noble metal nanostructures surface, the organic ligand 11-(4-mercaptobenzamido)undecanoate (ligand 1) has been designed and synthesized by the research group where I worked during my PhD.¹¹¹

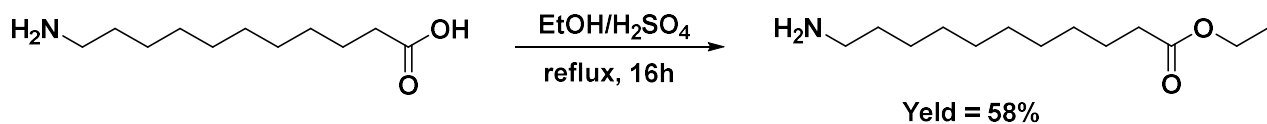
In order to allow the formation of a good self-assembled monolayer, the ligand molecular structure is composed by a thiol as head group, due of its high affinity towards noble metals, a long chain and an ester ending group (**paragraph 1.5**).

The synthesis of this ligand requires four steps. The first step consisted the synthesis of 4,4'-disulfanediyldibenzoic acid realized through the oxidation of commercially available 4-mercaptobenzoic acid with iodine in ethanol in order to obtain the corresponding disulphide (**Scheme 1**).



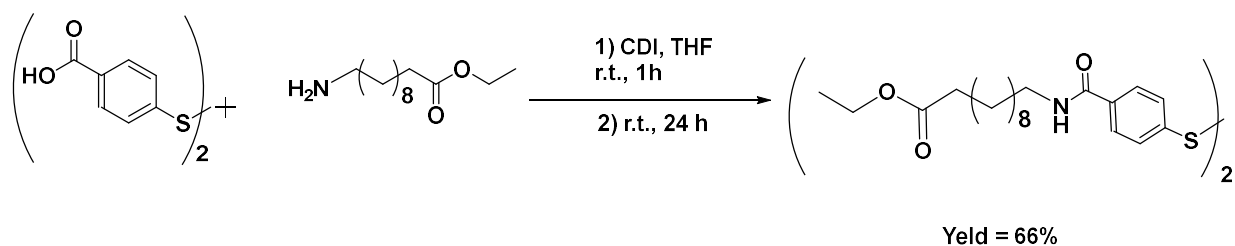
Scheme 1. Synthesis of 4,4'-disulfanediyldibenzoic acid

This allows the protection of the thiol group and simultaneously it ensures the non-reactivity of the same as nucleophile during the following steps. The second step of this synthesis consisted in esterification of the commercially available 11-aminoundecanoic acid with ethanol, giving in this way the corresponding ethyl ester (**Scheme 2**).



Scheme 2. Synthesis of ethyl 11-aminoundecanoate

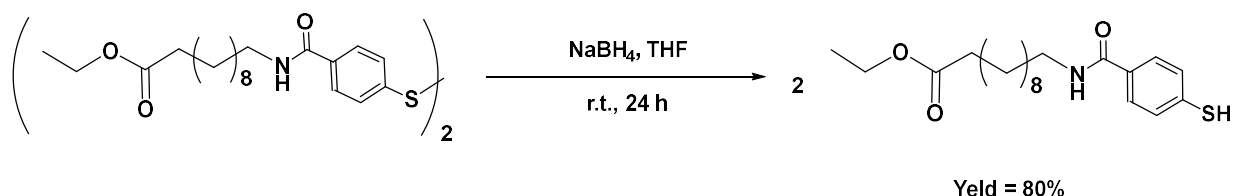
Once obtained, the two precursors were linked through an amide junction using 1,1-carbonyldiimidazole (CDI) as activating agent for the carboxylic acids present into the disulphide, and anhydrous tetrahydrofuran (THF) as solvent (**Scheme 3**).



Scheme 3. Synthesis of bis-ethyl 12-(4-benzamido)undecanoate disulfide

Finally, the disulphide was reduced with sodium borohydride in order to restore the original thiol group and to obtain the final desired ligand (**Scheme 4**).

This ligand, having an ester-ending group, will ensure great stability to the coated nanostructures in organic solvents, allowing a good entrapment into polymeric nanoparticles.



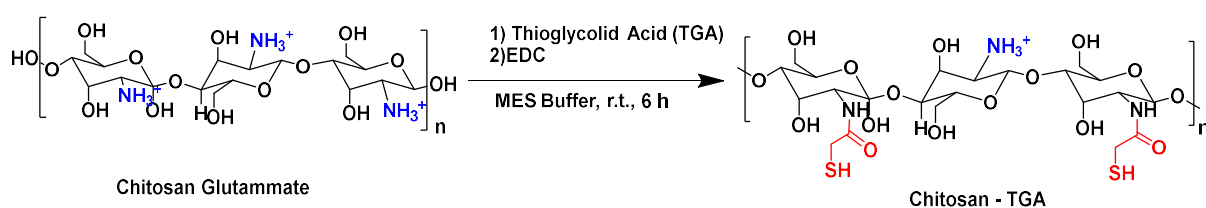
Scheme 4. Synthesis of ethyl 11-(4-mercaptobenzamido)undecanoate

3.1.2 Organic functionalization of chitosan

Due to its biocompatible, biodegradable, and bioactive properties, chitosan has been widely investigated as biomaterials for biomedical and pharmaceutical applications.

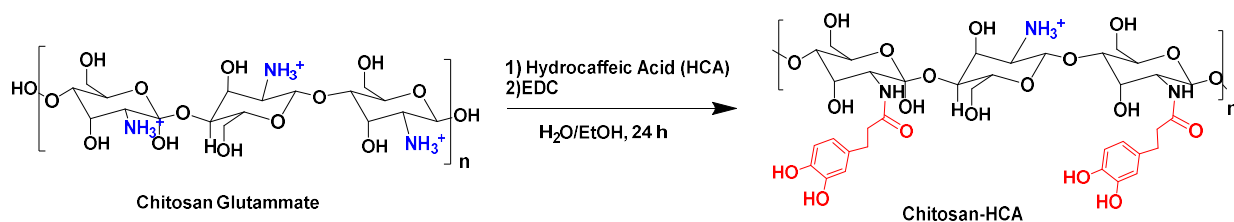
Chitosan, a natural polymer constitutes of glucosamine and N-acetyl-D-glucosamine, has been used in this project as metallic nanoparticles coating in order to improve their colloidal stability and *in vivo* biodistribution.

For this purpose, two different organic functionalization have been carried out by following reported method in literature.^{112,113} In one case the chitosan chains has been modified with thioglycolic acid (TGA), introducing thiol groups onto its chain (chitosan-TGA) in order to bind the surface of noble metallic nanostructures. The reaction consisted in the formation of amide bond between the free amine groups of chitosan chains and the carboxylic acid of thioglycolic activated by using the 1-ethyl-3-(3-dimethylaminopropyl)carbodiimide (EDC) as coupling reagent (**Scheme 5**).



Scheme 5. Synthesis of thiol-modified chitosan chains (Chitosan-TGA)

In the other case, by using EDC as coupling reagent, hydrocaffeic acid (HCA) has been linked to amine moieties of chitosan chains, leading to the formation of catechol-functionalized chitosan (chitosan-HCA), able to coat the metal oxide nanoparticles surface.



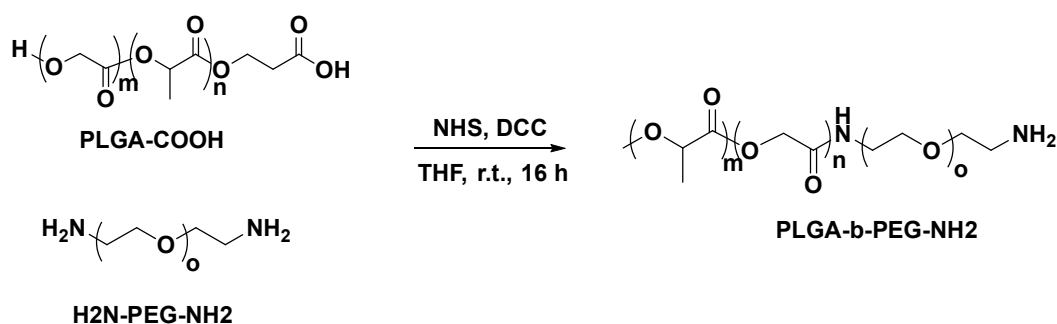
Scheme 6. Synthesis of catechol-modified chitosan chains (Chitosan-HCA)

3.1.3 Preparation of copolymers for polymeric nanocarriers

Poly(d,l-lactic-co-glycolic acid)-block-poly(ethylene glycol) (PLGA-b-PEG) is a di-block copolymer constituted of an hydrophobic portion made of poly(d,l-lactic-co-glycolic acid) (PLGA) and an hydrophilic one, made of poly(ethylene glycol) (PEG) used for the synthesis of polymeric nanoparticles (PNPs). The synthesis has been achieved through the formation of an amide bond between carboxylic ending group of PLGA (PLGA-COOH) and the amine group of bi-functionalized PEG.

In this project, PLGA-b-PEG has been synthesized either by using α,ω -bis-amino PEG (PLGA-b-PEG-NH₂) or by using α -amino- ω -carboxy PEG (PLGA-b-PEG-COOH). Depending on the bi-functionalized PEG, nanoparticles characterized on the surface by different functional groups can be obtained.

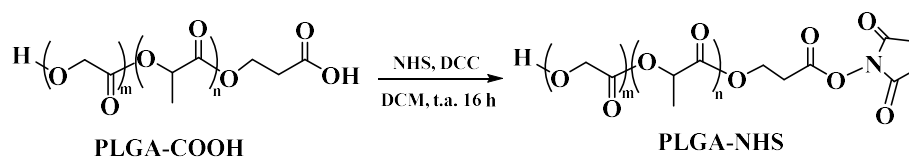
The synthesis of PLGA-b-PEG-NH₂ is a one-pot synthesis, consisting of the preparation of an organic solution by dissolving PLGA-COOH in anhydrous tetrahydrofuran with N,N'-dicyclohexylcarbodiimide (DCC) and N-hydroxysuccinimide (NHS), agents able to activate the carboxylic group. The mixture has been kept under magnetic stirring for one hour; then, the α,ω -bis-amino PEG (H₂N-PEG-NH₂) has been introduced in the reaction environment and the obtained solution has been reacted for 24 hours at room temperature. In order to avoid amide bonds formation at both the extremities of PEG, a larger amount of H₂N-PEG-NH₂ compared to PLGA-COOH has been used. The so-obtained PLGA-b-PEG-NH₂ has been purified by filtration of dicyclohexylurea (DCU) and precipitation in diethylether (**Scheme 7**).



Scheme 7. Synthesis of PLGA-b-PEG-NH₂

On the other hand, the synthesis of PLGA-b-PEG-COOH is carried out in two steps. In the first step, the activation of carboxylic group of PLGA-COOH is achieved in anhydrous dichloromethane in the presence of the activating reagents (DCC\NHS). The reaction is left to

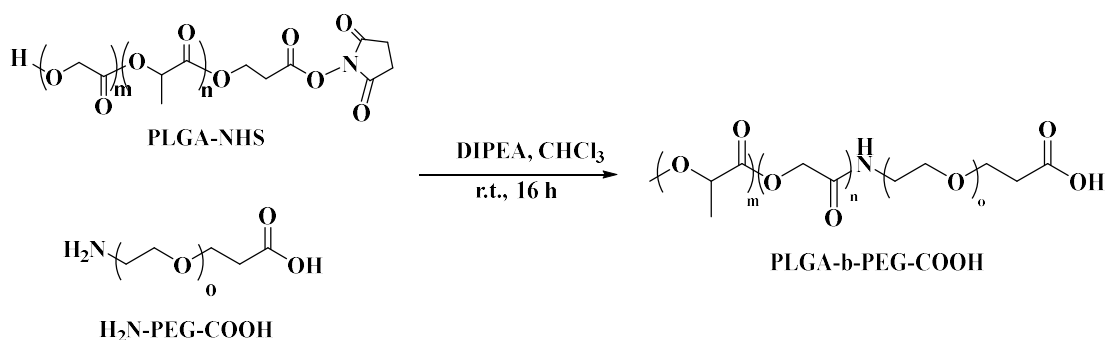
react for 24 hours and then the polymer PLGA-NHS has been purified by filtration of dicyclohexylurea (DCU) and precipitation in diethyl ether (**Scheme 8**).



Scheme 8. Synthesis of PLGA-b-PEG-NHS

In a second step, the α -amino- ω -carboxy PEG hydrochloride ($\text{H}_2\text{N-PEG-COOH}\cdot\text{HCl}$) is added to a solution of the pre-activated PLGA-NHS in anhydrous chloroform, in the presence of an organic base like N,N-Diisopropylethylamine (DIPEA) (**Scheme 9**).

The reaction is left to react for one day and the resulting co-polymer is purified by precipitation, washings in diethylether and subsequently in water.



Scheme 9. Synthesis of PLGA-b-PEG-COOH

The copolymers have been characterized by mean of $^1\text{H-NMR}$ and stored in freezer at $-18\text{ }^\circ\text{C}$, where they are stable for several months.

3.2. Polymeric nanoparticles as drug delivery systems against Glioblastoma Multiforme

Glioblastoma Multiforme (GBM) is the most common type of primary brain tumour and the astrocytoma of the highest grade. It is characterized by highly proliferative and invasive properties, remarkable biological heterogeneity and poor response to traditional therapies, which make it the most aggressive primary brain tumour. The main causes of poor prognosis of GBM are its tendency to recur and the impediment represents by the blood–brain barrier (BBB). Regarding the tendency to recur, clinical results have shown that for over 90% of the cases the area of recurrence develops at the borders of the surgical cavity, within 2 cm of the original tumour, or at distant sites when the tumour is at later stage.

On the other hand, the BBB limits the passage of pharmaceutical molecules into the brain tissue, representing the major hurdle in the clinical management of GBM. Although, large and advanced brain tumours exhibit disrupted BBB integrity, the presence of peripheral areas of brain tumours that contain regions with intact BBB, leading to the spreading glioma cancer cell and treatment resistance. For this reason, the median overall survival of GBM patients with the best currently available therapy is approximately 15 months, and the 5-year survival rate is only 9.8% at present. Thus, the reaching of the dispersed and invading GBM cells remains a big challenge for the successful treatment of GBM.

Given the intrinsic difficulty for most conventional drugs to reach the brain, in this project the use of nanoparticles has been investigated as an innovative therapeutic strategy. The conducted researches led to the development of two different polymeric nanosystems characterized by the presence of active targeting on their surface, in order to investigate their ability of the transporting of the loaded agents within the cerebral tissue with minimal off-target toxicity. Due to its well-known properties and its ability to create micelle-like nanocarriers (**paragraph 1.2.2**), poly(lactic-co-glycolic)- block-poly ethylene glycol (PLGA-b-PEG) copolymer has been used for the synthesis of the two developed nanosystems.

The first system consisted in the polymeric nanoparticles conjugated to a peptide able to bind selectively glioma cells (chlorotoxin, CTX), in which silver nanoparticles were entrapped to allow detection and quantification of the cellular uptake by confocal microscopy, both *in vitro* and *in vivo* (Ag-PNP-CTX).¹¹⁴ In the other system, a chemotherapeutic drug has been entrapped into polymeric nanoparticles functionalized with an aptamer (Gint4.T) able to recognize platelet-derived growth factor receptors β on the blood–brain barrier (BBB).¹¹⁵ Both the developed nanosystems have been tested *in vitro* and *in vivo* biological assays.

3.2.1. Synthesis of chlorotoxin functionalized polymeric nanovectors for the treatment of Glioblastoma Multiforme in a combined approach with radiation therapy

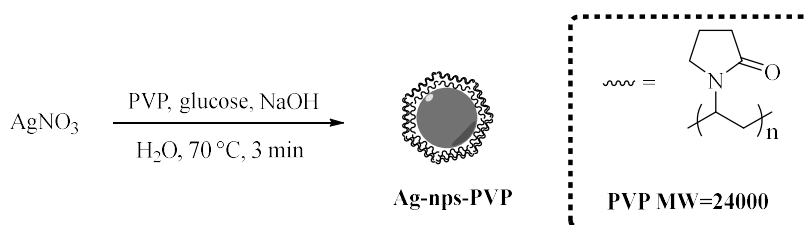
All the procedures and results about the development of chlorotoxin targeted polymeric nanovectors for GBM treatment are completely described in:

- A Combined Approach Employing Chlorotoxin-Nanovectors and Low Dose Radiation To Reach Infiltrating Tumor Niches in Glioblastoma; ACS Nano 2016, 10, 2509–2520.

3.2.1.1 Synthesis and surface functionalization of silver nanoparticles (Ag-nps)

Silver nanoparticles have been synthesized following a reported procedure optimized by our the research group, based on the so called “salt-reduction method”, in which a strong reducing agent and a stabilizing agent are required.¹¹¹

The synthesis is based on the use of polyvinylpyrrolidone (PVP), selected as surfactant agent because its good ability able to stabilize nanoparticles during their formation, avoiding the aggregation phenomena, and allowing the nanoparticles to growth with high uniformity. Moreover, because PVP is a non-ionic surfactant, it shows a less toxicity compared with surfactant positively charged, that could interfere with DNA, characterized by a globally negative charge. Hydrophilic silver nanoparticles (Ag-nps-PVP) have been synthesized by preparing a water solution made of PVP, glucose and sodium hydroxide (NaOH) in water. Glucose is used as reducing agent, in order to completely reduce silver ions. The solution is warmed and when the temperature reached 70°C, a solution of silver nitrate (AgNO₃) is rapidly added into the reaction mixture (**Scheme 10**).



Scheme 10. schematic representation of the Ag-nps-PVP synthesis

After only three minutes at the same temperature, the nanoparticles formation was completed, and the colloidal solution was purified and concentrated with high-speed centrifugation, washing with fresh water. Once purified, the Ag-nps-PVP were characterized by using UV-

Vis spectroscopy, transmission electron microscopy (TEM) analysis and dynamic light scattering (DLS) (**Figure 37**).

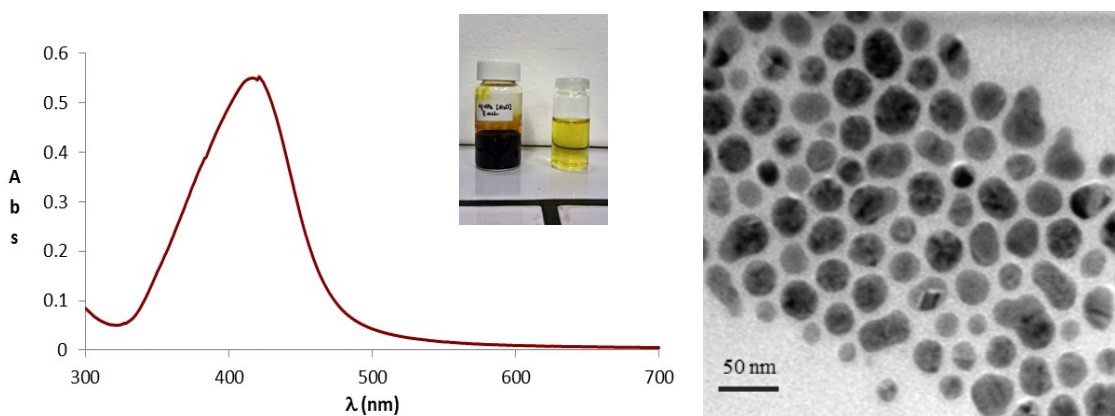


Figure 37. UV-VIS spectrum (on the left) and TEM image (on the right) of Ag-nps-PVP.

UV-Vis spectroscopy revealed the typical absorption band of Ag NPs at 410 nm, attributed to the surface plasmon resonance, which confers the intense yellow colour to these particles. TEM analysis confirmed the obtainment of silver nanospheres with great uniformity and in high concentration, without the presence of macro-aggregates.

DLS analysis showed also that Ag-nps-PVP have an average diameter of 35.4 ± 5.3 nm and a polydispersity index (PDI) value of 0.21 ± 0.011 . Moreover, an elemental analysis by atomic absorption spectroscopy (AAS) gave an Ag value of 34064 ppm (315.8 mM).

In order to achieve the entrapment in polymeric nanoparticles of the obtained silver nanoparticles, a self-assembled monolayer has been formed on the Ag-nps-PVP by using 11-(4-mercaptobenzamido)undecanoate (**ligand 1**) as organic ligand (**paragraph 3.1.1**). Through the thiol group, the ligand 1 can interact with the silver nanoparticles surface, replacing the PVP (ligand exchange reaction) and conferring lipophilic properties to Ag-nps-1.

The reaction consisted in the preparation of a reaction mixture made of an organic solution of ligand 1 in ethanol, which has been added to a diluted aqueous solution of Ag-nps-PVP. The reaction mixture has been left to react under mechanical stirring for 24 hours; then, the obtained Ag-nps-1 have been purified and concentrated with high-speed centrifugation washing with fresh ethanol, in order to remove PVP and the excess of ligand 1.

The collected lipophilic Ag-nps-1 showed a good solubility in organic solvents, as demonstration of the successful of the ligand exchange reaction that was confirmed through the $^1\text{H-NMR}$ analysis. Indeed, $^1\text{H-NMR}$ spectrum of Ag-nps-1 showed the characteristic signals of ligand 1, demonstrating its presence on the metallic surface. In particular, the

disappearance of signal of -SH (3.47 ppm), confirm its anchoring on Ag-nps surface through a covalent bond (**Figure 38**).

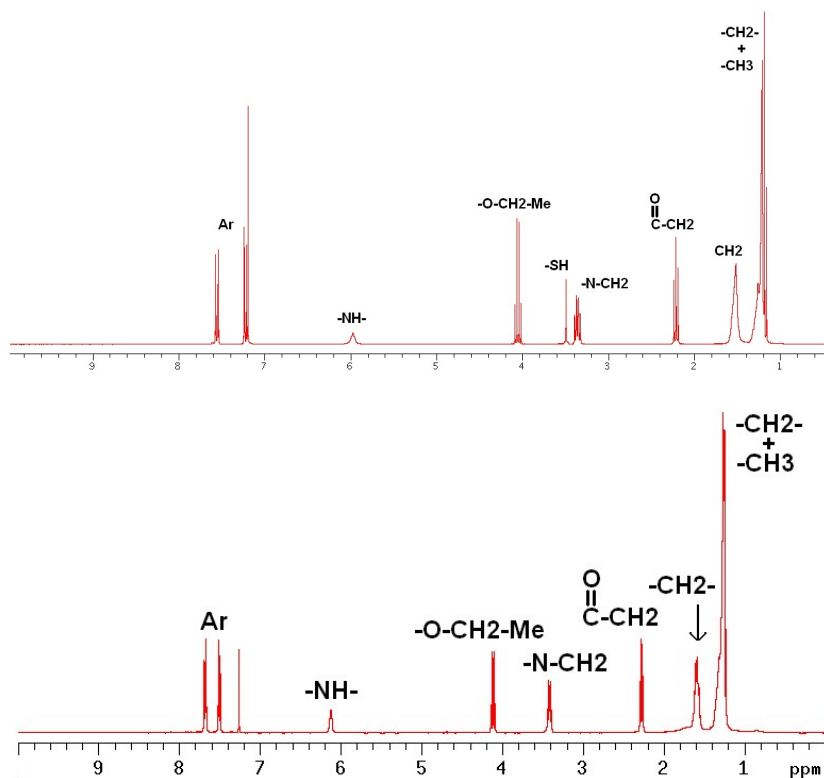


Figure 38. $^1\text{H-NMR}$ spectrum of ligand 1 (above) and of Ag-nps-1 (below).

The DLS results for Ag-nps-1 showed an increased diameter after the coating of 40 ± 7.6 nm, with a polydispersity index (PDI) of 0.24. The determination of the metal content has been done with atomic absorption spectroscopy (AAS) giving a yield for the ligand exchange step of 80%, while the thermogravimetric analysis shows a 16% loss in organic compound (corresponding to the ligand anchored on the surface of Ag-nps-1).

3.2.1.2 Entrapment of lipophilic silver in targeted polymeric micelles (Ag-PNP-CTX)

Once obtained, lipophilic silver nanoparticles (Ag-nps-1) have been entrapped into polymeric nanoparticles. For this purpose, the copolymer PLGA-b-PEG, synthesized by using α -amino- ω -carboxy PEG (**paragraph 3.1.3**), has been synthesized and used for the formation of the micelles. Due to the high solubility of Ag-nps-1 in dimethylformamide (DMF), a solvent miscible with water, the nanoprecipitation technique has been applied for this step.

The procedure consists in the preparation of an organic phase, by dissolving Ag-nps-1 in dimethylformamide (DMF) with PLGA-b-PEG-COOH, that was mixed with an aqueous

phase in a vigorously stirred reactor, maintaining the water/organic ratio constantly 10/1 with removal of the resulting colloidal solution. The obtained water solution, containing the Ag-PNP, was maintained under magnetic stirring for 30 minutes, in order to allow the system to reach the stability. Indeed, the nanoprecipitation process led to polymeric nanoparticles formation through an interfacial desolvation of the polymer and subsequent aggregation of small nuclei into nanometric particles. Because in this case the aggregation process requires time to form and reach a stable state, the system must be left to incubate until this process is completely ended. After the necessary time, the colloidal solution resulted completely stable and with an opal, yellow-brownish coloration.

The Ag-PNP have been purified with centrifugation, washing several times with fresh water in order to remove the dimethylformamide and characterized in order to verify the effective entrapment.

The DLS results show a hydrodynamic diameter of 71.0 nm, a PDI value of 0.19 and a Z-potential of -51.5 mV (at pH = 7.4), features considered suitable for biomedical applications. Then, TEM image clearly show the entrapment of the lipophilic Ag-nps-1 into the PLGA core (**Figure 39**).

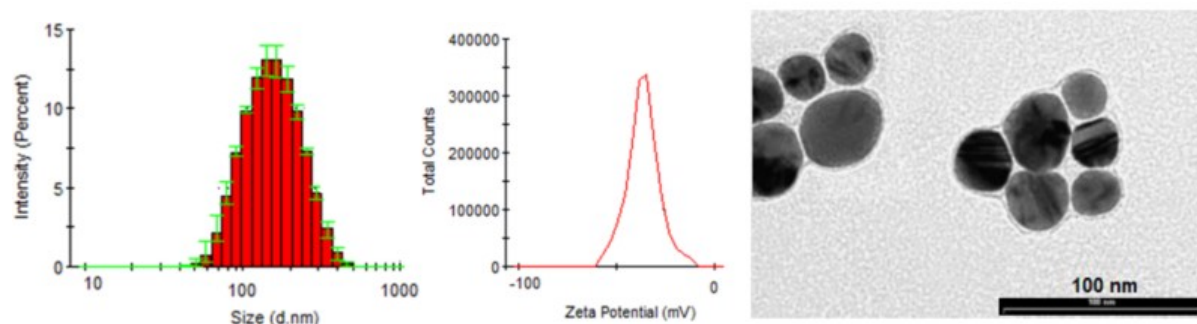
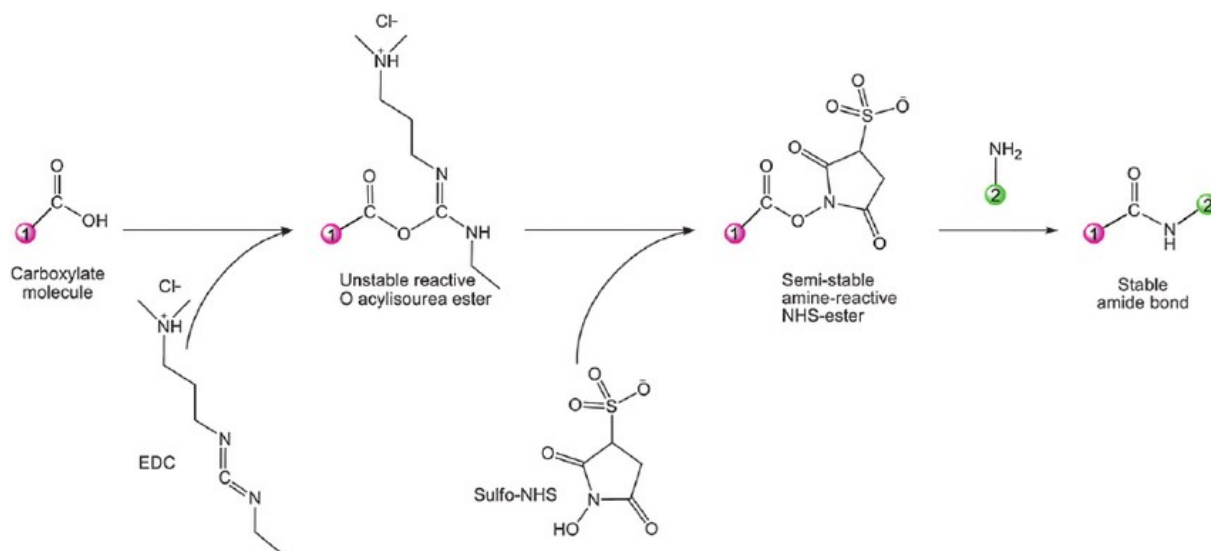


Figure 39. On the left, DLS characterizations of the size and Zeta Potential of Ag-PNP; on the right, TEM image of Ag-PNP.

Once obtained the Ag-PNP, chlorotoxin (CTX), a 36-amino acid peptide originally isolated from *Leiurus quinquestriatus* venom, has been selected as active targeting and conjugated onto their outer shell because its ability to specifically and selectively bind glioma cells.^{116,117} CTX, as well as many other peptides, presents a free-amino group at one end, which can be exploited for amidation reaction with carboxylic acids present on the Ag-PNP, derived from PEG chains.

The reaction of conjugation has been achieved through EDC/NHS chemistry, that consists in the activation of the carboxylic acids by using 1-ethyl-3-(3-dimethylaminopropyl) carbodiimide (EDC) hydrochloride and N-hydroxysulfosuccinimide (sulfo-NHS) in water. As

shown in the **scheme 11**, EDC reacts with carboxylic acids to form an active O-acylisourea intermediate that is unstable in water and subjected to hydrolysis, with restoration of the carboxylic acid and the consequent release of urea by-products. Therefore, O-acylisourea must react immediately with a primary amino group, which easily displaces the activating agent by a nucleophilic attack, leading to the formation of an amide bond and the release of the EDC by-product as a soluble urea derivative.¹¹⁸



Scheme 11. Schematic Representation of amide bond formation between a amide functionalized peptide (2-green) and polymeric nanoparticles (1-red) using EDC and Sulfo-NHS.

Although EDC can be used in neutral conditions, optimal effectiveness is achieved under moderate acidic media (pH = 4-6). When a phosphate buffer (pH 7.2) or simple water is used, the efficiency of EDC is reduced, and a water-soluble N-hydroxysuccinimide (Sulfo-NHS) has to be added in the reaction mixture. The formation of an NHS ester instead of O-acylisourea increases the stability of the system also at neutral pH values.

Following this procedure, the conjugation has been realized by dissolving the activating reagents (EDC/NHS) in a water solution containing Ag-PNP, followed by the addition of CTX (**Figure 40**). After 24 hours of reaction, the Ag-PNPs-CTX were purified with centrifugation to remove small molecules and aggregates.

Ag-PNP-CTX characterized by DLS, showed a diameter equal to 114 ± 2 nm, a low polydispersity index (PDI) of $0.21 (\pm 0.01)$, and a negative Zeta potential of -31.6 mV.

In addition, silver concentration determined with AAS resulted to be 3.81 mM.

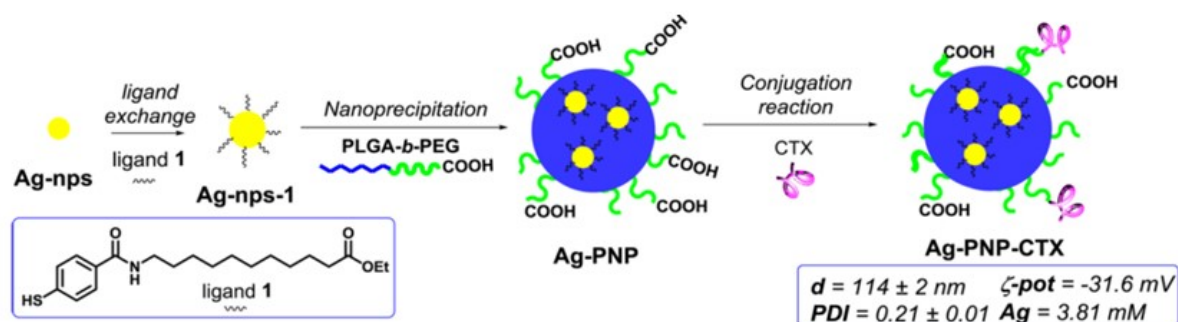


Figure 40. Schematic procedure of the synthesis of Ag-PNP-CTX

3.2.1.3 *In vitro* and *in vivo* biological studies

In collaboration with the *Laboratory of pharmacology and brain pathology* at the Humanitas Research Hospital in Milan, the developed chlorotoxin-targeted nanosystem has been tested through *in vitro* and *in vivo* studies in order to investigate its potential for the treatment of Glioblastoma (GMB) combined with radiotherapy.

Radiotherapy represents one of the traditional therapies used for GBM treatment, and as reported in literature, the use of ionizing radiations seems to damage BBB integrity and induce matrix metalloproteinase-2 (MMP-2) expression.^{119,120} These phenomena can enhance the BBB permeabilization to nanovectors, that usually show a limited mobility and diffusion through the brain interstitial spaces, which are 38–64 nm in normal brain and 70–100 nm in regions with tumour.^{121,122}

In the biological studies carried out, the enhancement of the Ag-PNP-CTX in brain tissue and, in particular, in the infiltrating niches of GBM, after applying ionizing radiations has been investigated. In these experiments, Ag-nps were used as contrast agents for optical microscopy detection and imaging of PNPs without needing to add fluorescent dyes, thus avoiding chemical modification of the outer shell of the nanocarriers, which can modify PNPs behaviour inside the body. Due to their high stability and the absence of photobleaching, Ag-nps represent a valuable imaging tool with superior quality and precision respect to standard fluorescence. Moreover, a fluorescent moiety linked or adsorbed onto the external surface, may undergo leakage phenomena from the nanosystem once in the body environment, which can lead in turn to unspecific fluorescence detection in not really targeted cells; on the contrary, Ag-nps, being strongly entrapped inside the polymeric matrix, are stable and not subjected to this inconvenience.

First of all, the activity of chlorotoxin as active targeting agents has been evaluated *in vitro* through intracellular quantification of Ag-PNPs in human GBM-derived cell lines, performed by confocal microscopy in reflection mode. The results showed that conjugation with CTX significantly increases the intracellular accumulation of Ag-nps in GBM cells as shown by comparison between Ag- PNP-CTX and Ag-PNP nanocarriers (**Figure 41**).

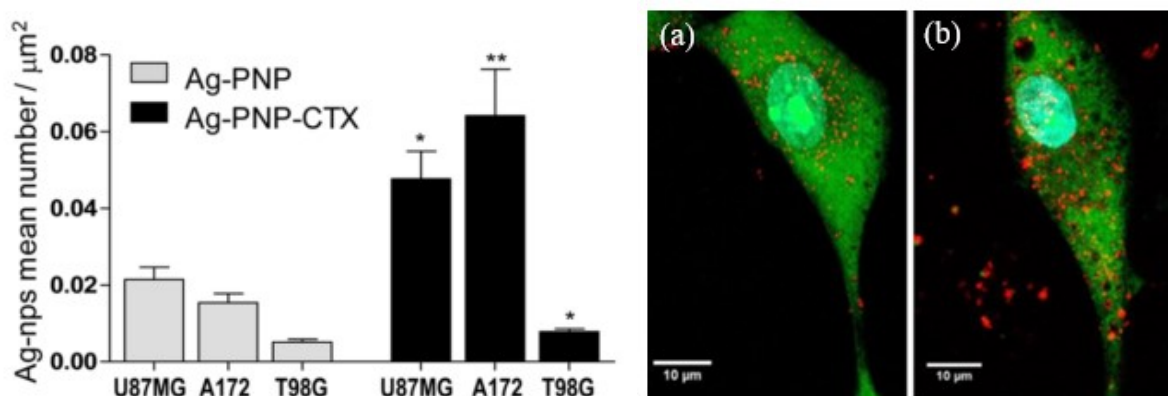


Figure 41. On the left, human-derived GBM cell lines U87MG, A172 and T98G were incubated in the presence of targeted (Ag-PNP-CTX) or non-targeted (Ag-PNP) nanovectors at Ag concentration of 100 μM . On the right, the images showed the intracellular accumulation in of Ag-PNP (a) and Ag-PNP-CTX (b) determined by confocal laser scanning microscopy. Ag-nps have been acquired in reflection mode upon 488 nm excitation and are shown in red. In green is the human nestin immunostaining, and the nuclei are in blue (DAPI).

After that, to exploit the bio-distribution of Ag- PNP-CTX *in vivo*, the amount of Ag-nps accumulating into the tumour and the healthy brain tissue was evaluated in an orthotopic mouse model of human GBM. The experiment consisted in the intra-peritoneally administration of Ag-PNP-CTX at a dose of 1 mg/mouse, in one case to a group of mice not treated with brain radiation, and in the other case after brain radiation treatment.

About the intensity of radiation, a dosage of 2 gray (Gy) has been used by considering that the clinical protocol of radiation therapy used to treat patients affected by GBM is of 60 Gy delivered in fractions of 2 Gy.

The Ag-nps quantification, performed in brain tissues via confocal microscopy showed a significant higher level of accumulation (4-6 fold) in the GBM-tumor after the brain radiation treatment compared to the animals not treated with radiation (**Figure 42 a**), and also showed that no Ag-nps were present in healthy brain tissues (**Figure 42 b**).

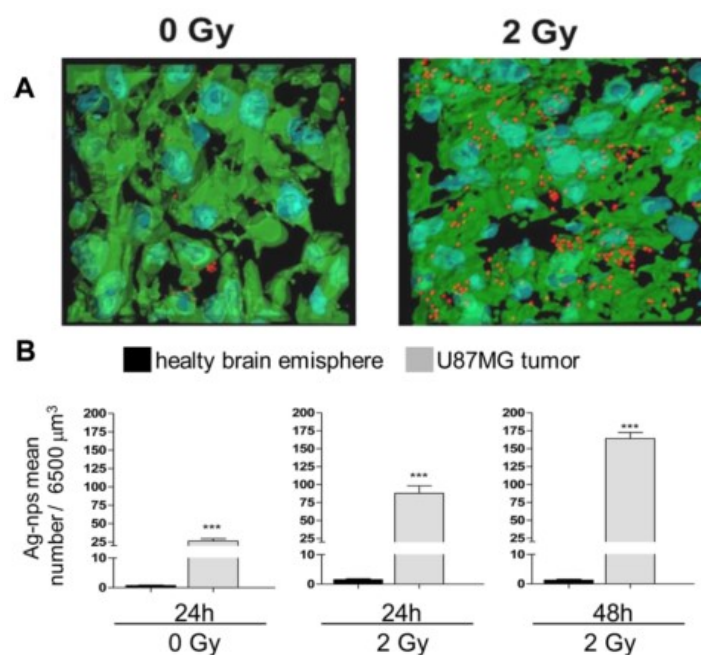


Figure 42. (a) Cryosections of U87MG tumour mass from irradiated (2 Gy) and non-irradiated (0 Gy) mice injected with Ag-PNP-CTX. Ag-nps have been acquired in reflection mode upon 488 nm excitation and are shown in red. In green is the human nestin immunostaining, and the nuclei are in blue (DAPI). (b) Ag-nps quantification in healthy and in tumour brain tissues expressed as mean number of Ag-nps \pm SE in a fixed volume of 6500 μm^3 . About 60 microscopy fields randomly taken from 4 mice in each experimental group were acquired and analysed.

The obtained results revealed that despite CTX allows the Ag-PNP-CTX nanovectors internalization into GBM cells, it is not an agent for BBB crossing, limiting the nanovectors biodistribution in the brain tissue where the barrier is not damaged.

Further studies have been conducted on the cytotoxic effect of silver nanoparticles. The results shown in **Figure 43** show that tumour areas of the animals treated with a combination of radiations and CTX-nanovectors caused the inhibition of tumour growth and progression. On the other hand, no inhibitory effect was observed in mice treated with either radiations or Ag-PNP-CTX alone. The observed increased level of apoptosis together with the *in vivo* inhibition of tumour growth would suggest a positive antitumor effect of Ag-nps.

In conclusion, the investigation conducted on the biological properties of the developed Ag-PNP-CTX nanovectors provide the proof-of-concept of the therapeutic validity of a combination strategy based on radiation therapy and CTX-targeted polymeric nanovectors, which is expected to enhance the antitumor efficacy of any cytotoxic molecules entrapped into PNP-CTX nanovectors.

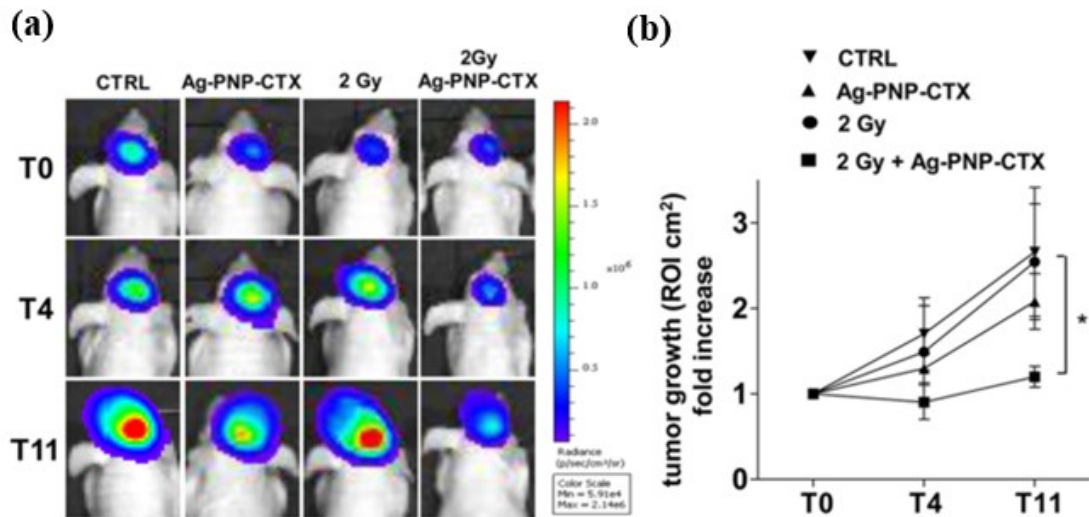


Figure 43. (a) Luciferase imaging of representative mice: untreated (CTRL, 4 mice); injected with Ag-PNP-CTX nanovectors as single agent (2 doses of 1 mg/mouse followed by 2 doses of 0,5 mg/mouse, administration interval: 48–72 h, 5 mice); irradiated (2 Gy single dose, 6 mice); treated with radiations and concomitant Ag-PNP-CTX nanovectors (6 mice). Treatments started 11 days after U87MGluc2 cell implantation (T0 = D11). (b) Tumor growth during 11 days of observation measured by area detected setting automatic ROI (50%).

3.2.2. Synthesis of aptamer functionalized polymeric nanovectors for the treatment of Glioblastoma through the BBB

All the procedures and results about the development of aptamer functionalized polymeric nanovectors for GBM treatment are completely described in:

- Aptamer Functionalization of Nanosystems for Glioblastoma Targeting through the Blood–Brain Barrier; J. Med. Chem. 2017, 60, 4510–4516

3.2.2.1. Entrapment of the chemotherapeutic drug NVP-BEZ235 in aptamer functionalized polymeric nanoparticles

NVP- BEZ235 (Dactolisib) is an imidazo[4,5-c]quinoline derivative that have shown promising anticancer therapeutic activity as inhibitor the phosphatidylinositol 3-kinase/Akt/mammalian target of rapamycin (PI3K/Akt/mTOR) pathway deregulation, common in human cancer and associated with tumour cell proliferation, growth, and apoptosis. As the PI3K/Akt/ mTOR pathway is highly activated in most human cancers, this pathway has become a favourable therapy target of cancer.

Currently, NVP-BEZ235 is in phase I/II clinical trials and is showing great results in the inhibition of PI3K and mTOR catalytic activity by competitively binding to the ATP-binding cleft, allow the controlling of solid tumours in preclinical mouse models

However, NVP-BEZ235 is characterized by a low water-solubility, which reduces its bioavailability and makes necessary a huge administration doses for ascertaining a significant effect. In order to overcome this challenge, NVP-BEZ235 has been entrapped in polymeric nanovectors characterized on the surface by the presence of an aptamer as active targeting. Aptamer are short, artificial, single- stranded oligonucleotides that, similarly to antibodies, interact at high affinity with their targets by recognizing a specific three- dimensional structure. Gint4.T is a novel platelet-derived growth factor receptors β (PDGFR β) specific antagonist represented by a nuclease-resistant RNA-aptamer, generated by the systematic evolution of ligands by exponential enrichment (SELEX) method. Recently Gint4.T showed a great potential in the inhibition of cell migration and proliferation, induction of differentiation, and in obstruction of the tumour growth *in vivo*.¹²³ For this purpose, Gint4.T aptamer has been selected as active targeting for its ability to interact with platelet-derived growth factor receptors β (PDGFR β) overexpressed on the BBB, that make it able to cross the blood–brain barrier (BBB).

As well as for the polymeric nanosystem described in the previous paragraph, the copolymer PLGA-b-PEG-COOH has been synthesized and used for the formation of polymeric micelles. Because of the high solubility of NVP-BEZ235 in chloroform, double-emulsions *water-in-oil-in-water* technique (w/o/w) has been used in this case. The double emulsion technique has been selected instead of the single emulsion because the inner aqueous core can offer the opportunity to further encapsulate a hydrophilic agent, such as a diagnostic agent.

With the intent to visualize the developed aptamer-targeted nanovector in the biological tissues, a nanosystem containing the lipophilic dye BODIPY505-515 (BODY-PY@PNPs) has been synthesized as described in the next paragraph. Indeed, the use of a fluorescent dye encapsulated in the polymeric nanoparticles leads to a detection of the effective particles localization, instead of a dye conjugated or adsorbed on the surface.

The *water-in-oil-in-water* procedure consisted in a first emulsion step, in which an organic phase, containing the NVP-BEZ235 and PLGA-b-PEG-COOH dissolved in chloroform, was emulsified with an aqueous phase (w_1) with a tip probe sonicator, able to furnish the necessary energy for the self-assembling process to the system. In this step, the organic phase was used in larger amount than the water phase, leading to the formation of inverse polymeric micelles. In the second step of w/o/w, a second water phase (w_2) has been prepared by dissolving a surfactant agent (sodium cholate) in water. This solution has been added to the organic phase in larger amount, obtaining a biphasic solution that was emulsified with a tip probe sonicator for 3 minutes, leading to the formation of water-soluble micelles (**Figure 44**). Once terminated the process, chloroform has been evaporated and the obtained NVP-BEZ235@PNPs have been purified with centrifugation and washed several times with fresh water. The DLS characterization revealed that the obtained polymeric nanoparticles were characterized by a hydrodynamic diameter of 76.0 nm, a PDI value of 0.22 and a Zeta potential of -28.5 mV.

After purification, the amino-terminated aptamer (Gint4.T) has been conjugated on the obtained NVP-BEZ235@PNPs, by exploiting the superficial residual carboxylic groups onto the PNPs surface, derived from PEG chains, as described in the previous paragraph (**Scheme 11**). NVP-BEZ235@PNPs-Gint4.T was then purified and characterized by DLS, which revealed particles with diameter equal to 52 ± 1 nm, a low polydispersity index (PDI = 0.169), and negative zeta potential value of -13.1 mV due to unreacted carboxylic acid groups.

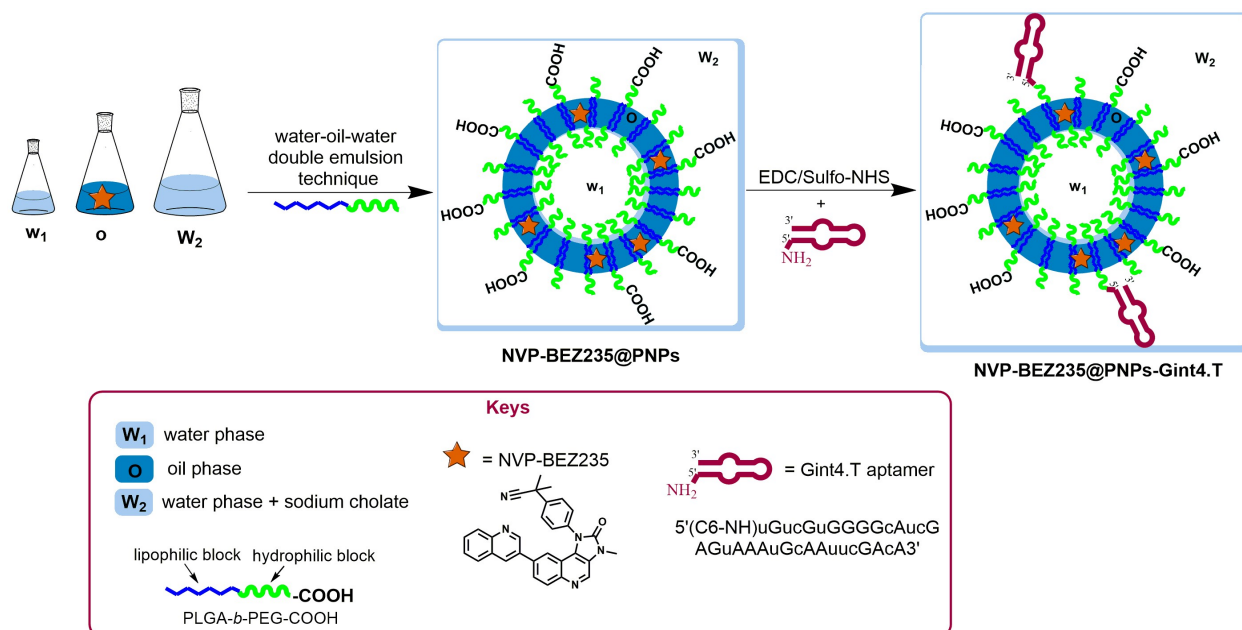


Figure 44. Schematic representation of the procedure for the obtention of the NVP@PNPs-Gint4.T.

The amount of NPV-BEZ235 entrapped in the polymeric nanoparticles NVP-BEZ235@PNPs-Gint4.T, has been quantified with fluorescence quantitative determination by using an excitation wavelength of 270 nm and an emission wavelength of 425 nm (**Figure 45**).¹²⁴ The amount of NVP-BEZ235 entrapped resulted to be 25.2 μM .

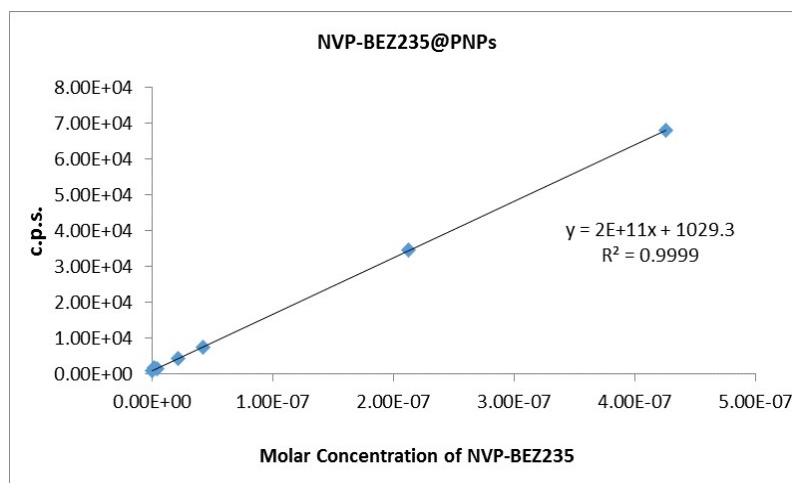


Figure 45. Fluorimetric determination of NVP-BEZ235. The calibration line has been obtained with the counts per second (c.p.s.) measured for different molar concentrations of NVP-BEZ235 in dichloromethane ($\lambda_{em} = 450$ nm).

On the other hand, the amount of aptamer conjugated to the NVP-BEZ235@PNPs-Gint4.T was evaluated by a real-time quantitative polymerase chain reaction (RT-qPCR) analysis on NVP-BEZ@PNPs-Gint4.T that revealed a Gint4.T concentration of 1.4 nM, corresponding to a conjugation efficiency of 5.4%.

To prove a direct correlation between obtained results and the presence of a specific aptamer onto the surface of the nanoparticles, NVP-BEZ235@PNPs were also conjugated with a 2'-Fluoropyrimidine (2'F-Py) RNA with no affinity for PDGFR β receptor, consisting in the scrambled (SCR) sequence of a previously generated anti-EGFR aptamer and herein used as negative control (indicated as NVP-BEZ235@PNPs-SCR).¹²³ The obtained NVP-BEZ235@PNPs-SCR showed a diameter of 48 ± 0.5 nm, a PDI of 0.207 and a Zeta potential value of - 23.7 mV, and an entrapped NVP-BEZ235 concentration of 22.3 μ M.

3.2.2.2. Entrapment of a lipophilic dye BODIPY 505-515 in aptamer functionalized polymeric nanoparticles

In order to achieve fluorescence-based studies, such as internalization studies performed by confocal laser microscopy and *in vivo* tumour targeting studies, a lipophilic dye (BODIPY505-515) has been encapsulated in aptamer targeted polymeric nanoparticles.

Due to its high solubility in chloroform, BODIPY505-515 has been encapsulated in polymeric nanoparticles through the *w/o/w* technique as described in the previous paragraph.

The DLS characterization showed that of BODI-PY@PNPs were characterized by a hydrodynamic diameter of 82.0 nm, a PDI value of 0.23 and a Z-potential of -25.5 mV.

After that, the Gint4.T and the scrambled aptamers have been conjugated on the BODI-PY@PNPs through the EDC/NHS chemistry (**Scheme 11**).

The DLS analysis revealed that a BODI-PY@PNPs-Gint4.T were characterized by a hydrodynamic diameter of 78 ± 1 nm, a PDI of 0.182 and a zeta potential value of - 44.0 mV, while the BODIPY@PNPs-SCR were characterized by a diameter equal to 78 ± 1 nm, polydispersity index (PDI) of 0.182 and negative Zeta potential value of - 44.0 mV.

The concentration of BODIPY®505-515 was estimated by fluorimetric measurements acquired at the emission wavelength of 512 nm (λ_{em}) by using the excitation wavelength of 368 nm (λ_{ex}) (**Figure 46**). The concentration of the entrapped BODIPY®505-515 in BODIPY@PNPs-Gint4.T resulted to be 9.5 μ M, while the concentration in BODIPY@PNPs-SCR resulted to be 8.7 μ M.

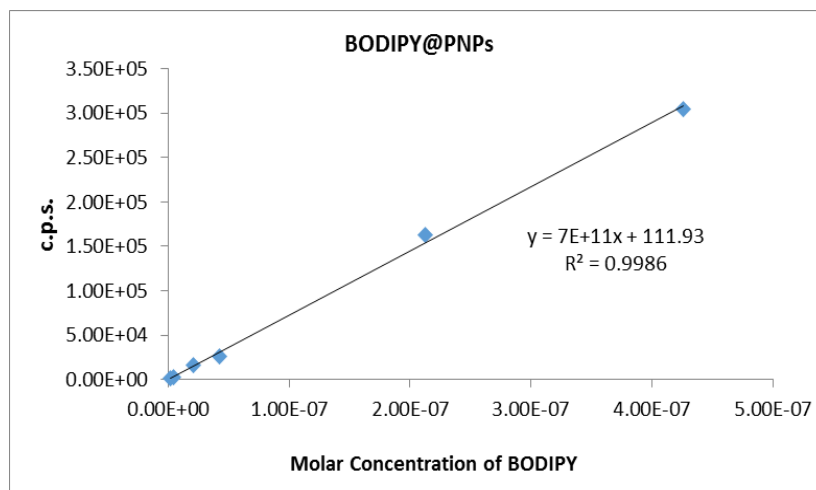


Figure 46. Fluorimetric determination of BODIPY@505-515. The calibration line has been obtained with the counts per second (c.p.s.) measured for different molar concentrations of BODIPY@505-515 in dichloromethane ($\lambda_{em} = 512$ nm).

3.2.2.3. *In vitro* and *in vivo* biological studies

The investigation of the biological activity of the developed nanosystems has been carried out through several *in vitro* and *in vivo* experiments.

In vitro studies have been realized in collaboration with the Istituto Toscano Tumori (ITT) in Siena, and the Istituto Nazionale per lo Studio e la Cura dei Tumori “Fondazione G. Pascale” in Naples.

First, the targeting efficiency of aptamer conjugated on nanovectors has been tested with internalization and cytotoxicity studies.

For the internalization studies, BODIPY@PNPs conjugated with Gint4.T or scrambled (SCR) aptamers, were incubated with GBM cell line (U87MG cells), and nanovectors were visualized by confocal microscopy by taking advantage of the BODIPY. The results showed that PNP conjugated with Gint4.T aptamer have been easily internalized in U87MG cells, becoming clearly visible 10 min after the beginning of the treatment, while SCR decorated nanovectors were undetectable until 50 min (**Figure 47**). These data demonstrated that the conjugation of polymeric nanoparticles with the anti-PDGFR β aptamer strongly enhanced the internalization of the nanovectors in GBM cells.

To additionally control that the specificity of targeting depended on the recognition of the PDGFR β by the Gint4.T aptamer, U87MG clonal cells depleted from this receptor have been used for further internalization studies. The results showed that, after an incubation of 40 min, fluorescent BODIPY@PNPs-Gint4.T were clearly internalized exclusively in U87MG clonal cells, characterized by a reduced number of PDGFR β , while untargeted fluorescent

BODIPY@PNPs-SCR were not internalized in any of the clonal cells. Thus, these data clearly indicated that the Gint4.T aptamer specifically targets PNPs to GBM cells, strongly enhancing their intracellular uptake.

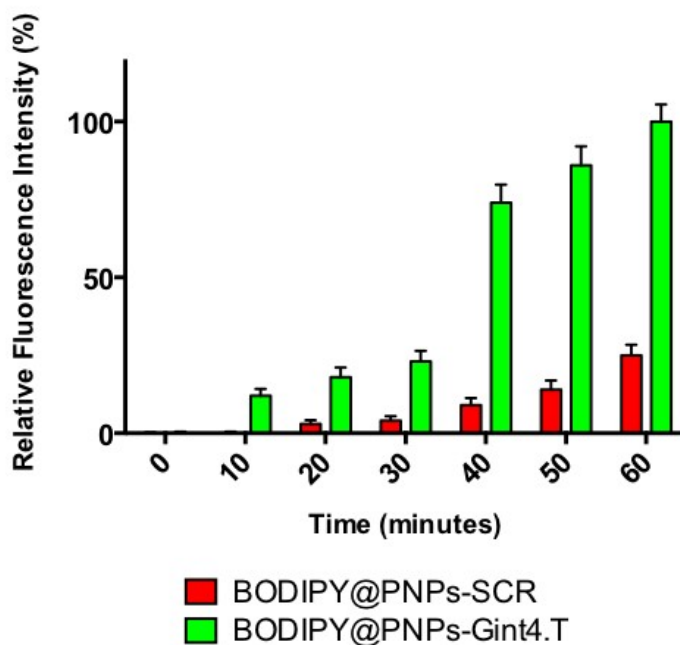


Figure 47. The number of cells that incorporated Bodipy fluorophore after treatment with Bodipy@PNPs-SCR or Bodipy@PNPs-Gint4.T has been evaluated across the time from 0 to 60 minutes. The number of cells with a mean relative fluorescence intensity higher than median fluorescence of control has been evaluated by Velocity software (Quantitation module, PerkinElmer). A minimum of 400 cells for each sample for each experiment (n=3) has been analysed.

On the other hand, the cytotoxicity studies revealed that the efficiency of the drug on its specific biochemical targets is unchanged also after its entrapment in polymeric nanoparticles. In particular, the ability of drug-loaded nanovectors of killing U87MG target cells was investigated through the measure of the EC_{50} (half maximal effective concentration values) for “free” NVP-BEZ235, NVP-BEZ235@PNPs-SCR, and NVP-BEZ235@PNPs-Gint4.T. The results reported in **table 1**, showed that NVP-BEZ235@PNPs-Gint4.T resulted in being at least 1000-fold more cytotoxic, comparing with “free” NVP-BEZ235 and about 4-fold more effective than NVP-BEZ235@PNPs-SCR, demonstrating a strongly improved bioavailability of the drug encapsulated in aptamer functionalized nanoparticles.

Table 1. EC₅₀ for free NVP-BEZ235, NVP-BEZ235@PNPs-SCR and NVP-BEZ235@PNPs-Gint4.T were evaluated after continuous incubation (EC₅₀ at 72h) and after 40 minutes incubation followed by washes (WO = washout) and 72 hours recovery.

	EC ₅₀ (72h)	EC ₅₀ (40 min + WO + 72h)
NVP-BEZ235	165693 pM	1017.58 nM
NVP-BEZ235@PNPs-SCR	156 pM	10.44 nM
NVP-BEZ235@PNPs-Gint4.T	38 pM	0.16 nM

In order to investigate the targeting ability of the developed nanosystems *in vivo*, further experiments have been conducted in collaboration with the NorLux Neuro-Oncology Laboratory of Department of Oncology at Luxembourg Institute of Health.

The aim of these experiments consisted in to prove the ability of the developed nanovectors to pass the BBB and to be specifically accumulated into brain tumour.

For this purpose, BODIPY@PNPs-Gint4.T or BODIPY@PNPs-SCR nanovectors were systemically administered to nude mice with intracranial U87MG tumour xenografts.

After two hours (2h), the mice were sacrificed and the whole brains were analysed with high-resolution fluorescence microscopy. The collected images showed that a clear fluorescent signal was present in the brain of the animals treated with BODIPY@PNPs-Gint4.T, while no specific signal was observed in tumours from mice treated with the negative control nanovectors (**Figure 49a**).

In addition, the fluorescence from the control nanoparticles was almost undetectable also at four hours (4h) after injection while the fluorescence from the Gint4.T-nanovectors was significantly higher at 4 h than at the 2 h time point (**Figure 49b**).

Although the BBB is partially damaged at the tumour core of the intracranial U87MG model, in the brain areas distant from the central tumour mass is fully intact, preventing the drug penetration. Therefore, to confirm that the developed delivery system was able to cross an intact BBB, the amount of fluorescence in the areas of normal brain distant from the tumour has been analysed. The results revealed that a greater fluorescence has been detected in the brain from mice that received Gint4.T-PNPs injection compared to those treated with the scrambled nanovectors, supporting that conjugation with the anti-PDGFR β aptamer allows the nanoparticles to cross the BBB (**Figure 48 a and b**).

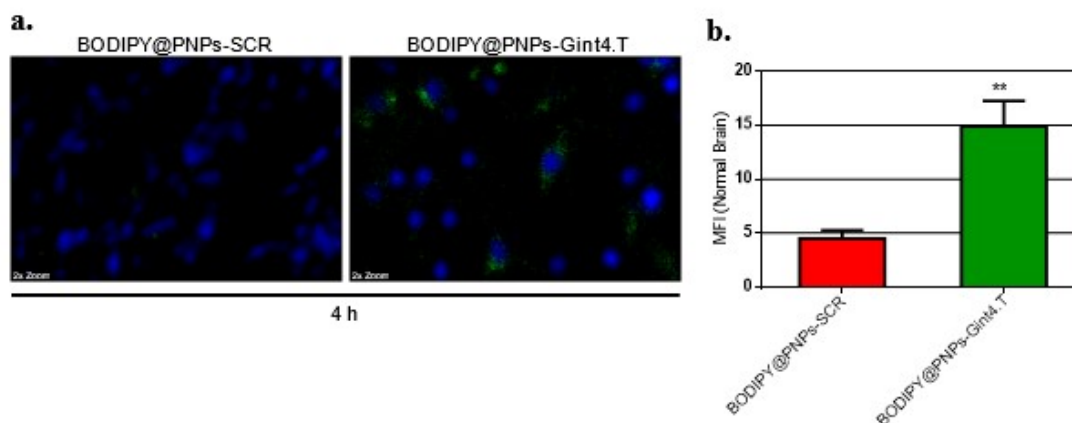


Figure 48.(a) Representative confocal microscopy images of normal brains at 4h post injection of BODIPY@PNPs-Gint4.T or BODIPY@PNPs-SCR. All digital images were captured at the same setting to allow direct comparison of staining patterns. Blue: nuclei; green: aptamer-PNPs. (b) Aptamer-PNPs fluorescence was quantified on 6 separate slices for each experimental group and expressed as mean fluorescence intensity (MFI) \pm SD of 10 microscopy fields randomly taken from each slice. **P < 0.01.

Next, to confirm the tumour-specific targeting of nanovectors, we assessed the effectiveness of the Gint4.T-PNPs in delivering the drug to mouse brain tumours. To this aim, NVP-BEZ235@PNPs-SCR and NVP-BEZ235@PNPs-Gint4.T were systemically administered daily over five consecutive days to tumour-bearing mice. At the end of the treatment, the grade of inhibition of phospho-4EBP1 has been measured in the tumours isolated from the brains in order to investigate the activity of the drug. Indeed, NVP-BEZ235 as inhibition of mTOR pathway can cell cycle arrest in G1/G0 phase in glioma cell lines, though the inhibition of PI3K/Akt/mTOR pathway by decreasing the expression of phospho-4EBP1.¹²⁵ The results indicated that also with a short and acute treatment, the phospho-4EBP1 levels were significantly lower in Gint4.T-PNPs treated tumors than in the control tumours (**Figure 49c**). In conclusion, the results obtained from *in vitro* and *in vivo* studies prove the efficacy of the developed nanosystems to overcome the BBB and to be accumulated in the tumour and suggest that both these processes are mediated by Gint4.T aptamer-dependent recognition of the PDGFR β expressed on these cells.

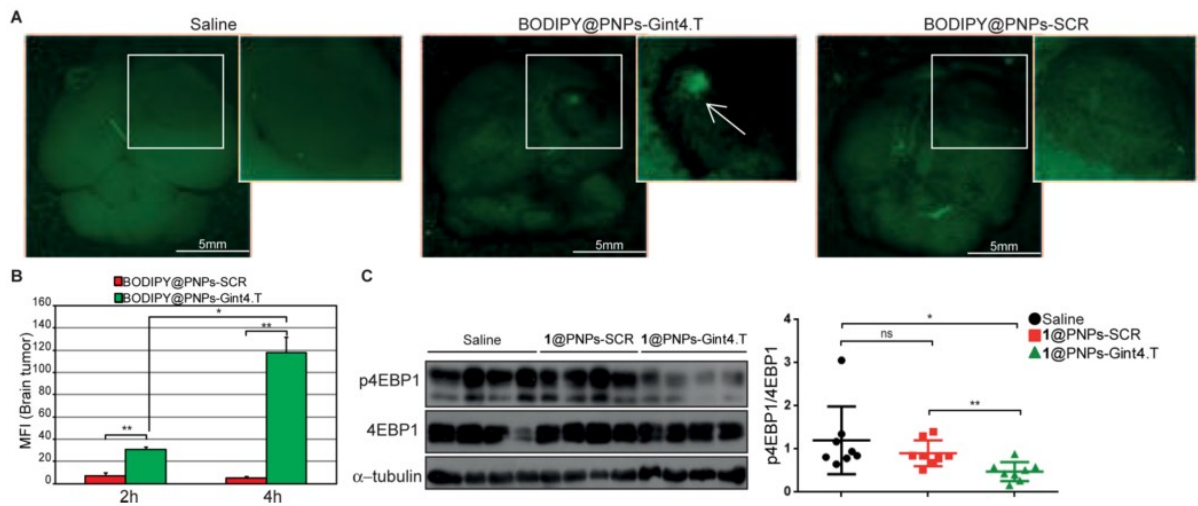


Figure 48. (A) Ex vivo fluorescence imaging of entire brains explanted from mice bearing U87MG orthotopic xenografts 2 h after injection of PBS, BODIPY@PNPs-Gint4.T, or BODIPY@PNPs-SCR. Magnified views of the tumour areas (white square) are indicated in the insets. White arrows indicate fluorescent signals from Gint4.T-PNPs. (B) Aptamer-PNPs fluorescence in the tumour, at 2 and 4 h post injection, was quantified on six separate slices for each experimental group and expressed as mean fluorescence intensity (MFI) \pm SD of 10 microscopy fields randomly taken from each slice. (C) Western blot of p4EBP1 and total 4EBP1 in intracranial U87MG xenografts after completion of the 5-day treatment with saline, NVP-BE2235@PNPs-SCR (1@PNPs-SCR), or NVP-BE2235@PNPs-Gint4.T (1@PNPs-Gint4.T). (left) Four representative tumors per group are shown. α -tubulin was used as internal control. (right) Quantitation of p4EBP1/4EBP1. Each data point represents the sample from an individual mouse (n = 8). One-way ANOVA followed by Tukey's multiple comparison test (C) or student's t-test (B). **P < 0.01; *P < 0.05; ns, no significance.

3.3 Synthesis of nanosystems for hyperthermia therapy

Hyperthermia therapy is a cancer treatment that consists in the exposition of body tissue to an increasing of temperature above the physiological temperature (42-45°C) to induce cytotoxic effects on cancer cells.

Photothermal therapy (PTT) is a hyperthermia therapy based on the use of near infrared (NIR) laser photoabsorbers to generate heat in order to induce thermal ablation of cancer cells upon NIR laser irradiation. PTT is a non-invasive, highly efficient and well-tolerated therapy against various cancer types. In order to improve its efficiency, new agents able to generate therapeutic hyperthermia when irradiated, are needed and must have precise biocompatibility in order to avoid damage to healthy tissues and prevent system toxicity-related events. Safe metals in the form of nano- (NPs) and micro-particles (MPs) have been studied as potential Photo-Thermal (PTT) agents. Among these PTT agents able to absorb the light in the so-called biological windows, are particularly suitable in order to reduce the non-selective heating of healthy tissue and, at the same time allow deeper tissue treatments.

For this purpose, two different photothermal systems based on metal nanoparticles have been developed. The first system consisted in the use of gold nanorods (GNRs) as light activated agents, due their well-known ability to absorb and scatter the electromagnetic radiation in the near-infrared (NIR) region. By using the *oil-in-water* technique, GNRs have been surface modified and entrapped in polymeric nanoparticles in order to enhance their biocompatibility. Also, curcumin has been entrapped in the same system and used as therapeutic agent for its potential for prevention, and therapy of cancer. With the intention to study the efficacy of a combined photothermal cancer treatment with local drug delivery of curcumin, three different systems have been synthesized by entrapping lipophilic GNRs (GNR-1@PMs), Curcumin (Curc@PMs) and lipophilic GNRs together with the Curcumin (GNR-1/Curc@PMs). On the other hand, chitosan-microparticles containing very small magnesium nanoparticles (Chit-Mg MPs) represent the second developed photothermal system. Chit-Mg MPs have been synthesized in one-pot reaction through MgCl₂ reduction to magnesium nanoparticles with a salt reduction methodology. The stability and biocompatibility of the obtained nanoparticles (Mg-NPs) have been improved by using chitosan as coating, because of the strong affinity of amino and hydroxyl groups for the magnesium nanocrystal surfaces.

The photothermal behavior for cancer treatments of both the developed systems have been tested *in vitro* and *in vivo*.

3.3.1 Gold nanorods as tools for photothermal therapy of Barrett Oesophagus

All the procedures and results about the development of photothermal nanosystems based on the use of gold nanorods, are completely described in:

- Gold nanorods and curcumin-loaded nanomicelles for efficient in vivo photothermal therapy of Barrett Esophagus. *Nanomedicine (Lond)* 1–11 (2015).

3.3.1.1 Synthesis and surface functionalization of gold nanorods (GNRs)

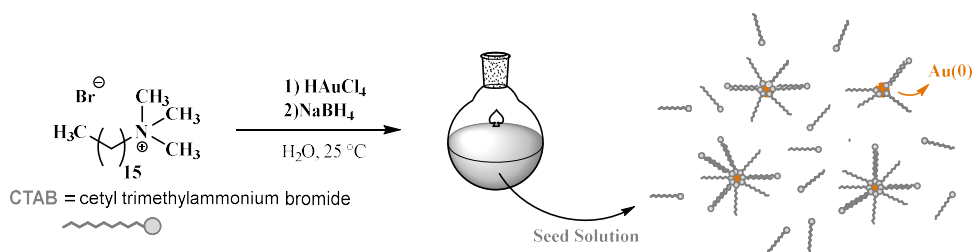
Gold nanorods have been synthesized by using a methodology fine-tuned of the research group where I worked, based on “seed-mediated and surfactant-assisted growth” method developed by Nikobakht and El-Sayed.¹²⁶ This method allows obtaining GNRs characterized by different aspect ratio (length/width) and a low amount of spherical particles that could be formed during the synthesis as impurities.

The method consists in the preparation of the "seeds" of the nucleation by reducing a small amount of tetrachloroauric acid (HAuCl_4) in aqueous solution, in the presence of the surfactant with a strong reducing agent, such as sodium borohydride (NaBH_4).

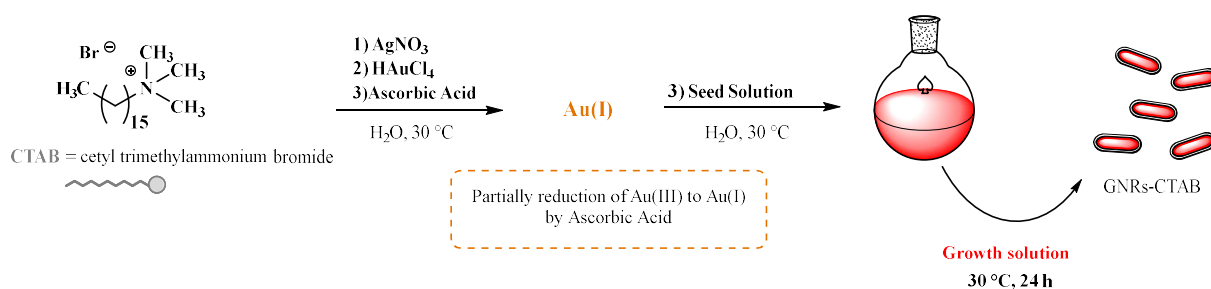
The formed seeds are later added in a growth solution, constitutes of ions of the adjuvant Ag^+ , a substantial excess of the surfactant and a more abundant amount of HAuCl_4 partially reduced by Au^{3+} to Au^{1+} with ascorbic acid in order to facilitate the deposition of metal atoms to the seeds in growth (**Scheme 12**). In a general procedure, a high concentration of the cationic surfactant cetyltrimethylammonium bromide (CTAB) is used to achieve GNRs formation and to avoid GNRs aggregation and precipitation once they are synthesized.

After 24 hours at controlled temperature (27-30 °C) a diluted solution of GNRs coated with surfactant is obtained, showing the typical red-purple coloration. Once obtained, GNRs-CTAB have been purified with high-speed centrifugation and then characterized through transmission electron microscopy (TEM) and UV-Vis spectroscopy.

Seed Solution:



Growth Solution:



Scheme 12. Schematic representation of the procedure for the obtainment of gold nanorods (GNRs).

TEM analysis confirmed the obtainment of GNRs characterized by an *aspect ratio* around 4, being length 50 nm and width 12-13 nm (**Figure 50**). UV-Vis spectroscopy showed the typical two absorption bands of GNRs, one with a maximum wavelength at 740 nm (longitudinal plasmon resonance, LPR) and the other with a maximum at 520 nm (transversal plasmon resonance, TPR), typical values for the obtained aspect ratio (**Figure 50**).

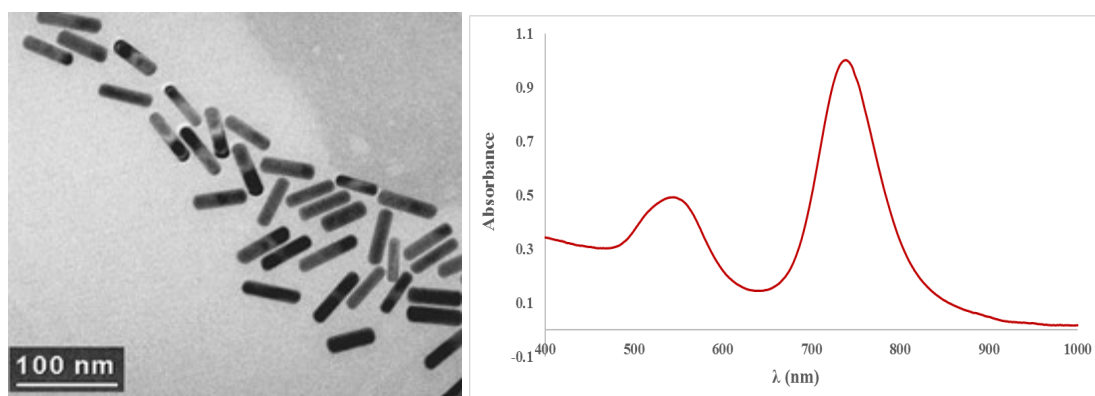


Figure 50. On the left, TEM image of GNRs and, on the right, the corresponding UV-Vis spectrum.

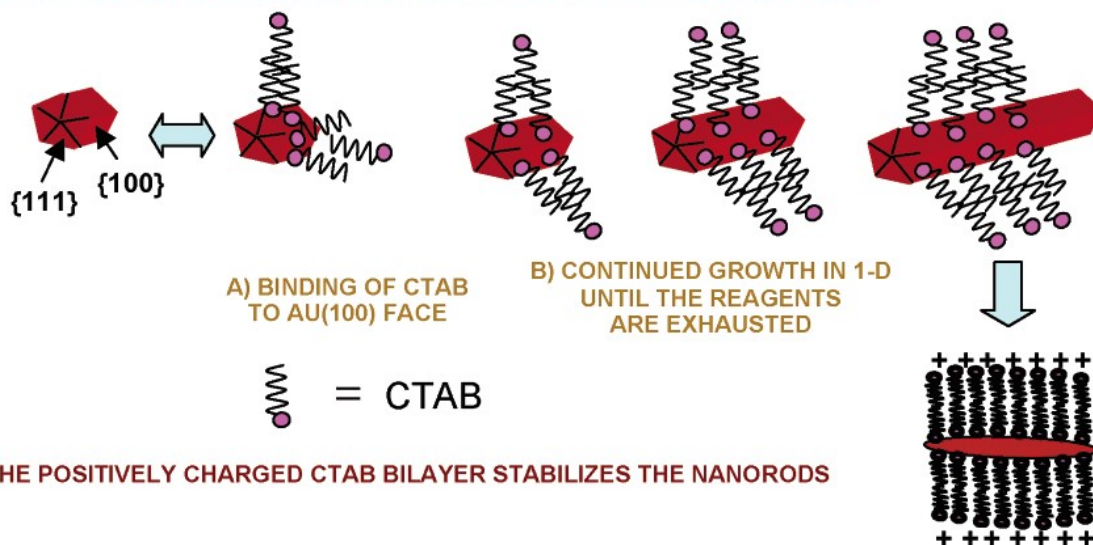
The roles played by the surfactant and the silver ions in the mechanism, have been extensively investigated but up today is not completely clarified. About the surfactant, several studies confirmed that CTAB form a double layer (bilayer) around GNRs in the growth phase, constitutes by the first layer, in which the head-group of CTAB is oriented towards the

nanorods surface, and a second layer, directed towards water, leaving the two hydrophobic tails in the centre, similar to a cellular membrane.¹²⁷ In addition, the CTAB has an important role during the nucleation step, creating a preliminary facial differentiation of the seeds in order to allow the preferential growth in one direction rather than in all the possible directions. Once immersed in the growth solution, the seeds undergo a preferential attack by the surfactant on the more accessible face $\{100\}$, while the face $\{111\}$ remaining free from CTAB can grow, thus leading to the elongated cylindrical structure. For the same reason, the $\{111\}$ face remains more reactive in each stage than the $\{100\}$ face, which is the fact that influences all the surface chemistry of these nanostructures (**Figure 51**).¹²⁸

STEP 1: SYMMETRY BREAKING IN FCC METALS



STEP 2: PREFERENTIAL SURFACTANT BINDING TO SPECIFIC CRYSTAL FACES



THE POSITIVELY CHARGED CTAB BILAYER STABILIZES THE NANORODS

Figure 51. Formation mechanism of GNRs.
Figure from J. Phys. Chem. B **109**, 13857–13870 (2005).

About the role of silver, it has been shown that within certain limits, by increasing the amount of silver ions in the grow solution, GNRs with increased aspect ratio can be obtained. Indeed, positively charged silver ions are able to intercalate the negatively charged bromine head groups on the surface of the nanostructure, limiting the tendency of the negative charged heads to repel each other, and promoting the elongation of the GNRs.

However, synthetic GNRs with CTAB are toxic to cultured cells and to animals, thus the surface modification is the key factor determining the cytotoxicity of GNRs.

Indeed, in physiological conditions free CTAB molecules desorb from the surface of the GNRs and diffuse across cell membrane. Once into the cells, due to its positive charge, CTAB molecules interact with negative charged DNA and RNA molecules, leading to a strong cytotoxic effect on healthy cells.

In order to enhance the GNRs biocompatibility, CTAB replacement appears to be the only alternative. However, it represents a great challenge due to the different reactivity of the {111} and {100} faces of the nanorods, which can induce to GNRs aggregation after the complete elimination of CTAB from the GNRs surface. For this reason, the CTAB removal has been achieved through ligand exchange reaction by using 11-(4-mercaptobenzamido)undecanoate (ligand 1), as well as done for the silver nanoparticles surface functionalization (paragraph 3.2.1.1).

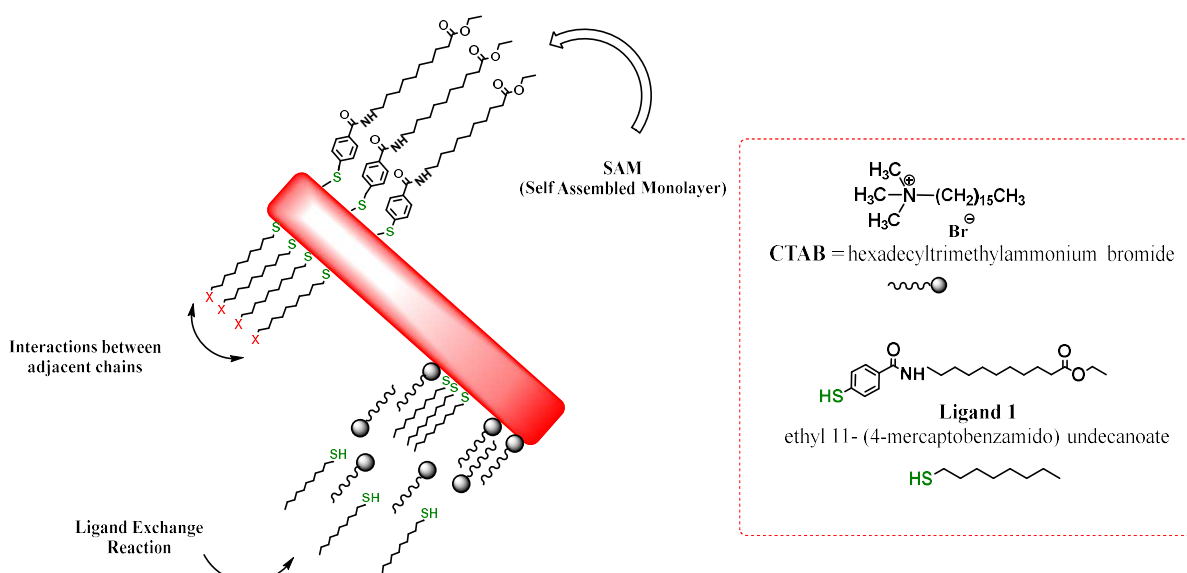


Figure 52. Representation of ligand exchange reaction performed on GNRs by using ligand 1.

The method requires the preparation of an organic solution obtained by dissolving the ligand 1 in ethanol that has been further added to an aqueous solution contains GNRs-CTAB (Figure 52). The obtained hydro-alcoholic solution has been put under slight mechanical stirring for 24 hours, in order to allow the self-assembled monolayer formation on GNRs. After completing the ligand exchange, purification by several washes with ethanol has been carried out in order to remove the unreacted ligand molecules and the replaced CTAB. Once formed SAM on GNRs, ligand 1 are able to confer high stability to the nanoparticles and a drastical change in their solubility, leading the obtainment of lipophilic GNRs soluble in

dichloromethane (GNRs-1). GNRs-1 have been characterized by $^1\text{H-NMR}$ and infrared IR spectroscopy in order to confirm the presence of ligand 1 on GNRs surface.

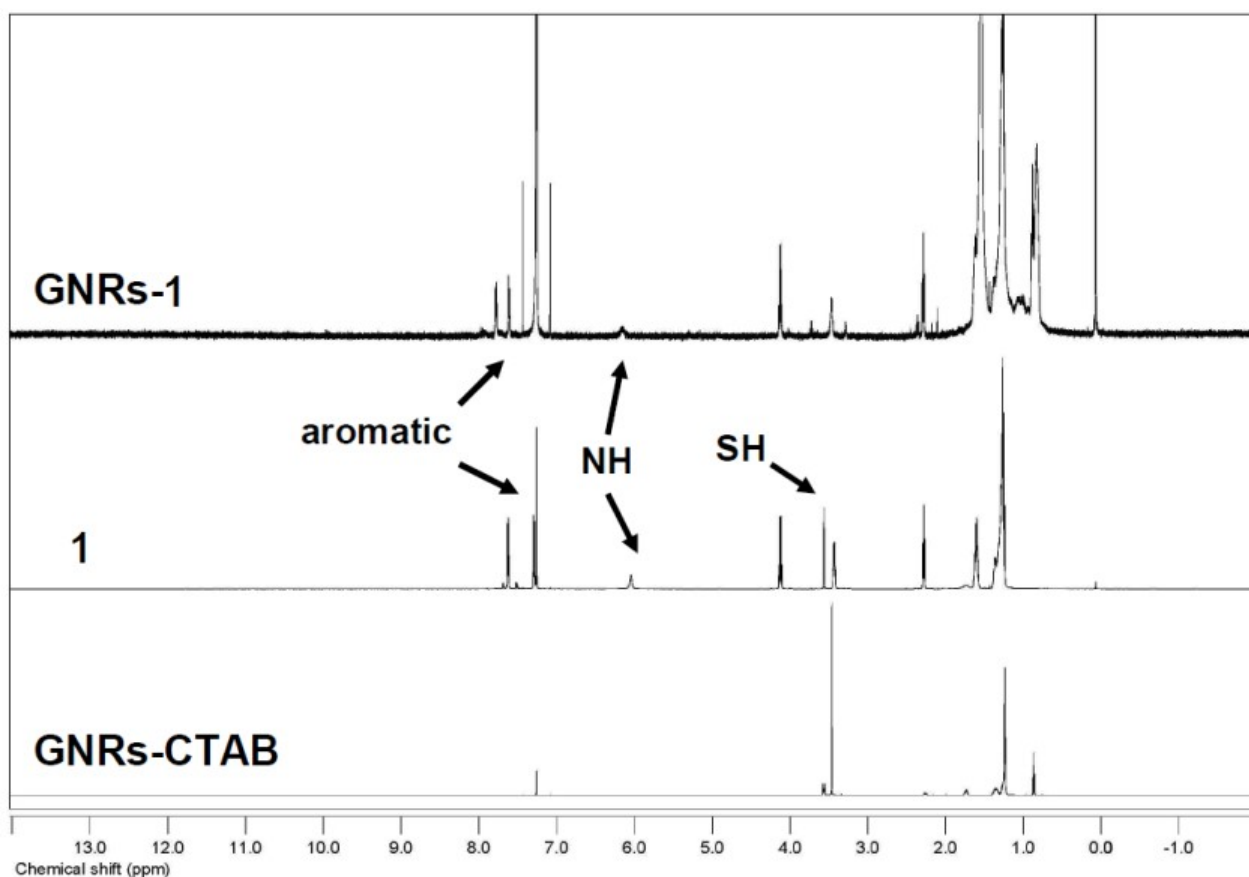


Figure 53. $^1\text{H-NMR}$ analysis of GNRs-1, ligand 1 and GNRs-CTAB in CDCl_3

The comparison of the $^1\text{H-NMR}$ spectra of the ligand 1 and free CTAB with the spectrum of GNRs-1 clearly showed that CTAB molecules have been completely removed from the metal surface, and that the ligand 1 is clearly attached onto the metal surface. In particular, the presence of all the significant signals of the ligand 1, and the disappearance of the -SH hydrogen, meaning that the link with the metal surface has been effective (**Figure 53**).

In addition, IR spectroscopy confirmed once again the effective ligand exchange and the removal of CTAB (**Figure 54**).

In order to estimate the metal content into the solution, Atomic Absorption Spectroscopy (AAS) has been used, showing a reaction yield of about 80% meaning that a good amount of nanoparticles can be recovered after the ligand exchange. Also, gravimetric analysis revealed that the ligand anchored to the surface is about the 35-40% of the entire system, which is

satisfactorily high and surely high enough to ensure stability to GNRs during the following steps.

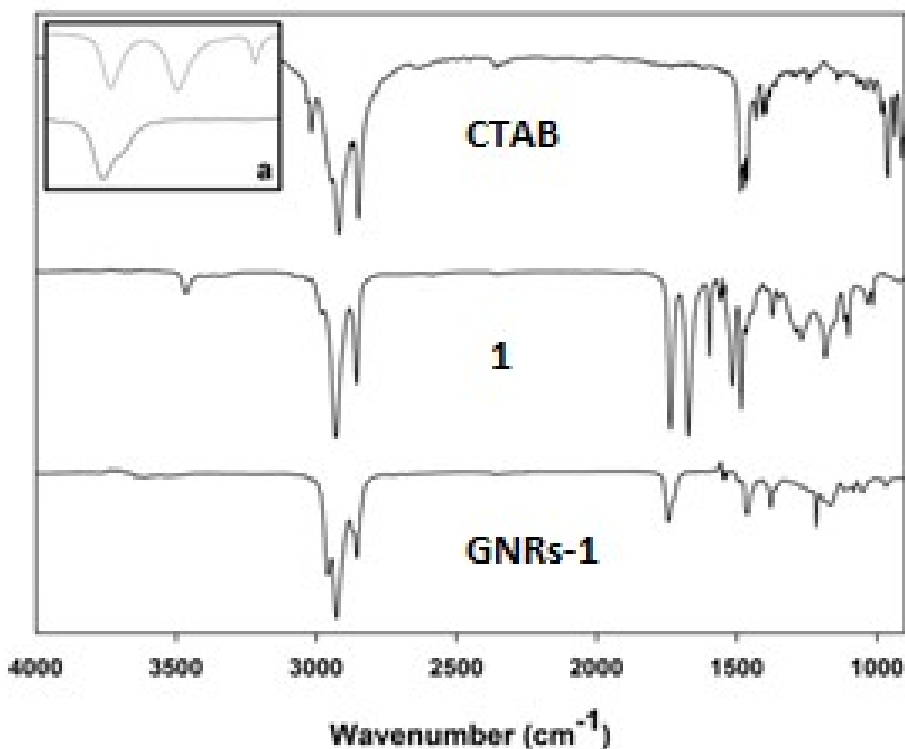


Figure 54. FTIR spectra of GNRs-1, ligand 1 and GNRs-CTAB in KBr.

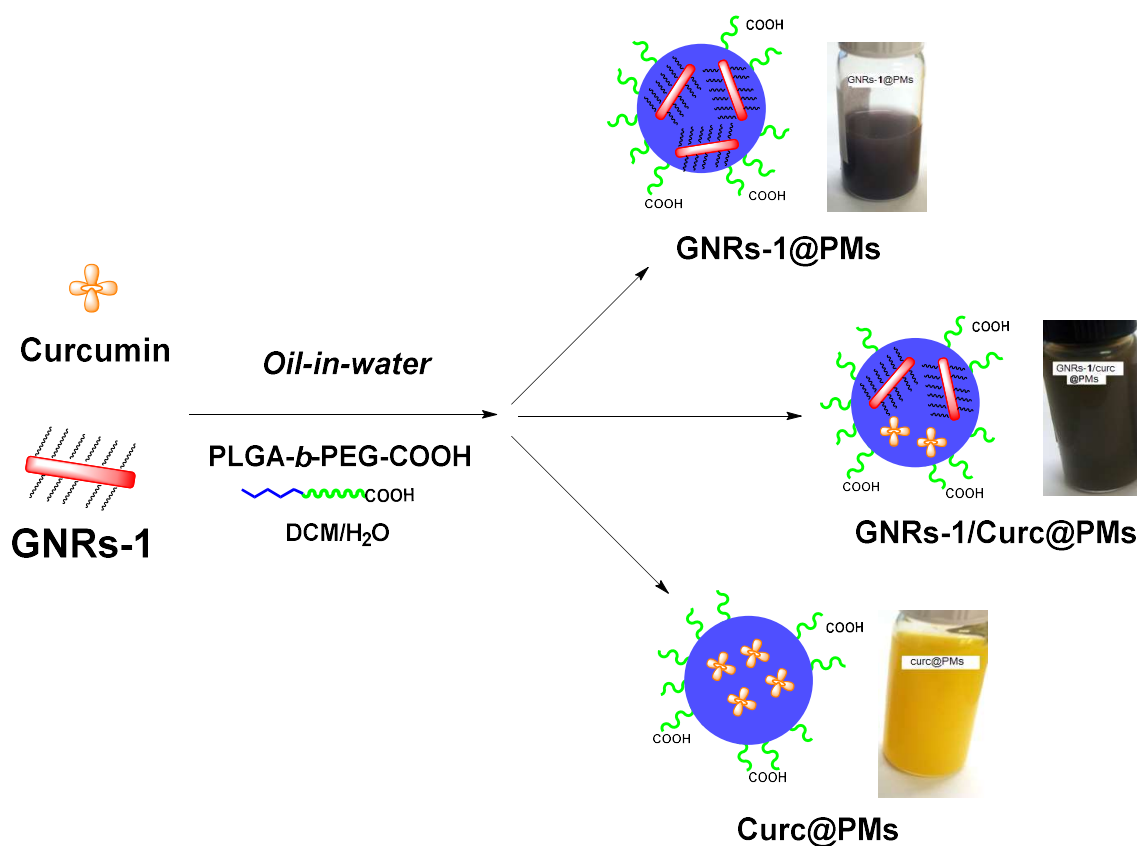
3.3.1.2 GNRs-1 and Curcumin loaded in polymeric micelles as a novel theranostic system

Curcumin (diferuloylmethane) is a polyphenol derived from the *Curcuma longa* plant, commonly known as turmeric. Due to its non-toxicity and its variety of therapeutic properties including anti-oxidant, analgesic, anti-inflammatory and antiseptic activity, curcumin has been used extensively in Ayurvedic medicine for centuries. Currently, curcumin has been found to possess anticancer activities ascribed to its effect on a variety of biological pathways involved in mutagenesis, oncogene expression, cell cycle regulation, apoptosis, tumorigenesis and metastasis.¹²⁹

Clinical trials studies revealed that curcumin could stop the precancerous changes becoming cancer, but the main problem laid to its bad bio-distribution.¹³⁰ Indeed, pharmacokinetic studies of curcumin indicated in general a low bioavailability of curcumin following oral application. In order to improve its bio-distribution, an injectable form of curcumin, which

may improve the bio-distribution has been developed.¹³¹ Although the results seem promising, further clinical trials in humans might be performed in order to know if curcumin has any potential to treat cancer in people.

Taking in account this problematic, in this project the entrapment of curcumin in polymeric nanomicelles made of PLGA-*b*-PEG polymer has been realized. In addition, the synergic effects of photothermal properties of GNRs and the anticancer properties of curcumin has been investigated by synthesized three different nanosystems: polymeric nanomicelles loaded with lipophilic GNRs-1 (GNRs-1@PMs), with curcumine (Curc@PMs) and, with curcumine and lipophilic GNRs-1 (GNRs-1/Curc@PMs) (**Scheme 13**).



Scheme 13. Schematic representation of the formation of GNRs-1@PMs, Curc@PMs and GNRs-1/Curc@PMs. Because of the high solubility of GNRs-1 and curcumin in dichloromethane, the *oil-in-water* technique has been used to form the polymeric nanomicelles.

For the synthesis of GNRs-1@PMs and Curc@PMs, the procedure consists in the dissolution of PLGA-*b*-PEG-COOH into dichloromethane solution containing, in one case, GNRs-1, and in the other case, curcumin. Once prepared the organic solution, an aqueous phase containing a surfactant (sodium cholate) was then slowly added on the top of this, led to the formation of a biphasic solution that underwent to sonication with a trip probe sonicator in order to furnish

the necessary energy to the system for the self-assembling process. After a short time (1-2 minutes), the two phases resulted completely mixed, and the polymeric micelles have been obtained. The organic solvent remained entrapped in the lipophilic core was removed by evaporation under vacuum and the resulting aqueous solution was purified with centrifuge in order to eliminate the small un-reacted molecules. The obtained GNRs-1@PMs and Curc@PMs were characterized by dynamic light scattering (DLS), atomic absorption analysis (AAS), transmission electron microscopy (TEM), UV-Vis analysis and gravimetric analysis. Regarding the GNRs-1@PMs, the entrapment of GNRs into micelles has been confirmed by TEM images (**Figure 55**).

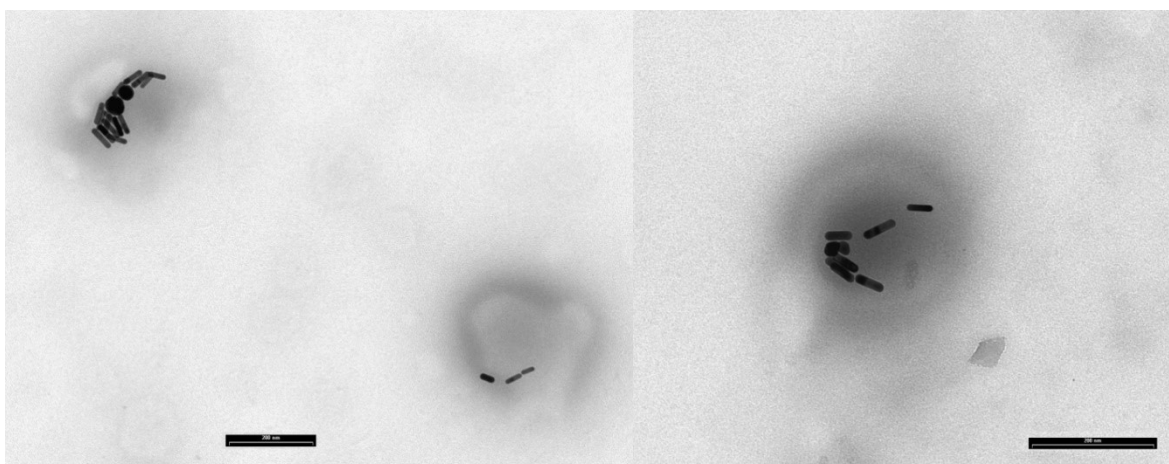


Figure 55. TEM images of GNRs-1@PMs

DLS analysis showed that GNRs-1@PMs were characterized by a hydrodynamic radius of 137.0 ± 1.6 nm, a PDI of 0.227 ± 0.042 and a high negative zeta potential value (-43.9 mV). The negative Zeta potential is due to the presence in the micelles outer shell of free carboxylic acids groups deriving from the free end of PEG chains.

In addition, UV-Vis spectrum revealed that the optical properties of GNRs were unchanged after the entrapment, showing the typical GNRs maximum absorption peak at 730–740 nm. The amount of gold in GNRs-1@PMs measured through the AAS resulted to be 0.158 mg/ml, corresponding to a solution 0.802 mM and a GNRs-1 entrapment efficacy of 71.8%.

On the other hand, dealing with Curc@PMs, DLS result shows a hydrodynamic diameter of 99.4 ± 0.8 nm with a PDI of 0.210 ± 0.010 and a negative zeta potential of -50.1 mV. Through UV-Vis analysis the curcumin amount entrapped into PMs was determined, obtaining a concentration value of 2.0 mM with an entrapment yield of 37%. In addition, the UV-Vis

spectrum of Curc@PMs showed a blue-shifted of peak of curcumin at 419 nm (instead of 430 nm) after its entrapped, suggested an effective entrapment in the polymeric micelles.

Finally, polymeric nanoparticles containing both GNRs-1 and curcumin were prepared. The simultaneous entrapment into micelles of two moieties is a challenging aim, due to the possible interferences that could arise from the proximity of these two reactive compounds. For this reason, to ensure the obtainment of a nanosystem containing both the two active agents a similar procedure was exploited: two separated emulsions containing GNRs-1@PMs and Curc@PMs not completely stabilized were obtained by using the same described procedure but reducing the sonication time (from 2 min to 1 min). Then, the two solutions were mixed together and re-emulsified for the remaining time in order to allow complete micelles formation and reorganization.¹³²

With this method, micelles formation proceeds through a fast-initial aggregation of unimers into small metastable micelles that can further grow toward the minimum Gibbs energy only if some of them shrink, dissolve and release unimers. Metastable phase of micelles has been exploited by mixing together the two active moieties without direct interaction between them since they are surrounded by unimers.

The obtained system containing GNRs and curcumin has been completely characterized. The DLS showed a hydrodynamic radius for GNRs-1/Curc@PMs of 119.0 ± 1.6 nm with a PDI of 0.282 ± 0.030 and a zeta potential value of -41.6 mV. The hypothesis of GNRs and curcumin entrapped together in one micelle, instead of a mixture of GNRs-1@PMs and Curc@PMs was confirmed by the presence of a single population in the DLS analysis and by the UV-Vis characterization. Indeed, UV-Vis analysis confirmed, on one hand, the keeping of optical properties both for GNRs and for curcumin, and on the other hand, showed a blue-shift in the GNRs absorption peak when entrapped with curcumin in comparison to when entrapped alone (**Figure 56**).

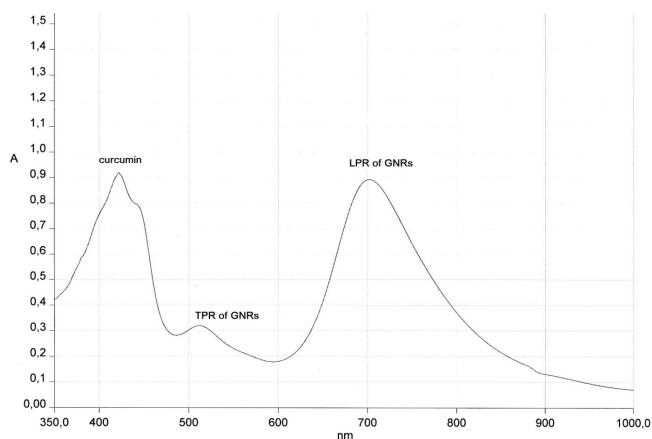


Figure 56. UV-Vis spectrum of GNRs-1/Curc@PMs

This evidence suggested the proximity of the two moieties, which would bring to the collapse of GNRs if not for the double emulsification procedure.

Also in this case, the gold concentration was measured with AAS and resulted to be 0.098 mg/mL, corresponding to a solution 0.53 mM, while curcumin concentration was determined to be 2.2 mM, meaning that both the two moieties were entrapped into PMs with a yield of 44% for GNRs and 41% for curcumin.

3.3.1.3. *In vitro* and *in vivo* biological studies

Adenocarcinoma is one of the two common pathologic subtypes of oesophageal cancer, a serious malignancy with high mortality particularly common in the United States and certain European countries, associated with obesity and gastroesophageal reflux disease.

The grim statistics highlight the importance of extensive and urgent research on mechanisms, prevention, detection and therapy of oesophageal cancer and its premalignant precursor Barrett's Oesophagus (BE). Surgery and chemoradiation are the usual treatment for patients with advanced but resectable oesophageal cancers. However, the prognosis and further management largely depends upon the pathologic tumor-node-metastasis. A potential to overcome these limitations is through a combined sequential therapy, which exploits the synergistic effect of different drugs or agents to enhance their efficacy and avoid the dose limiting toxicities and poor response rates. For this purpose, the synergism of photothermal behavior of GNRs and the anticancer activity of curcumin for the treatment of Barrett's oesophageal and oesophageal adenocarcinoma (EAC) has been investigated, through a deep biological investigation carried out in collaboration with the research group of the Dr. Robert Martin of the Division of Surgical Oncology at the University of Louisville (USA).

First of all, photothermal properties of GNRs have been exploited in combination with triggered curcumin release through *in vitro* studies on Barrett's oesophageal cell line (BAR-T) and an oesophageal adenocarcinoma (EAC) cell line. A BE cell line (BAR-T) and an EAC cell line (OE-19) were treated for 12 hours with the three developed systems (GNRs-1@PMs, GNRs-1/Curc@PMs and Curc@PMs). Then, the cell lines were exposed to near-infrared spectroscopy (NIR) light laser using a Diode Pumped Solid State laser (DPSSL) system at a wavelength of 808 nm and a power density of 3 W/cm² for 1 min. \

Twelve hours after the laser treatment, the cell viability has been valuated with a 3-(4,5-dimethyl-thiazol-2-yl)- 2,5-diphenyltetrazolium bromide (MTT, Sigma- Aldrich) reduction assay.

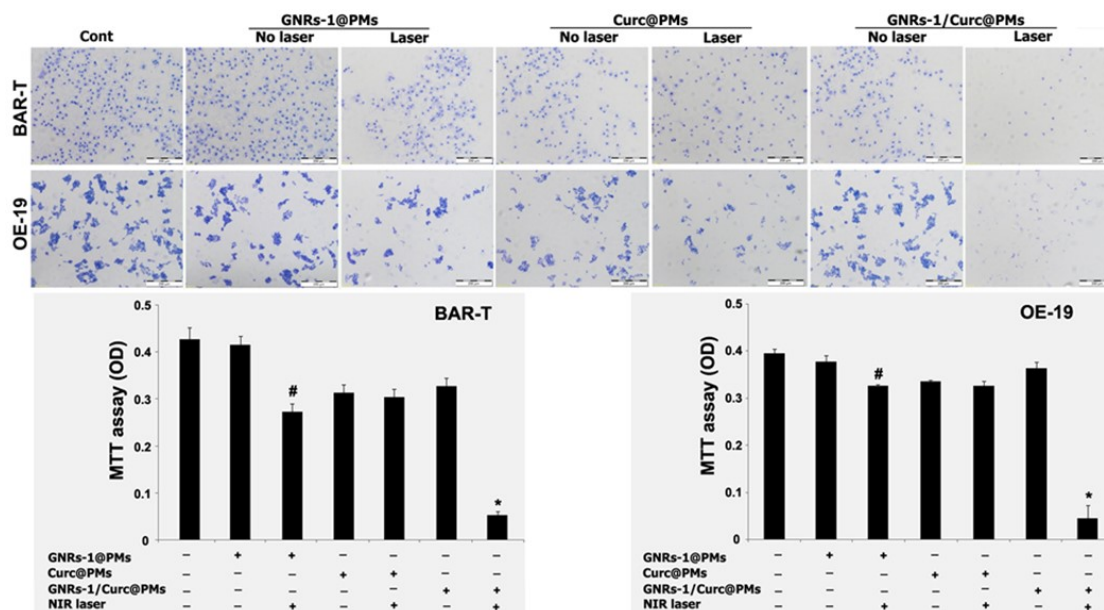


Figure 57. *In vitro* laser irradiation. Upper, a representative images of cells treated with GNRs- 1@PMs at 40 μ M (in gold), GNRs-1/Curc@PMs (40 μ M in gold and 166 μ M in curcumin) and Curc@PMs (166 μ M) with or without laser irradiation. (C) Cytotoxicity experiments. The cell viability by 3-(4, 5-dimethyl-thiazol-2-yl)-2, 5-diphenyltetrazolium bromide assay. Data present as mean \pm SD, * $p < 0.05$, compared with GNRs-1/Curc@PMs no laser. # $p < 0.05$, compared with GNRs-1@PMs no laser. Cont: Control; Curc@: Curcumin loaded; GNR: Gold nanorod; MTT: 2,5-diphenyltetrazolium bromide; NIR: Near-infrared spectroscopy; PM: Polymeric nanomicelle

The results reported in **Figure 57**, showed that the cells treated with GNRs-1/Curc@PMs show a significant mortality after laser treatment, more than GNRs-1@PMs treated cells. On the other hand, the cells treated with Curc@PMs showed an anticancer activity but demonstrated a less efficacy compared to the other systems, especially after laser treatment. The obtained data demonstrated higher efficacy by the synergistic effect between curcumin and GNRs using GNRs-1/Curc@PMs on cells that has been confirmed by the results obtained through *in vivo* experiments.

The *in vivo* studies have been performed on Barrett's Oesophagus bearing rats; the GNRs-1/Curc@PMs and GNRs-1@PMs were delivered at the same concentration tested *in vitro* through precise endoscopy to the lower oesophageal lumen, where the mucosa of Barrett's Oesophagus appeared. Twelve hours after GNRs-1/Curc@PMs and GNRs-1@PMs delivery, the lower oesophagus was exposed to NIR light with an output power of the laser of 10 W/cm² for 15 seconds. Later, the oesophageal tissues were harvested to investigate GNRs localization and histological changes by silver staining.

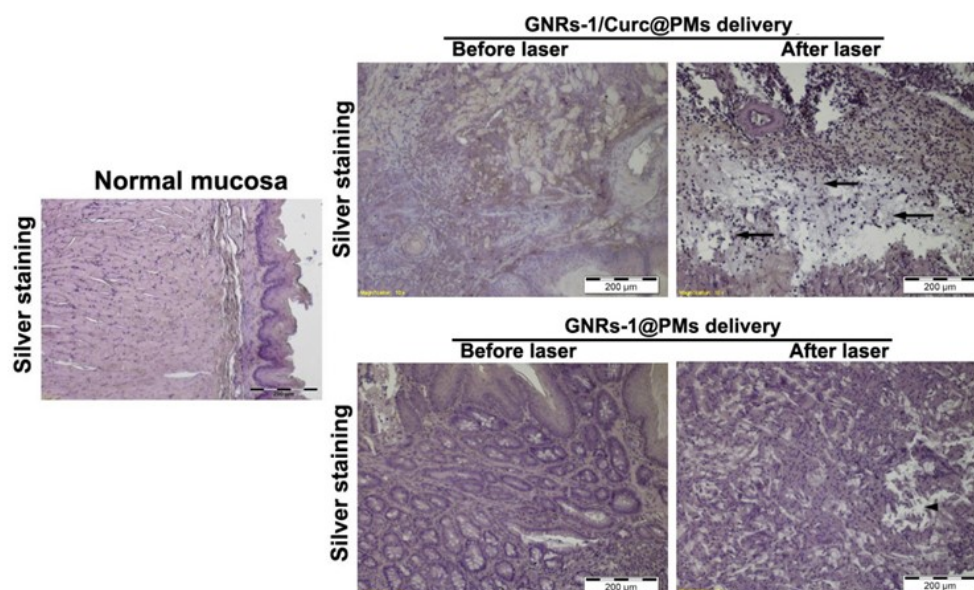


Figure 58. Lipophilic gold nanorods/curcumin loaded polymeric micelles localization by silver staining and Barrett's Oesophagus mucosal destruction by near infrared light. In the mid-panel, normal rat oesophageal mucosa. In the right-panel, both GNRs-1/Curc@PMs and GNRs-1@PMs distributed into the mesenchyma of Barrett's Oesophagus mucosal, in which the GNRs were detected by the silver staining. The Barrett's oesophageal mucosa was destroyed extensively (arrow) and most Barrett's cells died (arrow) in the GNRs-1/Curc@PMs treatment 24 h after near infrared light exposure. Regional loss of the Barrett's oesophageal mucosa and Barrett's cells (arrow head) were found in GNRs-1@PMs treatment 24 h after near infrared light exposure. Curc@: Curcumin loaded; GNR: Gold nanorod; PM: Polymeric nanomicelle.

The images reported in **Figure 58**, showed that GNRs from both GNRs-1/Curc@PMs and GNRs-1@PMs were detected in the mesenchyme of Barrett's Oesophagus mucosa but not in normal oesophageal mucosa 12 h after the endoscopic delivery, before laser irradiation (**Figure 58**, mid-panel). This phenomenon demonstrated the ability of the developed nanosystems to bind tumour tissue without noticeable toxicity to the surrounding normal cells. As expected, the Barrett's oesophageal mucosa with GNRs-1/Curc@PMs treatment was eradicated extensively at 24 h after NIR light exposure (**Figure 58**, top right-panel). However, the mucosa destruction in the Barrett's oesophageal mucosa with GNRs-1@PMs treatment and NIR light exposure was limited in some local regions (**Figure 58**, bottom right-panel)

The *in vivo* results confirmed that the extensive mucosa destruction after laser exposure in animals treated with GNRs-1/Curc@PMs is ascribed to the synergistic effect of GNRs thermal delivery and curcumin released from the micelles. In addition, the obtained data suggested that curcumin's anti-inflammatory and anti-oxidant activities could also help in protecting surrounding healthy tissue from laser contingent induced damages. Indeed, a positive effect of curcumin on radiation-induced apoptosis has been shown in human cancer cells.¹³³

3.3.2 Magnesium nanoparticles as a highly biocompatible photothermal agent for hepatocellular carcinoma treatment

All the procedures and results about the development of photothermal nanosystems based on the use of magnesium nanoparticles, are completely described in:

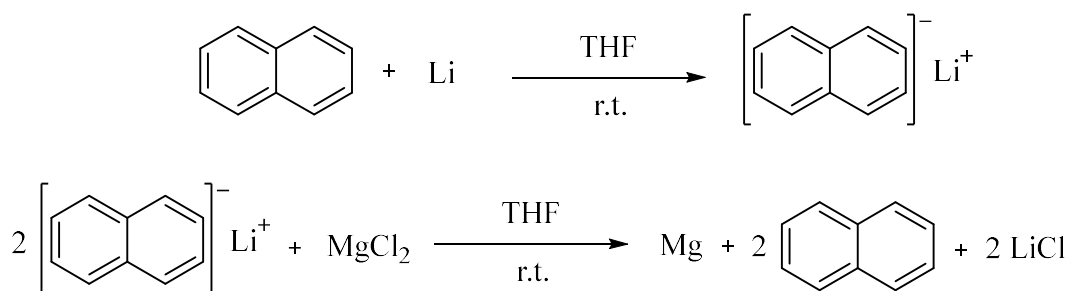
- One-pot synthesis of magnesium nanoparticles embedded in chitosan microparticles: a highly biocompatible tool for in vivo cancer treatment. *J. Mater. Chem. B*, **4**, 207–211 (2015).

3.3.2.1. Synthesis of chitosan coated magnesium nanoparticles

In the last decades, magnesium nanoparticles have been investigated in order to realize high compatible materials for biomedical applications. In addition, recently the photothermal behaviour of magnesium nanoparticles has been largely investigated for hyperthermia applications (**paragraph 1.3.3**).^{67,68,70,71}

However, the synthesis of magnesium nanoparticles (Mg NPs) is quite challenging because of their high reduction potential and high affinity toward oxidation. Indeed, in order to obtain magnesium nanoparticles able to respond to laser irradiation, they must exhibit a dark black colour, corresponding to their not-oxidized form. On the other hand, the oxidized magnesium nanoparticle (MgO nanoparticles) show usually a white colour and are not able to absorb light. Several methods for the preparation of magnesium nanoparticles have been reported in literature, such as electrochemical reduction,¹³⁴ sonoelectrochemistry,¹³⁵ infiltration of nanoporous carbon with molten magnesium, gas phase synthesis,¹³⁶ deposition from ethereal solutions,¹³⁷ high energy ball milling, and the gas-condensation method.

In this project, the magnesium nanoparticles synthesis has been achieved through a fine-tuned method in our laboratories. This method is based on the reduction of metal salts using alkali metal aromatic radical anions, which allows to obtain magnesium crystals in tetrahydrofuran (THF) via lithium reduction of the corresponding magnesium salt exploiting naphthalene as an electron carrier (**Scheme 14**).^{71,138}



Scheme 14. Schematic representation of the mechanism involves in the reduction of magnesium salts using alkali metal aromatic radical anions

This developed process involved the dissolution of naphthalene and MgCl_2 in anhydrous tetrahydrofuran (THF) under a constant flux of argon. After that, lithium bars were added to the solution and the reaction was left to react for 24 hours. After 24 hours the nanoparticles were centrifuged (6000 rpm) and purified by washing several times with anhydrous THF in order to remove lithium-naphthalene complex, LiCl by-product and unreacted MgCl_2 .

In order to optimize the process a deep investigation on the reagent ratios was carried out to better understand the limits of the reaction. The results showed that, particles formation were not influenced by the amount of lithium while the naphthalene concentration is an important parameter since no reaction was observed when the concentration was too low. In addition, it has been demonstrated that the reaction time also played an important role for the magnesium nanoparticles synthesis. Indeed, if the reaction is stopped before than 24 hours, Mg crystals are not stable and may form aggregates of more than 5 μm in size.

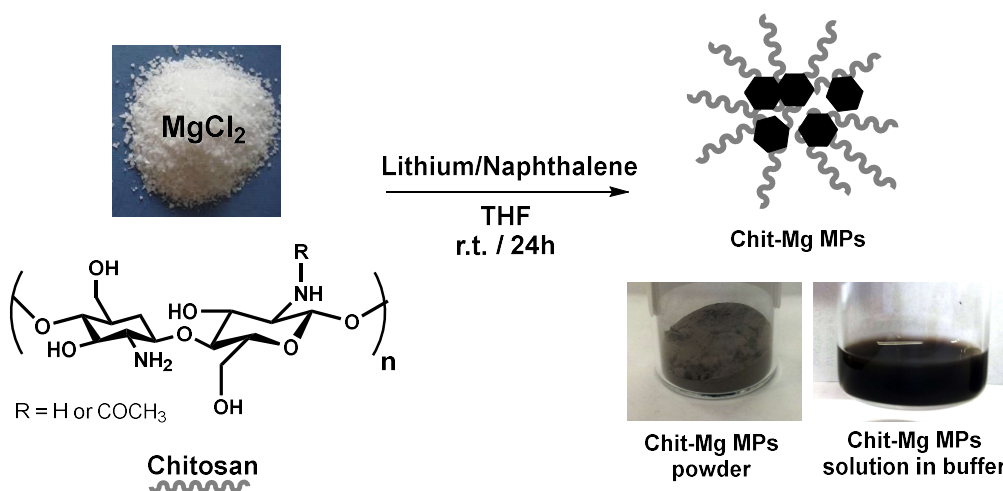
The described method allowed to synthesize magnesium nanoparticles highly heterogeneous in size and with an average diameter of about 50 nm; however, because of the absence of any stabilizing agent, these nanoparticles result usually aggregated in sub-micron clusters. With the intent to enhance the magnesium nanoparticles stability, in this project one-pot strategy to form chitosan coated magnesium nanoparticles has been developed by slightly modifying the previous described method.

Chitosan has been selected as nanoparticles coating because is a non-toxic, biodegradable and biocompatible natural sugar. It is obtained as waste material by shrimps and other crustacean shells and its molecular structure is characterized by amino and hydroxyl groups.

Because these functional groups are not reducible by the lithium-naphthalene complex formed during the reaction, chitosan molecules are able to survive to in the strong reducing reaction environment of the magnesium nanoparticles reaction. In addition, both amino and hydroxyl groups have strong affinity for the magnesium nanocrystals surface, thus chitosan may form a

stable linkage onto the surface of magnesium particles stabilizing them either against aggregation and oxidation.

Therefore, the modified synthesis provided the introduction of chitosan-glutamate at the beginning of the process, simultaneously with the other reagents, thus having the coating agents present during the magnesium nanocrystals formation (**Scheme 15**).



Scheme 15. Representative scheme of Chit-Mg MPs synthesis and photographs of both powder and MPs re-dispersed in acetate buffer.

After 24 hours, the formed chitosan coated magnesium microparticles (Chit-Mg MPs) have been recovered by centrifugation. Also in this case, a good purification is required in order to remove all the reaction by-products and in particular naphthalene and LiOH, deriving from the reducing agent. For this reason, Chit-Mg MPs were washed three times with THF and centrifuged before drying under vacuum. Finally, they can be re-dispersed in acetate buffer (pH 4.6) or slightly acidic water (pH 5) without visible agglomeration.

After the accurate purification, the obtained Chit-Mg MPs have been fully characterized. Dynamic light scattering (DLS) of Chit-Mg MPs revealed particles with hydrodynamic diameter of $1.15 \pm 0.07 \mu\text{m}$ and a positive surface charge of +38 mV, due to the presence of several protonated amino groups in the chitosan chains.

In order to investigate size and morphology of the magnesium nanoparticles entrapped into the chitosan matrix, Transmission Electron Microscopy (TEM) was performed. The TEM images showed in **Figure 59**, revealed the formation of polygonal-shaped nanoparticles with a diameter ranging between 5 and 10 nm. By comparing these data with the results obtained with the methodology without the introduction of chitosan in the reaction, in this case the obtained magnesium nanoparticles are characterized by a smaller size.

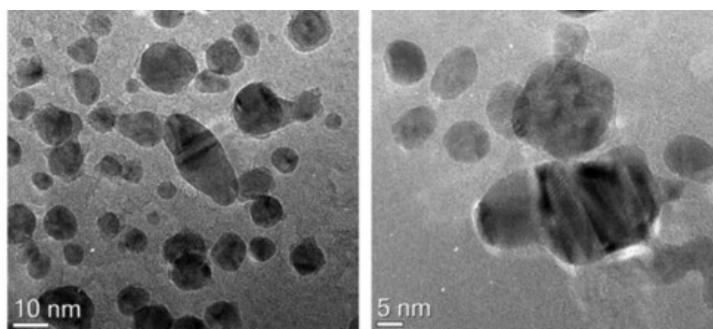


Figure 59. TEM images of Chit-Mg-MPs

These results can be ascribed to the presence of a capping agent placed directly into the reaction mixture, which allows an immediate stabilization of the particles and avoids their uncontrolled growth. Anyway, the DLS findings were in good agreement with scanning electron microscopy (SEM) images, which showed well homogeneous particles with approximately round shape and size slightly smaller than one μm (**Figure 60**). The difference between DLS and SEM results can be explained by considering the normalcy as DLS can only reveal hydrodynamic diameter, while SEM the effectively size.

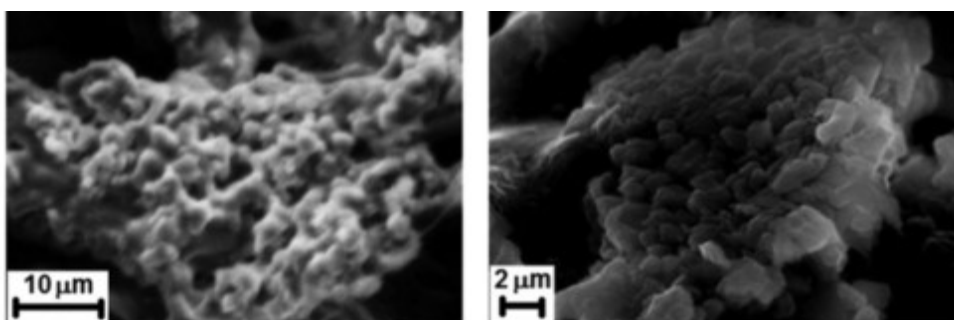


Figure 60. SEM images of Chit-Mg MPs after vacuum drying. Lower magnification (left side) and higher magnification (right side).

Moreover, X-ray diffraction (XRD) analysis showed crystalline nanoparticles and the typical reduced-magnesium pattern (**Figure 61**).

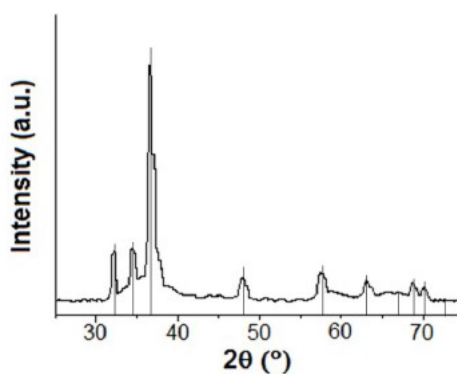


Figure 61. XRD analysis of Chit-Mg-MPs

Through the atomic absorption spectroscopy (AAS) a concentration in magnesium equal to 589 mg/L (24.2 mM) has been determined in a solution prepared by dissolving 10 mg of powder in 1 mL of buffer. In addition, thermogravimetric analysis (TGA) has been carried out. The spectrum showed the degradation of the organic layer between 150 and 350 °C, and an immediate and intense weight gaining at 600 °C, when the gas flow was changed from nitrogen to air. These results can be due to the oxidation of the magnesium core that after the complete degradation of chitosan matrix becomes uncoated and prone to oxygen attack.

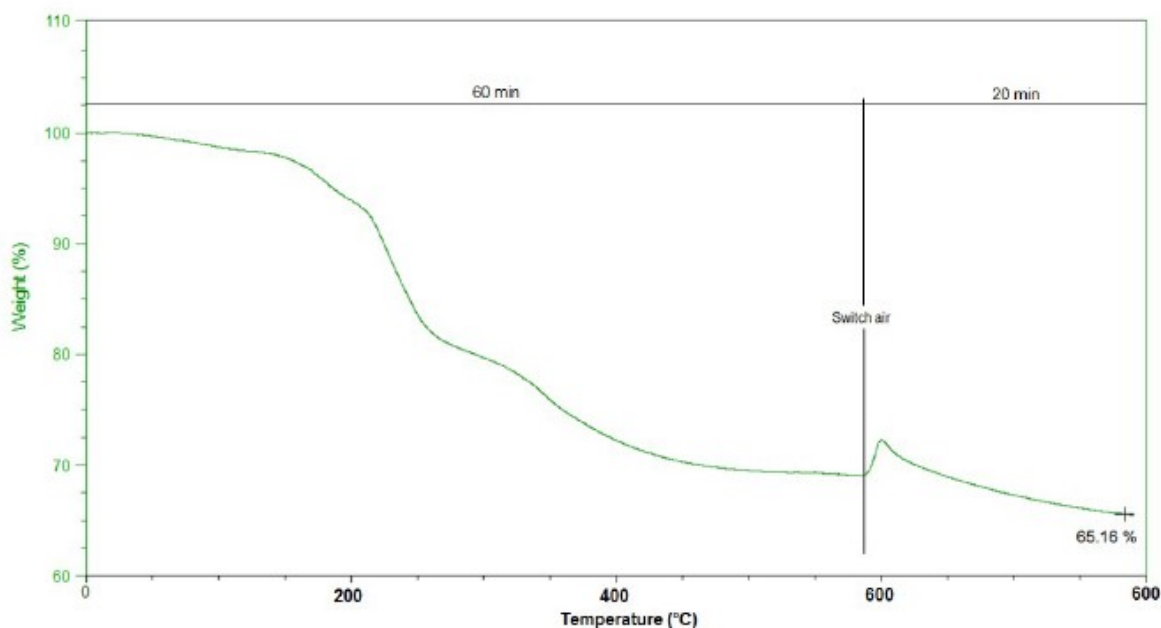


Figure 62. TGA of Chit-Mg MPs (from r.t. to 600 °C in 60 min in nitrogen flow, then isotherm at 600 °C for 10 minutes in air)

At the end, Fourier Transform Infrared Spectroscopy analysis confirmed the presence of the organic matrix onto the surface of the nanoparticles by showing the characteristic signals of chitosan: glycosidic linkage ($-C-O-C-$) at 1064 cm^{-1} , amines and protonated amines at 1510-1580 cm^{-1} and at 2800-2900 cm^{-1} , and intermolecular bonded $-OH$ as broad band between 2800 and 3000 cm^{-1} (**Figure 63**).

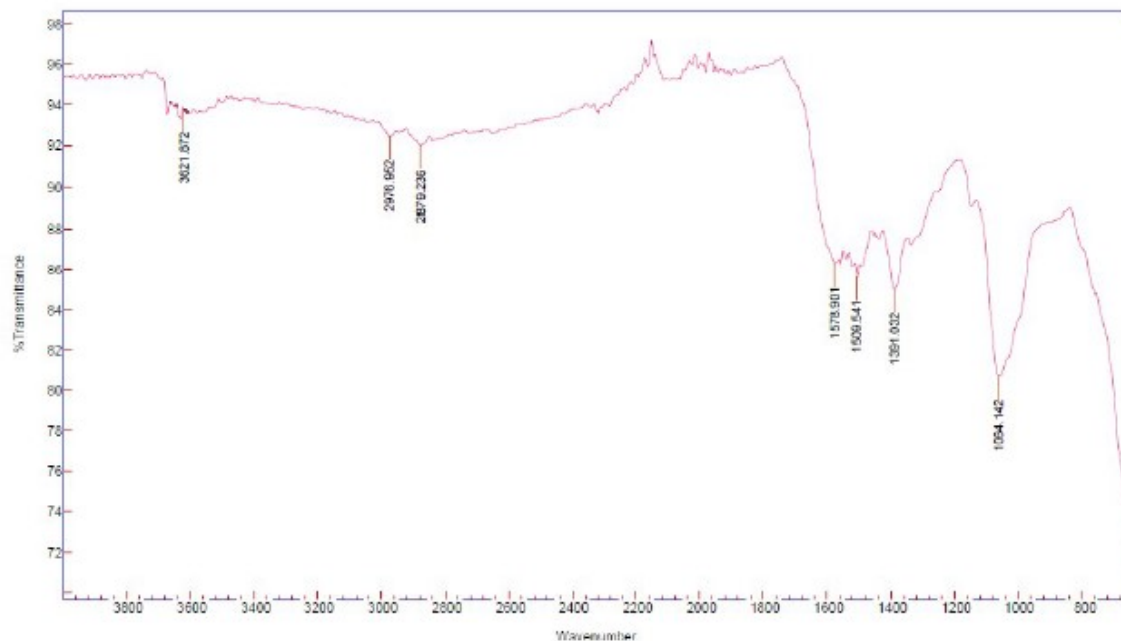


Figure 63. FTIR of Chit-Mg MPs.

3.3.2.1. *In vitro* and *in vivo* biological studies

The therapeutic effect of the Chit-Mg MPs has been investigated on Hepatocellular carcinoma (HCC) tumour model in collaboration with the research group of the Dr. Robert Martin of the Division of Surgical Oncology at the University of Louisville (USA).

Hepatocellular carcinoma (HCC) is the fifth most common cancer in men and seventh in women worldwide, accounts for the third major cause of cancer related deaths. Despite advances in prevention techniques, screening, and new technologies in both diagnosis and treatment, incidence and mortality continue to rise. Because of the highly vascularization in the HCC, the angiogenesis process allows the tumour to develop, invade and metastasize, restraining the therapy to limited options.¹³⁹ For this reason, research into new diagnostic and therapeutic fields for HCC offer a wide range of possibilities by trying to adapt to the tremendous potential and variability of the nanotechnology field.¹³⁹

In this project, the biocompatibility and the photothermal behaviour of the developed chitosan-magnesium microparticles (Chit-Mg MPs) have been tested through *in vitro* and *in vivo* biological studies.

The photothermal behaviour has been investigated by using a NIR laser illumination able to trigger a temperature rise from an aqueous dispersion of Chit- Mg MPs at different concentration. The experiments have been conducted by using a 810 nm diode laser operating in continuous wave (cw) mode at 13 W cm⁻². The results, shown in **Figure 64 a**, showed an

uniform and characteristic temperature profile including a temperature rise as soon as laser light is turned on and a fast cooling phase after switching off the laser. Particularly, after 0.5 – 1 minute of irradiation, the temperature enhancement was enough to reach temperature values of interest for photothermal therapy (i.e. ~ 40 to 50 °C) despite of the concentration considered. An exemplary map of temperature registered after 3 minutes of irradiation (at 13 W cm^{-2}) is displayed in **Figure 64b**. The picture highlights the confinement of the photothermal effect within the illuminated laser spot immediate outcomes include an effective and well-localized photothermal response that can be obtained with particle concentrations typically employed within the protocols of photothermal therapies.

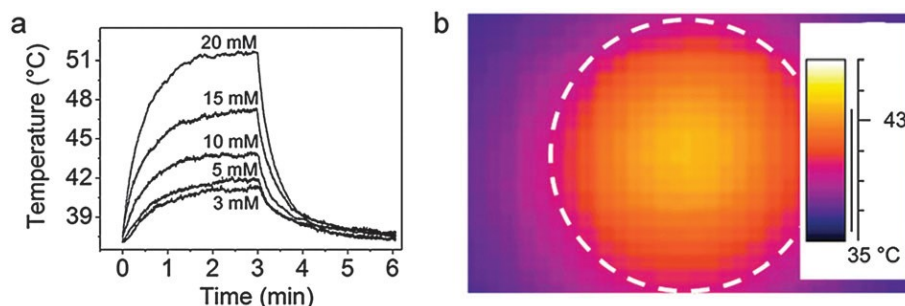


Figure 64. (a) Temperature profiles obtained by illuminating Chit–Mg MP solutions at different concentrations with a laser intensity of 13 W cm^{-2} and a $t_{irr} = 3 \text{ min}$. (b) Exemplary map of temperature registered after 3 min of irradiation of a 10 mM Chit–Mg MP solutions at 13 W cm^{-2} . The illuminated area is displayed by a dashed line.

After that biocompatibility of Chit-Mg MPs were assessed firstly by cell viability studies on hepa1-6 cell line (**Figure 65**). For this experiment, the cells were incubated with the Chit-Mg MPs particles at 48 or 72 hours in a magnesium concentration range of 0-100 $\mu\text{g/mL}$. The results revealed no mortality for both cells lines in this conditions, which are standard time points and concentrations values for evaluating the toxicity of a novel nanosystem.

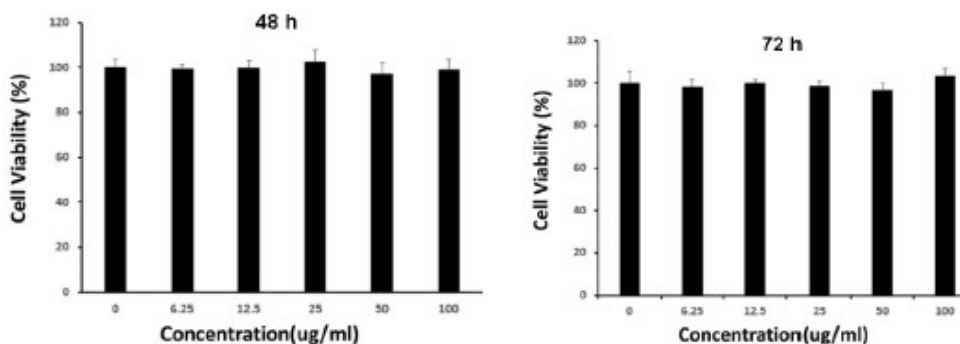


Figure 65. 3-(4,5-dimethyl-thiazol-2-yl)- 2,5-diphenyltetrazolium bromide (MTT, Sigma- Aldrich) reduction assay on hepa1-6 cell lines exposed to Chit-Mg MPs at different concentration for 48 and 72 hours respectively.

In vivo photothermal therapy was then performed on xenograft hepa1-6 tumour bearing mice. For this experiment, a solution of Chit-Mg MPs at 5 mM was administrated through an intratumoral injection in the animals, and after twelve hours the tumour area was illuminated with a near-infrared (NIR) laser irradiation of power density of 1 or 3 W/cm² for 0.5 or 2 minutes. The results showed that in the area subjected to photothermal therapy the most tumour cells were destroyed. Also, it has been demonstrated that a lower laser intensities were required *in vivo*, as compared to those employed for effective irradiation of nanoparticle solutions. These data can be due to the presence of an accumulation of the particles in the tumour site, allowing a major heat confinement. Three days after NIR exposure, the tissues were harvested for histological analysis. The results showed in **Figure 66**, clearly showed an extensive damage to tumour tissue after only 2 minutes of laser irradiation, while no damage was recorded when the tumour was treated with laser and saline alone.

In addition, the results showed that with an intratumoral injection, the laser exposure for 0.5 minute and 3 watt/cm² caused cell death in the tumour instead of the benign muscle, and when laser exposure was increased up to 2 minutes, most tumour cells were ablated while the benign muscle was unaffected.

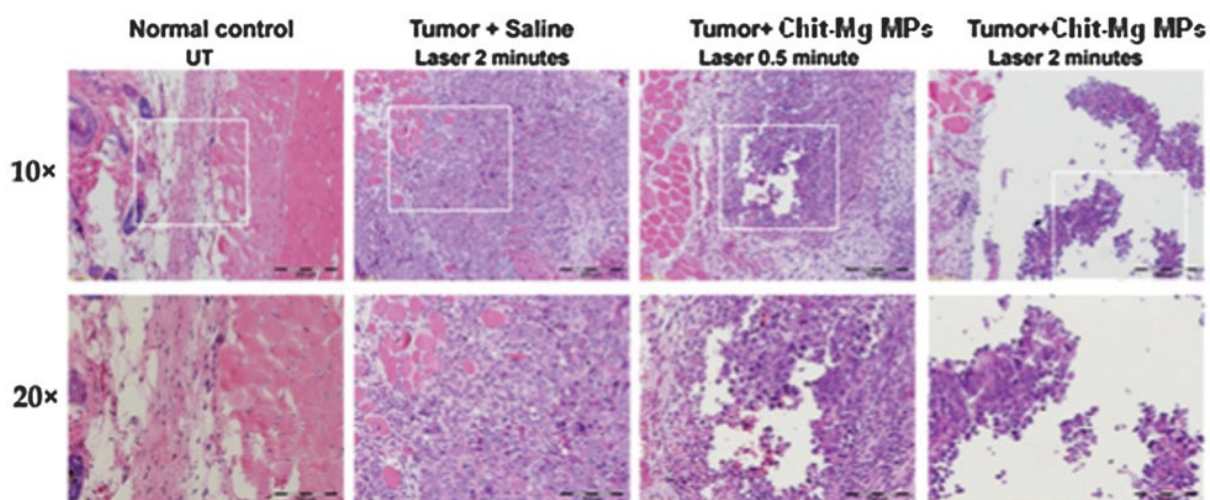


Figure 66. Histological changes in tumour with Chit-Mg MPs and laser exposure.

3.4 Synthesis of multicomponent nanosystems as dual imaging and theranostic agents against cancer

In the previous paragraphs, the therapeutic potential of metallic nanoparticles in nanomedicine applications has been exhaustively described.

In this last paragraph, the investigation about the employment of metallic nanoparticles in the development of imaging tools will be reported.

For this purpose, the intrinsic chemical-physic properties of different metallic nanomaterials have been combined by realizing multicomponent nanosystems suitable for multimodal imaging or theranostic agents. Among the several possible metals, iron and gold are the most used due to their lack of toxicity and intrinsic properties that are well suited for nanomedicine applications. On one hand, the well-known magnetic properties of iron oxide, make these nanoparticles able to realize a magnetic-guided delivery towards the target organ, on the other hand the optical properties of gold nanomaterials can be exploited for both imaging, such as the novel and non-invasive photoacoustic imaging (PAI), and for photothermal therapy (PTT). In according of this, in this project two different multifunctional nanomaterials based on the incorporation of iron oxide and gold nanoparticles in the same nanosystem, have been realized.

The first systems consisted in dumbbell-like gold iron oxide nanoparticles synthesized in a one-step synthesis through the high temperature polyol method. In order to enhance their biocompatibility, the obtained nanoparticles have been coated on the surface using chitosan chains, previously modified by introducing thiol and catechol moieties, able to interact respectively with the gold and iron metallic surfaces.¹⁴⁰ The *in vitro* studies, revealed the theranostic potential of the obtained system, that showed a photothermal behaviour and also capabilities as photoacoustic imaging contrast agents, due to the presence of gold nanoparticles. In addition, the incorporation of iron oxide nanoparticles lead the possibility to use these multifunctional nanomaterials in MRI-PAI dual-imaging applications. For this purpose, in a different work, the second multifunctional systems based on core-shell $\text{Fe}_3\text{O}_4@\text{SiO}_2@\text{Au}$ NPs have been synthesized for *in vivo* active targeting and MRI-PAI dual imaging.¹⁴¹ The first step of the synthesis consisted in the formation of a silica shell on hydrophobic iron oxide nanoparticles, achieved by using the sol-gel and Stober method. The silica shell thickness was controlled by adjusting the methyltriethoxysilane (MTEOS)/ Fe_3O_4 NPs concentration, after that (3-aminopropyl)trimethoxysilane (APTMS) was added to produce a positively charged amino groups onto silica surface. This allowed the

electrostatically coating of the gold seeds, obtained by Duff and Baiker's method, on the obtained $\text{Fe}_3\text{O}_4@\text{SiO}_2$ core-shell system. The formation of an entire shell of gold was performed by a shell growth reaction, in which gold is mildly reduced, led to the multilayered $\text{Fe}_3\text{O}_4@\text{SiO}_2@\text{Au}$ NPs. The obtained nanoparticles were modified on the surface by ligand exchange reaction, in which an organic ligand formed a self-assemble monolayer on the outer gold shell in order confer hydrophobicity properties to the nanoparticles. The obtained hydrophobic nanoparticles were encapsulated in PLGA-b-PEG based polymeric micelles by using the *oil-in-water* single emulsion technique. Finally, the study shows the use of PLGA-b-PEG based polymeric micelles as delivery platform able to incorporate multifunctional metallic structures and also to conjugate on the surface an active targeting moiety, the folic acid. The *in vivo* studies revealed an improving of MRI and PAI signals, due to a higher accumulation in the tumor cells of the folic acid targeted nanosystems compared to not-targeted.

3.4.1. Synthesis of Dumbbell-Like Gold-Iron Oxide Nanoparticles (dl-AuFe NPs) as multifunctional nanosystems

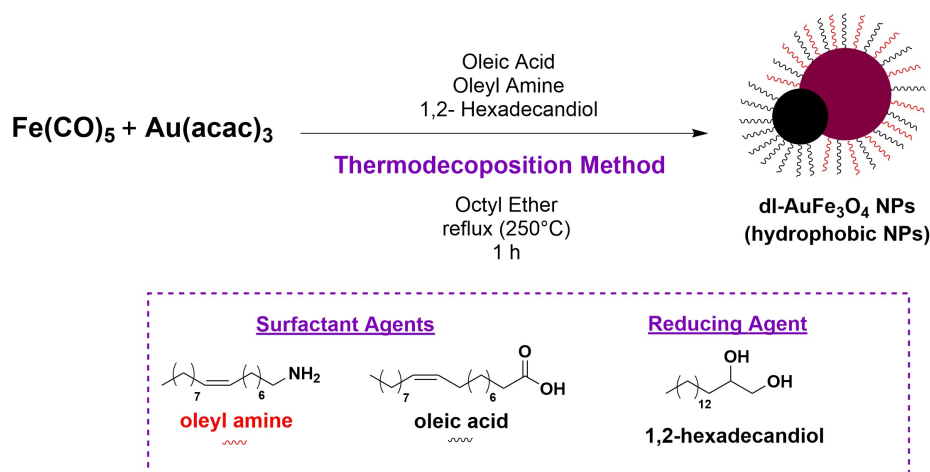
All the procedures and results about the development of multifunctional nanosystems based on the use of dumbbell-like gold-iron oxide nanoparticles, are completely described in:

- The one-step synthesis and surface functionalization of dumbbell-like gold–iron oxide nanoparticles: a chitosan-based nanotheranostic system. *Chem. Commun.* 52, 378–381 (2015).

3.4.1.1 Synthesis of dumbbell-like gold–iron oxide nanoparticles

Nanoparticles characterized by a dumbbell-like (dl) structure consisted in two different functional nanoparticles in intimate contact. In this kind of materials, the interfacial interactions originated from electron transfer across the nanometer contact at the interface of these two nanoparticles can induce new property that is not present in the individual component.

In this project, dumbbell-like gold–iron oxide nanoparticles (dl-Au/Fe₃O₄ NPs) have been obtained through a one-step synthesis. The reaction is based on the high temperature polyol method that involves the reduction of gold acetate and thermal decomposition of iron pentacarbonyl in the presence of the reducing agent (1,2-hexadecandiol), and oleylamine (OLA) and oleic acid (OA) acting as the capping agents (**Scheme 16**).



Scheme 16. Schematic representation of dumbbell-like gold–iron oxide nanoparticles (dl-Au/Fe₃O₄ NPs) synthesis

Briefly, the iron pentacarbonyl and gold acetate were dissolved in dibenzyl ether that contained surfactants oleic acid and oleylamine. Finally, 1,2-hexadecanediol was added as reducing agent to the reaction mixture that was left to homogenize by stirring at room temperature under argon atmosphere for one hour. Then, the temperature was raised to 250°C in 45 minutes and the reaction mixture was refluxed for 1 h to form dl-AuFe₃O₄ NPs. Subsequently, the reaction mixture was cooled to room temperature and the obtained hydrophobic dl-AuFe₃O₄ NPs were precipitated by the addition of ethanol and purified with centrifugation. In order to study the mechanism of the reaction, an accurate investigation on nucleation has been carried out through transmission electron microscopy (TEM).

The results revealed that during the heating, the high difference in the reduction potential between gold and iron leads to a much faster nucleation of gold nanoparticles (Au NPs). Moreover, due to the presence of oleic acid, iron forms a very stable complex (presumably, iron oleate), which slows the iron nucleation and growth. Therefore, the fast reduction of the Au(III) salt enables the Au NPs to be formed first in the reaction mixture. Then, at higher temperatures, the presence of the Au NPs catalyses the decomposition of iron pentacarbonyl and, consequently, heterogeneous nucleation of iron oxide crystals occur at the surface of the formed gold nanoparticles. These nuclei then grow epitaxially and form dl-Au/Fe₃O₄ NPs.

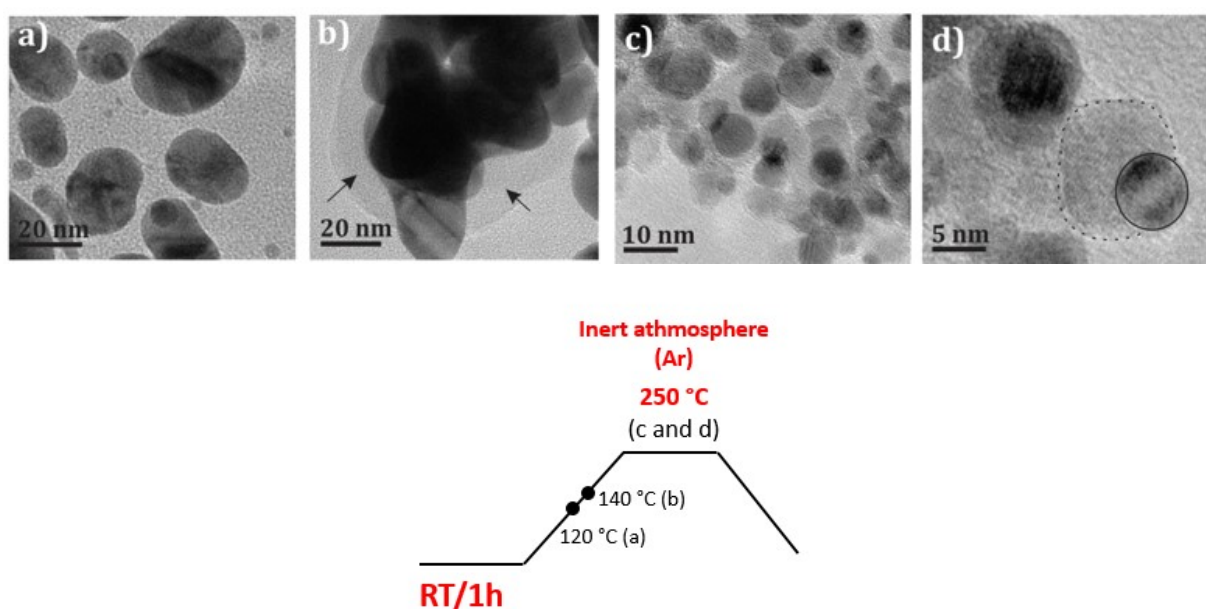


Figure 67. Reaction scheme and the TEM images showing the nucleation at a) 120°C, b) at 140°C, where arrows indicate iron oxide phase and at 250°C/1h with a c) lower and d) higher magnification, where the dashed curve indicate iron oxide phase and a solid line the Au phase.

In particular, the collected TEM images reported in **Figure 67 a and b** showed that the dark phase constituted by the gold nanoparticles is already form at 120 °C, instead of brighter phase, corresponding to iron oxide phase, that is not evident until 140°C. When the temperature reaches 200°C, the crystalline iron oxide material start forming as shell around gold core and as individual nanoparticles, leading to the formation of dl-Au/Fe₃O₄ NPs (**Figure 67 c and d**). In addition, the images showed that no agglomerates of the dl-Au/Fe₃O₄ NPs are found, due to the steric stabilization with the surfactants agents (oleic acid and oleyl amine). TEM characterization allowed measuring the average size of dl-Au/Fe₃O₄ NPs, which resulted be 7 ± 1 nm. Also High-angle annular dark-field (HAADF)-STEM has been performed in order to analyse the interface between individual Au and Fe-oxide NPs at the atomic-resolution (**Figure 68 a and b**). The structural analysis of the corresponding crystal phases confirmed that the bright particle, shown on the left hand-side of the image, corresponds to the Au fcc structure (inorganic crystal structure database “ICSD” 52700) observed in the [101] Au zone axis. On the other hand, the crystal structure of the particle located on the right hand-side of the interface matches perfectly with cubic Fe₃O₄ with the inverse spinel structure (ICSD 65340), which was also observed in the [101] Fe₃O₄ crystallographic projection.

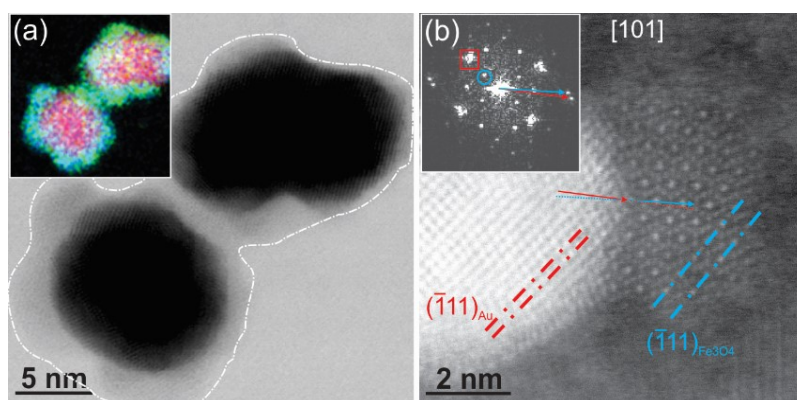


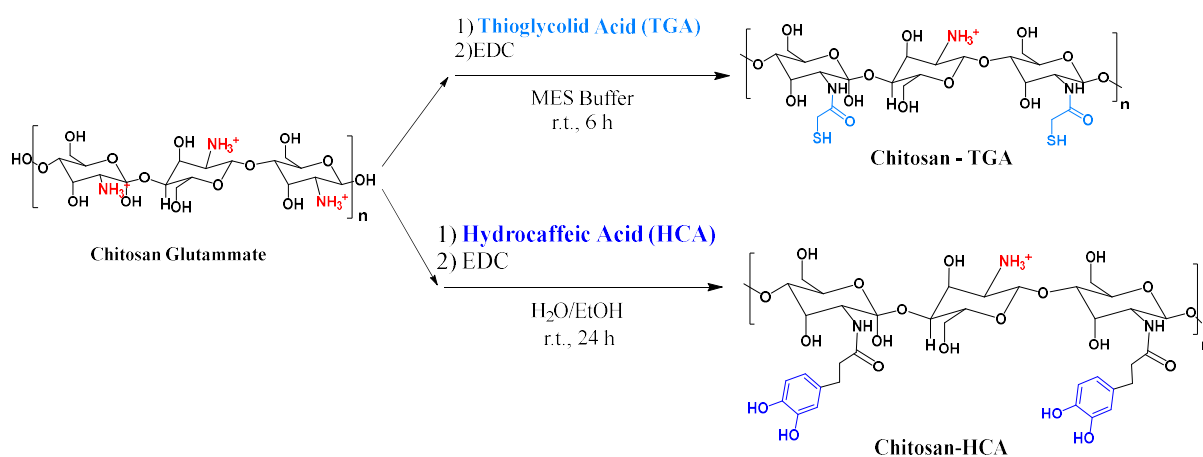
Figure 68. a) High-resolution BF-STEM image of Au and Fe-oxide NPs. The dashed contour lines discriminate the Fe-oxide particles from the support carbon film. The inset shows the corresponding composed elemental map (Au: red, Fe: green and O: blue). (b) Atomic resolution HAADF-STEM image of interface between Au and Fe₃O₄ particles observed in [101] zone axis. The red and blue dashed parallel lines represent the (111) lattice planes for Au and Fe₃O₄ crystal structure, respectively. The corresponding diffraction spots for Au and Fe₃O₄ phase are indicated in the FFT (inset image) by the rectangle and circle, respectively

3.4.1.2. Synthesis of chitosan coated dumbbell-like gold–iron oxide nanoparticles (dl-AuFe₃O₄@Chit)

The capping agents present on the as-synthesized dl-Au/Fe₃O₄ NPs enabled good steric stabilization in organic solvents. However, for biomedical applications nanoparticles soluble in water-based suspensions are required. For this reason, a chemical modification of the dl-Au/Fe₃O₄ NPs surface have been performed by using specially designed chitosan chains. The highly biocompatible chitosan has been selected as coating agent in order to enhance biocompatibility and confer hydrosolubility to the obtained dl-AuFe₃O₄@Chit.

However, in order to form a stable layer on the dl-Au/Fe₃O₄ NPs, the chitosan chains have to be modify by introducing functionalized moieties able to bind the nanoparticles surface, such as catechol groups, characterized by an high affinity for metal oxide surface, and thiol groups able to well interact with noble materials (**paragraph 3.1.2**).

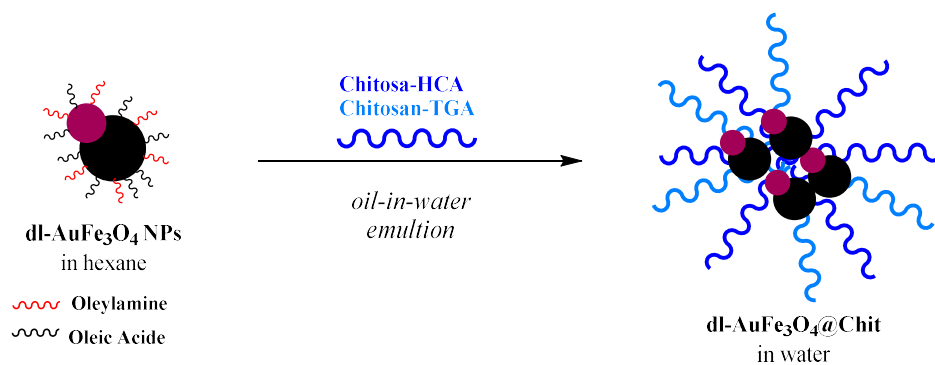
Therefore, the chitosan biopolymer was modified either with thioglycolic acid (TGA), thus introducing thiol groups onto its chain (chitosan-TGA), or with hydrocaffeic acid (HCA), thus introducing catechol moieties (chitosan-HCA). Both reagents were linked to the amine groups of chitosan by the formation of an amide bond exploiting the 1-ethyl-3-(3-dimethylaminopropyl)- carbodiimide (EDC) coupling reagent (**Scheme 17**).



Scheme 17. Schematic representation of the synthesis of thiolated modified chitosan chains (Chitosan – TGA) and catechol modified chitosan chains (Chitosan – HCA).

The anchoring of the two modified chitosan biopolymers onto the NPs surface and consequently nanocarrier formation were performed using a single, one-pot step, through an *oil-in-water* emulsion technique (**Scheme 18**). In this process the hydrophobic dl-Au/Fe₃O₄ NPs dispersed in chloroform were mixed with a water-solution containing both the modified chitosan chains. The two phases were emulsified with a tip probe sonicator, thus ensuring the

ligand exchange reaction on the dl-Au/Fe₃O₄ NPs surface and the formation of a stable nanosystem. Chitosan-TGA and chitosan-HCA alone, as well as a mixture of the two, were all tested in order to establish the best formation of a stable nanosystem. All the obtained nanosystems were easily purified by magnetic decantation taking advantage of the properties of iron-oxide and redispersed in water before analysis: notably, they are perfectly soluble in water at neutral pH (6.5–7).



Scheme 18. Schematic representation of the chitosan coating formation on dl-Au/Fe₃O₄ NPs

The obtained dl-AuFe₃O₄@Chit NPs have been completely characterized by using dynamic light scattering (DLS), z-potential, atomic absorption spectroscopy (AAS), thermogravimetric analysis (TGA), infrared spectroscopy (IR), UV-Vis and transmission electron microscopy (TEM).

The DLS results revealed that dl-Au/Fe₃O₄ NPs embedded in the chitosan-HCA showed a diameter of 140.0 nm but also a high polydispersity index (PDI of 0.560) and a poor zeta potential value of + 0.46 mV. On the other hand, it was not possible to synthesize dl-Au/Fe₃O₄ NPs embedded only in chitosan-TGA since any attempt to do so led to the aggregation of the particles. The best nanosystem was obtained by the use of both chitosan-HCA and chitosan-TGA together (50/50 w/w), which showed a diameter of 121.2 nm, a PDI of 0.212 and zeta potential of +37.0 mV. For this system, the high zeta potential value could be ascribed to the protonated amino group of chitosan, and suggested a better coating of the dl-Au/Fe₃O₄ NPs surface than Chitosan-HCA alone. The stability of this system in physiological medium and at various pH values was also checked, by incubating the obtained nanoparticles in phosphate buffered saline (PBS) at pH 7.4 for two weeks. The DLS results showed a slight increase of the mean hydrodynamic diameter, which moved from 120 nm to 130–140 nm, demonstrating the stability of the particles under the tested conditions. Moreover, the stability of the particles at various pH values was checked by recording the change in the zeta potential value and diameter against pH. The results showed a good stability of the particles between a large interval of pH 3.5 and 9.5.

In particular, the dl-Au/Fe₃O₄ NPs modified with both chitosan-TGA and Chitosan-HCA (denoted from now on as dl-AuFe₃O₄@Chit) showed the best features in terms of size, polydispersity and stability, resulting from the fact that the iron and gold atoms were exposed on the external, reactive surface of the NPs. The presence of chitosan on the nanoparticles has been confirmed with the FT-IR spectrum of dl-Au/Fe₃O₄@Chit in which the signal of chitosan glycosidic linkage (–C–O–C–) appeared at 1150–1040 nm (**Figure 69**).

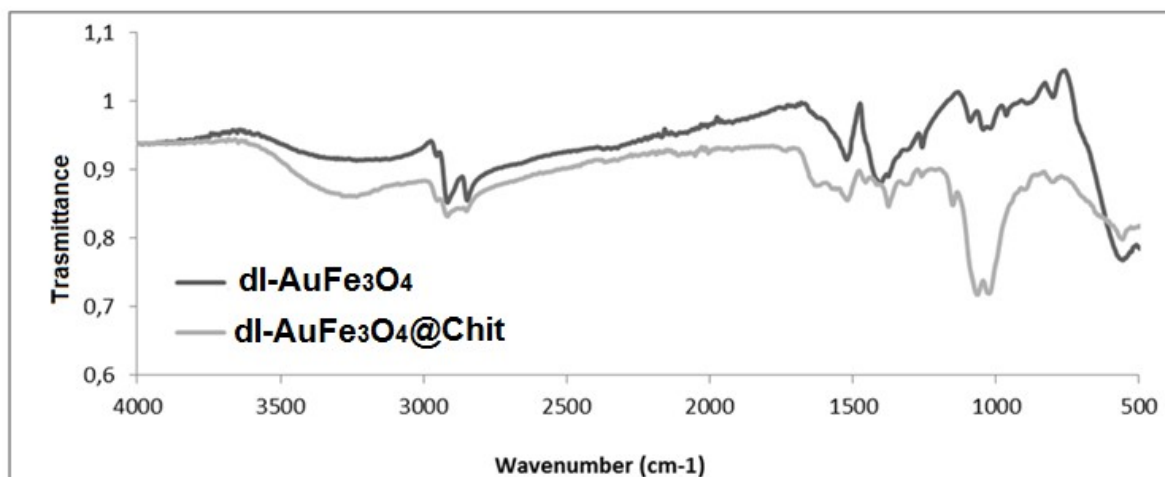


Figure 69. FTIR analysis comparing dl-AuFe₃O₄ NPs and dl-AuFe₃O₄@Chit spectra.

In addition, thermogravimetric analysis showed a typical weight loss (30.3 %) in temperature range between 100 and 270 °C due to the presence of chitosan on the dl-Au/Fe₃O₄ NPs surface. AAS analysis revealed the incorporation of high payloads into the chitosan matrix whereas the concentration was found to be 2.8 mM in iron and 8.0 mM in gold.

The optical properties of dl-Au/Fe₃O₄ NPs, before and after the formation of chitosan coating, have been investigated through UV-Vis spectroscopy (**Figure 70**). The recorded spectra showed the typical maximum absorption peak of gold nanoparticles at 550 nm, which remained unchanged after the surface functionalization.

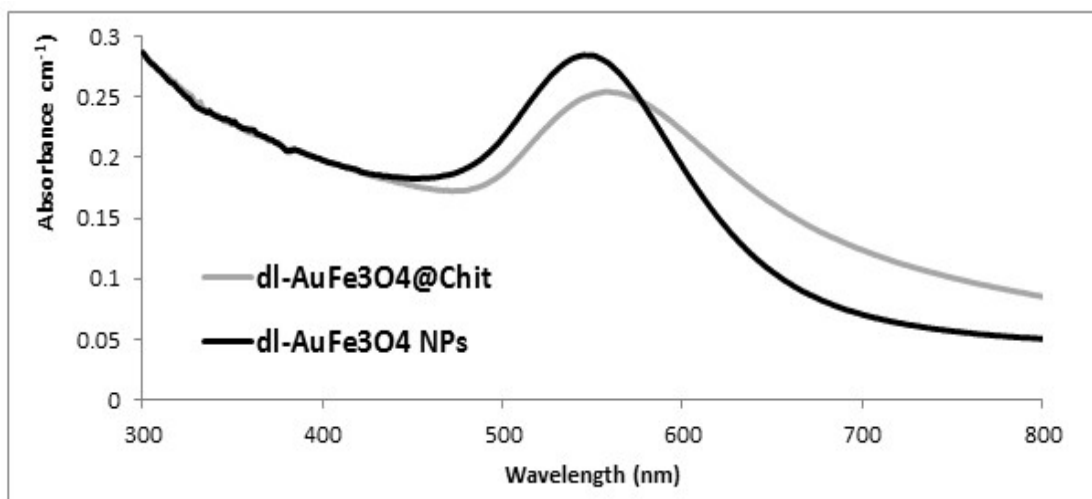


Figure 70. UV-Vis spectra of dl-AuFe₃O₄ NPs and dl-AuFe₃O₄ NPs@Chit

On the other hand, the magnetic properties of the chitosan-coated dl-Au/Fe₃O₄ NPs were measured using a vibrating-sample magnetometer (VSM) at room temperature (298 K) and are presented in **Figure 71**. The results showed that dl-AuFe₃O₄@Chit were characterized by a saturation magnetization value of 4.3 emu/g. This value is lower than for the pure iron oxide nanoparticles of similar size, which is expected due to the dilution of the magnetic phase by the presence of the nonmagnetic components in the sample, Au and chitosan.

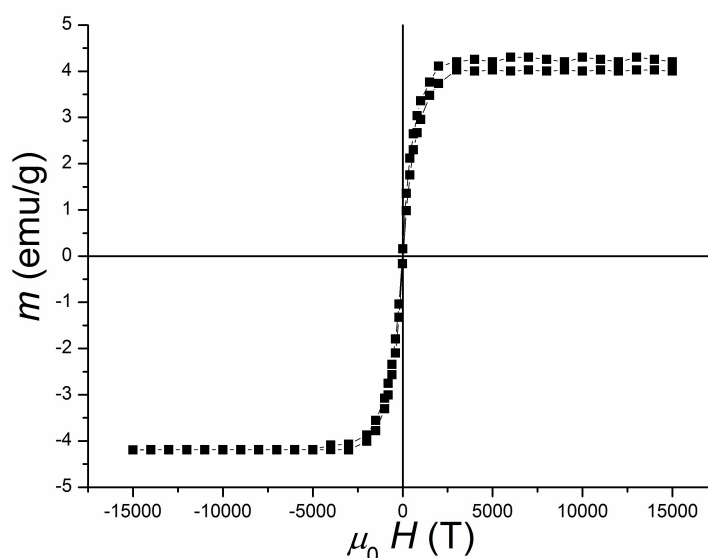


Figure 71. Magnetic properties of the dl-AuFe₃O₄@Chit sample.

In the end, the morphology of the dl-Au/Fe₃O₄@Chit NPs has been investigated with TEM. The collected image (**Figure 72**) showed dl-Au/Fe₃O₄ NPs aggregates in an amorphous matrix

of chitosan. The Au and Fe₃O₄ NPs are shown by arrows, where AuNPs can be observed as objects of a dark contrast, enclosed by the relatively bright Fe-oxide. The measured size of the capsules was in the range of 60 to 150 nm, in good agreement with the results obtained by DLS. Also, no free-standing dl-Au/Fe₃O₄ NPs could be found, which indicates the successful entrapment of all NPs by the chitosan.

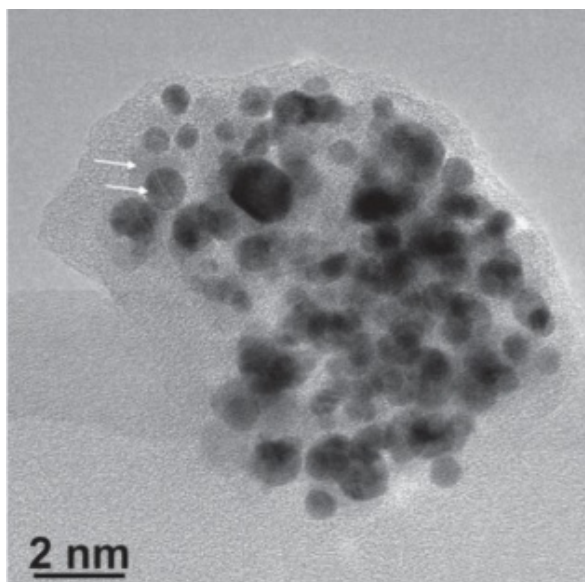


Figure 72. TEM image of dl-Au/Fe₃O₄@Chit

3.4.1.3. *In vitro* biological studies

Once synthesized and fully characterized, the dl-AuFe₃O₄@Chit NPs have been tested in biological studies in order to investigate their potential as dual imaging and theranostic agents in nanomedicine applications. For this purpose, *in vitro* experiments have been performed in collaboration with the department of Molecular Biotechnology and Health Sciences, Center of Excellence for Preclinical Imaging (CEIP) at University of Torino.

First of all, the photothermal heating properties of dl-AuFe₃O₄@Chit have been characterized to investigate the photothermal therapy (PTT) performance of the nanocomposite. The experiment consisted in the formation of aqueous solution in which dl-AuFe₃O₄@Chit NPs have been dissolved at different concentrations (8 mM, 4 mM, and 0.4 mM in gold).

The obtained solution were irradiated for one minute under three different laser intensities (15 W/cm², 5W/cm² and 1 W/cm²) by using a near-infrared fiber coupled diode laser, with a central wavelength of the output radiation is 808 nm and the maximum output power is 25 W.

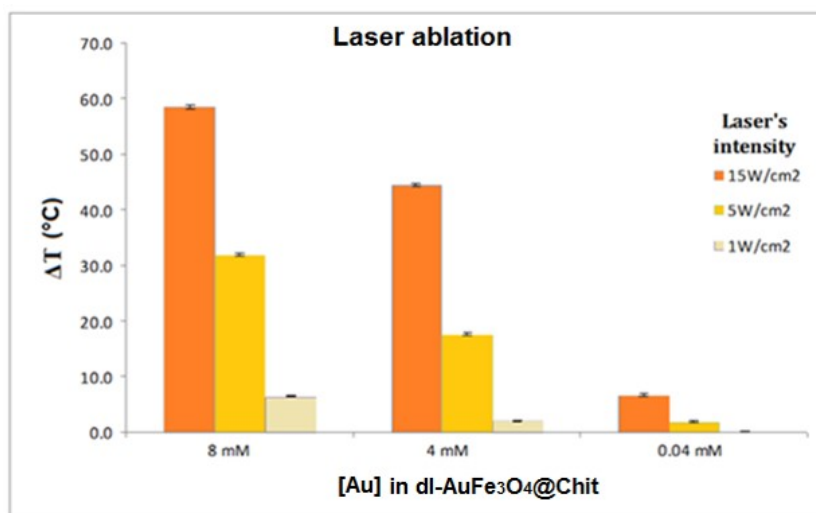


Figure 73. DeltaT induced after irradiation at different laser intensity and gold concentration

The results, shown in **Figure 73**, demonstrated the decrease of the gold concentrations and the laser intensity, led to a decrease of the induced temperature variations. However, the photothermal response still remained detectable up to a concentration of 0.4 mM in gold, with DeltaT of a few degrees. On the other hand, the highest concentration of gold (8 mM) irradiated with 15 W/cm² caused the highest DeltaT, which almost reaches 60 °C, bringing the solution at 85 °C, almost up to the boiling point. These conditions are obviously not necessary for future PTT, where DeltaT of only 5–10 °C is generally requested.

By using a thermocamera, images representing the temperature increase before and after the laser irradiation with 5W/cm² intensity have been collected (**Figure 74**).

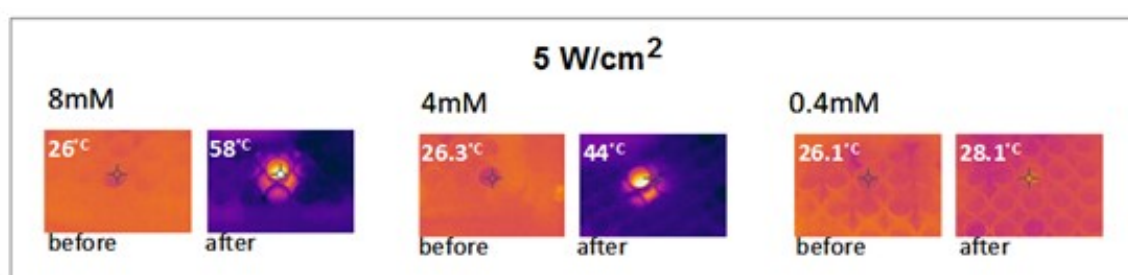


Figure 74. Images taken with the thermocamera before and after laser irradiation

After that, photoacoustic imaging analyses were carried out to determine the PA characteristics of the dl-AuFe₃O₄@Chit NPs. For this purpose, *in vitro* tests have been performed to establish the minimum signal intensity threshold exerted by the nanoparticles as detected by the PA system. However, the maximum absorption peak of dl-AuFe₃O₄ NPs is at

550 nm, the irradiation was carried out at 680 nm since it could be more suitable for the future *in vivo* biomedical applications.

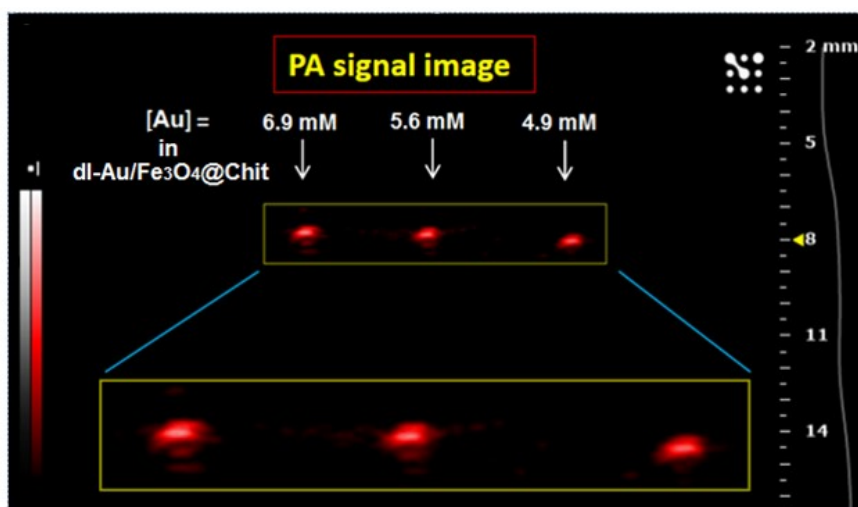


Figure 75. PA intensity signal recorded at 680 nm for dl-AuFe₃O₄@Chit solutions at different concentrations.

As shown in **Figure 75**, samples with a gold concentration in the range of 8.0 mM to 4.9 mM produced signals suitable for PA analyses after an irradiation at 680 nm. Therefore, the collected data suggested that a combination of PTT and PAI imaging of dl-AuFe₃O₄@Chit nanocomposites is possible at a concentration of gold around 4 and 5 mM.

On the other hand, further *in vitro* studies revealed that the magnetic properties of iron oxide nanoparticles constituted the dl-AuFe₃O₄@Chit were not able to reduce the transversal relaxation time (T_2) enough to produce a contrast signal suitable for MRI applications.

This phenomenon can be ascribed to the low saturation magnetization value (4.3 emu/g, **Figure 71**) caused by the dilution of the magnetic phase by the presence of the nonmagnetic components in the sample, gold and chitosan.

3.4.2. Synthesis of a novel magnetic resonance–photoacoustic dual imaging nanosystem based on core–shell Fe₃O₄@SiO₂@Au NPs

All the procedures and results about the development of multifunctional nanosystems based on the use of Core–Shell Fe₃O₄@SiO₂@Au nanoparticles, are completely described in:

- Synthesis of Lipophilic Core–Shell Fe₃O₄@SiO₂@Au Nanoparticles and Polymeric Entrapment into Nanomicelles: A Novel Nanosystem for in Vivo Active Targeting and Magnetic Resonance–Photoacoustic Dual Imaging; *Bioconjugate Chem.* 2017, 28, 1382–1390

3.4.2.1 Synthesis of core–shell iron oxide–silica–gold nanoparticles (Fe₃O₄@SiO₂@Au NPs)

Iron oxide nanoparticles (Fe₃O₄ NPs) have been synthesized by following the reported in literature by *Sun et al.*,¹⁴² based on the thermal decomposition method. In this method, the use of high temperature for the synthesis of magnetic nanoparticles allows a good control of their dimensions, leading to obtain nanoparticles characterized by small dimension and a good low saturation magnetization value, a fundamental requirement for achieving magnetic properties suitable in MRI. The reaction involved the dissolution of iron (III) acetylacetonate in diphenyl ether in presence of surfactant agents, oleic acid and oleylamine, and 1-2 hexadecanediol, as reducing agent. The mixture was heated to reflux (267°C) for 60 minutes under nitrogen atmosphere, to prevent unwanted oxidation. The reaction was then cooled down to room temperature and the formed Fe₃O₄ NPs were purified by magnetic precipitation with excess of cold ethanol, in order to remove the excess of surfactant agents. The surfactant agents used in the synthesis conferred hydrophobic properties to Fe₃O₄ NPs, making them soluble only in organic solvents. The morphology of synthesized nanoparticles were investigated through the transmission electron microscopy (TEM), showing Fe₃O₄ NPs characterized by an average diameter of 7 nm (**Figure 76**).

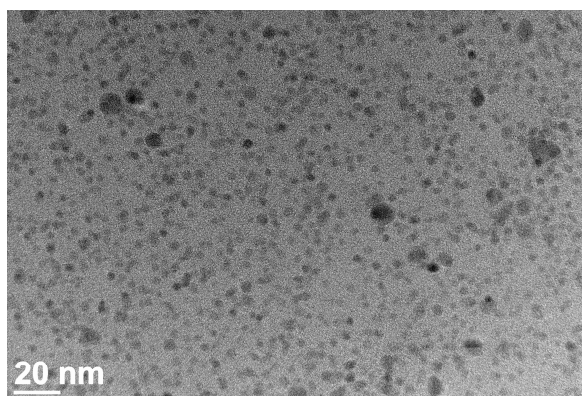
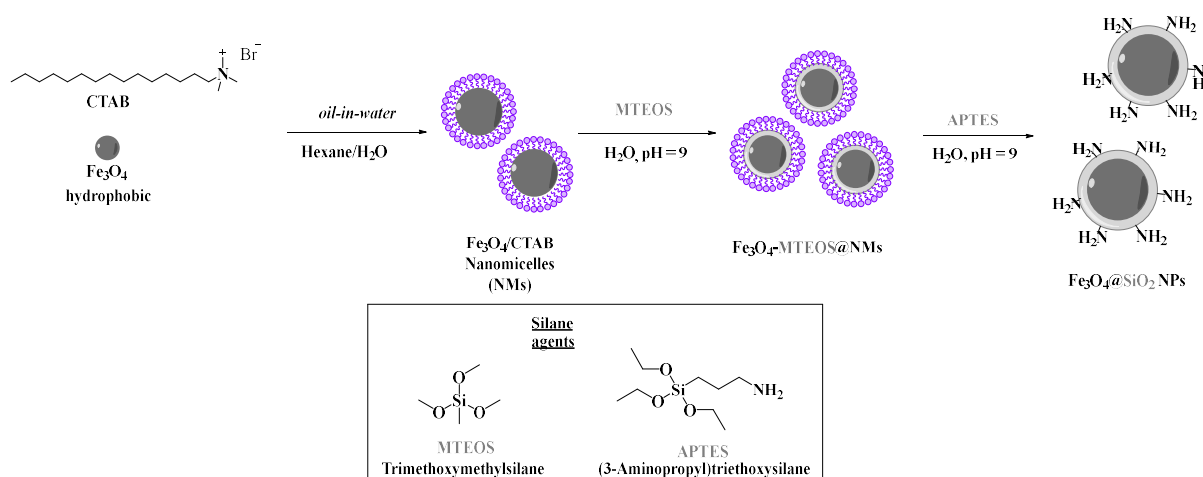


Figure 76. TEM image of Fe₃O₄ NPs

Once synthesized, a silica shell has been formed on Fe₃O₄ nanoparticles surface in order to confer them hydrophilic properties and enhance their stability.

For this purpose, a reaction process based on the reverse microemulsion method and the Stöber method (**paragraph 1.5.2**) has been fine-tuned. The reverse microemulsion method has been used in the first step, which consisted in the entrapment of hydrophobic Fe₃O₄ NPs into micelles constituted of cetyltrimethylammonium bromide (CTAB), a surfactant agent.

The micelles were formed through *oil-in-water* technique. Briefly, a biphasic solution has been formed by adding an organic phase (Fe₃O₄ NPs dispersed in hexane) to a water phase, containing CTAB, in a volume ratio respectively of 1 to 10. The formed solution has been emulsified through a tip-probe sonicator, until obtaining a homogenous phase. After that, the organic solvent has been removed by warming the obtained emulsion at 60°C for 30 minutes. Once formed the Fe₃O₄/CTAB micelles, the silica shell has been formed on the micelles surface by using Stöber method with slightly modifications. This reaction involved two consecutive reactions that essentially govern the growth of silica shell. The first step consisted in the hydrolysis of methyltriethoxysilane (MTEOS) in aqueous solution containing the Fe₃O₄/CTAB and a basic pH, due the addition of a small amount of ammonium solution (28% NH₃ in water) (**Scheme 19**). The alkaline environment catalysed the hydrolysis between the methoxyl groups (-Si-OMe) of MTEOS monomers and the silanol groups (-Si-OH) of other MTEO monomers, leading to the formation of a silica shell on the micelles surface. By adjusting the ratio between the silica precursor (methyltriethoxysilane, MTEOS) and the Fe₃O₄ NPs concentration, it is possible to control the thickness of a silica shell.



Scheme 19. Representative scheme of $\text{Fe}_3\text{O}_4@\text{SiO}_2$ NPs synthesis

In the second step, 3-aminopropyl-methoxysilane (APTMS) has been added to the reaction mixture, taking place in the hydrolysis reaction led to the formation of a silica-shell characterized by amino group on the surface (**Scheme 19**). The reaction was left under magnetic stirring for 3 days at 30°C. After that, $\text{Fe}_3\text{O}_4@\text{SiO}_2$ NPs were purified by centrifugation (6000 rpm) in water for one hour, and the collected precipitate has been washed twice with clean water. Because of the cytotoxicity of CTAB, the obtained $\text{Fe}_3\text{O}_4@\text{SiO}_2$ NPs were stirred for 30 minutes in a mixture of ethanol and acetic acid 95/5 (v/v) in order to remove the surfactant molecules from the formed micelles. Indeed, once hydrolysis reactions of the silica precursors occurred on the $\text{Fe}_3\text{O}_4/\text{CTAB}$ micelles, the CTAB molecules were not necessary to maintain the nanoparticles structure and can be removed without affecting the stability of the nanosystem.

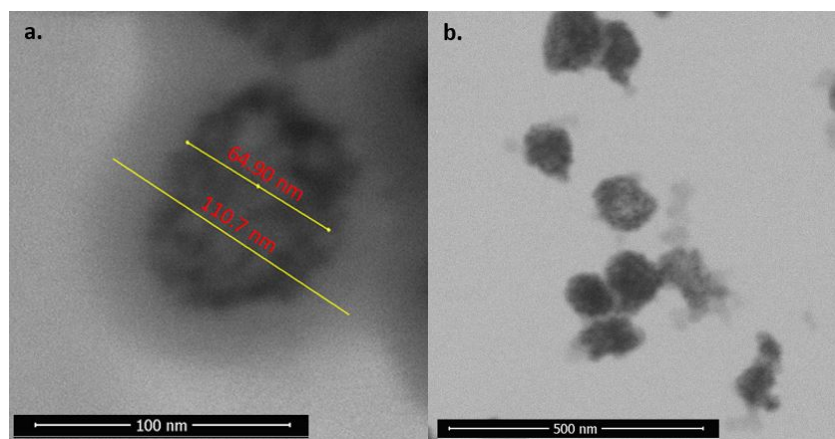
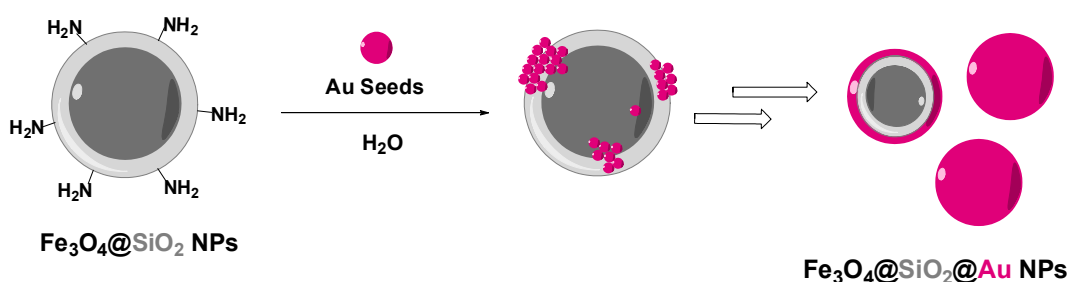


Figure 77. (a) TEM image of $\text{Fe}_3\text{O}_4@\text{SiO}_2$ (scale bar 100 nm) and (b) $\text{Fe}_3\text{O}_4@\text{SiO}_2$ NPs (scale bar 500 nm).

Once removed the CTAB, the $\text{Fe}_3\text{O}_4@\text{SiO}_2$ were further purified through centrifugation, by washing several times the collected precipitate with water and ethanol. Then the $\text{Fe}_3\text{O}_4@\text{SiO}_2$ NPs morphology has been investigated with transmission electron microscopy (TEM, **Figure 77**). TEM images, shown in **Figure 77**, confirmed the obtainment of $\text{Fe}_3\text{O}_4@\text{SiO}_2$ NPs, characterized by an average diameter of 100 nm and a silica shell thickness about 20 nm. On the other hand, dynamic light scattering analysis performed on $\text{Fe}_3\text{O}_4@\text{SiO}_2$ NPs, revealing a hydrodynamic diameter of 180 ± 3 nm and a Zeta potential of +25 mV. As expected, the use of APTMS in the core-shell nanoparticles synthesis allowed obtaining $\text{Fe}_3\text{O}_4@\text{SiO}_2$ characterized by amino groups on the surface, which make them a positive zeta potential. This feature assumed great importance in the formation of gold shell on the synthesized $\text{Fe}_3\text{O}_4@\text{SiO}_2$ NPs surface. Indeed, this step involved the electrostatically coating formation of negatively charged gold seeds (small gold NPs of 1–3 nm in size) on the positive charged $\text{Fe}_3\text{O}_4@\text{SiO}_2$ NPs surface. The gold seeds were synthesized with the Duff and Baiker's method, consisting in the reduction of chloroauric acid (HAuCl_4) with tetrakis-(hydroxymethyl)-phosphonium chloride (THPC).¹⁴³ After the coating of $\text{Fe}_3\text{O}_4@\text{SiO}_2$ NPs surface with the gold seeds, the formation of an entire shell of gold have been formed through shell growth reaction, in which gold was mildly reduced, leading to the multilayered $\text{Fe}_3\text{O}_4@\text{SiO}_2@\text{Au}$ NPs (**Scheme 20**).



Scheme 20. Representative scheme of the gold shell formation on of $\text{Fe}_3\text{O}_4@\text{SiO}_2@\text{Au}$ NPs

The obtained particles were fully characterized by dynamic light scattering (DLS) and showed a hydrodynamic diameter of 222 ± 1.5 nm with a PDI of 0.251 ± 0.4 and a Zeta potential of -32 mV. In the meantime, TEM images confirmed the successful of gold shell formation indicated by the black spots formed on $\text{Fe}_3\text{O}_4@\text{SiO}_2$ NPs surface (**Figure 80**).

The different results obtained by DLS and TEM characterizations for both $\text{Fe}_3\text{O}_4@\text{SiO}_2$ NPs and $\text{Fe}_3\text{O}_4@\text{SiO}_2@\text{Au}$ NPs, can be ascribed to the difference between the hydrodynamic

diameter of the nanoparticles dissolved in water and their real size, but also to a slight particle aggregation due to the lacking of a steric stabilizer on their surface.

Energy-dispersive X-ray spectroscopy (EDX) mapping analysis showed a typical profile of core-shell systems, confirmed the presence of the three different shells with iron in the core, silica in the middle, and gold onto the surface (**Figure 78**). Metal concentrations were calculated through atomic absorption analysis (AAS), revealing an iron and gold concentration of 4.1 and 12.3 mM, respectively.

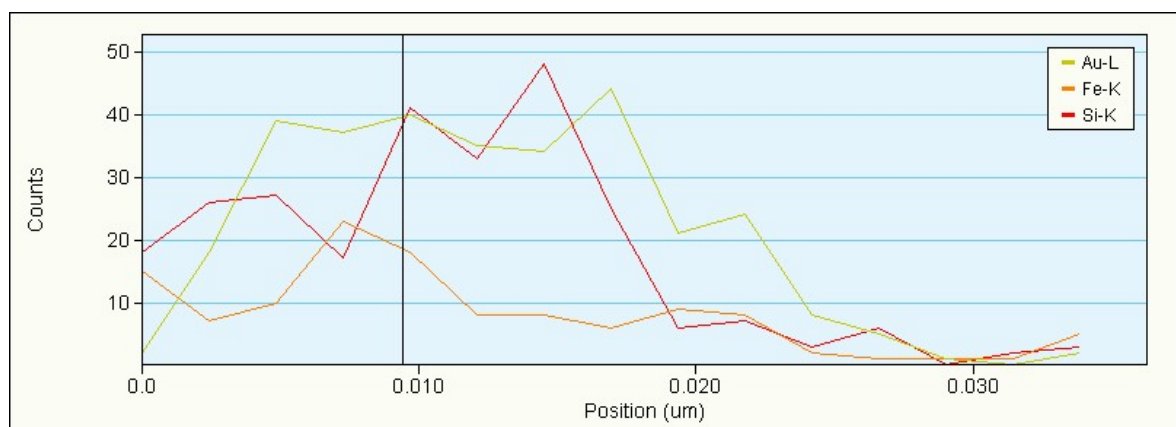


Figure 78. EDX mapping of Fe₃O₄@SiO₂@Au NPs.

3.4.2.2 Surface modification Fe₃O₄@SiO₂@Au NPs and entrapment into polymeric nanoparticles

The lacking of a steric stabilizer on the surface Fe₃O₄@SiO₂@Au NPs make them inclined to form aggregates. In order to improve their stability, a self-assembled monolayer (SAM) has been formed on the core-shell nanosystems by using the organic molecule ethyl 11-(4-mercaptobenzamido)undecanoate (**ligand 1**) (**paragraph 3.1.1**).

The SAM has been performed through the ligand exchange reaction; briefly, an organic solution, obtained by dissolving the ligand **1** in ethanol, has been added to a water solution containing the Fe₃O₄@SiO₂@Au NPs. The reaction mixture has been stirred at room temperature for 12 hours. After this time, the Fe₃O₄@SiO₂@Au-**1** have been purified with centrifugation method, by washing the precipitate with ethanol (2 times). The obtained Fe₃O₄@SiO₂@Au-**1** exhibited a good solubility in the most common organic solvents, especially chloroform and dichloromethane, as demonstration of the successful of the ligand exchange reaction, which was further confirmed by thermogravimetric analysis.

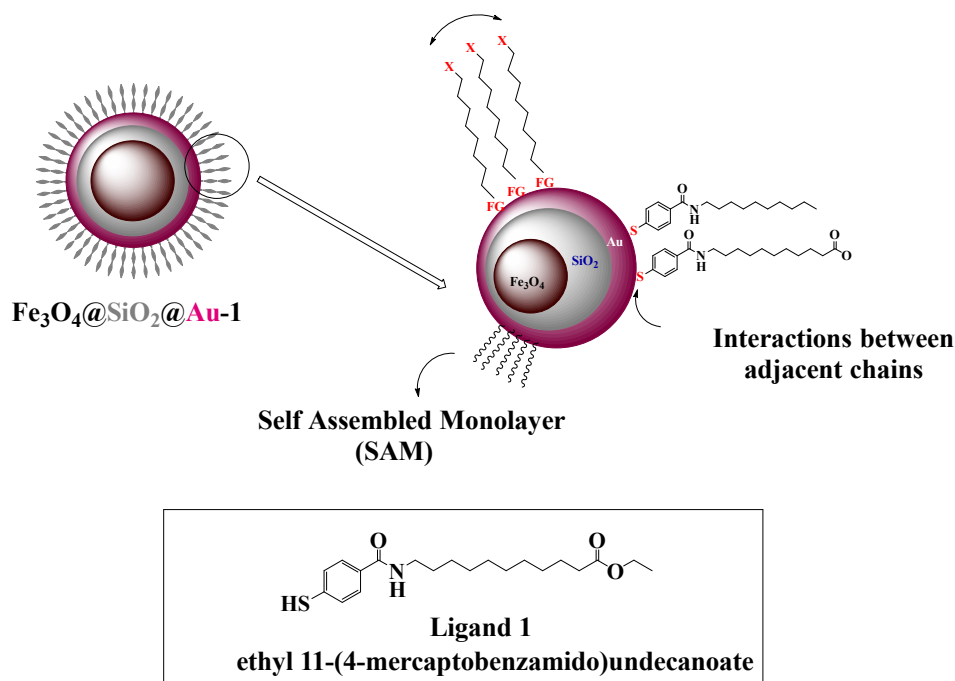


Figure 79. Self Assembled Monolayer of ligand 1 on $\text{Fe}_3\text{O}_4@\text{SiO}_2@\text{Au}$ NPs

In order to confer stability in biological environment, the $\text{Fe}_3\text{O}_4@\text{SiO}_2@\text{Au}$ -1 have been entrapped in polymeric micelles by using the *oil-in-water* technique.

For this purpose, the well-known poly(lactic-co-glycolic)-block-polyethylene glycol (PLGA-b-PEG) has been selected. In particular, in this case, PLGA-b-PEG-NH₂ was used due to the amino functional groups required for the subsequent surface functionalization with the active targeting (**paragraph 3.1.3**).

For the synthesis of the $\text{Fe}_3\text{O}_4@\text{SiO}_2@\text{Au}@$ PMs, the procedure consisted in the dissolution of PLGA-b-PEG-NH₂ into chloroform solution containing $\text{Fe}_3\text{O}_4@\text{SiO}_2@\text{Au}$ -1. Once prepared the organic solution, an aqueous phase containing a surfactant (sodium cholate) was then slowly added on the top of this, led to the formation of a biphasic solution that underwent to sonication with a trip probe sonicator in order to furnish the necessary energy to the system for the self-assembling process. After a short time (1-2 minutes), the two phases resulted completely mixed, and the polymeric micelles have been obtained. The organic solvent remained entrapped in the lipophilic core was removed by evaporation under vacuum and the resulting aqueous solution was purified with centrifuge in order to eliminate the small unreacted molecules. The DLS characterization of the $\text{Fe}_3\text{O}_4@\text{SiO}_2@\text{Au}@$ PMs particles indicated a hydrodynamic diameter of 157 ± 0.4 nm, a PDI value of 0.300 ± 0.3 , and a zeta potential of -14 mV, while TEM analysis showed the maintenance of the nanoparticles morphology and their confinement into an organic matrix (**Figure 79**).

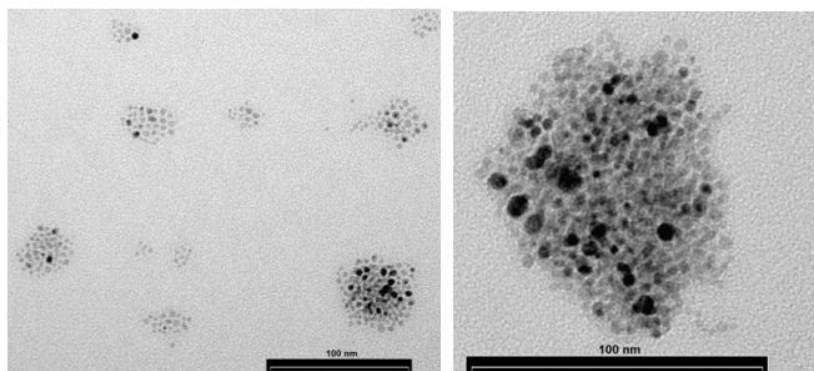


Figure 80. TEM image of $\text{Fe}_3\text{O}_4@\text{SiO}_2@\text{Au}@PMs$ (scale bar 100 nm).

In addition, UV-vis analysis confirmed that the optical proprieties of gold were retained after polymeric entrapment (**Figures 81**).

In the last preparative step, an active-targeting vector has been chemically conjugated on $\text{Fe}_3\text{O}_4@\text{SiO}_2@\text{Au}@PMs$ surface. For this purpose, folic acid (FA) was chosen as targeting agent due to its high affinity to the folate receptor, which is a membrane-anchored protein over-expressed on many cancer cells. The conjugation of folic acid was pursued upon the activation of its carboxylic group through EDC Chemistry, making it suitable for the reaction with the amine groups at the polymeric nanoparticles surface (**Scheme 21**). The so-obtained $\text{Fe}_3\text{O}_4@\text{SiO}_2@\text{Au}@PMs-FA$ were purified and characterized by DLS, atomic absorption spectroscopy (AAS), and UV-vis. DLS analysis showed that the conjugation with FA did not significantly affect the diameter of the particles (165 ± 0.3 versus 157 ± 0.4 nm) as well as the polydispersion index that was unchanged.

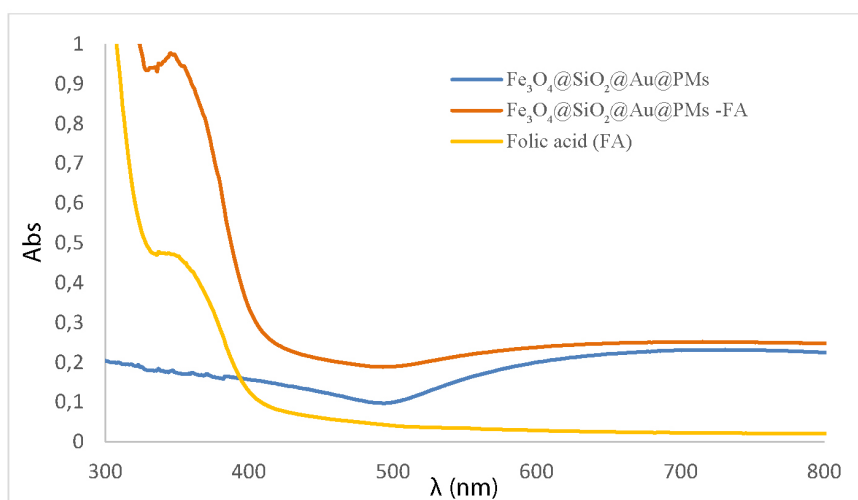
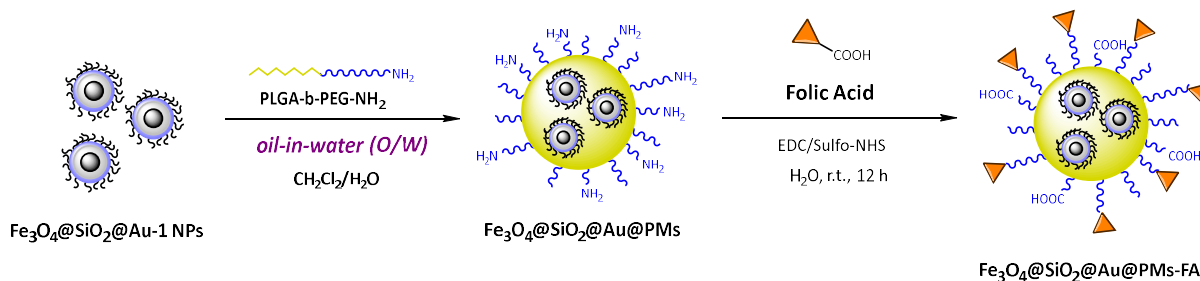


Figure 81. UV-Vis characterization of $\text{Fe}_3\text{O}_4@\text{SiO}_2@\text{Au}@PMs-FA$

As expected, the Zeta potential of the FA-conjugated particles decreased (from -14 to -23 mV) due to the free carboxylate group on the FA molecule. AAS analysis indicated that the amount of iron and gold in the micelles was 0.1 and 1.2 mM, respectively.



Scheme 21. Representation of the entrapment of hydrophobic core-shell $\text{Fe}_3\text{O}_4@SiO_2@Au-1$ into polymeric micelles.

3.4.2.3. *In vitro* and *in vivo* biological studies

Photoacoustic imaging (PAI) represents an emerging diagnostic method with non-invasive and non-ionizing properties with ease of applicability in clinical setups (**paragraph 1.4.1**). The combination of magnetic resonance imaging (MRI) with PAI, can offer some mutual benefits, like the possibility to detect the multimodal nanoparticles overcoming the depth and resolution limits of PAI and improving the relatively poor sensitivity of MRI in contrast agent detection (**paragraph 1.4.4**). MRI-PAI dual detectable nanoparticles are of particular interest in the theranostic field. For this reason, the potential as bimodal MRI-PAI agent of the so-obtained $\text{Fe}_3\text{O}_4@SiO_2@Au@PMs-FA$ and the targetable ability of folic acid has been investigated through *in vitro* and *in vivo* biological experiments.

The *in vitro* studies have been carried out in collaboration with the Institute for Maternal and Child Health- IRCCS “Burlo Garofolo” at Trieste (Italy). In order to assess the biocompatibility of the developed nanosystems, cytotoxicity assays have been carried out on two human carcinoma cell lines characterized by a high expression of folate receptors (ovarian (IGROV) and cervical (HeLa) carcinomas) and a healthy cell line of primary human fibroblasts. The results revealed that the $\text{Fe}_3\text{O}_4@SiO_2@Au@PMs-FA$ did not show any significant cytotoxicity to HeLa cells at different nanoparticles concentrations (0.5 , 2.5 , 5 , and 10 $\mu\text{g/mL}$) after 24 hours. However, IGROV cells were shown to be more sensitive than HeLa cells, and, upon increasing nanoparticles concentration above 5 $\mu\text{g/mL}$, a modest statistically significant decrease was noticed in the relative cell viability. On the other hand, fibroblasts (HF_s) were found to be more sensitive to $\text{Fe}_3\text{O}_4@SiO_2@Au@PMs-FA$ (**Figure 82**).

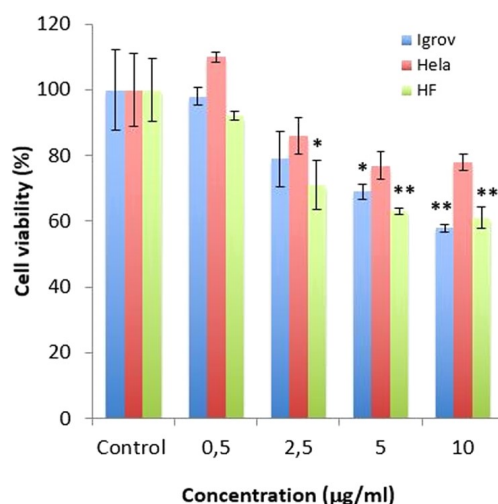


Figure 82. In vitro cytotoxicity of nanoparticles at different concentration on IGROV, HeLa, and HF cells after incubation for 24 h. Note that cell viability was evaluated by MTT assay. Results are expressed as means \pm SD of experiments performed in triplicate. Significance: *, $p < 0.05$ and **, $p < 0.01$. Abbreviations: MTT, 3-(4,5-dimethylthiazol-2-yl)-2,5-diphenyltetrazolium bromide; HF, human fibroblast.

In order to study the targetable ability of folic acid, cellular uptake has been investigated through the fluorescent microscopy. For this purpose, a fluorescein dye (fluorescein-NHS) has been linked on $\text{Fe}_3\text{O}_4@\text{SiO}_2@\text{Au}@PMs$, in order to trace the nanoparticles in the cells with fluorescent microscopy. **Figure 83** shows fluorescence images of IGROV cells after incubation in media containing 10 $\mu\text{g/mL}$ of $\text{Fe}_3\text{O}_4@\text{SiO}_2@\text{Au}@PMs\text{-FA/fluor}$. It can be seen that green fluorescence appears to be localized inside the cell, suggesting that the cells are effective in taking up $\text{Fe}_3\text{O}_4@\text{SiO}_2@\text{Au}@PMs\text{-FA}$ (**Figure 83**).

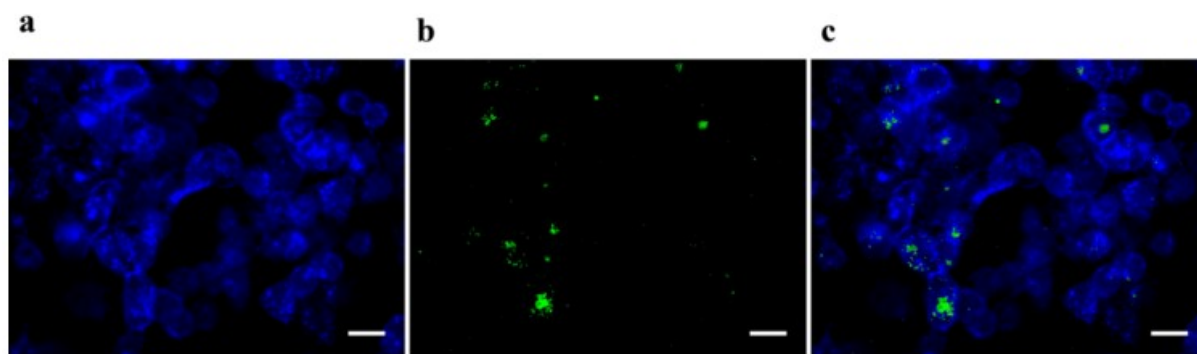


Figure 83. IGROV cells were incubated with $\text{Fe}_3\text{O}_4@\text{SiO}_2@\text{Au}@PMs\text{-FA}$ (10 $\mu\text{g/mL}$) at 37 $^\circ\text{C}$ for 24 h to allow nanoparticle cell internalization before microscopy analysis. Representative cell images are shown. DAPI and Alexa Fluor 350 staining were carried out to visualize nuclei and cell membranes, which appear in blue, while fluorescein-labeled nanoparticles appear in green. (a) DAPI and Alexa Fluor 350 staining; (b) green fluorescence emission; (c) merged images (bar: 20 μm).

After that, Fe₃O₄@SiO₂@Au@PMs-FA have been tested *in vivo* as MRI and PAI agents in collaboration with Molecular and Preclinical Imaging Centers at the Department of Molecular Biotechnology and Healthy Sciences of the University of Torino.

First, MRI *in vivo* experiments were carried out by administrating through intravenous injection the Fe₃O₄@SiO₂@Au@PMs and its folate-targeted form, in mice bearing the IGROV subcutaneous xenograft. Then, T_{2w} MR images were acquired before (pre) and 1, 4, and 24 h after the treatment at a magnetic field strength of 1 ton.

MR images were analysed to calculate the relative signal intensity (rSI) in liver, spleen, kidneys, and tumour according to the following equation:

$$r = \frac{SI_{(\text{organ})} - SI_{(\text{muscle})}}{SI_{(\text{organ})} + SI_{(\text{muscle})}}$$

where SI_(organ) is the average value obtained from three measurements of each organ, and SI_(muscle) is the corresponding value measured on the paraspinal muscle.

Next, the percent signal intensity reduction was calculated by comparing the rSI_(organ) before and after the injection of the agents.

The results reported in **Figure 84**, showed the T_{2w} MR images acquired before and after the treatments, revealing that the targeted nanoparticles induced a tumour contrast signal that reached the maximum value 4 hours post-injection. In particular, the fraction of contrast-enhanced pixels in the tumour 4 hours after the nanoparticles injection was almost three-fold higher for Fe₃O₄@SiO₂@Au@PMs-FA than the control system (27.5% versus 10%).

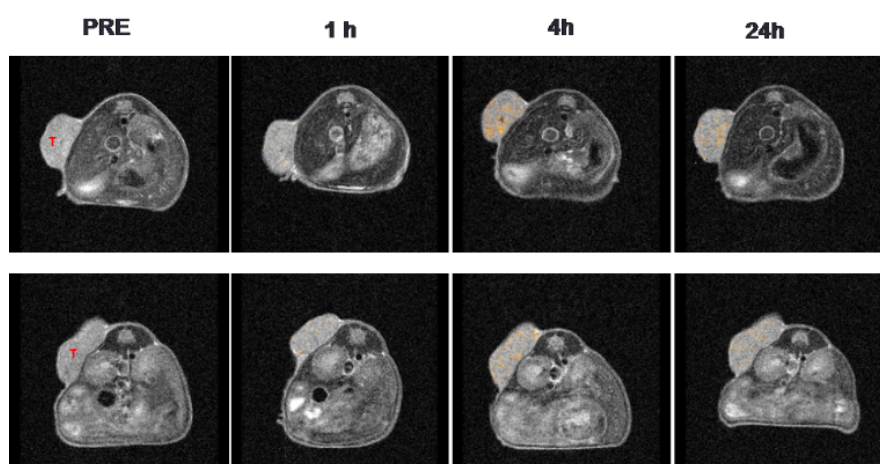


Figure 84. T_{2w} MR images acquired at 1T before, and 1 h, 4 h and 24h after the intravenous injection of Fe₃O₄@SiO₂@Au@PMs-FA (upper panel) or Fe₃O₄@SiO₂@Au@PMs (lower panel) at the dose of 0.17 mg Fe/kg bw. The orange-coloured spots correspond to the pixels with a statistically significant T₂ contrast enhancement.

On the other hand, PAI *in vivo* experiments have been performed by injecting NPs systemically in the tail vein of the tumour-bearing mice at a gold concentration of 8.0 mg Au/kg. PA images of the tumour upon excitation at 860 nm were acquired 4 hours post-injection, when the particles showed the maximum MRI T2 contrast. The results confirmed the targetable ability of folic acid, showing the increased accumulation of the FA-targeted system in the tumour lesion 4 hours after their injection (**Figure 85**).

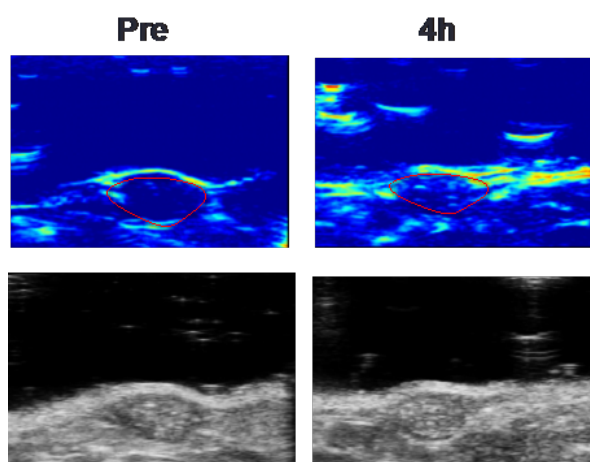


Figure 85. Representative PA (upper) and US (lower) images of the tumour xenograft acquired before (pre) and 4 h after the injection of $\text{Fe}_3\text{O}_4@\text{SiO}_2@\text{Au}@P\text{Ms-FA}$. PA excitation wavelength was set at 860 nm.

4. Conclusions

In conclusion, the progresses in nanotechnology led to the different challenges and opportunities in nanomedicine.

In this project, the potential of polymeric nanoparticles as drug delivery systems have been deeply investigated. The biocompatibility and biodegradability of PLGA-b-PEG allowed the formations of polymeric nanoparticles or nanomicelles characterized by morphological properties suitable for drug delivery applications. In addition, the possibility to encapsulate lipophilic and/or hydrophilic agents into the inner core of the formed polymeric nanoparticles, led to the development of multifunctional nanosystems able to deliver *in vivo* therapeutics to tumours when conjugated to specific targeting agents.

Taking advantages of these properties, PLGA-b-PEG based nanoparticles have been studied as drug delivery systems in the treatment of glioblastoma multiforme. As reported in the previous paragraphs, the conjugation of chlorotoxin peptide as active targeting on the developed polymeric nanoparticles provide the *proof-of-concept* of the therapeutic validity of a combination strategy based on radiation therapy and chlorotoxin-targeted polymeric nanovectors.

In addition, the entrapment of chemotherapy drug in polymeric nanoparticles can achieve its antitumor efficacy enhancement, as demonstrated with the very promising but low water-soluble drug NVP-BEZ235. Indeed, after the encapsulation of NVP-BEZ235 in polymeric nanoparticles, the obtained systems (NVP-BEZ235@PNPs) showed a strongly enhancement of its bioavailability with a 1000-fold augmented cytotoxicity as compared to the free drug. Once synthesized, NVP-BEZ235@PNPs have been functionalized on the surface with the Gint4.T aptamer, able to specifically recognize platelet-derived growth factor receptor β overexpressed on the blood-brain-barrier (BBB) and to cross the BBB after the interaction with these receptors. The results showed the ability of the developed nanovectors to specifically target GBM tumours and demonstrated for the first time the *in vivo* specific GBM tumour uptake on orthotopic cancer-bearing mice after intravenously administration.

Simultaneously with the investigation of the potential of polymeric nanoparticles as drug delivery systems, a deep investigation on the fascinating features of metallic nanoparticles have been carried out in order to develop novel multimodality imaging tools and theranostic systems for nanomedicine applications.

Accordingly, several kinds of metallic nanoparticles have been successfully designed, synthesized, modified on the surface and characterized, such as silver nanoparticles, gold

nanorods, iron oxide nanoparticles, magnesium nanoparticles, and also multifunctional nanomaterials as dumbbell-like gold iron oxide nanoparticles and iron-gold core-shell systems have been obtained as well. In addition, taking advantage of the features of the developed nanomaterials, different diagnostic techniques have been investigated in order to find the suitable field of nanomedicine applications.

Optical properties of gold nanomaterials have been employed for the development of photothermal therapy agents as well as photoacoustic imaging contrast agents. For this purpose, one pot-synthesis of chitosan coated magnesium nanoparticle has been fine-tuned in order to obtain nanoparticles characterized by high biocompatibility and unexpected photothermal behaviour. Also, gold nanorods have been investigated as photothermal agents showed the possibility to easily deliver and irradiate the only nanosystem in the site of interest giving promising results in terms of destruction of tumour tissue without affecting surrounding healthy.

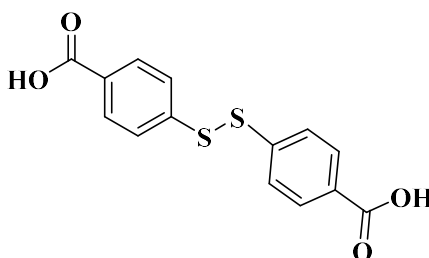
At the end, the good results achieved by using polymeric nanoparticles as drug delivery systems together with the potential of metallic nanoparticles as diagnostic tools, led to the development of iron/silica/gold core-shell nanoparticles and their subsequent surface functionalization and entrapment into polymeric micelles. The developed systems showed great potential as PAI/MRI dual imaging agents in the treatment of ovarian cancer using folic acid targeting agent *in vivo* on tumour-bearing mice.

In some of the mentioned papers, we demonstrated the advantages that can be achieved through the well-fashioned, highly selective and specifically designed surface chemistry modifications of these nanostructures. The *in vitro* and *in vivo* biological assessments revealed the potential in nanomedicine applications of the realized nanosystems and encouraged to carry on the aim of this research. By improving the knowledge of tumour biology, it will be possible to develop drug delivery and theranostic systems able to overcome big biological hindrances and to deal with crucial biological mechanism in order to improve efficacy of current therapies.

5. Experimental section

5.1 Synthesis of ethyl 12-(4-mercaptobenzamido)dodecanoate (**ligand 1**)

5.1.1 Synthesis of 4,4'-disulfanediylidibenzoic acid



To a stirred solution of 4-mercaptobenzoic acid (1.00 g, 6.48 mmol) in ethanol (20 mL) a saturated solution of iodine in ethanol (3.35 mL) was added drop wise. The reaction was left to react for 3 hours at room temperature then the precipitate was filtered and washed with cold ethanol (3 x10 mL). 0.87 g (yield 87%) of product were recovered in the form of a white powder.

Data:

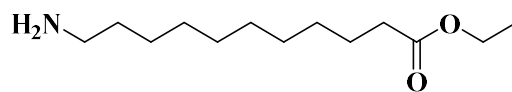
m.p.: 346 - 348 °C;

¹H NMR (300 MHz, DMSO-d₆): δ= 13.0 (bs, 2H), 8.0 (d, 2H), 7.7 (d, 2H) ppm;

¹³C NMR (75 MHz, DMSO-d₆): δ= 166.6, 140.8, 130.3, 129.7, 126.1 ppm;

GC-MS ESI : ES⁻ 305 (M⁻¹).

5.1.2 Synthesis of ethyl 11-aminododecanoate



To a suspension of 12-aminododecanoic acid (3.0 g, 13.2 mmol) in ethanol (50 mL) was added slowly concentrate sulfuric acid (0.8 mL). The mixture was refluxed for 18 h, cooled to room temperature, and the solvent was evaporated under reduced pressure. The crude was suspended in ethyl acetate (200 mL), washed with 1 M ammonia aqueous solution (3 x 50 mL). The organic layer was dried over MgSO₄ and evaporated to yield 3.2 g (98 %) of product as a white solid.

Data:

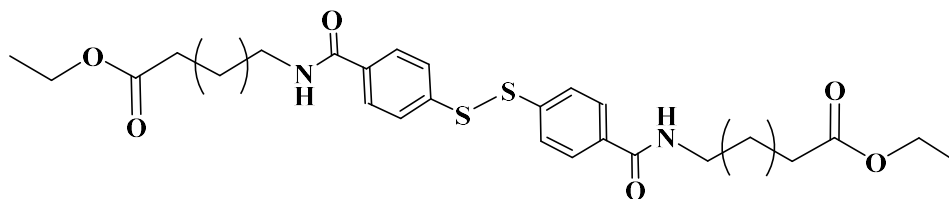
m.p. = 56-58 °C;

¹H NMR (300 MHz, DMSO-d₆): δ= 1.15 (t, 3H), 1.22 (s, 12H), 1.31 (bs, 2H), 1.48 (bs, 2H), 2.24 (bs, 2H), 2.86 (d, 2H), 4.02 (q, 2H) ppm;

¹³C NMR (75 MHz, CDCl₃): δ= 173.8, 60.0, 41.3, 34.3, 29.4, 29.3, 29.2, 29.1, 26.8, 24.9, 14.2 ppm;

GC-MS ESI: 244 (M+1).

5.1.3 Synthesis of bis-ethyl 11-(4-benzamido)dodecanoatedisulfide



To a stirred solution, of 4,4'-disulfanediyldibenzoic acid (1.8 g, 2.47 mmol) under nitrogen, in 25 mL of anhydrous THF, *N,N'*-carbonyldiimidazole (595 mg, 3.70 mmol) was slowly added. The reaction was stirred for one hour at room temperature and then ethyl 11-aminododecanoate (1.13 g, 4.94 mmol) in 5 mL of anhydrous THF were added. The reaction mixture was stirred for additional 3 hours at room temperature, then the solvent was removed under reduced pressure and EtOAc (10 mL) was added. The solution was washed three times (3x10 mL) with water and the organic layer was dried over MgSO_4 and dried giving 2.31 g (78.8%) of product as a white solid.

Data:

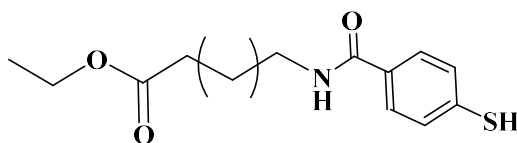
m.p. = 145-146 °C;

$^1\text{H NMR}$ (300 MHz, CDCl_3): δ = 7.65 (d, 4H), 7.42 (d, 4H), 6.57 (bs, 2H), 4.09 (q, 4H), 3.35 (m, 4H), 2.24 (t, 4H), 1.56 (m, 8H), 1.37-1.19 (m, 30H) ppm;

$^{13}\text{C NMR}$ (75 MHz, CDCl_3): δ = 173.9, 166.6, 140.0, 133.6, 127.7, 126.6, 60.1, 40.1, 34.3, 29.6, 29.4, 29.3, 29.2, 29.2, 29.0, 26.9, 24.9, 14.2 ppm;

MS: 751 $[\text{M}+\text{Na}]^+$

5.1.4 Synthesis of ethyl 12-(4-mercaptobenzamido)dodecanoate (**ligand 1**)



After cooling at 0°C, to a stirred suspension of bis-ethyl 11-(4-benzamido)dodecanoatedisulfide (0.91 g, 1.2 mmol) in a mixture of ethanol/THF (1:1, 50 mL) was added slowly NaBH₄ (0.17 g, 4.4 mmol). After complete addition, the mixture was allowed to reach room temperature and react for 4 h. Afterwards, the solvents were evaporated under reduced pressure and the crude was suspended in ethyl acetate (40 mL), washed with diluted HCl aqueous solution (0.1 M, 3x15 mL) and water (3x15 mL). The organic layer was dried over MgSO₄, evaporated to yield 0.79 g (87 %) of compound **1** as a white solid.

Data:

m.p. = 86-87 °C;

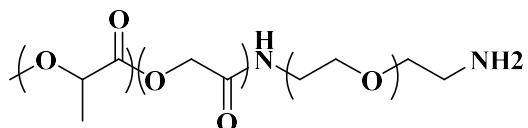
¹H NMR (300 MHz, CDCl₃): δ= 7.61 (d, 2H), 7.26 (d, 2H), 6.25 (bs, 1H), 4.10 (q, 2H), 3.56 (s, 1H), 3.40 (m, 2H), 2.27 (t, 2H), 1.58 (m, 4H), 1.36-1.21 (m, 15H) ppm;

¹³C NMR (75 MHz, CDCl₃): δ= 173.8, 166.7, 135.7, 131.7, 128.4, 127.6, 60.1, 40.0, 34.3, 29.5, 29.3, 29.2, 29.2, 29.1, 29.0, 26.9, 24.9, 14.2 ppm;

MS: 388 [M+Na]⁺

5.2 Synthesis of poly(lactic-co-glycolic acid)-block-poly(ethylene glycol) (PLGA-*b*-PEG) copolymers

5.2.1 Synthesis of PLGA-*b*-PEG-NH₂



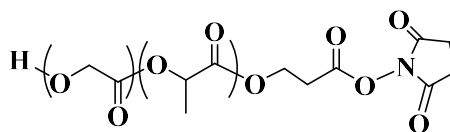
PLGA-COOH (0.5 g, 0.071 mmol) was dissolved in anhydrous tetrahydrofuran (20 mL) followed by addition of 1,1'-Carbonyldiimidazole (CDI, 0.011 g, 0.071 mmol). After 2 h, H₂N-PEG-NH₂ dissolved in 5 mL of anhydrous tetrahydrofuran (0.857 g, 0.285 mmol) has been added to the reaction dropwise.

After 16 h the tetrahydrofuran has been evaporated and the obtained with solid has been dissolved in a small amount of methanol (MeOH, 3 x 10 mL) and precipitated by adding cold diethyl ether (3 x 20 mL) in order to remove the un-reacted products. The resulting white solid PLGA-*b*-PEG-NH₂ (0,554 g, 0,055 mmol) was dried under vacuum and stored at -20 °C, where it is stable for more than one year

Data

¹H-NMR (300 MHz, CDCl₃): δ= 5.28-5.10 (m, 1H), 4.92-4.70 (m, 4H), 3.64 (s, 2H), 1.62-1.50 (d, 3H).

5.2.2 Synthesis of PLGA-NHS

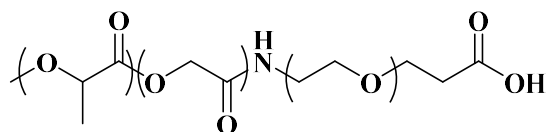


Poly(D,L-lactide-co-glycolide) (PLGA-COOH, 3 g, 0.43 mmol) and *N*-hydroxysuccinimide(NHS, 0.20 g, 1.7 mmol) were dissolved in dichloromethane (15 mL). After cooling at 0°C *N,N'*-dicyclohexylcarbodiimide (DCC, 0.38 mg, 1.8 mmol) was added and the mixture was left to warm up at room temperature and react for 24 h. Afterwards, dicyclohexylurea (DCU) was removed by filtration and PLGA-NHS was precipitated with cold diethylether (20 mL), and repeatedly washed with the same solvent (3 x 10 mL). After drying, the resulted white solid PLGA-NHS (2.91 g, 0.42 mmol) was collected. The product could be stock at -20 °C for no more than one week.

Data

¹H-NMR (300 MHz, CDCl₃): δ = 5.11-5.31 (m, 1H), 4.63-4.92 (2H, m), 1.50-1.61 (m, 3H).

5.2.3 Synthesis of PLGA-*b*-PEG-COOH



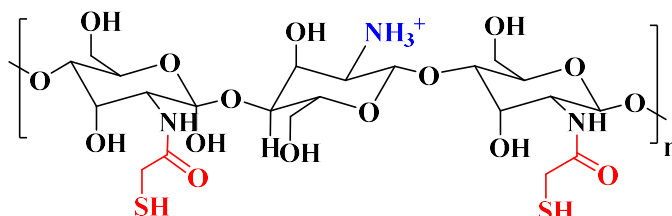
PLGA-NHS (2.91 g, 0.42 mmol) was dissolved in chloroform (20 mL) followed by addition of NH₂-PEG-COOH (1.24 g, 0.42 mmol) and *N,N*-diisopropylethylamine (0.21 mL, 1.20 mmol). After 24 h the copolymer was precipitated with cold diethyl ether (30 mL) and washed with the same solvent (3 x 10 mL) and cold water (3 x 20 mL) in order to remove the unreacted products. The resulting white solid PLGA-*b*-PEG-COOH (3.36 g, 0.33 mmol) was dried under vacuum and stored at -20 °C, where it is stable for more than one year.

Data

¹H-NMR (300 MHz, CDCl₃): δ = 5.11-5.31 (1H, m), 4.63-4.92 (4H, m), 3.63 (s, 2H), 1.50-1.61 (m, 3H).

5.3 Synthesis of modified chitosan chains

5.3.1 Synthesis of Chitosan-Thioglycolic Acid (Chitosan-TGA)

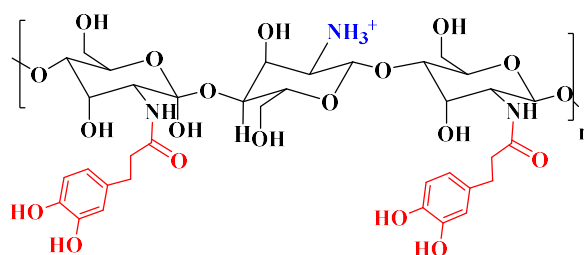


Chitosan glutamate ($\beta(1\rightarrow4)$ linked N-acetyl-D-glucosamine and D-glucosamine glutamate, MW $\sim 50 \div 150$ kDa, DD = 75 \div 90 %) (200 mg) has been dissolved in 20 mL of 1% v/v CH_3COOH solution. After the complete dissolution, 200 μL of TGA (thioglycolic acid, 70% in H_2O) has been added under moderate magnetic stirring. Then, N-(3-Dimethylaminopropyl)-N'-ethylcarbodiimide hydrochloride (50 mg) has been added to the reaction mixture. The reaction was allowed to take place by stirring at room temperature for 6 h. Purification of the thiolated product was performed by overnight dialysis against ultrapure water (cutoff 3.5 kDa). The final volume of product solution was 22.5 mL).

Data

$^1\text{H-NMR}$ (600 MHz, D_2O): $\delta = 4.0\text{-}3.80$ (3H, m), 3.8-3.6 (m, 2H), 3.20 (s, 2H), 3.2-3.1 (m, 1H), 2.08 (m, NHAc).

5.3.2 Synthesis of Chitosan- Hydrocaffeic Acid (Chitosan-HCA)



Hydrocaffeic acid (1.180 g) and N-(3-Dimethylaminopropyl)-N'-ethylcarbodiimide hydrochloride (EDC, 1866.2 mg) were dissolved in 50 mL of deionized water/ethanol mixture (1:1, v/v). This solution was slowly added to a stirred solution (100 mL, pH 5.5) containing 1 g of chitosan glutamate ($\beta(1\rightarrow4)$ linked N-acetyl-D-glucosamine and D-glucosamine glutamate, MW $\sim 50 \div 150$ kDa, DD = 75 \div 90 %) and reacted for 12 h.

The solution pH was maintained at 5.5 to avoid irreversible oxidation of catechol group of hydrocaffeic acid. The resultant chitosan-HCA conjugate has been purified by extensive dialysis against ultrapure water (pH 5.0) for 2 days (Mw cutoff of 3.5 kDa) and then lyophilized.

Data

¹H-NMR (400 MHz, D₂O): δ = 6.5-6.9 (3H, m), 4.0- 3.80 (3H, m), 3.8-3.6 (m, 2H), 3.2-3.1 (m, 1H), 2.08 (m, NHAc).

5.4 Synthesis of chlorotoxin functionalized polymeric nanovectors for the treatment of Glioblastoma Multiforme in a combined approach with radiation therapy

5.4.1 Synthesis of AgNPs

A glucose solution (2 mL, 1.11 M) and NaOH (125 mg, 3.13 mmol) were added under vigorous magnetic stirring to a solution of polyvinylpyrrolidone k25 (PVP, 1.38 g, 0.055 mmol) in water (35 mL) and the mixture was heated to 90 °C; subsequently, a solution of silver nitrate (10 mL, 0.22 M) was rapidly injected into the hot mixture. The reaction was kept at the same temperature for 3 minutes, maintaining magnetic stirring, then it was allowed to cool to room temperature. The so formed AgNPs were purified by washing with water (2 x 20 mL) and concentrated using high speed centrifugation (6000 rpm, 60 min) until the final volume of 5mL.

5.4.2 Synthesis of AgNPs-1

To a solution of ligand **1** (75 mg, 0.21 mmol) in ethanol (17 mL) a water suspension of AgNPs (5 mL) was slowly added. The mixture was allowed to react one hour in the ultrasonic bath then overnight under mechanical stirring at room temperature. After that, the so obtained AgNPs-1 were collected and purified by centrifugation (6000 rpm, 30 min) washing with ethanol (22 mL) 3 times and re-suspended in chloroform (5 mL). Finally, the solvent was gently evaporated under nitrogen flux and the nanoparticles re-suspended again in dimethylformamide (DMF, 5 mL). The so-obtained lipophilic silver nanoparticles were immediately used in the following steps

5.4.3 Synthesis of AgNPs-1-PNPs

50 mg of PLGA-*b*-PEG-COOH (7 kDa-3 kDa, 0.005 mmol) were dissolved into a 5 mL dispersion of AgNPs-1 in DMF. The organic phase was mixed to 50 mL of ultrapure water under vigorous stirring, maintaining water/organic ratio 10/1 with a constant removal of the resulting solution. The mixture was kept under magnetic stirring for 30 minutes then purified and concentrated using centrifugal filter devices (Amicon Ultra, Ultracell membrane with 100.000 NMWL, Millipore, USA) until the final volume of 5 mL that was filtered on syringe filter SterivexTM-GP 0.22 μ m of polyether sulfone (Millipore, USA) and stored at 4 °C.

5.4.4 Synthesis of AgNPs-1-PNPs-Cltx

To a dispersion of AgNPs-1-PNPs (5 mL) in PBS (20 mL, 0.01 M) under magnetic stirring, *N*-hydroxysulfosuccinimide (1.3 mg, 11.0 μmol) and a solution of 1-ethyl-3-(3-dimethylaminopropyl) carbodiimide 0.28 M (7.1 mL) were added. The mixture was allowed reacting at room temperature for one hour. Subsequently, Chlorotoxin (MCMPCFTTDHQMARKCDDCCGGKGRGKCYGPQCLCR, 150 μg , 0.038 μmol) dissolved in 1 mL of water was added and reacted for 24 hours. The mixture was purified washing with PBS solution 3 times and concentrated into centrifugal filter devices (Amicon Ultra, Ultracell membrane with 100.000 NMWL, Millipore, USA), to a final volume of 5 mL. Finally, AgNPs-1-PNPs-Cltx were filtered on syringe filter SterivexTM-GP 0.22 μm of polyether sulfone (Millipore, USA) and stored at 4 °C.

5.5 Synthesis of aptamer functionalized polymeric nanovectors for the treatment of Glioblastoma through the BBB

5.5.1 Synthesis of NVP-BEZ235@PNPs

100 mg of PLGA-b-PEG-COOH and 6 mg (0.013 mmol) of NVPBEZ-235 were dissolved in 10 mL of dichloromethane and admixed to 1 mL of water. Then the two-phase mixture was emulsified, in an ice bath, with a tip probe sonicator (600 W input, 50% ampl) for 45 s. Then 40 mL of 1.25% sodium cholate solution in water was slowly added to the obtained emulsion: the resulted two-phase mixture was further emulsified for 3 min, in an ice bath, at the above-reported amplitude. The solvent was evaporated under reduced pressure and the resulting particles washed and concentrated by using centrifugal filter devices (Amicon Ultra, Ultracell membrane with 100,000 NMWL, Millipore) to a final volume of 2 mL and finally filtered by using a syringe filters Phenex-PES of polyether sulfone (26 mm, 0.20 μm , Phenomenex, Italy).

5.5.2 Synthesis of NVP-BEZ235@PNPs-GintT.4 and NVP-BEZ235@PNPs-SCR

NVP-BEZ235@PNPs were diluted in PBS (5 mL, 0.01 M) and a solution of N-hydroxysulfosuccinimide 2.3 mM (4.3 mL), and a solution of 1-ethyl-3-(3-(dimethylamino)propyl) carbodiimide 0.28 M (1.8 mL) was added. The reaction was carried out at room temperature for 15 min, then 102 pmol of 2'F-Py RNA Gint4.T aptamer or the scrambled sequence (SCR) of the anti-EGFR aptamers,²¹ dissolved in 1 mL of water, was added and left to react for 24 h

5.5.3 Synthesis of BODIPY@PNPs

100 mg of PLGA-b-PEG-COOH and 0.5 mg (0.02 mmol) of BODIPY505-515 were dissolved in 10 mL of dichloromethane and admixed to 1 mL of water. Then the two-phase mixture was emulsified, in an ice bath, with a tip probe sonicator (600 W input, 50% ampl) for 45 s. Then 40 mL of 1.25% sodium cholate solution in water was slowly added to the obtained emulsion: the resulted two-phase mixture was further emulsified for 3 min, in an ice bath, at the above-reported amplitude. The solvent was evaporated under reduced pressure and the resulting particles washed and concentrated by using centrifugal filter devices (Amicon Ultra, Ultracell membrane with 100,000 NMWL, Millipore) to a final volume of 2 mL and finally filtered by using a syringe filters Phenex-PES of polyether sulfone (26 mm, 0.20 μm , Phenomenex, Italy).

5.5.2 Synthesis of BODIPY@PNPs-GintT.4 and BODIPY@PNPs-SCR

BODIPY@PNPs were diluted in PBS (5 mL, 0.01 M) and a solution of N-hydroxysulfosuccinimide 2.3 mM (4.3 mL), and a solution of 1-ethyl-3-(3-(dimethylamino)propyl) carbodiimide 0.28 M (1.8 mL) was added. The reaction was carried out at room temperature for 15 min, then 102 pmol of 2'F-Py RNA Gint4.T aptamer or the scrambled sequence of the anti-EGFR aptamers,²¹ dissolved in 1 mL of water, was added and left to react for 24 h.

5.6 Gold nanorods as tools for photothermal therapy of Barrett Esophagus

5.6.1 Preparation of GNRs-CTAB

Water-soluble GNRs-CTAB were prepared by a seed-mediated growth method. This method provides the formation of a seed solution consisting of vigorously stirred mixture of cetyl trimethylammonium bromide (CTAB, 1 mmol) and chloroauric acid (HAuCl_4 , 0.1 M, 0.08 μmol) was prepared then ice-cold sodium borohydride (NaBH_4 , 0.1 M, 0.39 mmol) was quickly added. Stirring was stopped after 2 min and the seed solution was kept undisturbed for 10 min at 25 °C.

Growth solution was prepared by addition of silver nitrate (AgNO_3 , 0.4 M, 0.4 mmol) to a CTAB (0.1 M, 0.03 mol) and HAuCl_4 (0.1 M, 0.17 mmol) aqueous solution. Afterwards ascorbic acid aqueous solution was added under vigorous stirring at 25 °C and when the growth solution became colorless, the seed solution was added. Stirring was stopped after 5 min and the growth solution was kept undisturbed overnight at 30 °C.

At the beginning the purification of GNRs was done by tangential flow filtration, TFF, which is driven by a peristaltic pump attached to a commercially available diafiltration membrane (Pellicon XL filter device, Biomax membrane with 500.000 NMWL, Millipore, USA), washing with an equal amount of water (300 mL). Then GNRs were diluted in water (5 ml in 50 ml H_2O) and centrifuged (6000 rpm, 40 min). This procedure was repeated twice in order to obtain GNRs-CTAB.

5.6.2 Preparation of GNRs-1

GNRs-CTAB (2.5 mL, 20 mM) were diluted with 2.5 mL of water then added to a solution of ligand ethyl 11-mercaptoundecanoate **1** (30 mg, 0.08 mmol) in 5 mL of ethanol. The mixture was left to react firstly one hour into a sonication bath then overnight at room temperature under mechanical stirring. After that GNRs-1 were precipitated by centrifugation (6000 rpm, 30 min) and washed with ethanol (2x10 mL) in order to remove excess ligand and CTAB. GNRs-1 were then redispersed in 3.5 mL of chloroform, dried under a stream of nitrogen and re-dispersed again in 7 mL of dichloromethane. Finally, the solution was sonicated for 30 minutes and use immediately for next step.

5.6.3 Synthesis of GNRs-1@PMs

100 mg of PLGA-*b*-PEG-COOH were solubilized in 10 ml of CH₂Cl₂ containing GNRs-1 at a concentration of 0.11 mg/ml then 100 ml of ultrapure water were slowly added: the mixture was emulsified with a tip probe sonicator (600 W input, 1 min, 40% ampl).

Afterwards, the residual organic solvent was evaporated under reduced pressure. The particles were then concentrated and purified with a centrifugal filter device (Amicon Ultra, Ultracel membrane with 100,000 NMWL, Millipore, USA) washing with water and filtered on syringe filter Sterivex™-GP 0.22 μm of polyether sulfone (Millipore, USA). Finally, the volume was adjusted to 5 ml with PBS 0.01 M.

5.6.4 Preparation of Curc@PMs

100 mg of PLGA-*b*-PEG-COOH and 10 mg of curcumin were solubilized in 10 ml of CH₂Cl₂. One milliliters of ultrapure water were slowly added to the previous solution and after mutual phase separation, the mixture was emulsified with a tip probe sonicator (600 W input, 2 min, 80% ampl). Afterward residual organic solvent was evaporated under reduced pressure. The so-obtained Curc@PMs were then concentrated and purified with a centrifugal filter device (Amicon Ultra, Ultracel membrane with 100,000 NMWL, Millipore, USA) washing with water and filtered on syringe filter Sterivex™-GP 0.22 μm of polyether sulfone (Millipore, USA). Finally, the volume was adjusted to 5 ml with PBS 0.01 M

5.6.5 Preparation of GNRs-1/Curc@PMs

Solution 1: 100 mg of PLGA-*b*-PEG-COOH were solubilized in 10 ml of CH₂Cl₂ containing GNRs-1 at a concentration of 0.11 mg/ml then 100 ml of ultrapure water were slowly added: the mixture was emulsified with a tip probe sonicator (600 W input, 1 min, 40% ampl).

Solution 2: 10 mg of curcumin were dissolved in 10 ml of CH₂Cl₂ then 100 ml of ultrapure water were slowly added: the mixture was emulsified with a tip probe sonicator (600 W input, 1 min, 40% ampl). Afterwards, solution 1 and 2 were mixed together and re-emulsified (600 W input, 1 min, 40% ampl) in order to allow completing of micelles formation and creation of nanocarriers containing both GNRs-1 and curcumin.

The residual organic solvent was evaporated under reduced pressure. The particles were then concentrated and purified with a centrifugal filter device (Amicon Ultra, Ultracel membrane with 100,000 NMWL, Millipore, USA) washing with water and filtered on syringe filter Sterivex™-GP 0.22 µm of polyether sulfone (Millipore, USA). Finally, the volume was adjusted to 5 ml with PBS 0.01 M.

5.7 Magnesium nanoparticles as a highly biocompatible photothermal agent for hepatocellular carcinoma treatment

5.7.1 Synthesis of Chit–Mg MPs

MgCl₂ (142 mg, 1.5 mmol), naphthalene (192 mg, 1.5 mmol) and chitosan glutamate ($\beta(1\rightarrow4)$ linked N-acetyl-D-glucosamine and D-glucosamine glutamate, MW $\sim 50 \div 150$ kDa, DD = 75 \div 90 %, 284 mg) were dispersed under vigorous stirring in anhydrous THF (10 mL) under argon. After that, lithium (37 mg, 5.4 mmol) was added: the reaction started after 20 minutes highlighted by the colour change from white to black. After 24 hours the microparticles were centrifuged (6000 rpm) and purified by washing 3 times with 20 mL of anhydrous THF in order to remove all the by-products. The so-obtained Chit–Mg MPs were recovered as black powder, dried under vacuum and store at +4 °C.

5.8 Synthesis of Dumbbell-Like Gold-Iron Oxide Nanoparticles (dl-AuFe NPs) as multifunctional nanosystems

5.8.1 Synthesis of dl-AuFe₃O₄ NPs

Iron pentacarbonyl (Fe(CO)₅, 0.15 mL) and gold acetate (Au(ac)₃, 0.18 g) were dissolved in 20 mL of dibenzyl ether that contained surfactants oleic acid (0.1 mL) and oleylamine (0.1 mL). Finally, reducing agent (1,2-hexadecanediol, 350 mg) was added to the flask and the mixture was homogenized by stirring at room temperature under argon atmosphere for 1 hour. Then the temperature was raised to 250°C (in 45 minutes) and the reaction mixture was refluxed for 1 h to form dl-AuFe₃O₄ NPs. Subsequently, the reaction mixture was cooled to room temperature and NPs were precipitated by the addition of ethanol. NPs were purified with centrifugation (6000rpm/10min/3cycles) and finally dispersed in hexane.

5.8.2 Synthesis of dl-AuFe₃O₄@Chit

Chitosan-TGA (16 mg) and chitosan-HCA (16 mg) was dispersed in 10 mL of water and the solution was stirred over night to allow the complete dissolution of the polymers. Then dl-AuFe₃O₄ NPs (20 mg, dried from hexane in nitrogen flux) have been dissolved in 1 ml of chloroform and the obtained suspension has been added dropwise to the chitosan water solution. The mixture was sonicated for 3 minutes by using a Branson sonicator 450 equipped with a microtip (600 W input, 40% ampl). Organic solvent was removed under vacuum and the obtained solution was concentrated and purified washing with water into centrifugal filter devices (Amicon Ultra, Ultracel membrane with 100.000 NMWL, Millipore, USA) until a final volume of 5 mL.

5.9 Synthesis of a novel magnetic resonance–photoacoustic dual imaging nanosystem based on core–shell $\text{Fe}_3\text{O}_4@ \text{SiO}_2@ \text{Au}$ NPs

5.9.1 Synthesis of Native Iron Oxide Nanoparticles, Fe_3O_4 NPs.

Iron triacetylacetonate (0.002 mmol; 1 equiv) was dissolved in diphenyl ether (20 mL). Oleic acid (0.0044 mmol; 2.2 equiv), oleyl amine (0.00395 mmol; 2 equiv), and hexadecanediol (0.00994 mmol; 5 equiv) were then added, and the mixture was heated to reflux (267 °C) for 60 min under nitrogen atmosphere to prevent unwanted oxidation. The mixture was then cooled to room temperature. The Fe_3O_4 NPs were purified by magnetic precipitation with excess of cold ethanol, dispersed in 5 mL of hexane, and washed by four centrifugations (6000 rpm, 45 min) in ethanol. The NPs were redispersed in 5 mL of hexane (30 mg/mL).

5.9.2 Synthesis of Core–Shell Iron Oxide–Silica Nanoparticles $\text{Fe}_3\text{O}_4@\text{SiO}_2$ NPs

Hydrosoluble cetyltrimethylammonium bromide (CTAB) micelles loaded with Fe_3O_4 NPs were prepared. A total of 500 mg of CTAB was dissolved in 25 mL of water and sonicated with a tip-probe sonicator (600 W, 50% amplitude, 6 min) with 2.5 mL of a solution of Fe_3O_4 NPs (73 mg) in hexane. The hexane was then removed by heating at 60 °C for 30 min. The as-synthesized micelles were diluted with 125 mL of water, and 2.5 mL of ethyl acetate and 3.4 mL of a 28% NH_3 solution were added under vigorous stirring. After 10 min, 1.5 mL of MTEOS was added drop-wise, and the mixture was stirred for 3 days at room temperature (25–30 °C). Next, 1.3 mL of 3-aminopropyl-methoxysilane (APTMS) were added dropwise, and the mixture was stirred for 3 more days at room temperature.

The $\text{Fe}_3\text{O}_4@\text{SiO}_2$ NPs were purified by centrifugation (6000 rpm, 1 h) in water. To remove the CTAB, the $\text{Fe}_3\text{O}_4@\text{SiO}_2$ NPs were stirred for 30 min in a mixture of ethanol and acetic acid (95:5) and centrifuged (6000 rpm, 30 min) three times. Finally, the last purifications were performed by centrifugation in ethanol and water (1:1). The $\text{Fe}_3\text{O}_4@\text{SiO}_2$ NPs were dispersed in 20 mL of ethanol (2 mg/mL).

5.9.3 Synthesis of Core–Shell Iron Oxide–Silica–Gold Nanoparticles, $\text{Fe}_3\text{O}_4@\text{SiO}_2@\text{Au}$ NPs

Gold seeds were prepared by reduction of chloroauric acid (HAuCl_4) with tetrakis (hydroxymethyl)phosphonium chloride (THPC). Briefly, 91 mL of water, 3 mL of a 0.2 M NaOH solution, and 2 mL of a THPC solution (120 μL of THPC, 80%, in 10 mL of water) were mixed. Next, 4 mL of a 25 mM HAuCl_4 solution were added under vigorous stirring. Then, 40 mg of $\text{Fe}_3\text{O}_4@\text{SiO}_2$ NPs were dispersed in 40 mL of ethanol and water (1:1). This mixture was diluted with 100 mL of water and vigorously stirred for 10 min. A total of 50 mL of the previous gold seeds solution was added, and the mixture was stirred overnight at room temperature. The resulting $\text{Fe}_3\text{O}_4@\text{SiO}_2$ -gold seeds NPs were purified by centrifugation (6000 rpm, 1 h) in water four times and then dispersed in water (2 mg/mL). The synthesis of an entire shell of gold was performed by a shell-growth reaction. HAuCl_4 was mildly reduced using hydroxylamine as a reducing agent: 101 mg of potassium carbonate was dissolved in 393 mL of water, and then 7.05 mL of a 25 mM solution of chloroauric acid solution was added. The solution was stirred overnight in darkness at room temperature.

To 100 mL of the so-obtained solution, 10 mL of $\text{Fe}_3\text{O}_4@\text{SiO}_2$ -gold seeds NPs solution (20 mg) was added under vigorous stirring. A total of 65 mL of a 1.87 mM hydroxylamine hydrochloride solution was added drop-wise in 30 min. The obtained $\text{Fe}_3\text{O}_4@\text{SiO}_2@\text{Au}$ NPs were purified by centrifugation (6000 rpm, 30 min) in water three times and dispersed in water. The size of the gold shell was increased by iteration of the previous shell-growth reaction.

5.9.4 Synthesis of Lipophilic Fe₃O₄@SiO₂@Au NPs by Ligand Exchange

The hydrophilic Fe₃O₄@SiO₂@Au NPs were free of any organic coating agent, and they were made lipophilic by organic coating with the ligand ethyl 11-(4-mercaptobenzamido)undecanoate (ligand 1). A total of 50 mg of ligand 1 was dissolved in 10 mL of ethanol. A total of 3.5 mg of Fe₃O₄@SiO₂@Au NPs was dispersed in 10 mL of water. The two solutions were mixed, sonicated in an ultrasound bath for 45 min, and left to react overnight on a vortexer. These lipophilic NPs were purified by centrifugation (6000 rpm, 15 min) in ethanol and water (1:1) twice and dispersed in chloroform.

5.9.5 Synthesis of Fe₃O₄@SiO₂@Au@PMs.

A solution of lipophilic Fe₃O₄@SiO₂@Au NPs (3 mg) and PLGA-b-PEG-NH₂ (50 mg) in 4 mL of chloroform was prepared. This organic mixture was sonicated (600 W input, 50% amplitude, 3 min) with 40 mL of water in an ice bath. The organic solvent was removed under vacuum, and the nanoparticles were purified and concentrated to 2 mL with centrifugal filter devices (Amicon Ultra, Ultracel membrane with 100.000 NMWL, Millipore).

5.9.6 Conjugation of Folic Acid on Fe₃O₄@SiO₂@AuNPs@PMs

The surface of the PMs was conjugated with the folic acid as a targeting agent. A total of 2 mg of folic acid was dispersed in 0.1 mL drops of DMSO and diluted in 1 mL of water. To activate the carboxylic moiety of the active targeting, 1 mL of a 1-ethyl-3-(3-(dimethylamino)propyl)carbodiimide (EDC) solution (3.5 mg in 5 mL) and 1 mL of N-hydroxysulfosuccinimide (sulfo-NHS) solution (4.4 mg in 5 mL) were added to the acid folic, and the obtained solution was stirred for 30 min. Next, 2 mL of the Fe₃O₄@SiO₂@AuNPs@PMs were added, and the mixture was stirred overnight at room temperature. The conjugated PMs were purified and concentrated into centrifugal filter devices (Amicon Ultra, Ultracel membrane with 100.000 NMWL, Millipore).

6. Bibliography

1. Shi, J., Kantoff, P. W., Wooster, R. & Farokhzad, O. C. Cancer nanomedicine: progress, challenges and opportunities. *Nat. Rev. Cancer* **17**, 20–37 (2016).
2. Bray, F., Jemal, A., Grey, N., Ferlay, J. & Forman, D. Global cancer transitions according to the Human Development Index (2008-2030): A population-based study. *Lancet Oncol.* **13**, 790–801 (2012).
3. Siegel, R. L., Miller, K. D. & Jemal, A. Cancer statistics, 2017. *CA. Cancer J. Clin.* **67**, 7–30 (2017).
4. Shi, J., Votruba, A. R., Farokhzad, O. C. & Langer, R. Nanotechnology in drug delivery and tissue engineering: From discovery to applications. *Nano Lett.* **10**, 3223–3230 (2010).
5. Ainslie, K. M. & Desai, T. a. Microfabricated implants for applications in therapeutic delivery, tissue engineering, and biosensing. *Lab Chip* **8**, 1864 (2008).
6. Barenholz, Y. Doxil® - The first FDA-approved nano-drug: Lessons learned. *J. Control. Release* **160**, 117–134 (2012).
7. Roser, M., Fischer, D. & Kissel, T. Surface-modified biodegradable albumin nano- and microspheres. II: Effect of surface charges on in vitro phagocytosis and biodistribution in rats. *Eur. J. Pharm. Biopharm.* **46**, 255–263 (1998).
8. Petersen, G. H., Alzghari, S. K., Chee, W., Sankari, S. S. & La-Beck, N. M. Meta-analysis of clinical and preclinical studies comparing the anticancer efficacy of liposomal versus conventional non-liposomal doxorubicin. *J. Control. Release* **232**, 255–264 (2016).
9. Ahn, H. K. *et al.* A phase II trial of Cremophor EL-free paclitaxel (Genexol-PM) and gemcitabine in patients with advanced non-small cell lung cancer. *Cancer Chemother. Pharmacol.* **74**, 277–282 (2014).
10. Kato, K. *et al.* Phase II study of NK105, a paclitaxel-incorporating micellar nanoparticle, for previously treated advanced or recurrent gastric cancer. *Invest. New Drugs* **30**, 1621–1627 (2012).
11. Hrkach, J. *et al.* Preclinical Development and Clinical Translation of a PSMA-Targeted Docetaxel Nanoparticle with a Differentiated Pharmacological Profile. *Sci. Transl. Med.* **4**, 128ra39-128ra39 (2012).
12. Jun, Y. W., Lee, J. H. & Cheon, J. Chemical design of nanoparticle probes for high-performance magnetic resonance imaging. *Angew. Chemie - Int. Ed.* **47**, 5122–5135 (2008).
13. Choi, K. Y., Liu, G., Lee, S. & Chen, X. Theranostic nanoplatforams for simultaneous cancer imaging and therapy: current approaches and future perspectives. *Nanoscale* **4**, 330–342 (2012).
14. Barreto, J. A. *et al.* Nanomaterials: Applications in cancer imaging and therapy. *Adv. Mater.* **23**, (2011).
15. Carmeliet, P. & Jain, R. K. Angiogenesis in cancer and other diseases. *Nature* **407**, 249–257 (2000).
16. Iyer, A. K., Khaled, G., Fang, J. & Maeda, H. Exploiting the enhanced permeability and retention effect for tumor targeting. *Drug Discov. Today* **11**, 812–818 (2006).
17. Couvreur, P. & Vauthier, C. *Nanotechnology: Intelligent design to treat complex disease. Pharmaceutical Research* **23**, (2006).
18. Torchilin, V. Tumor delivery of macromolecular drugs based on the EPR effect. *Adv. Drug Deliv. Rev.* **63**, 131–135 (2011).
19. Xu, X., Ho, W., Zhang, X., Bertrand, N. & Farokhzad, O. Cancer nanomedicine: From targeted delivery to combination therapy. *Trends Mol. Med.* **21**, 223–232 (2015).
20. Gelaye, B., Rondon, M., Araya, P. R. & A, P. M. HHS Public Access. **3**, 973–982 (2016).
21. Corsi, F. *et al.* HER2 expression in breast cancer cells is downregulated upon active targeting by antibody-engineered multifunctional nanoparticles in mice. *ACS Nano* **5**, 6383–6393 (2011).
22. Li, X. *et al.* Epidermal growth factor-ferritin H-chain protein nanoparticles for tumor active targeting. *Small* **8**, 2505–2514 (2012).
23. Shahin, M., Ahmed, S., Kaur, K. & Lavasanifar, A. Decoration of polymeric micelles with cancer-specific peptide ligands for active targeting of paclitaxel. *Biomaterials* **32**, 5123–5133 (2011).

24. Wu, X., Chen, J., Wu, M. & Zhao, J. X. Aptamers: Active targeting ligands for cancer diagnosis and therapy. *Theranostics* **5**, 322–344 (2015).
25. Peer, D. *et al.* Nanocarriers as an emerging platform for cancer therapy. *Nat. Nanotechnol.* **2**, 751–760 (2007).
26. Lim, E.-K. *et al.* Nanomaterials for Theranostics: Recent Advances and Future Challenges. *Chem. Rev.* **115**, 327–394 (2015).
27. Ferrari, M. Cancer nanotechnology: opportunities and challenges. *Nat. Rev. Cancer* **5**, 161–171 (2005).
28. Banik, B. L., Fattahi, P. & Brown, J. L. Polymeric nanoparticles: The future of nanomedicine. *Wiley Interdiscip. Rev. Nanomedicine Nanobiotechnology* **8**, 271–299 (2016).
29. Panyam, J. & Labhasetwar, V. Biodegradable nanoparticles for drug and gene delivery to cells and tissue. *Adv. Drug Deliv. Rev.* **55**, 329–347 (2003).
30. Duan, X. & Li, Y. Physicochemical characteristics of nanoparticles affect circulation, biodistribution, cellular internalization, and trafficking. *Small* **9**, 1521–1532 (2013).
31. Champion, J. A., Walker, A. & Mitragotri, S. Role of particle size in phagocytosis of polymeric microspheres. *Pharm. Res.* **25**, 1815–1821 (2008).
32. Davis, M. E., Chen, Z. (Georgia) & Shin, D. M. Nanoparticle therapeutics: an emerging treatment modality for cancer. *Nat. Rev. Drug Discov.* **7**, 771–782 (2008).
33. Arvizo, R. R. *et al.* Modulating pharmacokinetics, tumor uptake and biodistribution by engineered nanoparticles. *PLoS One* **6**, 3–8 (2011).
34. Xiao, K. *et al.* The effect of surface charge on in vivo biodistribution of PEG-oligocholeic acid based micellar nanoparticles. *Biomaterials* **32**, 3435–3446 (2011).
35. Mohanraj, V., Chen, Y. & Chen, M. &. Nanoparticles – A Review. *Trop. J. Pharm. Res. Trop J Pharm Res* **5**, 561–573 (2006).
36. Torchilin, V. P. Targeted pharmaceutical nanocarriers for cancer therapy and imaging. *AAPS J.* **9**, E128–E147 (2007).
37. Owens, D. E. & Peppas, N. A. Opsonization, biodistribution, and pharmacokinetics of polymeric nanoparticles. *Int. J. Pharm.* **307**, 93–102 (2006).
38. Li, S. & McCarthy, S. Influence of crystallinity and stereochemistry on the enzymatic degradation of poly(lactide)s. *Macromolecules* **32**, 4454–4456 (1999).
39. Gross, R. A., MacDonald, R. T. & McCarthy, S. P. Enzymatic degradability of poly(lactide): Effects of chain stereochemistry and material crystallinity. *Am. Chem. Soc. Polym. Prepr. Div. Polym. Chem.* **37**, 436–437 (1996).
40. Muthu, M. Nanoparticles Based on PLGA and its Co-Polymer: An Overview. *Asian J. Pharm.* **3**, 266–273 (2009).
41. Locatelli, E. & Franchini, M. C. Biodegradable PLGA-b-PEG polymeric nanoparticles: Synthesis, properties, and nanomedical applications as drug delivery system. *J. Nanoparticle Res.* **14**, 1–17 (2012).
42. Rao, J. P. & Geckeler, K. E. Polymer nanoparticles: Preparation techniques and size-control parameters. *Prog. Polym. Sci.* **36**, 887–913 (2011).
43. Anton, N., Benoit, J. P. & Saulnier, P. Design and production of nanoparticles formulated from nano-emulsion templates-A review. *J. Control. Release* **128**, 185–199 (2008).
44. Rao, J. P. & Geckeler, K. E. Polymer nanoparticles: Preparation techniques and size-control parameters. *Prog. Polym. Sci.* **36**, 887–913 (2011).
45. Schubert, S., Delaney, Jr, J. T. & Schubert, U. S. Nanoprecipitation and nanoformulation of polymers: from history to powerful possibilities beyond poly(lactic acid). *Soft Matter* **7**, 1581 (2011).
46. Lepock, J. R. Cellular effects of hyperthermia: Relevance to the minimum dose for thermal damage. *Int. J. Hyperth.* **19**, 252–266 (2003).
47. Song, C. W. Effect of Local Hyperthermia on BloodFlow and Microenvironment : (1984).
48. Hildebrandt, B. *et al.* The cellular and molecular basis of hyperthermia. **43**, 33–56 (2002).

49. Wust, P. *et al.* Review Hyperthermia in combined treatment of cancer. 487–497
50. Behrouzkia, Z., Joveini, Z., Keshavarzi, B., Eyvazzadeh, N. & Aghdam, R. Z. Hyperthermia: How can it be used? *Oman Med. J.* **31**, 89–97 (2016).
51. Hervault, A. & Thanh, N. T. K. Magnetic nanoparticle-based therapeutic agents for thermo-chemotherapy treatment of cancer. *Nanoscale* **6**, 11553–11573 (2014).
52. Maier-Hauff, K. *et al.* Efficacy and safety of intratumoral thermotherapy using magnetic iron-oxide nanoparticles combined with external beam radiotherapy on patients with recurrent glioblastoma multiforme. *J. Neurooncol.* **103**, 317–324 (2011).
53. Jaque, D. *et al.* Nanoparticles for photothermal therapies. *Nanoscale* **6**, 9494–9530 (2014).
54. O’Neal, D. P., Hirsch, L. R., Halas, N. J., Payne, J. D. & West, J. L. Photo-thermal tumor ablation in mice using near infrared-absorbing nanoparticles. *Cancer Lett.* **209**, 171–176 (2004).
55. Weissleder, R. A clearer vision for in vivo imaging Progress continues in the development of smaller , more penetrable probes for biological imaging . Toward the phosphoproteome. *Nat. Biotechnol.* **19**, 316–317 (2001).
56. West, J. L. Nanoshell-mediated near-infrared thermal therapy of tumors under magnetic resonance guidance. **100**, (2003).
57. Kreibig, U. & Vollmer, M. Optical Properties of Metal Clusters. *J. Am. Chem. Soc.* **118**, 6098–6098 (1995).
58. Mulvaney, P. Surface Plasmon Spectroscopy of Nanosized Metal Particles. *Langmuir* **12**, 788–800 (1996).
59. Sharma, V., Park, K. & Srinivasarao, M. Colloidal dispersion of gold nanorods: Historical background, optical properties, seed-mediated synthesis, shape separation and self-assembly. *Mater. Sci. Eng. R Reports* **65**, 1–38 (2009).
60. Burrows, N. D. *et al.* Surface Chemistry of Gold Nanorods. *Langmuir* **32**, 9905–9921 (2016).
61. Jain, P. K., Lee, K. S., El-Sayed, I. H. & El-Sayed, M. A. Calculated absorption and scattering properties of gold nanoparticles of different size, shape, and composition: Applications in biological imaging and biomedicine. *J. Phys. Chem. B* **110**, 7238–7248 (2006).
62. Locatelli, E., Monaco, I. & Comes Franchini, M. Surface modifications of gold nanorods for applications in nanomedicine. *RSC Adv.* **5**, 21681–21699 (2015).
63. Maguire, M. E. & Cowan, J. A. Magnesium chemistry and biochemistry [Review]. *BioMetals* **15**, 203–210 (2002).
64. Saris, N.-E. L. E. A. Magnesium An update on physiological, clinical and analytical aspects. *Clin. Chim. Acta* **294**, 1–26 (2000).
65. Witte, F. Reprint of: The history of biodegradable magnesium implants: A review. *Acta Biomater.* **23**, S28–S40 (2015).
66. Walker, J., Shadanbaz, S., Woodfield, T. B. F., Staiger, M. P. & Dias, G. J. Magnesium biomaterials for orthopedic application: A review from a biological perspective. *J. Biomed. Mater. Res. - Part B Appl. Biomater.* **102**, 1316–1331 (2014).
67. Jeong, H.-H., Mark, A. G. & Fischer, P. Magnesium plasmonics for UV applications and chiral sensing. *Chem. Commun.* **52**, 12179–12182 (2016).
68. Sanz, J. M. *et al.* UV plasmonic behavior of various metal nanoparticles in the near- and far-field regimes: Geometry and substrate effects. *J. Phys. Chem. C* **117**, 19606–19615 (2013).
69. Sterl, F. *et al.* Magnesium as novel material for active plasmonics in the visible wavelength range. *Nano Lett.* **15**, 7949–7955 (2015).
70. comes franchini, mauro *et al.* One-pot synthesis of magnesium nanoparticles embedded in chitosan microparticles: a highly biocompatible tool for in vivo cancer treatment. *J. Mater. Chem. B* **4**, 207–211 (2015).
71. Locatelli, E. *et al.* Surface chemistry and entrapment of magnesium nanoparticles into polymeric micelles: a highly biocompatible tool for photothermal therapy. *Chem. Commun.* **50**, 7783 (2014).
72. Wang, Q., Xie, L., He, Z., Di, D. & Liu, J. Biodegradable magnesium nanoparticle-enhanced laser hyperthermia

- therapy. *Int. J. Nanomedicine* **7**, 4715–4725 (2012).
73. Jin, C., He, Z.-Z., Zhang, J., Yang, X.-Y. & Liu, J. Enhanced Thermographic Detection of Skin Cancer Through Combining Laser Scanning and Biodegradable Nanoparticles. *J. Nanotechnol. Eng. Med.* **4**, 11004 (2013).
 74. Lee, D.-E. *et al.* Multifunctional nanoparticles for multimodal imaging and theragnosis. *Chem. Soc. Rev.* **41**, 2656–2672 (2012).
 75. Weber, J., Beard, P. C. & Bohndiek, S. E. Contrast agents for molecular photoacoustic imaging. *Nat. Methods* **13**, 639–650 (2016).
 76. Louie, A. Multimodality Imaging Probes: Design and Challenges. *Chem. Rev.* **110**, 3146–3195 (2010).
 77. Wang, L. V & Yao, J. A practical guide to photoacoustic tomography in the life sciences. *Nat. Methods* **13**, 627–638 (2016).
 78. Wang, L. V. & Gao, L. *Photoacoustic Microscopy and Computed Tomography: From Bench to Bedside. Annual Review of Biomedical Engineering* **16**, (2014).
 79. van den Berg, P. J., Bansal, R., Daoudi, K., Steenbergen, W. & Prakash, J. Preclinical detection of liver fibrosis using dual-modality photoacoustic/ultrasound system. *Biomed. Opt. Express* **7**, 5081 (2016).
 80. Ermilov, S. A. *et al.* Laser optoacoustic imaging system for detection of breast cancer. *J. Biomed. Opt.* **14**, 24007 (2009).
 81. Heijblom, M. *et al.* Visualizing breast cancer using the Twente photoacoustic mammoscope: What do we learn from twelve new patient measurements? *Opt. Express* **20**, 11582 (2012).
 82. Luke, G. P., Myers, J. N., Emelianov, S. Y. & Sokolov, K. V. Sentinel Lymph Node Biopsy Revisited : Ultrasound-Guided Photoacoustic Detection of Micrometastases Using Molecularly Targeted Plasmonic Nanosensors. 5397–5409 (2014). doi:10.1158/0008-5472.CAN-14-0796
 83. Yao, J. & Wang, L. V. Photoacoustic brain imaging: from microscopic to macroscopic scales. *Neurophotonics* **1**, 11003 (2014).
 84. Huang, C. Aberration correction for transcranial photoacoustic tomography of primates employing adjunct image data. *J. Biomed. Opt.* **17**, 66016 (2012).
 85. Levi, J. *et al.* Molecular Photoacoustic Imaging of Follicular Thyroid Carcinoma. *Clin. Cancer Res.* **19**, 1494–1502 (2013).
 86. Li, P. *et al.* In vivo Photoacoustic Molecular Imaging with Simultaneous Multiple Selective Targeting Using Antibody-Conjugated Gold Nanorods. **16**, 18605–18615 (2008).
 87. Laufer, J. *et al.* In vivo preclinical photoacoustic imaging of tumor vasculature development and therapy. *J. Biomed. Opt.* **17**, 56016 (2012).
 88. Wang, P., Wang, P., Wang, H.-W. & Cheng, J.-X. Mapping lipid and collagen by multispectral photoacoustic imaging of chemical bond vibration. *J. Biomed. Opt.* **17**, 960101 (2012).
 89. Wu, C., Liang, X. & Jiang, H. Metal nanoshells as a contrast agent in near-infrared diffuse optical tomography. *Opt. Commun.* **253**, 214–221 (2005).
 90. Erickson, T. a & Tunnell, J. W. *Gold Nanoshells in Biomedical Applications. Nanomaterials for the life Science Vol. 3: Mixed Metal Nanomaterials* **3**, (2007).
 91. Huang, H.-C., Barua, S., Sharma, G., Dey, S. K. & Rege, K. Inorganic nanoparticles for cancer imaging and therapy. *J. Control. Release* **155**, 344–357 (2011).
 92. Preston, T. C. & Signorell, R. Growth and Optical Properties of Gold Nanoshells Prior to the Formation of a Continuous Metallic Layer. **3**,
 93. Mody, V., Siwale, R., Singh, A. & Mody, H. Introduction to metallic nanoparticles. *J. Pharm. Bioallied Sci.* **2**, 282 (2010).
 94. Na, H. Bin, Song, I. C. & Hyeon, T. Inorganic nanoparticles for MRI contrast agents. *Adv. Mater.* **21**, 2133–2148 (2009).

95. Ai, T. *et al.* A historical overview of Magnetic Resonance Imaging, focusing on technological innovations. *Invest. Radiol.* **47**, 725–741 (2012).
96. Bellin, M.-F. MR contrast agents, the old and the new. *Eur. J. Radiol.* **60**, 314–323 (2006).
97. Lohrke, J. *et al.* 25 Years of Contrast-Enhanced MRI: Developments, Current Challenges and Future Perspectives. *Adv. Ther.* **33**, 1–28 (2016).
98. Shokrollahi, H. Contrast agents for MRI. *Mater. Sci. Eng. C* **33**, 4485–4497 (2013).
99. Rogosnitzky, M. & Branch, S. Gadolinium-based contrast agent toxicity: a review of known and proposed mechanisms. *BioMetals* **29**, 365–376 (2016).
100. Manuscript, A. Molecular MR Contrast Agents for the Detection of Cancer: Past and Present. *Semin. Oncol.* **38**, 42–54 (2011).
101. Bashir, M. R., Bhatti, L., Marin, D. & Nelson, R. C. Emerging applications for ferumoxytol as a contrast agent in MRI. *J. Magn. Reson. Imaging* **41**, 884–898 (2015).
102. Lee, J.-H. *et al.* Artificially engineered magnetic nanoparticles for ultra-sensitive molecular imaging. *Nat. Med.* **13**, 95–99 (2007).
103. Smolensky, E. D., Park, H. Y. E., Berquó, T. S. & Pierre, V. C. Surface functionalization of magnetic iron oxide nanoparticles for MRI applications - effect of anchoring group and ligand exchange protocol. *Contrast Media Mol. Imaging* **6**, 189–199 (2011).
104. Vasanawala, S. S. *et al.* Safety and technique of ferumoxytol administration for MRI. *Magn. Reson. Med.* **75**, 2107–2111 (2016).
105. Love, J. C., Estroff, L. A., Kriebel, J. K., Nuzzo, R. G. & Whitesides, G. M. *Self-assembled monolayers of thiolates on metals as a form of nanotechnology.* *Chemical Reviews* **105**, (2005).
106. Nallathamby, P. D., Hopf, J., Irimata, L. E., McGinnity, T. L. & Roeder, R. K. Preparation of fluorescent Au–SiO₂ core–shell nanoparticles and nanorods with tunable silica shell thickness and surface modification for immunotargeting. *J. Mater. Chem. B* **4**, 5418–5428 (2016).
107. Jana, N. R., Earhart, C. & Ying, J. Y. Synthesis of water-soluble and functionalized nanoparticles by silica coating. *Chem. Mater.* **19**, 5074–5082 (2007).
108. Ding, H. L. *et al.* Fe₃O₄@SiO₂ core/shell nanoparticles: The silica coating regulations with a single core for different core sizes and shell thicknesses. *Chem. Mater.* **24**, 4572–4580 (2012).
109. Chen, Y., Frey, W., Kim, S., Kruizinga, P. & Emelianov, S. Amplifiers. **11**, 348–354 (2012).
110. Harris-Birtill, David; Singh, Mohan; Zhou, Yu; Shah, A; Ruenraroengsak, P; Gallina, M; Hanna, G; Cass, Anthony; Porter, Alexandra; Bamber, Jeffrey; Elson, D. Gold nanorod reshaping in vitro and in vivo using a continuous wave laser. *PLoS ONE PONE-D-17-19585 (In Press)*. 1–21 (2017). doi:10.1371/journal.pone.0185990
111. Locatelli, E. *et al.* Lipophilic silver nanoparticles and their polymeric entrapment into targeted-PEG-based micelles for the treatment of glioblastoma. *Adv. Healthc. Mater.* **1**, 342–347 (2012).
112. Bae, K. H. *et al.* Chitosan Oligosaccharide-Stabilized Ferrimagnetic Iron Oxide Nanocubes for Magnetically Modulated Cancer Hyperthermia. 5266–5273 (2012).
113. Guo, L. *et al.* Combinatorial photothermal and immuno cancer therapy using chitosan-coated hollow copper sulfide nanoparticles. *ACS Nano* **8**, 5670–5681 (2014).
114. Tamborini, M. *et al.* A Combined Approach Employing Chlorotoxin-Nanovectors and Low Dose Radiation to Reach Infiltrating Tumor Niches in Glioblastoma. *ACS Nano* **10**, 2509–2520 (2016).
115. Monaco, I. *et al.* Aptamer Functionalization of Nanosystems for Glioblastoma Targeting through the Blood-Brain Barrier. *J. Med. Chem.* **60**, 4510–4516 (2017).
116. Soroceanu, L., Gillespie, Y., Khazaeli, M. B. & Sontheimer, H. Use of Chlorotoxin for Targeting of Primary Brain Tumors Use of Chlorotoxin for Targeting of Primary Brain Tumors. 4871–4879 (1998).
117. DeBin, J. A., Maggio, J. E. & Strichartz, G. R. Purification and characterization of chlorotoxin, a chloride channel

- ligand from the venom of the scorpion. *Am. J. Physiol.* **264**, C361-9 (1993).
118. Bartczak, D. & Kanaras, A. G. Preparation of peptide-functionalized gold nanoparticles using one pot EDC/Sulfo-NHS coupling. *Langmuir* **27**, 10119–10123 (2011).
 119. Yuan, H. *et al.* Radiation-induced permeability and leukocyte adhesion in the rat blood-brain barrier: Modulation with anti-ICAM-1 antibodies. *Brain Res.* **969**, 59–69 (2003).
 120. Baumann, B. C. *et al.* Enhancing the efficacy of drug-loaded nanocarriers against brain tumors by targeted radiation therapy. *Oncotarget* **4**, 64–79 (2013).
 121. Sawyer, A. J. *et al.* Convection-enhanced delivery of camptothecin-loaded polymer nanoparticles for treatment of intracranial tumors. *Drug Deliv. Transl. Res.* **1**, 34–42 (2011).
 122. Thorne, R. G. & Nicholson, C. In vivo diffusion analysis with quantum dots and dextrans predicts the width of brain extracellular space. *Proc. Natl. Acad. Sci. U. S. A.* **103**, 5567–72 (2006).
 123. Camorani, S. *et al.* Inhibition of Receptor Signaling and of Glioblastoma-derived Tumor Growth by a Novel PDGFR β Aptamer. *Mol. Ther.* **22**, 828–841 (2014).
 124. Lin, F., Chandrasekaran, G., de Gooijer, M. C., Beijnen, J. H. & van Tellingen, O. Determination of NVP-BEZ235, a dual PI3K and mTOR inhibitor, in human and mouse plasma and in mouse tissue homogenates by reversed-phase high-performance liquid chromatography with fluorescence detection. *J. Chromatogr. B Anal. Technol. Biomed. Life Sci.* **901**, 9–17 (2012).
 125. Xin, P. *et al.* Efficacy of the dual PI3K and mTOR inhibitor NVP-BEZ235 in combination with imatinib mesylate against chronic myelogenous leukemia cell lines. *Drug Des. Devel. Ther.* **11**, 1115–1126 (2017).
 126. Nikoobakht, B. & El-Sayed, M. A. Preparation and growth mechanism of gold nanorods (NRs) using seed-mediated growth method. *Chem. Mater.* **15**, 1957–1962 (2003).
 127. Nikoobakht, B. & El-Sayed, M. A. Evidence for bilayer assembly of cationic surfactants on the surface of gold nanorods. *Langmuir* **17**, 6368–6374 (2001).
 128. Murphy, C. J. *et al.* Anisotropic metal nanoparticles: Synthesis, assembly, and optical applications. *J. Phys. Chem. B* **109**, 13857–13870 (2005).
 129. Wilken, R., Veena, M. S., Wang, M. B. & Srivatsan, E. S. Curcumin: A review of anti-cancer properties and therapeutic activity in head and neck squamous cell carcinoma. *Mol. Cancer* **10**, 12 (2011).
 130. Sharma, R. A. *et al.* Phase I Clinical Trial of Oral Curcumin : Biomarkers of Systemic Activity and Compliance. *Phase I Clinical Trial of Oral Curcumin : Biomarkers of Systemic Activity and Compliance.* **10**, 6847–6854 (2004).
 131. Park, S. H. *et al.* An intratumoral injectable, electrostatic, cross-linkable curcumin depot and synergistic enhancement of anticancer activity. *NPG Asia Mater.* **9**, e397 (2017).
 132. Dormidontova, E. E. Micellization kinetics in block copolymer solutions: scaling model. *Macromolecules* **32**, 7630–7644 (1999).
 133. Baatout, S. *et al.* Effect of curcuma on radiation-induced apoptosis in human cancer cells. 321–329 (2004).
 134. Mary, Q., Kingdom, U. & Madrid, D. Synthesis of Colloidal Magnesium : A Near Room. 400–402 (2007).
 135. Haas, I. & Gedanken, A. Synthesis of metallic magnesium nanoparticles by sonoelectrochemistry. *Chem. Commun. (Camb)*. 1795–1797 (2008). doi:10.1039/b717670h
 136. Kooi, B. J., Palasantzas, G. & De Hosson, J. T. M. Gas-phase synthesis of magnesium nanoparticles: A high-resolution transmission electron microscopy study. *Appl. Phys. Lett.* **89**, 1–4 (2006).
 137. Aurbach, D. *et al.* Prototype systems for rechargeable magnesium batteries. *Nature* **407**, 724–727 (2000).
 138. Song, M. R., Chen, M. & Zhang, Z. J. Preparation and characterization of Mg nanoparticles. *Mater. Charact.* **59**, 514–518 (2008).
 139. Balogh, J. *et al.* Hepatocellular carcinoma: a review. *J. Hepatocell. carcinoma* **3**, 41–53 (2016).
 140. Kostevsek, N. *et al.* The one-step synthesis and surface functionalization of dumbbell-like gold–iron oxide nanoparticles: a chitosan-based nanotheranostic system. *Chem. Commun.* **52**, 378–381 (2015).

141. Monaco, I. *et al.* Synthesis of Lipophilic Core-Shell Fe₃O₄@SiO₂@Au Nanoparticles and Polymeric Entrapment into Nanomicelles: A Novel Nanosystem for in Vivo Active Targeting and Magnetic Resonance-Photoacoustic Dual Imaging. *Bioconjug. Chem.* **28**, 1382–1390 (2017).
142. Sun, S. & Zeng, H. Size-controlled synthesis of magnetite nanoparticles. *J. Am. Chem. Soc.* **124**, 8204–8205 (2002).
143. Duff, D. G., Baiker, A. & Edwards, P. P. A new hydrosol of gold clusters. *J. Chem. Soc. Chem. Commun.* **272**, 96 (1993).